MONITORING AND MODELLING OF THE PALAEOLITHIC ARCHAEOLOGICAL RESOURCE AT CHARD JUNCTION QUARRY, HODGE DITCH PHASES II & III ASSESSMENT STAGE (5695)

Project Report Stage II

Prepared for

English Heritage
1 Waterhouse Square
138-142 Holborn
London, EC1N 2ST

For funding from the Historic Environment Enabling Fund (HEEP), English Heritage

A Project administered by University of Southampton

Principal Investigator
Professor Tony Brown, University of Southampton with Dr P. S Toms & Dr L. S. Basell

Project reference Number: 5695
Version: 1.0
UPD date: 10th November 2009
Status: Report Stage 2
Contact: Tony Brown, Project Manager
Submission Date: 28th October 2011
Palaeoecology Laboratory University of Southampton
School of Geography
Highfields Campus
Southampton
SO17 1BJ

INVESTOR IN PEOPLE

UNIVERSITY OF Southampton
School of Geography

Contents

1	**Executive summary……..**	1
2	**The evaluation of gamma cps (Gcps) logs……**	3
3	**Digital granulometry ……**	10
4	**Ground laser scanning…….**	22
5	**Clast analysis and burial dating sampling…….**	60
6	**The OSL dating programme……**	68
7	**Monitoring and mapping (Hodge Ditch Phase II) ……**	81
8	**Palaeoenvironmental provision…….**	88
9	**3D (volumetric) modelling……..**	92
10	**Outreach……**	110
11	**Project design for Stage 3……..**	111
12	**Concluding Comments……**	113
13	**References……..**	116

Appendix A: Guidesheets	120
Appendix B: Grain size & Sedimetrics results from other sites	123
Appendix C: Clast lithological data	128
Appendix D: OSL report	136
Appendix E: Catalogue of OSL sample locations (separate file)	189
Appendix F: Stage 3 budget	190

MONITORING AND MODELLING OF THE PALAEOLITHIC ARCHAEOLOGICAL RESOURCE AT CHARD JUNCTION QUARRY, HODGE DITCH PHASES II & III. ASSESSMENT STAGE 2. (PNUM5695)

This report of Stage 2 activities is structured by the Stage 2 Assessment Stage Aims and Objectives as per the Updated Project Design (UPD) of 10th November 2009. These are reported on in the order in which the objectives were specified in the UPD with additional information contained in the Appendices.

1 Executive summary

This report gives the results of the Stage II of the Project 5695 on Chard Junction Quarry conducted between January 2010 and March 2011. The project combined the development of new methodology with the monitoring of this difficult aggregate site.

The use of Gamma cps down-borehole log data is shown to be useful in aggregate sites for differentiating debris flow or matrix supported gravels from fluvial gravels where the geology permits. This has value in archaeological assessments as debris deposits (diamicton) and matrix supported gravels are typically periglacial making any lithics contained in them generally less useful in behavioural analyses and interpretations, thus warranting either no, or less frequent, monitoring. A single-page guide sheet is included which explains the use of Gcps for archaeologists and heritage planners. A similar trial was also undertaken of the use of digital photography for the analysis of sediment grain size. Grain size is the most fundamental parameter, and descriptor of gravels but in order to obtain statistically reliable results very large samples (over 100 Kg) are required. The result has been that grain size analysis is rarely undertaken by archaeologists. By adapting a commercially available software system (Sedimetrics©) it is shown that, with the use of a frame on relatively flat faces, digital photography can provide a good proxy for grain size analysis that is comparable with sieving. This does, however, depend on a variety of factors and a single-page guidesheet is included which advises on the application of the technique to aggregate quarries.

The third technique that was applied at Chard Junction, Hodge Ditch I-III is ground laser scanning (GLS). GLS is fairly commonly applied in industry for logistical and planning purposes, including the aggregate industry, and has been applied to the rapid recording of buildings in the heritage sector. This research is amongst the first application to archaeological excavations, within working aggregate quarries and site monitoring. This illustrates the high potential this technique has for the rapid record of difficult aggregate sites.

Clast analysis has also been undertaken at the site and this, along with the mapping around the site has identified the major sources for the gravels and sand and highlighted some erratic materials including Palaeozoic rocks (ultimately from Cornubia/Armorica), residual weathered clasts and sarsens. A structured set of samples have also been taken for possible cosmogenic isotope dating and this is in discussion with the Cosmogenic Isotopic Analysis Facility at East Kilbride.

The dating for this sequence is taken from both previous OSL dates and 15 new samples. Chard Junction Quarry now has one of the most comprehensive set of dates of any Pleistocene site in the UK has made a significant contribution to the methodological development of this technique, both through the comparison of dates generated by one lab, and through intercomparison with two other labs.

Throughout the programme of methodological work Hodge Ditch II, and latterly Hodge Ditch III, have been monitored. This has resulted in the discovery of 3 more finds (since 2008-2009) including a broken biface, a flake and a core. An additional flake was found during the geomorphological mapping of the valley slopes around the site. Right at the end of the monitoring the first organic sediment was located (under the superficial diamicton) and a preliminary analysis has shown it to be polliniferous and probably eroded remnants of an interglacial soil. Proposals are included in Phase III to undertake a full analysis of this material.

Standard methods of 3D modelling (GSI3D (BGS) & Rockworks) of the site were considered but found to be inappropriate and due to the efficacy of the ground-laser scanning approach a trial of using this data to provide a full quarry 3D model has been undertaken and is presented here. This allows both the finds and OSL dates to be displayed within a 3D volumetric model of the quarry.

A number of outreach activities have been undertaken involving both the aggregates industry, the public and interested parties. An outline project design is also included for Stage 3.

2 The evaluation of gamma cps (Gps) logs

Task 1: *To evaluate the use of gamma cps using correlation with sedimentology at Chard Junction Hodge Ditch (Phases I and II) and its wider use by the aggregates industry.*

Gamma cps (Gcps) is a standard tool, for the interpretation and correlation of geological boreholes (Slatt et al. 1992). It has also become an increasingly common method of resource assessment in the commercial aggregates industry worldwide (Ellis 1987; Pain 2008). It provides a rapid non-destructable method of characterising aggregate bodies (or bedrock) whilst drilling boreholes and for engineering investigations (Cripps and McCann 2000). The equipment is standard (Figure 2.1) and relatively cheap to deploy as part of a borehole survey.

Figure 2.1 Commercial gamma cps equipment rig. Picture courtesy of Amec Ltd..

The gamma cps data was made available to the authors by Bardon Aggregates Ltd. along with the drillers logs, as is common practise with the archaeological evaluation of aggregate sites. Because the gamma cps data was found useful in Stage 1 of this project (the assessment phase at Hodge Ditch 1) it was decided to further evaluate the technique for the archaeological evaluation stage of aggregate site planning and to produce advice to archaeologists on the technique in the form of a guidesheet (Appendix A).

2.1 Gamma cps Theory and Methodology.

Gamma cps (gamma radiation in counts per second) is recorded by a gamma detector, generally using a thallium-doped sodium-iodide crystal detector that is lowered down the borehole at incremental depths. It has for some time now been a standard procedure in the drilling industry (Schlumberger 1974). Natural gamma ray radiation is one form of spontaneous radiation emitted by unstable nuclei. Gamma (γ) radiation may be considered either as an electromagnetic wave similar to visible light or X-rays, or as a particle or photon. Gamma rays are electromagnetic radiations emitted from an atomic nucleus during radioactive decay, with the wavelength in the range of 10^{-9} to 10^{-11}cm. This is a function primarily of the mineralogy of the sediments and particularly the content of gamma radiation emitting elements such as potassium, thorium and uranium-radium (Figure 2.2). These are found in rock sequences containing potassium feldspars (e.g. granites, feldspathic sands), volcanic and igneous rocks, sands containing volcanic ash and most commonly in clay minerals. In general quartz sand and chert or flint dominated gravel has low emission levels whereas clays and volcanic materials have high emission. However, grain or clast size is strongly related to variation in lithology and thus gamma radiation emission, and this allows Gcps to be used as a proxy for grain size variation. It is this close

relationship to grain size and thus also to sedimentary environment that makes gamma cps a potentially valuable tool for both the correlation of logs or boreholes and also the identification of changes in sedimentary facies.

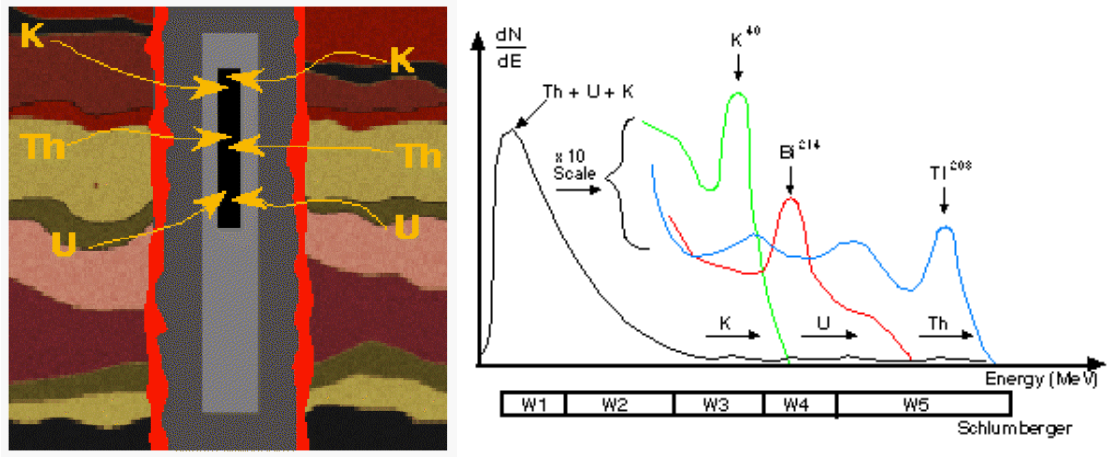

Figure 2.2 Diagrammatic representation of the gamma radiation from sediment in a borehole (left) and the Schlumberger graph of gamma radiation emission spectra. From IODP 2010.

Both correlation of units and facies variation are essential contextual elements in the archaeology that might be contained within a sand and gravel body.

Clay typing.

Potassium and thorium are the primary radioactive elements present in clays; because the result is sometimes ambiguous, it can be useful to combine these curves or the ratios of the radioactive elements.

Mineralogy.

Carbonates usually display a low gamma ray signature; an increase of potassium can be related to an algal origin or to the presence of glauconite, while the presence of uranium is often associated with organic matter.

Ash layer detection.

Thorium is frequently found in ash layers. The ratio of Th/U can also help detect these ash layers.

Due to the relative stability and immobility of high gamma emission elements weathering of most Lithologies will increase Gcps values. Statistical studies of fluvial deposits by Barrash and Morin (1997) have shown that Gcps can distinguish between sand dominated and cobble-dominated gravels. If the end members are different enough it should be possible to distinguish between poorly sorted unconsolidated deposits (e.g. diamictons), matrix-supported gravels and clast-supported gravels and this distinction can have archaeological importance (see later discussion).

In the case of Chard Junction the Lower Lias (Charmouth Mudstone) bedrock commonly has values of 50+ whereas clast-supported or framework chert gravels have values as low as 10. The range is relative and so this only represents differences between the emission of the lowest and highest levels on-site. In practice this is a fairly typical range due to the high contrast between most bedrocks (such as clay, mudstones, shales, igneous, metamorphic and even sandstones) and gravel mineralogy which is dominated by the most resistant mineralogy predominantly quartz.

However, the technique provides a valuable proxy for clay content and sorting/fabric and at Chard allowed the differentiation of 4 units; upper periglacial gravelly heads (diamictons), tributary alluvial-fan like sediments which have a high matrix component, bedrock and relatively clean or well-sorted fluvial gravels. In this site this highlighted the possibility of buried artefacts underlying the upper periglacially forced sedimentary unit was high especially given a probable correlation with the very rich sites at Broom only 3 kms to the south. This data is now routinely used by the industry and so is available for many sites and could be requested by the archaeological assessor or assessing company.

The 14 Gcps logs available from Hodge Ditch (Phases I-IV) were analysed using the following methodology;

A. The subdivision of each log into stratigraphic units using both loggers descriptions and our stratigraphic data.

B. The calculation of the average (and descriptive statistics) of each Gcps stratigraphic section and the statistical testing of the association between the Gcps statistics and the stratigraphic descriptions band using non-parametric statistics (analysis of variance and chi-squared) and a resultant estimate of the closeness of the association of the gamma Gcps with the core stratigraphy

2.2 Results

The drillers borehole logs make no sedimentological distinctions within the major body of the gravels, however, they do provide the altitude of bedrock, gravel thickness and the presence of clayey silts, sand and gravels and distinct from the (clean) sandy chert gravel. Also supplied with the sediment description was the gamma cps (Gcps) profile of each borehole. As can be seen from Figure 2.3 each Gcps log was segmented into stratigraphic units and the highest and lowest values within the record were used to create a stratigraphic Gcps value matrix. In total this produced 230 values from 166m of logs Table 2.1).

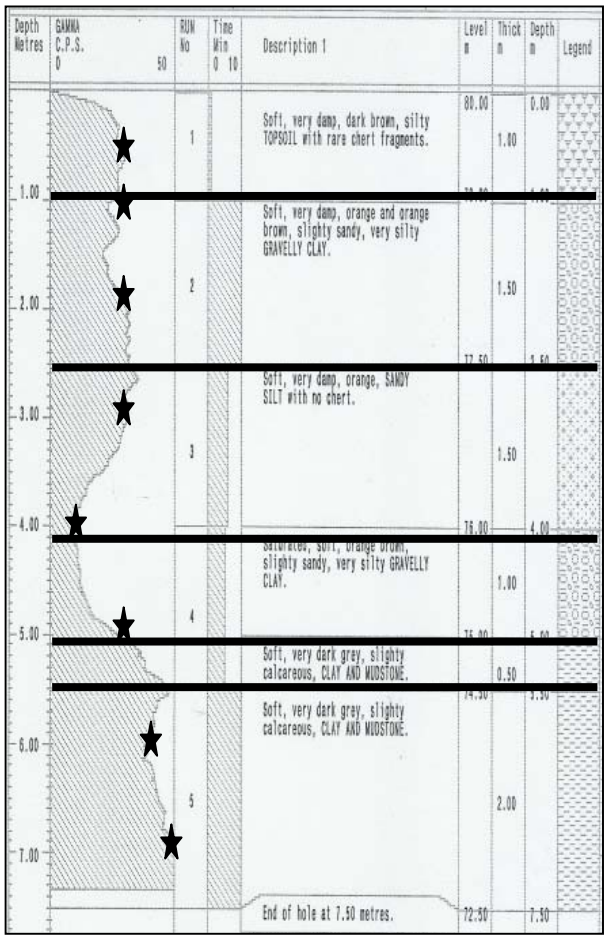

Gcps

Gcps measures the natural gamma radiation of sediments. This is a function of the mineralogy of the sediments and particularly the content of gamma radiation emitting elements such as Potassium, Thorium and Uranium-Radium. These are found in rock sequences containing potassium feldspars (e.g. granites), volcanic and igneous rocks, sands containing volcanic ash and clays. In general quartz sand and chert or flint dominated gravel have low emittance levels whereas clays and volcanic materials have high emittence. At Chard Junction the Lias bedrock (clay) has a high Gcps and the chert/flint gravels a low Gcps so Gcps is a proxy for the bedrock component of the matrix

Figure 2.3 The Gcps logs from a representative log showing the method of sampling (courtesy of Bardon Aggregates Ltd.)

Statistic	Bedrock	Weathered	Topsoil	Silt+	Sand	Chert/sand
Mean	49.26316	30	22.64286	30.91667	30.375	9.1144578
Standard Error	0.68331	3	2.450851	2.712089	5.577178	0.2811353
Median	50	28	24	32.5	33	8
Mode	50	30	24	31	50	8
Standard Deviation	2.97848	9.9498744	9.170246	9.394954	15.77464	3.6221752
Sample Variance	8.871345	99	84.09341	88.26515	248.8393	13.120153
Kurtosis	18.73489	-0.918967	-0.69449	1.763392	-1.52882	7.8096492
Skewness	-4.31772	0.1920739	0.186775	-0.56572	-0.051	2.4476116
Range	13	30	30	38	40	23
Minimum	37	15	10	10	10	4
Maximum	50	45	40	48	50	27
Sum	936	330	317	371	243	1513
Count	19	11	14	12	8	166
Confidence Level(95.0%)	1.435583	6.6844177	5.294741	5.969272	13.18792	0.5550862

Table 2.1 Descriptive statistics of bed by bed Gcps values. The 'Weathered' category is weathered bedrock at the bases of boreholes.

This data is then expressed by lithology in Figure 2.4 and shows a large variation between the Gcps of the Lithologies and most importantly between the bedrock

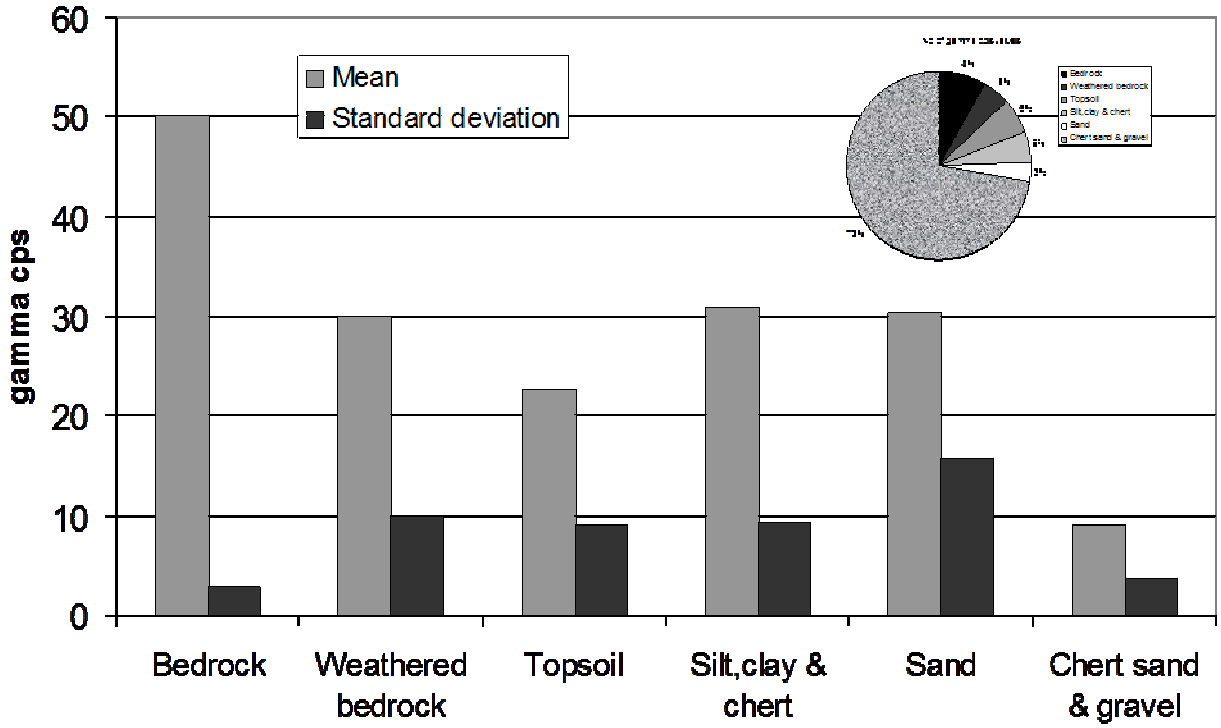

Figure 2.4 Statistical summary of the gamma cps values from 166m of logs at Chard Junction Hodge Ditch. Gamma cps is on a relative scale with the range of recorded values from 0-50 gamma cps. Inset is the relative proportions of measurements (taken at 1m intervals) from the different units as identified by the loggers description.

(highest values) and the chert sand and gravel (lowest values). These two 'end-members' also had the lowest standard deviations and were very different from the mean of the total dataset (16) and the overall standard deviation (0.9). The results are statistically significant with a Chi^2 value statistic of 30.9 with 5 degrees of freedom which at a two-tailed P value is less than 0.0001 and therefore by conventional criteria, this is considered to be extremely statistically significant. In the case of Hodge Ditch therefore it is possible to differentiate; bedrock from weathered bedrock, topsoil and silt/sand and chert gravel but it is not possible on Gcps alone to differentiate statistically between silt dominated units and sand dominated units.

A selection of the Gcps logs is given in Figure 2.5 showing how in practice the different units can be distinguished. At Chard (Hodge Ditch) it proved possible from the borehole logs and the Gcps logs to divide the sediment body into 4 categories; **A** fine silts and sands under the modern floodplain (Holocene), **B** slope and periglacial deposits, **C** tributary gravels and **D** main valley bedded terrace gravels (Figure 2.6). The logs show that soliflucted gravels (B) exist on the slopes up to an altitude of 80m at least 5m above the highest occurrence of fluvial sand and gravel and this can now be related to the cropping out of the clay with cherts in the valley through the mapping around the site (see Section 7). Due to high gamma radiation by the Lower Lias bedrock the gamma logs supplied along with the stratigraphic columns proved invaluable for differentiating between the soiflucted gravels (high to medium Gcps due to the inclusion of a bedrock-derived

matrix), the tributary units with medium Gcps and the main valley fluvial units which had a very low to negligible Gcps. From

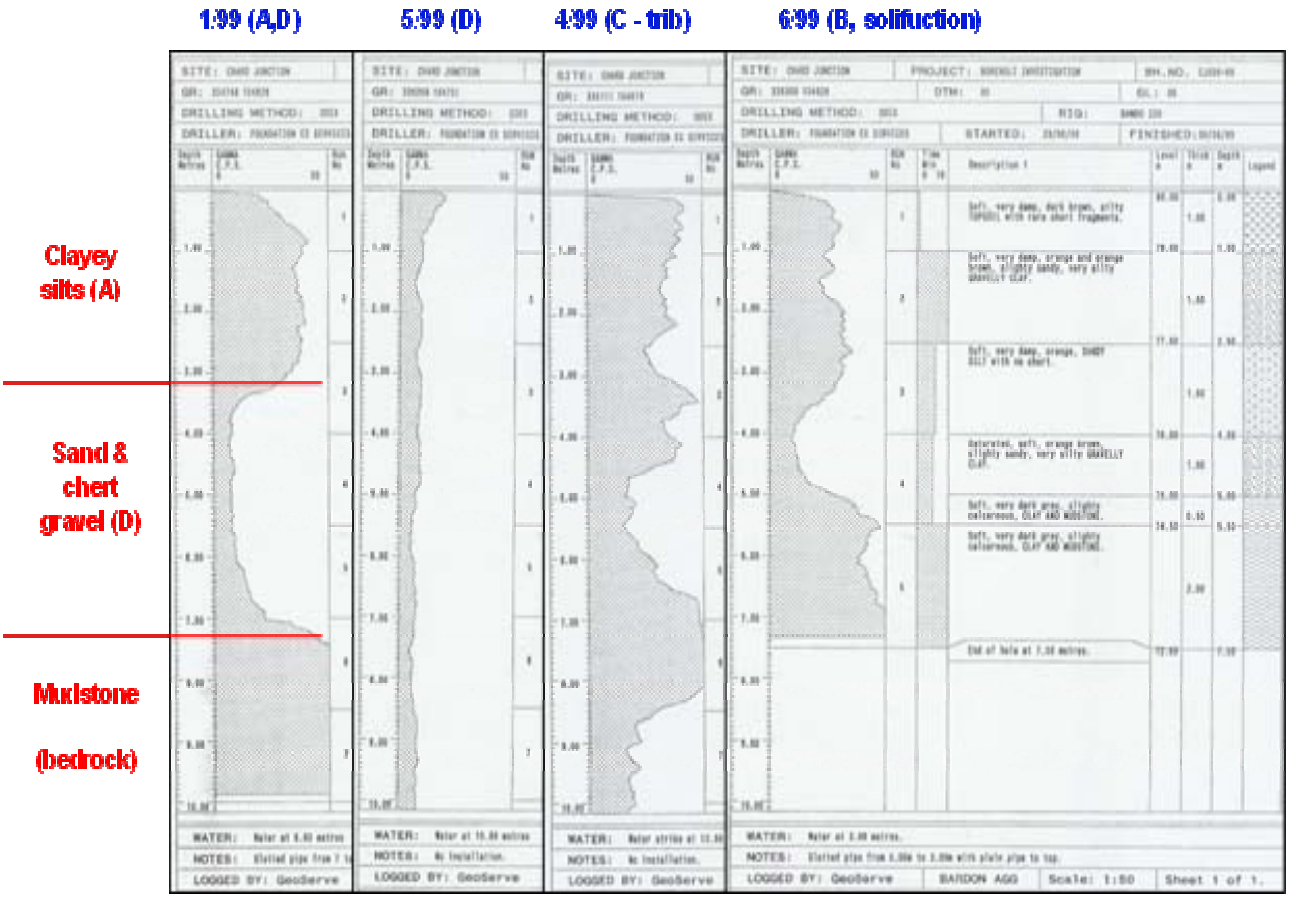

Figure 2.5 A selection of boreole Gcps from Chard showing the stratigraphic sub-division from the borehole drillers logs.

this data a composite cross-section has been constructed and an interpretation upon which the Hodge Ditch Phase I window has been superimposed.

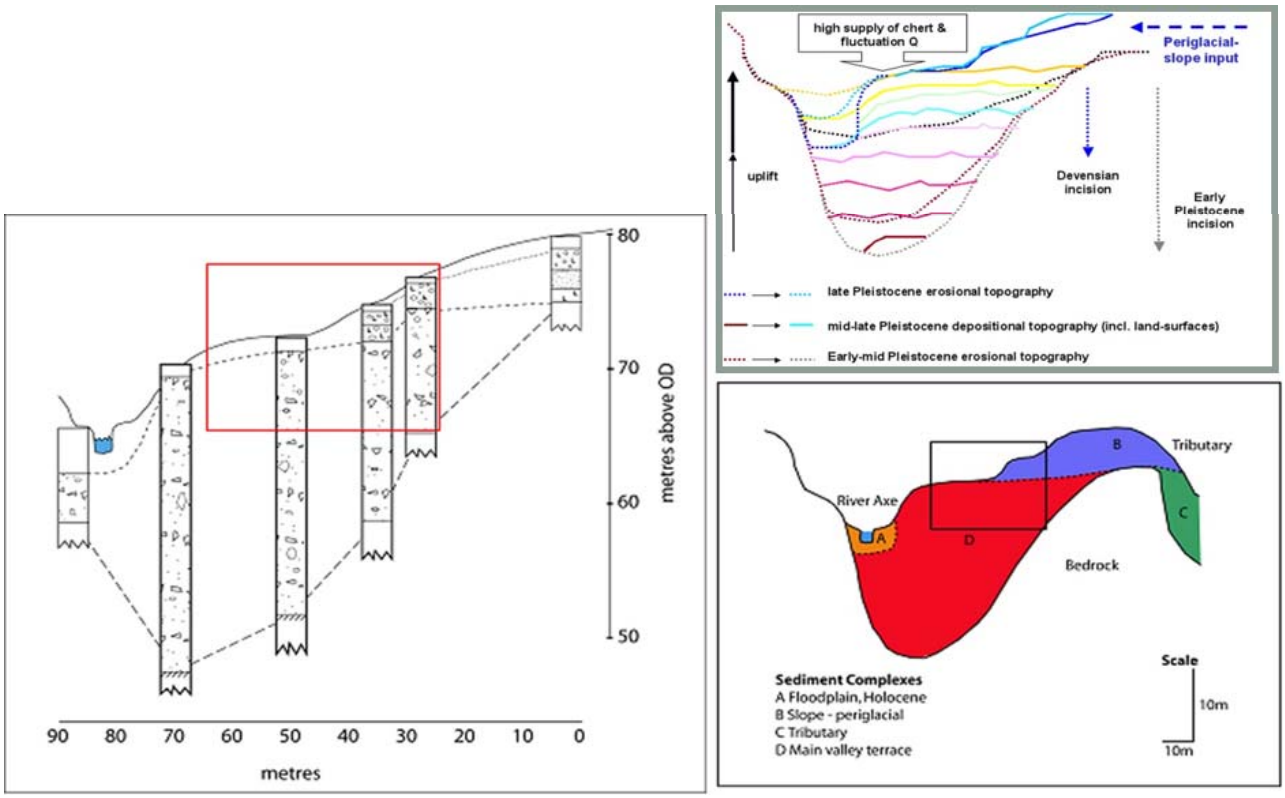

Figure 2.6 A composite cross-section though Hodge Ditch Phase I (left) and interpretation in relation to depositional and erosional events (right top) and the sedimentary facies (right bottom).

2.3 Conclusions

From the above analysis it can be shown that at a site with contrasting end-members such as Chard Junction it is possible to identify the superficial diamicton, mixed or matrix-supported chert/flint gravels, sands and clast-supported chert/flint gravels. The archaeological value at Chard is that it is known from both Chard and Broom that the artefacts (predominantly bifaces) do not occur in the upper diamicton but occur in the lower sand and chert/flint gravel. The value of the technique is not confined to the Axe valley as the geological context is very common. European Pleistocene gravels are dominated by resistant Lithologies such as quartz, flint, chert, quartzite etc. and in most cases where terrace gravels are preserved the bedrock will be composed of less-resistant Lithologies such as sandstones, mudstones, shales, clay etc. The case where this relationship may break-down, indeed be reversed is with gravels on relatively pure limestones such as chalk.

3. Digital granulometry

Task 2: *This will be undertaken on a number of contrasting sediment beds exposed as part of Hodge Ditch II. It will be accompanied by log description, section drawing and the sampling for traditional grain-size analysis.*

3.1 Introduction

The second methodological element of this project was the application of digital granulometry (also known as grain-size analysis). Although common in the analysis of sediment thin sections and fine sediments (Franciskovic-Bilinski et al. 2003) it has only recently been developed in geomorphology (Butler, et al. 2001; Whitman et al. 2003; Graham et al. 2005a, 2005b; Strom et all. 2010) and has not yet become standard in Quaternary science or archaeology. The grain size distribution (cf. particle size distribution) of sediments is the *most fundamental of sedimentological parameters* and can be related to both the provenance of the clasts and the energy conditions of deposition and therefore to the characteristics of the depositional environment and artefact taphonomy (Brown, 1997; Goldberg & Macphail, 2006; Canti, 2007) and there are two principle reasons for its use.

1. It is the standard sedimentological descriptor – indeed if a site is presented for publication without this information it is incomplete. Visual description, although the most applied method, is not adequate to differentiate between similar beds (e.g. a medium clast-supported and medium matrix-supported gravel) which may relate to the provenance, condition of artefacts. It is poor practice for archaeologists or Quaternary geologists to present such a site without such information but unfortunately this is routinely done due to the cost and time requirement of standard grain–size analyses of varied sediments. Hence the need for cheaper, faster in-situ methods.

2. Whilst this is not the place to go into palaeohydraulic theory, the grain size distribution is a direct measure of the energy of the depositing environment. Indeed it is very approximately a power function (3^{rd} power) of the energy as measured in specific stream power (stream power per unit area). The author has used related theory (often referred to as tractive force theory) to estimate if certain artefacts had or had not been transported with the gravel traction load at the site in question – ie. to identify them as residual or not. This should be done with bifaces and related to artefact density and condition. Again a visual assessment, even with maximum clast sizes measured, is not adequate to apply tractive load theory as it requires estimates of D_{50} and D_{95} (where D_{number} is the grain size of a particular percentile of the grain size distribution). Further details can be provided but the general approach is outlined in Brown 1997 (p.91-96, 322-327) and a specific application is given in Brown (2010).

3. All measures of grain size distribution have sources of error and all can be regarded as approximations to a notional true grain size distribution. However, by far the most commonly used and accepted method is by sieving through a stack of sieves with known and standard mesh sizes either with water or dry and the weighing of each sieve fraction. Because this is the standard measure and believed to have relatively low errors particularly at the medium to larger grain sixes (i.e. sand to fine gravel) it has been used here as the comparator for the use of Sedimetrics©.

However, the problem for archaeological studies is that in gravels with a coarse component, even excluding cobbles, a very large sample of about 250 Kg is required in order to obtain a statistically representative sample using sieving. Sieving is also time consuming, inconvenient and messy. The digital granulometry method uses digital photographs of small areas of the exposure face with a clear length scale and image analysis which extracts the grain size distribution from the differences in texture and colour given by the clast composition. It has been used successfully for modern river gravels (Strom et al. 2010) and it should work reasonably well with clast-supported Palaeolithic gravels although it is expected that samples of the matrix would still have to be sieved in matrix-supported gravels or where particularly accurate percentiles were required. However, even its partial use would be a significant reduction in time/cost and allow watching briefs to record grain-size data at the same time as taking a digital record of the aggregate face.

3.2 Theory and Methods

The application presented here uses a commercially available software - the Sedimetrics© system written by D. J. Graham and sold by Loughborough University. The basic approach generates a binary image in which each discrete region represents a grain.

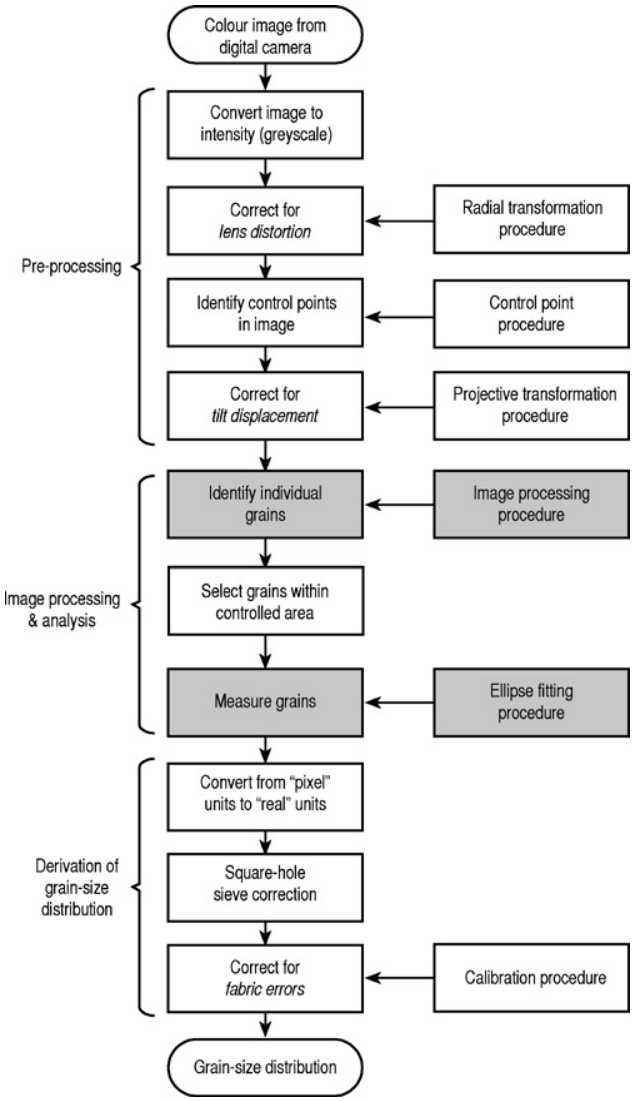

Figure 3.1 Illustration of the stages required to extract grain-size data from a digital image. The shaded gray boxes represent the image-processing and analysis procedures described in Graham et al. 2005a and the remainder of the steps are described in Graham et al. 2005b. From Graham et al. 2005a.

Subsequent image processing is a two stage process with the first stage being *image partitioning* and the second *watershed segmentation* which tidies the binary image and attempts to split regions representing more than one grain into singular objects (Graham et al. 2005a). In the development of the Digital Gravelometer Graham et al. (2005a) evaluated four methods of image processing for partitioning and the final software uses a double threshold approach (based on percentiles of the intensity frequency distribution in the bottom-hat transformed image as illustrated in Figure 3.2).

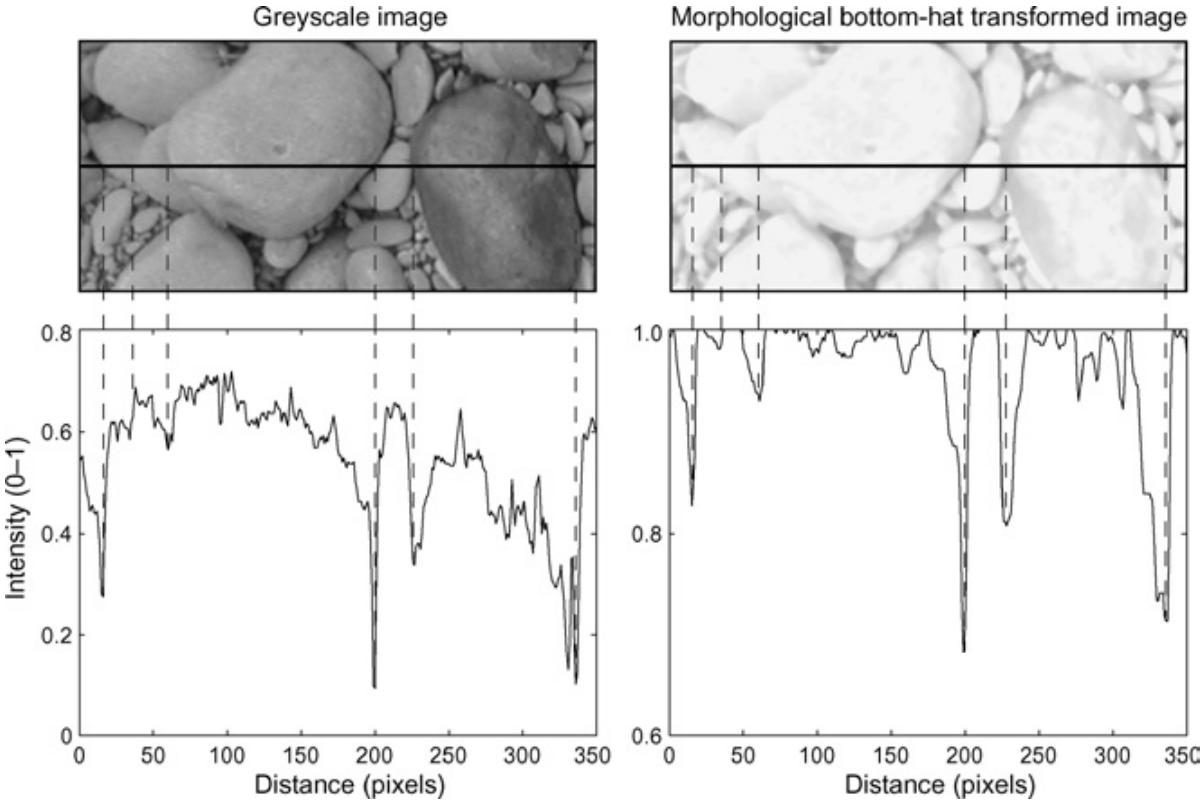

Figure 3.2 Illustration of the effect of the application of the morphological bottom-hat transform. The top panels show the original and transformed images. The bottom panels show an intensity profile (scaled from 0 to 1) across the images. Vertical (dashed) lines show the locations of the grain boundaries along the intensity profiles. Differences in intensity between and across grains in the grayscale image complicate the selection of appropriate threshold values. These differences are largely removed by the application of the transform and most of the intensity variations remaining are associated with grain boundaries. From Graham et al. (2005a).

The watershed segmentation is derived from the Euclidean Distance Map (EDM) of the binary image, in which each pixel that forms part of a sediment “grain” is given a value that is inversely proportional to its distance from the nearest ‘non grain’ pixel. The resulting grayscale image can be thought of as a topographic surface in which ‘grains’ are represented by basins. The ‘watersheds’ between these basins may be used to segment the binary image (Figure 3.3). Each basin is gradually ‘flooded’ until ‘water’ from one depression overflows into its neighbour. The line along which this occurs is then marked

as a watershed and the flooding and marking continues until the image is entirely submerged. The watersheds thus defined are then used to segment the binary image. The algorithms that the Digital Gravelometer use to accomplish this is are based on those published by Vincent and Soille (1991).

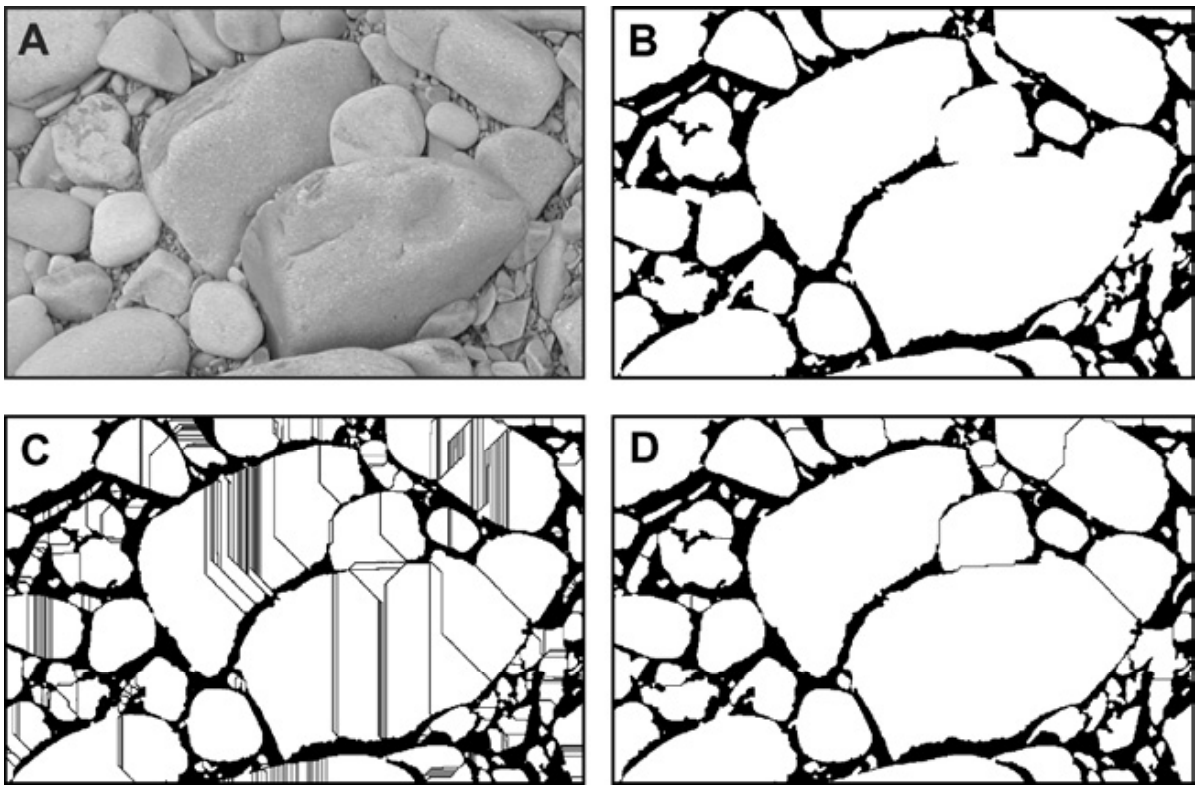

Figure 3.3 Example of the application of the watershed segmentation algorithm. A. The original grayscale image. B The image after the application of the morphological bottom-hat filter and double threshold (some adjacent grains have not been completely separated). C The result of applying the watershed segmentation algorithm to B (there is significant over-segmentation of many of the grains). D The result of applying the watershed segmentation algorithm after the application of the h-minima transform with a threshold value of 1 (the segmentation is much improved, with many formerly joined grains being separated and over-segmentation removed). From Graham et al. (2005a).

In theory any digital camera can be used to collect suitable images but the higher the pixel resolution the larger the sampling area can be for a given resolvable (minimum) grain-size. Any grains smaller than 23 pixels will be subject to significant measurement error and so the camera used will affect the minimum measurable grain size (MMGS) for a frame area (Figure 3.3). This is discussed further in the results section (3.3). A flash is also required for sections in deep shadow. This project used a Canon Powershot 10XIS with a 20x optical zoom lens. The 10 mega pixels of this camera give a minimum measurable grain size (MMGS) of approximately 4 mm for a 0.3 m^2 frame area.

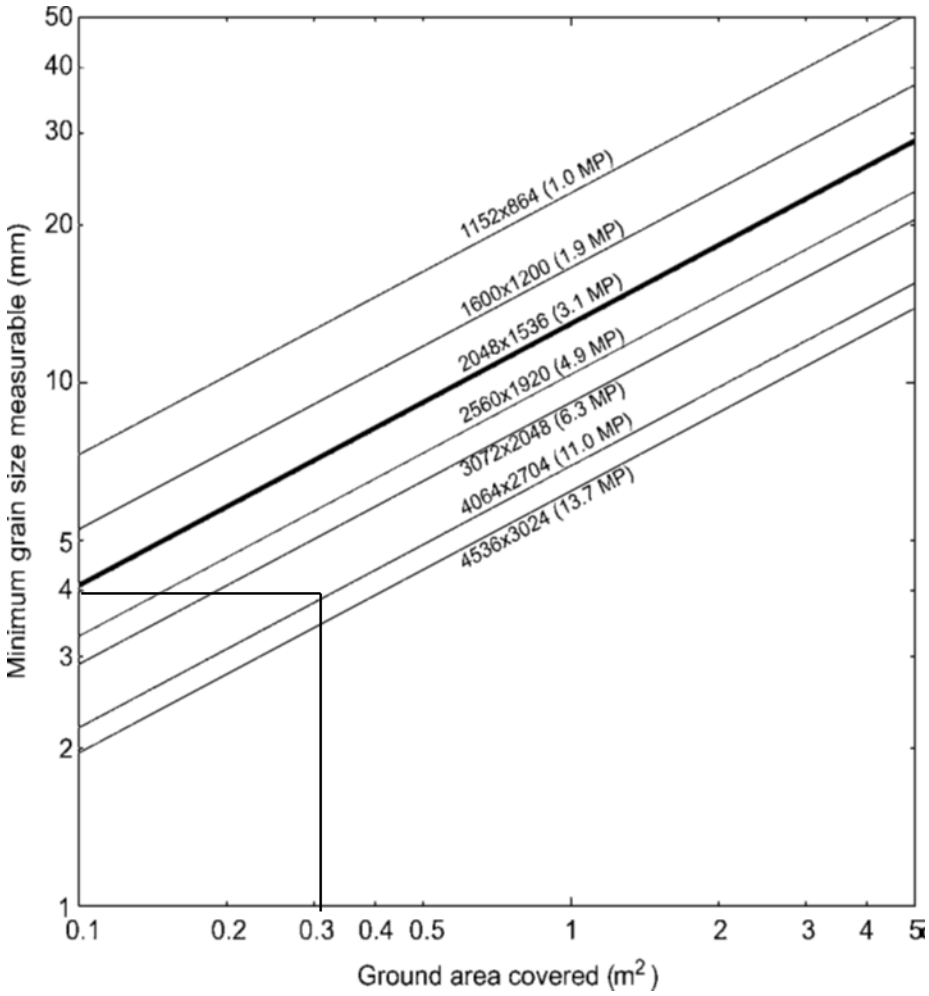

Figure 3.4 The relations between ground cover area (frame area), camera quality in megapixels and minimum measurable grain size (MMGS) for the Digital Gravelometer (Sedimetrics©).

In the field the method involves the following steps;

1) Setting up the sampling area of known dimensions with four markers
2) Composing the photograph so that it includes the sampling area and nothing else
3) Check lighting – the area must be shaded from direct sunlight
4) Set camera pixel resolution to maximum using minimum compression and store as jpeg images
5) Take the photograph, download and store
6) Process using the Sedimetrics® software.

In practice we found a number of factors came into play at each stage and influenced the final approach as advocated in the guidesheet (Appendix A);

1) Setting up the sampling area of known dimensions with four markers: this can be difficult on vertical (or even overhanging) faces and we experimented with pegs/pins, tipex and purpose-made frames. Pegs or pins alone were inadequate due to a lack of resolvability on the digital image. Tipp-ex® can be used but requires large enough suitably located grains. The easiest approach was to make up frames of three sizes (1.3x1.0m, 0.65x0.5m & 0.13x0.10m) which could then be secured to the face by pins (Figure 3.5). Although rapid two problems arise, firstly the uneven nature of the surface even after cleaning can cause variations in the camera-frame geometry and secondly the frame

crates an edge effect which has to be removed and this is discussed in Section 3.3. A useful modification of this approach would be to add a number board to the frame allowing the recording of the site number on each frame.

2) *Composing the photograph so that it includes the sampling area and nothing else*: this can be difficult but was made easier by using a frame and is discussed further in Section 3.3.

3) *Check lighting – the area must be shaded from direct sunlight*: in some cases a sun-shade was used.

In order to minimise the effect of additional variables the range (distance from camera to frame) was dictated by the frame size in order to maximise camera resolution without the optical zoom.

As part of the monitoring at Hodge Ditch, and in order to test the results of this approach, samples were taken from each frame photographed. Each large frame (1.3x1.0m) was divided into an upper and lower half and a sample one contained grain-size thick (defined by the largest grain) was excavated from each half into heavy-duty bags. In practice this produced two samples of approximately 30-40 Kg in weight.

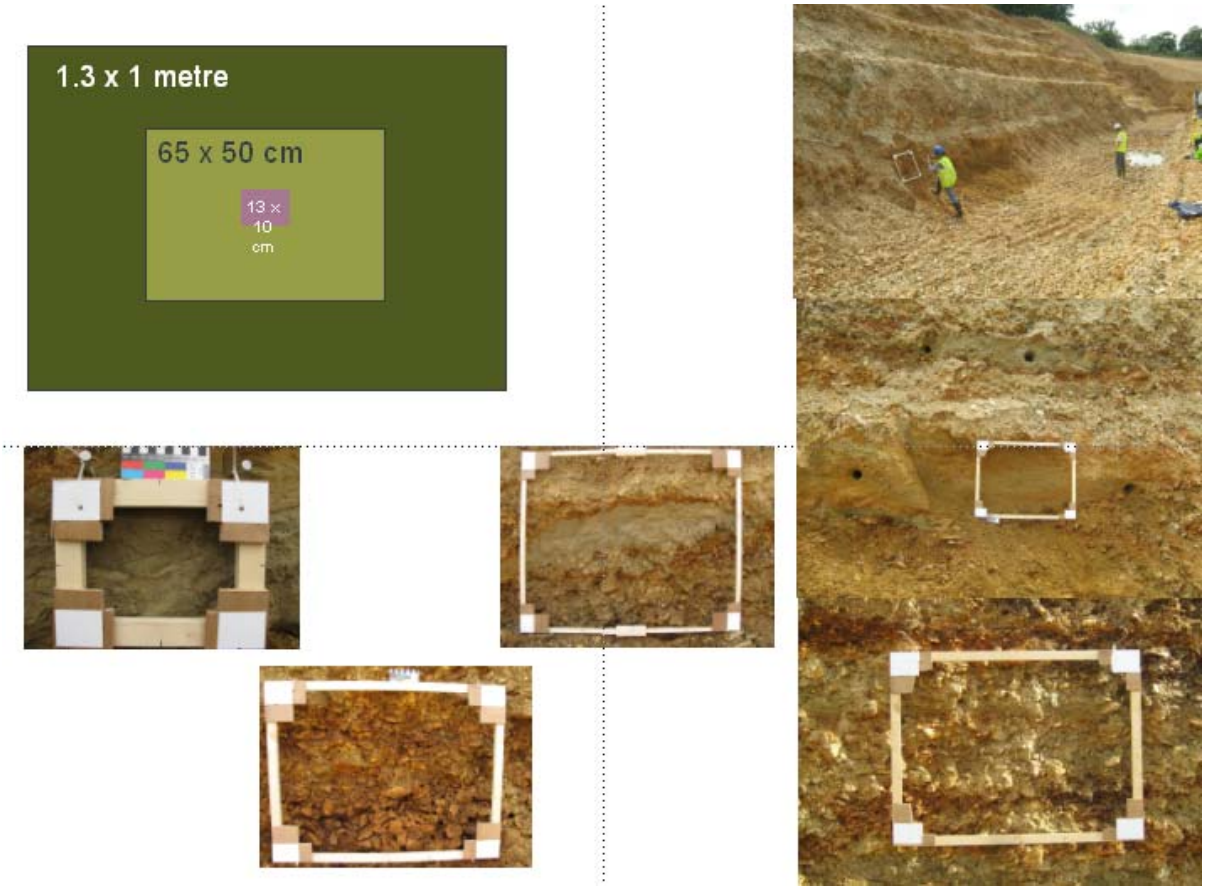

Figure 3.5 Examples and dimensions of the frames used for digital granulometry.

These very large bulk samples (of 50-100 kg) were then dried and put through a standard nest of sieves at the mesh sizes. Given the coarse nature of the deposits and lack of clay this can generally be done dry it is not always necessary to use a Rotap Shaker® although when required it was used.

The procedures undertaken by the Sedimetrics© software are sequential and include; geometric correction, scaling, vectorisation, cropping (to remove edge effects) and calculation. These are illustrated for one frame in Figure 3.6.

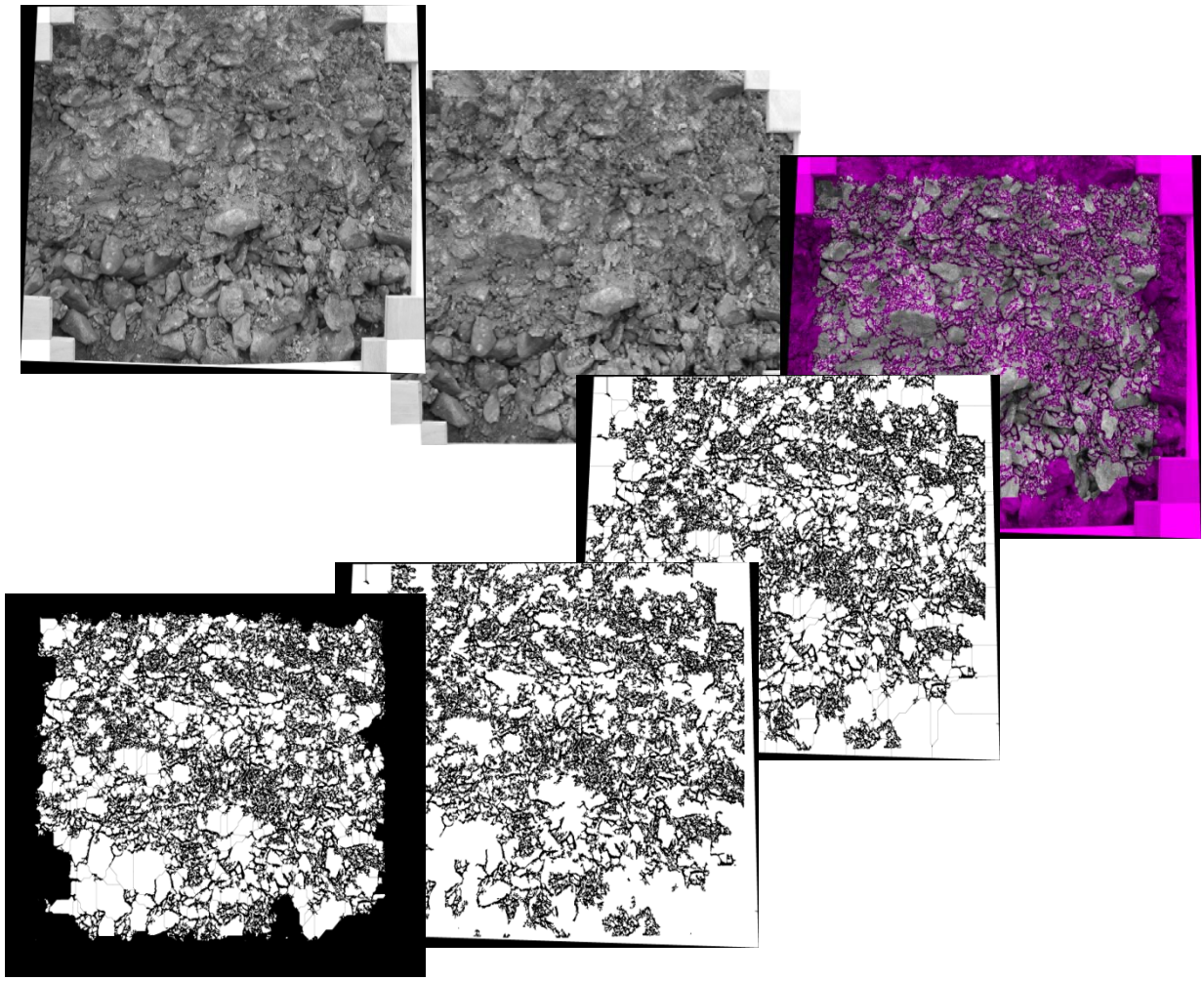

Figure 3.6 An illustration of the chain of processes used by the Sedimetrics© software on a single frame.

The aim of this procedure was to be able to fully evaluate the robustness, accuracy and sensitivity of the method and provide answers to the following questions;

1. How large an area of a unit has to be photographed
2. What is the optimum distance from the face for this to be accurate and does it vary with clast size distribution
3. Does lighting conditions make any difference
4. Does the digital camera used make any difference to the results
5. Do sedimentological characteristics other than clast size distribution make any significant difference (e.g. clast lithology/colour, shape or orientation).

3.3 Results

Over 30 frames were taken from Hodge Ditch I and II and some comparator sites (Black Hill Quarry and Shapwick Grange Quarry) although a limited number were sieved using

the procedure outlined above for large samples and a selection of these are illustrated in Figures 3.6 to 3.8. For several of the frames full clast samples were

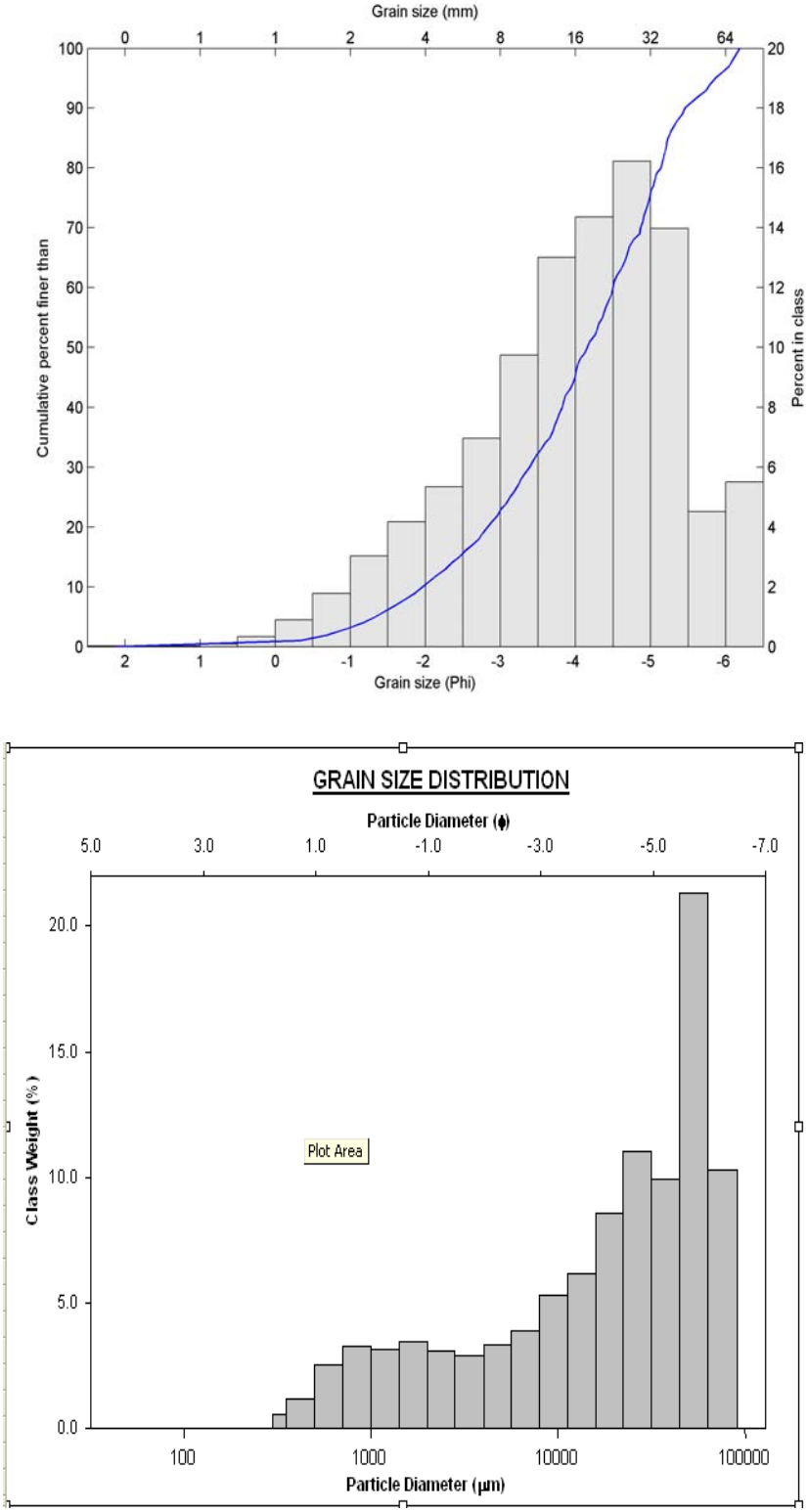

Figure 3.6 A comparison of the Sedimetrics© (above) and sieve analysis (below) for sample Chard 1A + 1B (22-7-10)

taken and these can be compared with the clast size distribution generated from the digital granulometry.

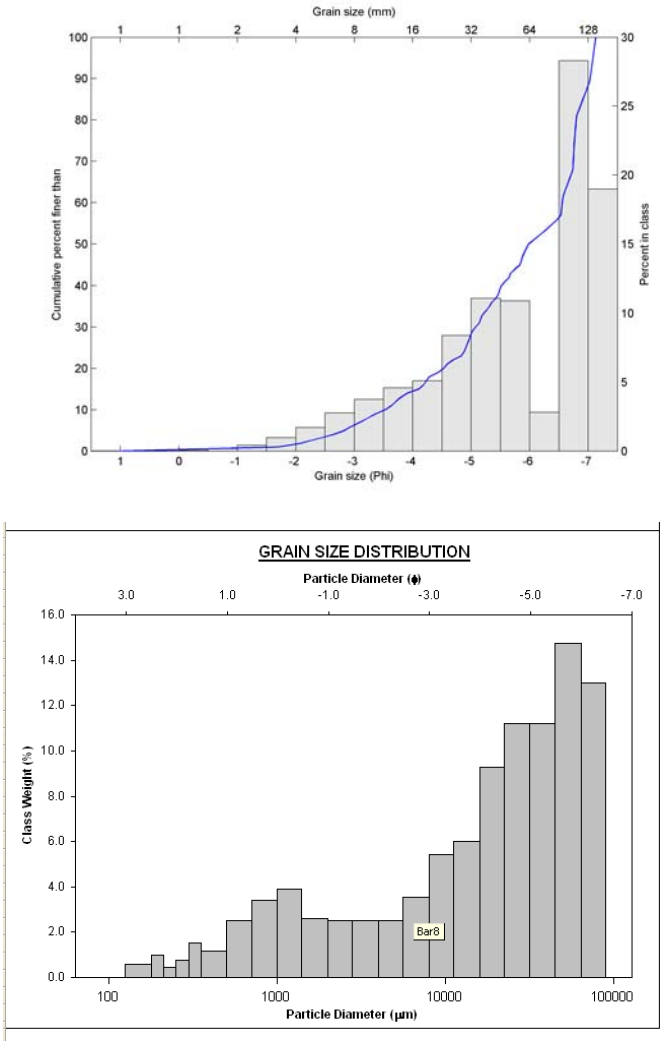

Figure 3.7 A comparison of the Sedimetrics© (above) and sieve analysis (below) for sample Chard 3A + 1B (22-7-10)

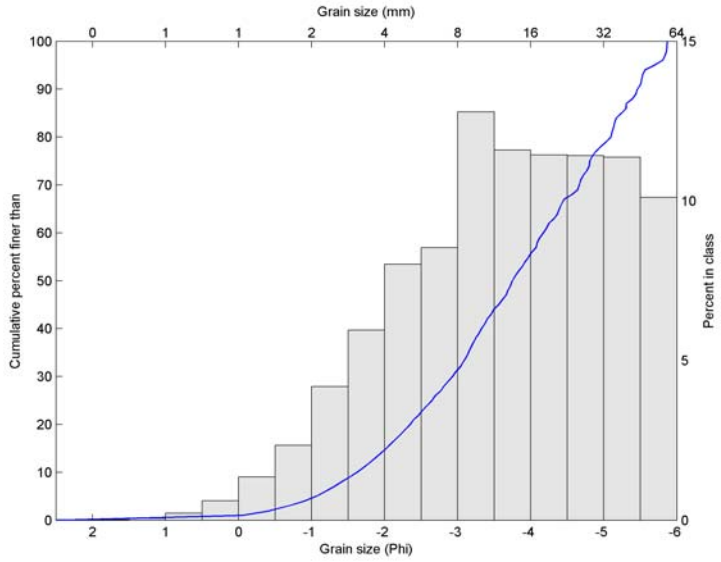

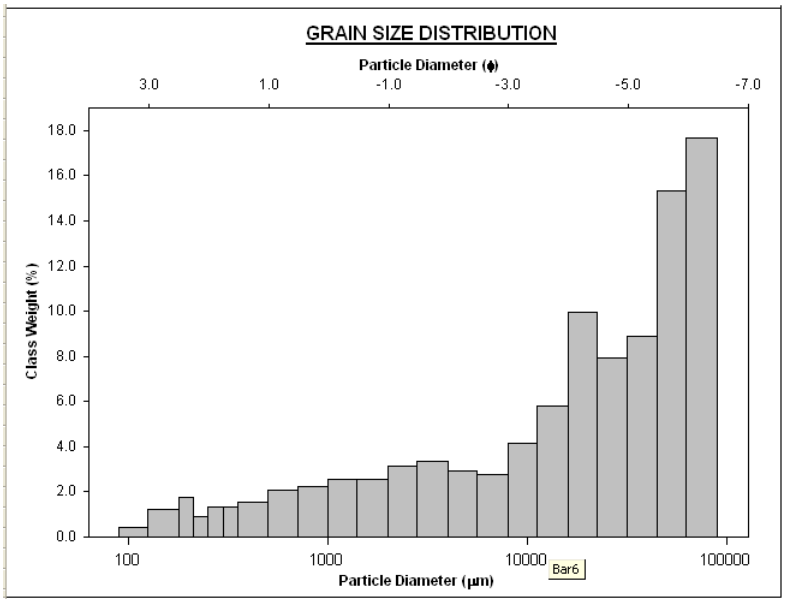

Figure 3.8 A comparison of the Sedimetrics© (above) and sieve analysis (below) for sample Chard Upper sample A+B (3-8-10)

In order to perform a quantitative comparison standard grain size statistics have been computed for both the Sedimetrics© data (performed by the software automatically) and from the sieve data using GRADISTAT© (Blott and Pye 2001).

	1 A+B 22-7-10		**2 A+B 22-7-10**		**3A+B 22-7-10**		**A & B 3-8-10**	
	Sed.	Sieve	Sed.	Sieve	Sed.	Sieve	Sed.	Sieve
Modal class	-5.5	-5.5	-6.0	-6.0	-7.0	-6.0	-3.0	-6.0
Max.	-6.5	-6.0	-7.0	-6.0	-7.5	-6.5	-6.0	-6.5
Min.	2.0	1.75	1.0	1.75	1.0	3.5	2.0	3.5
50%	-4.16	-4.62	-5.21	-4.5	-5.98	-4.61	-3.75	-4.99
Median class	-5	-2	-3	-3	-3	-1	-2.0	-1.5
Mean	-3.96	-3.95	-4.91	3.41	-5.68	-3.7	-3.6	-3.4
Modality	2	3	3	3	2	1	1	3
Sorting	1.37	2.09	1.57	2.17	1.42	2.33	1.45	2.60
Skewness	0.67	0.91	0.79	0.67	1.04	0.88	0.46	0.63
Kurtosis	3.07	2.71	2.97	2.93	3.35	2.63	2.58	2.09

Table 3.1 A comparison of Sedimetrics© and sieve analysis grain size distribution statistics for sieved and analysed frames from Hodge Ditch II only. All values are in Phi except for sorting, skewness and kurtosis which are non-dimensional. For modality the number of modes is given. It should be noted that both skewness and kurtosis are not reliable for non-unimodal distributions.

In order to compare the statistical summaries of the distributions they have been correlated and as can be seen in Figure 3.10 there is a strong relationship between the Sedimetrics and the sieve data. This has been tested and found statistically significant at the 2 standard deviation level (correlation coefficient of 0.941).

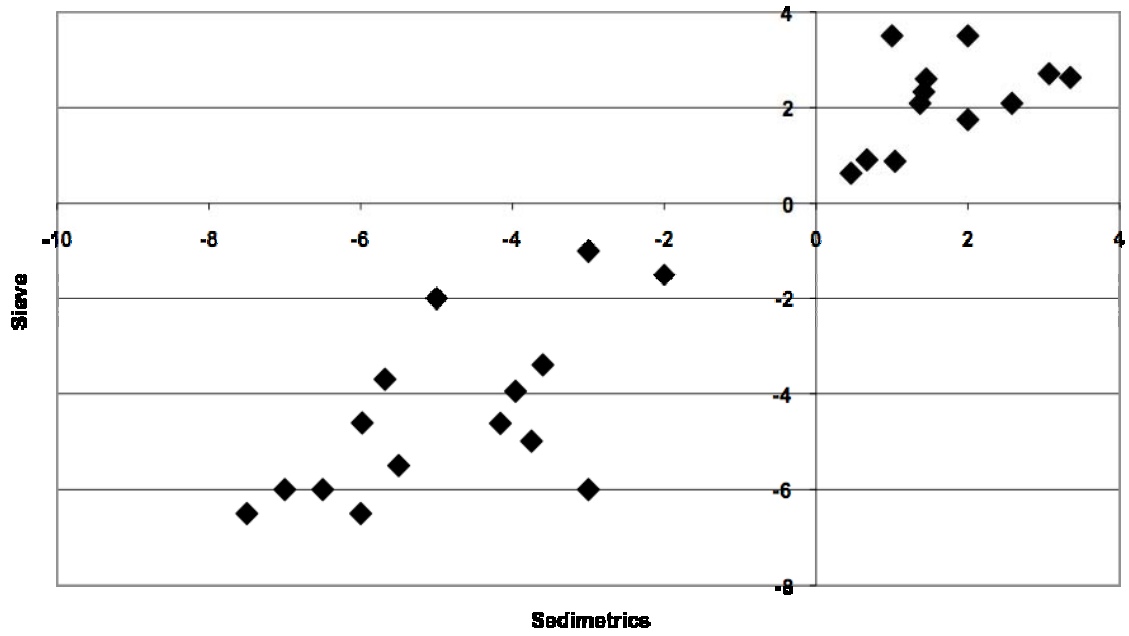

Figure 3.10 A plot of the distributional statistics derived from digital photography using Sedimetrics© (y axis) against the same statistics derived from the sieve analyses on the same samples (x axis).

Despite this strong correlation as can be seen from the graphs and the table there are differences that are significant in sedimentological terms. In general whilst means and medians are similar the maximum is generally greater from digital photography than from sieving. Since sieving is generally taken to be the standard grain size measure (with its own sources of error) this suggests that Sedimetrics© has a tendency to over-estimate the largest clast sizes present by a factor of about 0.5 to 1 phi interval. If this effect is constant than it does not cause problems within a site but it could be important in relation to estimating the relationships between naturally transported lithics and human loss or emplacement.

The work in Hodge Ditch II could only sample very similar gravels. Indeed all the gravels sampled were classified by both Sedimetrics© and sieving as very poorly to poorly sorted coarse to medium gravels. This was felt not to provide a great-enough range of sediment types to allow a full evaluation of the Sedimetrics© technique. In order to overcome this analyses were also carried out at four other sites, two in the Severn Valley (Frampton-on-Severn and Clifton) and two in the Blackdown Hills relatively close to Chard (Black Hill and Shapwick Grange). The results from these fluvial sediments are given in Appendix B

3.4 Conclusions

Reproducible results have been gained from the software and it is certainly a quick relative method of differentiating between different sedimentary units. All the frames taken from Hodge Ditch have also been sampled for traditional grain size analysis (by sieving) and the correlation of this data with the Sedimetrics© data is ongoing. The sites used to give a wide range of grain size distributions and sedimentary fabrics include Black Hill and Shapwick (Dorset) and also Frampton-on-Severn, Clifton and Ball Mill Quarry in the Severn Valley. This was necessary due to the relatively limited variation of the gravels in Hodge Ditch II and did not entail any additional costs from this project. As can be seen from these examples where the sediment is clearly bimodal such as in the case of the

sand with gravel this is clearly reflected in the Sedimetrics© plot and is clearly different both in form and absolute values from the unimodal gravels at the same site. Given the strengths and weaknesses of deriving grain size data from digital photography its far greater use is recommended but as a relative grain size proxy.

If digital granulometry becomes established practice then more sophisticated methodologies will be required in order to improve accuracy and exact more information including sediment fabric (the 3D arrangement of clasts). Such work is being undertaken in the material science area including the use of neural networks to dispense with image segmentation (Ferrari et al. 2008).

4 Ground laser scanning

Objective 3. *This will be undertaken on a number of contrasting faces (est. of 9 beds) exposed as part of Hodge Ditch II. It will be accompanied by log description, section drawing, digital granulometry and the sampling for traditional grain-size analysis.*

4.1 Introduction

The third methodological element of Stage 2 was ground laser scanning. Ground laser scanning has been used extensively by the Minerals Industry to record the morphology of quarries largely prior to blasting. It has also been used extensively now in archaeology and there are English Heritage guidelines on its use (English Heritage, 2006). More recently it has been used to obtain sedimentological/fabric information from metamorphic rocks by Camborne School of Mines (Shail, pers com.) and stratigraphic information from large exposures (Buckley et al., 2008) and to obtain orientation data from modern gravels (Milane et al., 2006). Pilot work by the applicants funded by the University of Southampton had shown that at Chard Junction elements of the stratigraphy are recorded by a scanner using a 2 mm posting at a range of approximately 30 m. Work on the post-processing of such data is required in order to create a “scanned stratigraphy” and the results of such processed data are discussed below. At Southampton other scanner users in the School of Geography were, and are using the equipment to record and model the gravel bed of rivers. This is essentially the same problem but in a different plane and collaboration with other users of the scanner has aided the interpretation of results presented here. Many if not most large archaeological contractors now have ground laser scanners and so would be able to employ them as a recording technique in watching briefs in suitable situations. There are clear advantages in the lack of a need for sedimentologically trained staff and time saving but most important of all it would lead to the preservation by a high-resolution 3D archive of the gravel body prior to or after any archaeology was located.

This component of Stage 2 is not proposed as a standard methodology but one which may be used if warranted by the importance of a face due to in-situ artefact finds and time pressure such as face collapse or safety considerations. An additional justification discovered during work funded prior to Stage 1 by the University of Southampton (initial use of the laser scanner) was its use when the site is effectively out-of bounds due to nesting sand martins (*Riparia riparia*). These birds will only nest in overhanging sand faces and are protected by legislation (Wildlife and Countryside Act 1981. Part 1 UK Protected Species) so that the disturbance of a single nest (hole) can result in a fine of up to £1000. Given the number of holes recorded in one face at Chard Junction (over 20) this amounts to a considerable potential liability and could prevent direct logging and sampling of a face. There could therefore be an advantage to deriving the stratigraphy from a combination of digital photography and laser scanning. There is also little doubt that as the cost of the equipment falls more and more contractors will have the equipment and so could potentially use it at a site under appropriate conditions.

The purpose of work undertaken during this phase was to evaluate the methodology before recommending it as standard or not. We intended to do at least a panel every 100m of quarry width (c. 2-3m in height) and depending upon faces available and the frequency of visits it is anticipated that this will amount to some 20 panels. We will experiment with the following parameters

1. Number of viewing positions (1, 2 and 3)
2. Range (distance from the face)

3. Resolution and gain settings
4. Angle and geometry of the face.
5. Viewing/weather conditions

4.2 Field Methods and Approach

Basic Principles

The ground scanning system used was a Leica ScanStation HDS3000. Ground laser scanning, also referred to as Ground LiDAR (as opposed to Airborne LiDAR), is the process of using the high definition surveying (HDS) system to "sample" (take measurements from) a scene in the real world. The generic term for this technique is terrestrial laser scanning or TLS. In the case of the HDS3000 distance is measured by the 'time of flight' but it is also possible to measure distance by a phase-shift approach as used by the Zeiss Z+F5010 system. Each individual laser measurement generates a 3D point, so a scan of a surface results in collections of these 3D points called "point clouds". Point clouds provide the basis for surface reconstruction or modelling. The basic principle of LiDAR (Light Detection and Ranging) is that the distance to an object is calculated by measuring the time delay between the transmission of a pulse and the detection of the reflected, ("return") signal. The scanner also measures the horizontal and vertical "direction" of the laser beam.

Once the ScanStation is set up on a tripod, (leveled, connected to the computer etc.) a surface can be scanned at different resolutions determined by the user. If only one set up location were to be used, and a single scan completed, a point cloud would be generated with arbitrary x,y,z co-ordinates which are internally accurate relative to each other. However, the normal situation is that more than one scan is required, and usually from more than one position. This is because the ScanStation cannot sample the parts of a surface it cannot "see". For example, if the laser scanner was set up in front of a person, their face could be scanned, but the back of their head would be missing. Further set up locations would be necessary to "acquire" the rest of their head. In order to "register" (stitch together) scans accurately, fixed points known as "control points" have to be established in the field, and individually scanned ("acquired") prior to scanning the desired surface.

If the location of control points does not change between scans, but they are called by the same name in each scan from each set up location, then they can be used to stitch together different scans using the common name only. This will result in a composite scan with arbitrary co-ordinates. In order to situate the control points, and therefore all point clouds generated by scans in a particular spatial framework, it is necessary to input the co-ordinates of each control point. This is usually done by using a known point or points, (a site specific co-ordinate system or real world co-ordinates), and a total station to establish the co-ordinates of each of the controls. The more control points are acquired prior to a scan the higher the accuracy of the scan registration (stitching together) is likely to be. It is possible to register different scans using only 2 control points, but a minimum of 3 is recommended, and ideally these should be spread geometrically as widely as possible.

Establishing the Control Grid

In practical terms then, the success, accuracy and speed of any scan is determined by the best possible positioning of the control points. In most scenarios where laser scanners have previously been employed in a heritage context, the scanned object tends not change very rapidly, (e.g. buildings); or in the case of excavation scanning could occur in a context where total stations are set up daily and a team are working in a relatively confined

area. This means that control points can be established that won't move (e.g. on the building) or set up daily on tripods and their position recorded as part of the normal process of excavation using a total station.

The major challenge at Hodge Ditch was the size of the excavation area, and the variation in the speed of the extraction process. Previous work at Hodge Ditch had led to recognition that the highly dynamic nature of the pit was a problem in establishing semi-permanent known points (Temporary Bench Marks (TBMs)) for surveying that could be employed over long periods. Several TBMs established when working at Hodge Ditch several years ago, had been destroyed, and others had been moved. Following careful examination of the pit, future extraction plans and discussions with quarry personnel, a number of new TBMs were established around the perimeter of the pit. These comprised: 1) ground points (metal rods driven through metal squares and spray painted, and in areas which remained at higher risk of further extraction or landscaping, wooden rods with nails in the top which were spray painted); and 2) tree points (yellow discs hammered into selected trees which could be seen from within the primary extraction area). These TBMs were used to situate the total station in an arbitrary grid, which was later put into real space (National Grid) co-ordinates) through using a differential GPS to record all ground points.

Figure 4.1 Example of metal Temporary Bench Mark in ground surveyed in using differential GPS

Figure 4.2 Example of wooden post used as Temporary Bench Mark in areas likely to be excavated of landscaped resulting in the destruction of the point. These were surveyed in using differential GPS.

Figure 4.3 Tree control points. Locations established in relation to TBMs using Total Station. These and the TBMS were then used to situate the Semi-Permanent control points established around the pit.

Initial test scans were conducted using temporary tripod set-ups as Control Points for scanning (Figure 4.4). This method, was very accurate and effective due to the proximity of the targets and the fact that it was possible to rotate the target heads so they were directly facing the scanner. However, it was quickly dismissed as impractical for long term scanning of the pit. Each trip required the transportation of at least five tripods, (one for the total station, one for the scanner and 3 for the targets), at least 3 targets, the ScanStation and the total station. Although achievable within the course of a day for one or two people, the vast majority of time on site was spent transporting equipment to the scan location, setting up and recording control points, with only a minimal amount of time left for scanning. There was also a risk of wasting the whole day's work, when, after setting up all the equipment, and establishing the position of the control points, it began raining too heavily to allow scanning to proceed. Tripods could not be left in place overnight, so each visit required the same procedure.

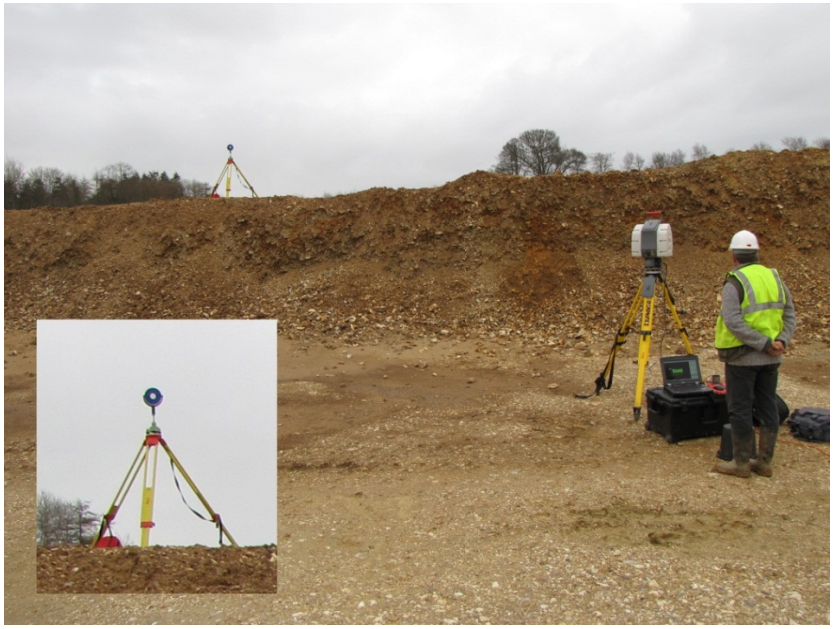

Figure 4.4: The use of standard ground laser targets.

A new system was therefore devised which allowed semi-permanent control targets to be established and linked in to the TBM grid (and therefore National Grid) described above, using the total station. This meant that with each visit, it was possible to arrive, set up the scanner, acquire the semi-permanent control targets and then spend the rest of the day scanning. This was easily achievable by one person. The primary difficulties identified in establishing a network of semi-permanent control points were:

1) establishing enough points that would not move so it was possible to acquire at least 3 targets from any point within the extraction area.
2) ensuring that the 3 targets would not be moved
3) ensuring that as excavation proceeded that the control points remained close enough to maintain an acceptable level of accuracy. I.e. as the pit became deeper, the distance to the control points increased and accuracy potentially decreased.
4) ensuring there were enough targets at the correct angles to allow good target acquisition. Because the semi-permanent targets did not rotate, acquiring the targets required them to be scanned at more oblique angles than usual in some cases, so it was essential to establish a range of controls at different angles to optimise target acquisition from scan locations all around the pit.
5) preventing the sticky control targets from falling off the posts and other surfaces to which they were attached.

The semi-permanent control points comprised self adhesive Leica targets which were stuck to flat surfaces such as the shed, signs, and half round posts rammed into the ground with a post driver. Twenty eight control points were established primarily on the posts and were used across HD1, HD2 and HD 3 over the course of a year. Due to the cost of the posts (£4) and targets (£10) staff of Bardon were asked not to destroy the control points if they needed to move them, but to keep them so they could be re-used with a different name elsewhere in the pit. On the whole this method was very successful, with only one post being destroyed, two signs with stickers on them moved so they were no longer useful, and three posts being reused over about a year.

The position of the targets on posts was outlined with marker pen in case they fell off (see inset on Figure 4.6). This only occurred in one instance, and the lines were effective in accurately re-positioning the target. After this, all targets were covered with plastic bags to protect them from the elements. Although condensation formed in the bags, and the targets wrinkled a little, this did not seem to affect the target acquisition when scanning, and would have a minimal (1mm at the outside) effect on the position of the target.

Figure 4.5 Control Targets on shed in HD1

Figure 4.6 Semi-permanent Control Targets on posts. Example on the left is the Leica stickers, and on the right is the marker pen trial version

Due to the cumulative cost of the targets (over 20 could be used at a large site), other target types were tested. These included marking the posts with marker pen, using a simple cross, and also a rough circle, but leaving a small un-inked hole in the middle of the mark, to mimic the metal point in the middle of the official targets (Figure 4.6). Provided the scanner was at less than c. 60 metres from the target, and was positioned so that the target face was straight on to the scanner (rather than oblique), the targets could be acquired remarkably well (see Figures 4.7 and 4.8 below). The main disadvantages are

that they do not last as long as the self-adhesive targets. In addition, during post processing, it is not possible for the software to recognise these as control points from scanned data. Although it is possible just to fence an area from the photographed control point, and acquire a target, at a general level, we found that photographing and then pre-scanning the target area at high resolution (2 – 5 mm) made the rapid acquisition of the target considerably easier. The pre-acquisition scan meant that the target could be fenced much more precisely and the control point cross hairs were placed in the correct location first time. In the case of slight mis-positioning, generally caused by the control point being at an oblique angle relative to the scanner, it was also possible to manually adjust the position of the cross hairs to the correct centre of scanned target. This was rarely necessary and when done, the scan was rotated and examined through many different angles to ensure the control point was indeed in the centre of the scanned target.

A further possible benefit of pre-scanning the posts noticed during this stage of the project, was that if the target name had been put on the post in a bright paint or by any method that resulted in a significant contrast with the post, the label could then be seen in the scanned data when displayed using the intensity values. This is useful in correcting labelling errors the user could make in Cylone when obtaining and defining the control points in the field, (e.g. “TMB2”, or “circ” in the figures below) as the label can be compared with the scanned label on the post. This is important because if the control point names do not match between the scanned control points and the co-ordinates of the control points obtained from total station and GPS data, when registering the scans (discussed further below) they cannot be used as the errors will be too large.

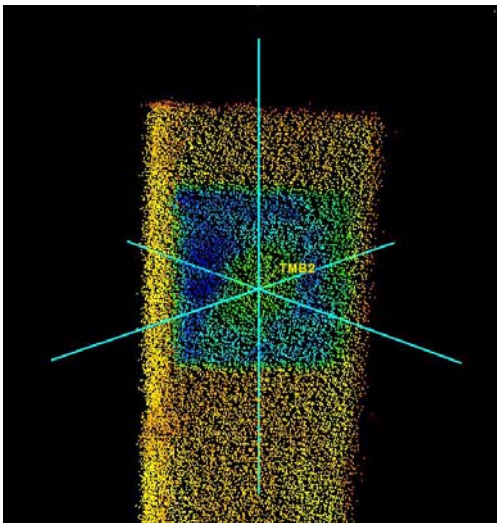

Figure 4.7 Example of scanned Leica Target control point displayed using intensity of return values

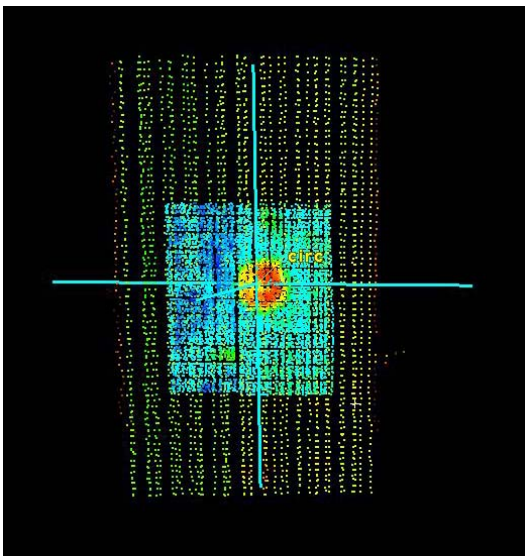

Figure 4.8 Example of scanned marker pen on wooden post control point displayed using intensity of return values

4.3 Processing and Analysis

As per the EH Guidance (2006) the data will be archived with ADS as simple text files (x,y,z) with intensity and colour data and in addition the data in the .imp format. The data was manipulated using the proprietary software package Cyclone which allows output of data in several formats including as TINs. Rendered models were also stored as Windows AVI animations and as jpgs and tiffs. Additional processing of the data was performed using several different pieces of software, but primarily Cyclone which is the software that comes with the scanner. The processing described here was conducted using Cyclone version 7.1.

Registration Process and Results

As described above, the control points were located in real space using differential GPS and total station. The GPS and total station data were extracted using Leica GeoOffice Combined version 7 (2008) in the usual way, and exported as x,y,z data as a .txt file. Naturally there is a degree of error in recording the co-ordinates using a differential GPS and total station. With the total station where resections were conducted and when averaging was being used, the Total station alerts the user to potential error when a point seems to be in the wrong location or inaccurate and won't record the point unless specifically permitted to do so. Consequently, the total station results are very accurate, (<1mm) and too small to be material to this discussion. For the GPS, the accuracy levels were set so that points would not be recorded unless they were better than 50 mm 3D CQ. The 3D CQ is the 3D co-ordinate quality and records the accuracy of all the x,y,z measurements considered together, i.e. the spherical co-ordinate quality. See Ayers, 2011 for full details. Examination of the results from the differential GPS shows that the position and height quality (3D CQ) for all the control points recorded at Chard are <30 mm and in most cases <10 mm. In the two cases where the 3D CQ quality was in the higher range of ~25 to 30mm, examination of the quality of the separate components that are used to calculate this figure (eastings, northing and height quality, with the error defined by the standard deviation), showed that the main factor affecting the overall 3D CQ was the height value. In both of the higher range 3D CQ cases, this had an accuracy of 26mm. All the ground TBM s were recorded on the same day, using the same differential GPS (a

Leica RX1250Xc GPS & GLONASS SmartRover using Leica SmartNet RTCMv3 corrections via the Leica SmartNet repeater box 'SmartBox'), by the same person, the overall error of the TBM grid is <30mm.

A list of the co-ordinates of the control points was then imported into Cyclone as a “ScanWorld” of real co-ordinates. Column headers were: TargetID, Eastings, Northings and Height. This file was then imported into Cyclone. This control Scan World was then used to register all the scans, so they appear in real space by matching the names from the Target ID to beween the Control Scan World, and each of the ScanWorlds recorded in the field. The total number of semi-permanent target control points established and used was 28. These are shown in Figure 4.9.

TARGETID	EASTINGS	NORTHINGS	HEIGHT
C5	334892.9277	104743.7645	72.958
NM1circ	334874.6483	104795.8848	72.6747
NM2cross	334874.6456	104795.8847	72.5829
NM3	334784.722	104729.882	73.0658
REDSIGN	335123.5056	104653.261	79.5462
SHED1	335091.0046	104634.4826	78.6598
SHED2	335091.1355	104634.512	78.5817
T1	334868.0092	104687.0298	74.8951
T2	334895.2018	104687.9253	73.8449
T3	335038.9355	104628.8161	78.2704
T4	335046.655	104632.9932	78.1394
T5	335194.1843	104762.222	76.2977
TMA	335035.5828	104824.5517	72.597
TMB	334979.569	104668.9983	67.4804
TMB2	334839.7832	104701.9067	74.6357
TMC	335034.8555	104786.8542	69.7631
TMD	335054.5051	104752.8217	69.7321
TME	335051.5995	104656.999	66.8075
TMF	335147.1174	104694.1445	62.0237
TMG	335133.5018	104785.132	63.2376
TMGb	335133.5252	104785.1745	63.2505
TMH	335108.5489	104717.7301	60.9549
TMI	335140.4392	104832.5437	67.5966
TMJ	334890.8469	104793.294	71.7918
TMK	334997.254	104800.8204	65.7779
TMK2	334820.2523	104788.1768	72.1459
TMX	334961.3609	104810.5184	74.2212
TMY	334946.515	104654.49	75.0641

Figure 4.9 List of Control Targets and their co-ordinates

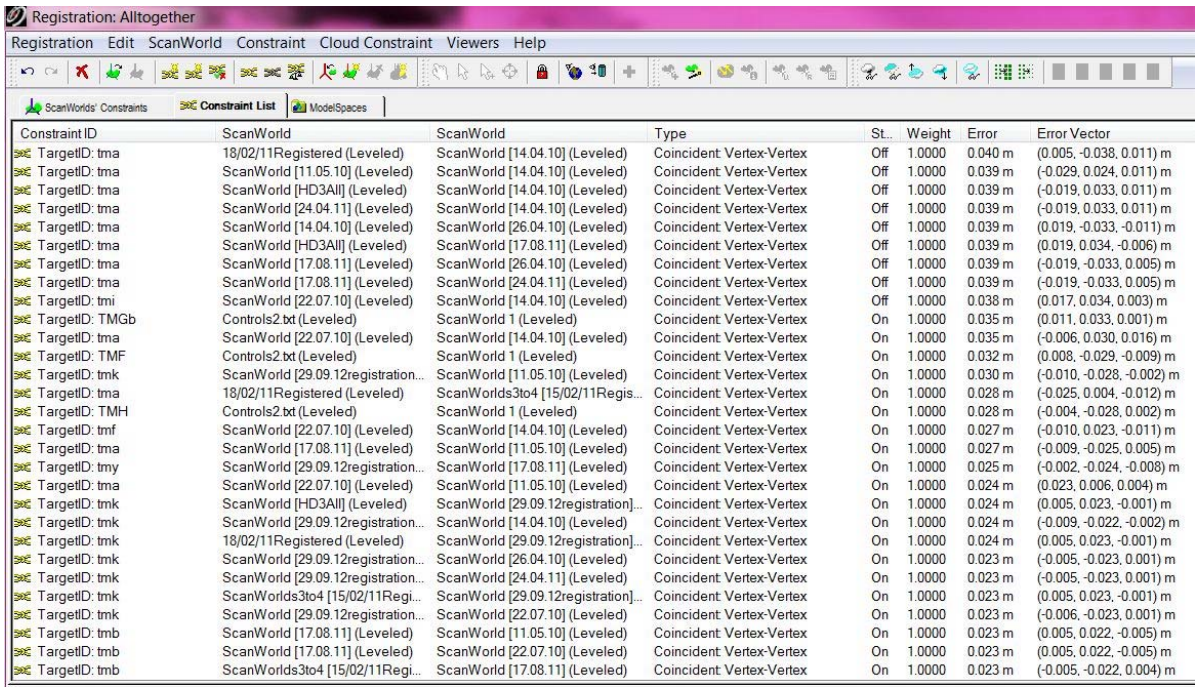

Constraint ID	ScanWorld	ScanWorld	Type	St..	Weight	Error	Error Vector
TargetID: tma	18/02/11Registered (Leveled)	ScanWorld [14.04.10] (Leveled)	Coincident Vertex-Vertex	Off	1.0000	0.040 m	(0.005, -0.038, 0.011) m
TargetID: tma	ScanWorld [11.05.10] (Leveled)	ScanWorld [14.04.10] (Leveled)	Coincident Vertex-Vertex	Off	1.0000	0.039 m	(-0.029, 0.024, 0.011) m
TargetID: tma	ScanWorld [HD3All] (Leveled)	ScanWorld [14.04.10] (Leveled)	Coincident Vertex-Vertex	Off	1.0000	0.039 m	(-0.019, 0.033, 0.011) m
TargetID: tma	ScanWorld [24.04.11] (Leveled)	ScanWorld [14.04.10] (Leveled)	Coincident Vertex-Vertex	Off	1.0000	0.039 m	(-0.019, 0.033, 0.011) m
TargetID: tma	ScanWorld [14.04.10] (Leveled)	ScanWorld [26.04.10] (Leveled)	Coincident Vertex-Vertex	Off	1.0000	0.039 m	(0.019, -0.033, -0.011) m
TargetID: tma	ScanWorld [HD3All] (Leveled)	ScanWorld [17.08.11] (Leveled)	Coincident Vertex-Vertex	Off	1.0000	0.039 m	(0.019, 0.034, -0.006) m
TargetID: tma	ScanWorld [17.08.11] (Leveled)	ScanWorld [26.04.10] (Leveled)	Coincident Vertex-Vertex	Off	1.0000	0.039 m	(-0.019, -0.033, 0.005) m
TargetID: tma	ScanWorld [17.08.11] (Leveled)	ScanWorld [24.04.11] (Leveled)	Coincident Vertex-Vertex	Off	1.0000	0.039 m	(-0.019, -0.033, 0.005) m
TargetID: tmi	ScanWorld [22.07.10] (Leveled)	ScanWorld [14.04.10] (Leveled)	Coincident Vertex-Vertex	Off	1.0000	0.038 m	(0.017, 0.034, 0.003) m
TargetID: TMGb	Controls2.txt (Leveled)	ScanWorld 1 (Leveled)	Coincident Vertex-Vertex	On	1.0000	0.035 m	(0.011, 0.033, 0.001) m
TargetID: tma	ScanWorld [22.07.10] (Leveled)	ScanWorld [14.04.10] (Leveled)	Coincident Vertex-Vertex	On	1.0000	0.035 m	(-0.006, 0.030, 0.016) m
TargetID: TMF	Controls2.txt (Leveled)	ScanWorld 1 (Leveled)	Coincident Vertex-Vertex	On	1.0000	0.032 m	(0.008, -0.029, -0.009) m
TargetID: tmk	ScanWorld [29.09.12registration...	ScanWorld [11.05.10] (Leveled)	Coincident Vertex-Vertex	On	1.0000	0.030 m	(-0.010, -0.028, -0.002) m
TargetID: tma	18/02/11Registered (Leveled)	ScanWorlds3to4 [15/02/11Regis...	Coincident Vertex-Vertex	On	1.0000	0.028 m	(-0.025, 0.004, -0.012) m
TargetID: TMH	Controls2.txt (Leveled)	ScanWorld 1 (Leveled)	Coincident Vertex-Vertex	On	1.0000	0.028 m	(-0.004, -0.028, 0.002) m
TargetID: tmf	ScanWorld [22.07.10] (Leveled)	ScanWorld [14.04.10] (Leveled)	Coincident Vertex-Vertex	On	1.0000	0.027 m	(-0.010, 0.023, -0.011) m
TargetID: tma	ScanWorld [17.08.11] (Leveled)	ScanWorld [11.05.10] (Leveled)	Coincident Vertex-Vertex	On	1.0000	0.027 m	(-0.009, -0.025, 0.005) m
TargetID: tmy	ScanWorld [29.09.12registration...	ScanWorld [17.08.11] (Leveled)	Coincident Vertex-Vertex	On	1.0000	0.025 m	(-0.002, -0.024, -0.008) m
TargetID: tma	ScanWorld [22.07.10] (Leveled)	ScanWorld [11.05.10] (Leveled)	Coincident Vertex-Vertex	On	1.0000	0.024 m	(0.023, 0.006, 0.004) m
TargetID: tmk	ScanWorld [HD3All] (Leveled)	ScanWorld [29.09.12registration]...	Coincident Vertex-Vertex	On	1.0000	0.024 m	(0.005, 0.023, -0.001) m
TargetID: tmk	ScanWorld [29.09.12registration...	ScanWorld [14.04.10] (Leveled)	Coincident Vertex-Vertex	On	1.0000	0.024 m	(-0.009, -0.022, -0.002) m
TargetID: tmk	18/02/11Registered (Leveled)	ScanWorld [29.09.12registration]...	Coincident Vertex-Vertex	On	1.0000	0.024 m	(0.005, 0.023, -0.001) m
TargetID: tmk	ScanWorld [29.09.12registration...	ScanWorld [26.04.10] (Leveled)	Coincident Vertex-Vertex	On	1.0000	0.023 m	(-0.005, -0.023, 0.001) m
TargetID: tmk	ScanWorld [29.09.12registration...	ScanWorld [24.04.11] (Leveled)	Coincident Vertex-Vertex	On	1.0000	0.023 m	(-0.005, -0.023, 0.001) m
TargetID: tmk	ScanWorlds3to4 [15/02/11Regi...	ScanWorld [29.09.12registration]...	Coincident Vertex-Vertex	On	1.0000	0.023 m	(0.005, 0.023, -0.001) m
TargetID: tmk	ScanWorld [29.09.12registration...	ScanWorld [22.07.10] (Leveled)	Coincident Vertex-Vertex	On	1.0000	0.023 m	(-0.006, -0.023, 0.001) m
TargetID: tmb	ScanWorld [17.08.11] (Leveled)	ScanWorld [11.05.10] (Leveled)	Coincident Vertex-Vertex	On	1.0000	0.023 m	(0.005, 0.022, -0.005) m
TargetID: tmb	ScanWorld [17.08.11] (Leveled)	ScanWorld [22.07.10] (Leveled)	Coincident Vertex-Vertex	On	1.0000	0.023 m	(0.005, 0.022, -0.005) m
TargetID: tmb	ScanWorlds3to4 [15/02/11Regi...	ScanWorld [17.08.11] (Leveled)	Coincident Vertex-Vertex	On	1.0000	0.023 m	(-0.005, -0.022, 0.004) m

Figure 4.10 Registration process screen grab

The registration process is important as it is here that any aberrant or inaccurate control target scans can be identified, and if necessary removed from the registration process. Such errors occur due to two principal causes: 1) improper labelling of a point in the ScanWorld or 2) inadequate control target acquisition in the field. This means that when the software tries to match the recorded (scanned) location of the control target, with the known target co-ordinates, taking into consideration its relationship to the other scanned control points used for to establish the position of a scan, it either cannot resolve the positions at all, or it can but with a 3 dimensional error. Given that the Scanstation was being pushed to its limit of its range in terms of scanning distance, this was important. Figure 4.10 shows a screen grab of the registration process, the overall error (rather like the 3DCQ described above for the GPS data) and the error vector, (which details the different components of the overall error).

On the whole there were few problematic control targets, the principal problems occurring where control points had been mislabelled causing extreme registration errors of for example 28 metres. This was easily rectified by checking that this was the cause of the problem, and re-naming the point in Cyclone. Other “large” errors (most commonly of ~ 80 to 60mm) were excluded from the registration process, resulting in improved accuracy for the other targets. As at least two and generally three or more targets are needed to register scans together, there is a limit to how many control target scans can be exclude. However it was possible in this case, to register all scans conducted over the year using only an overall 3D error of <30 mm. I.e. All errors > 40 mm were excluded from the registration process that “stitched together” all the scans conducted over a year. For the registration of individual scans, of specific areas, the accuracy was considerably better and often < 10mm.

Grain Size Analysis

Numerous faces were scanned over the course of the year through the pit at varying degrees of resolution and scan angles. These included detailed scans of five frames used

in the Sedimetrics analyses described above. The process and results of these scans are described below. In all cases the medium size frame was used.

Figure 4.11 below shows the location of the first scanned frame from HD 2. From Figure 4.12 it is clear that this frame comprises a framework gravel, grading to a clast supported gravel with a sand and stil matrix. It is generally quite poorly sorted.

Figure 4.11: Location of Frame 0 in Hodge Ditch 2

Figure 4.12: Frame 0 close up

Figure 4.13 shows the frame scanned from two directions. The top two images highlight different scans obtained from separate setup locations. The scan data are then cropped to focus just on the frame, and displayed as merged scans (i.e. all the data points are merged into a single point cloud) and displayed using the full range of intensity values recorded from both scans. The merged scans can then be shaded which emphasises the

surface micro-topography of the area of interest. The central image shows the same area, but using only one of the scan station locations (i.e. only a single angle). Note the black area where no data were recorded due to the frame obstructing the gravel surface behind. Both the single scan and the merged scan point clouds were then further cropped so that only the area within the frame markers (used for Sedimetrics analyses) were used. Once extracted these were rotated and examined for relic points of the scanned frame. This process is shown using images from Frame 3 (discussed below) in Figure 4.14. The relic frame points can clearly be seen at the top of Image c, but care must be taken when cleaning up these points, not to delete the scanned surface. This was achieved by rotating the image until the relic frame points could be isolated, and fenced (see white line in image d) by clicking around them, and then deleting. Often the difference in the intensity values aided the cleaning process. This was conducted for all the frames discussed below, irrespective of whether the point clouds extracted for analysis were generated using one of more merged point clouds from different scan locations.

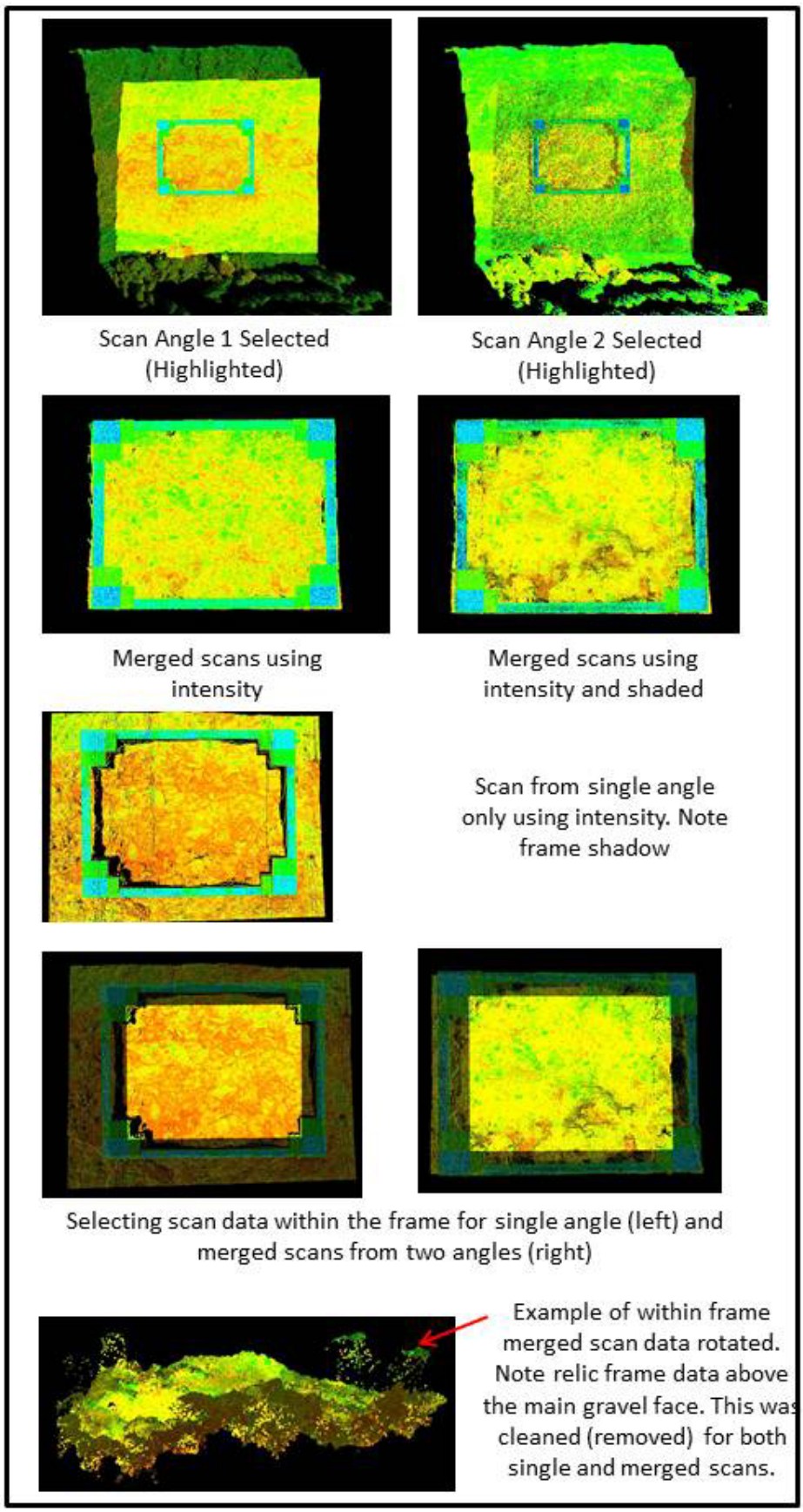

Figure 4.13 Scanned grain size data analysis using data from Frame 0

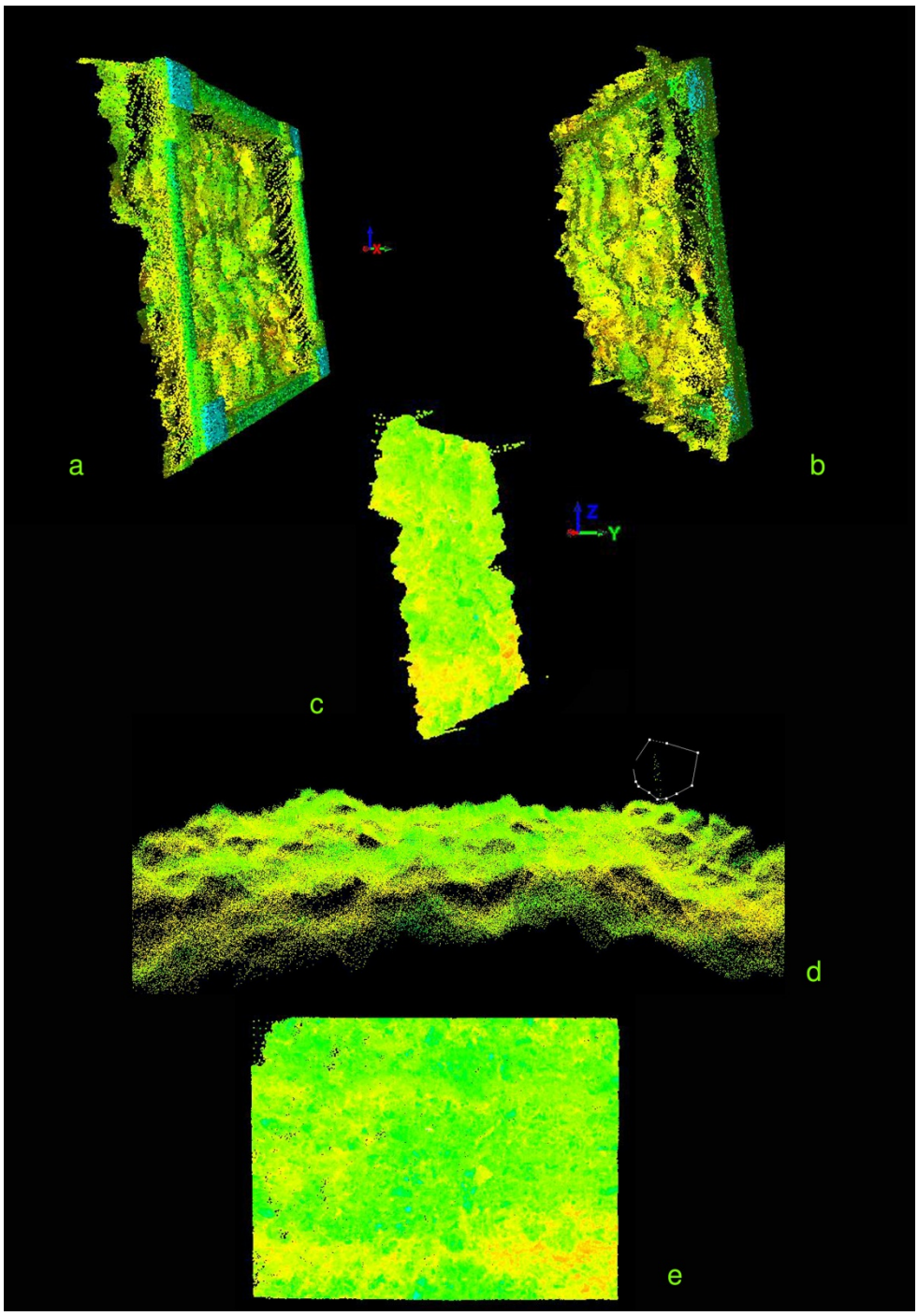

Figure 4.14 Example of sequence of "cleaning up" a frame of scanned points before processing in MatLab: Frame 3

Having extracted the relevant point cloud from the frame, which is fully georeferenced, a considerable amount of effort was spent trying to model the data within Cyclone to calculate roughness values. The principal problem encountered was that the co-ordinate system had to be redefined as the surface was approximately vertical, rather than horizontal. Figure 4.15 shows the original georeferenced scan data and the co-ordinate vertices. By selecting specific points, the co-ordinate system can be realigned, but all "real world" data are lost, although the relative distance between points obviously remains unaltered. This allows the z co-ordinate to be redefined as x or y and the x or y co-ordinate to become the z as in Figure 4.16. It is then possible to insert a reference plane relative to the point cloud data and to create basic, complex and TIN meshes as shown in Figures

4.17-4.20. These can then be contoured, (Figure 4.21) and basic measurements calculated relative to the user-defined plane. This method was not pursued as redefining the co-ordinate system was not user friendly, and somewhat subjective, did not take advantage of the real world data collected, was time consuming and not easy to use. Following discussions with other Scanstation users, two other options were then tested. The first method redefined the co-ordinate vertices as explained above, and then exported all the points into GIS. This was achievable for the medium frame size, but the number of scanned points could be large. For example in Figure 4.22 the frame is covered by 321260 points. It is important to note however, that the number of points exported can be decimated or reduced, if needed, and that although this may reduce the data quality, it can significantly speed up processing times. This applies to all other modelling using scan data and is discussed further in the Modelling section below.

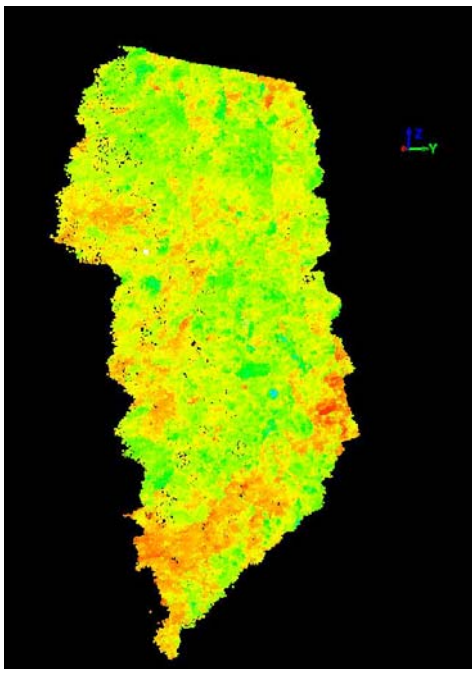

Figure 4.15: Frame scanned showing co-ordinate vertices in real space

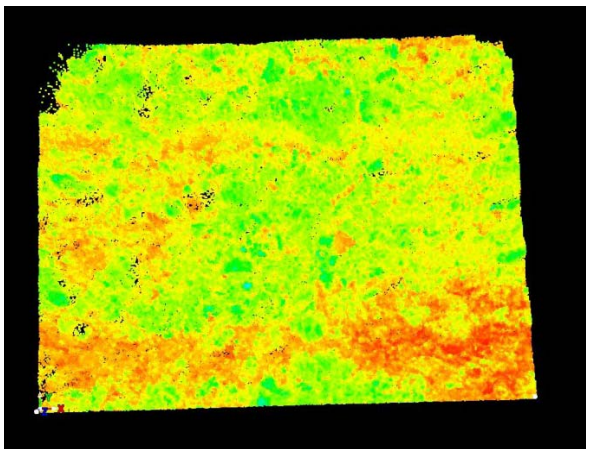

Figure 4.16: Frame scanned showing co-ordinate vertices redefined using selected pick points effectively making what was roughly the y-axis become the x axis.

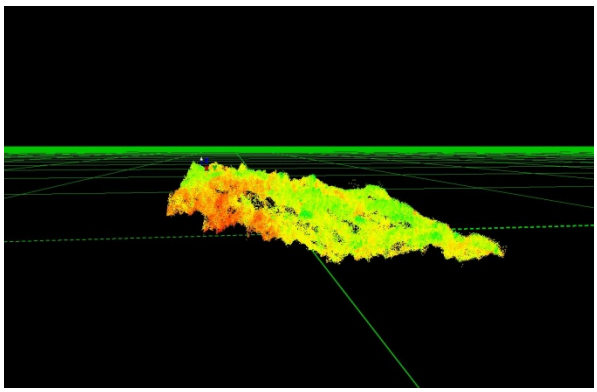

Figure 4.17 Scanned frame in redefined co-ordinate system displayed according to the new z axis relative to an arbitrary plane in Cyclone

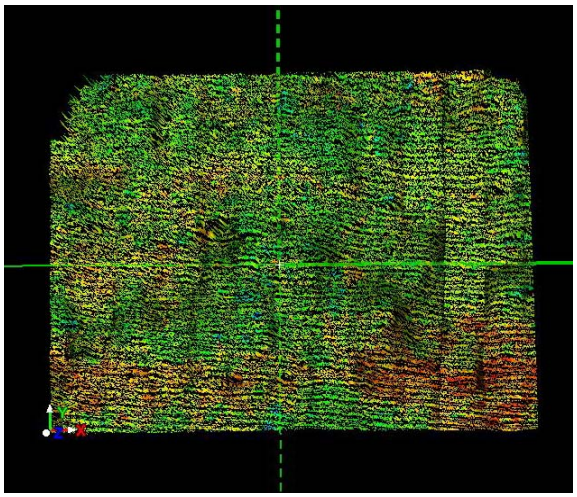

Figure 4.18 Basic meshing of data shown in Figure 4.9 within Cyclone

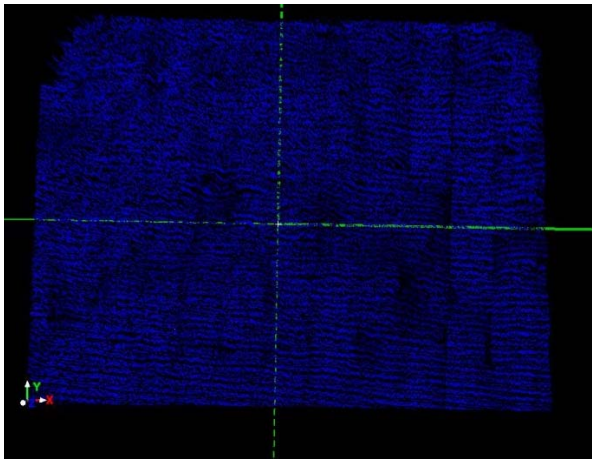

Figure 4.19 Complex meshing of data shown in Figure 4.9 within Cyclone

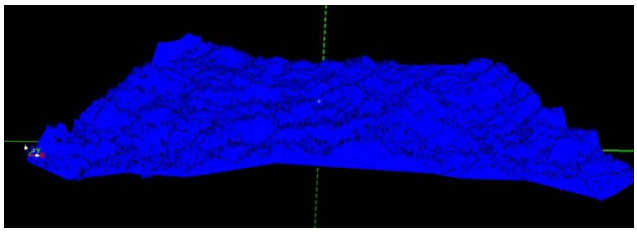

Figure 4.20 TIN meshing of data shown in Figure 4.9 within Cyclone

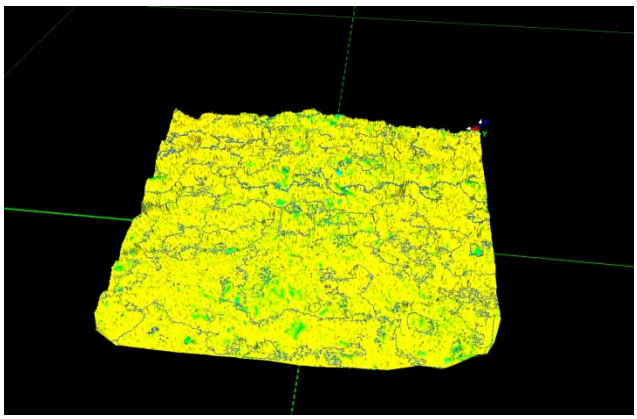

Figure 4.21 Contouring data shown in Figure 4.9 within Cyclone

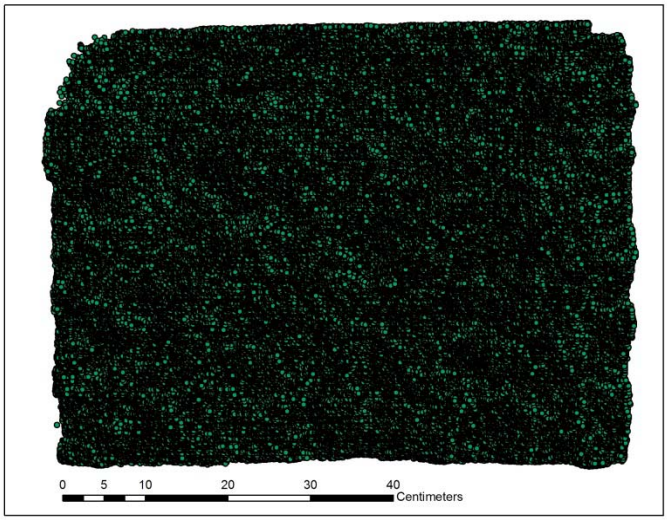

Figure 4.22 321260 points exported as csv file, from point cloud data of Frame 3 (as used in Figures 4.7 to 4.13), but displayed in ArcGIS. Although a co-ordinate system was not defined, the data frame of was defined in metres.

The tools available for interpolation in GIS between points are much better than in Cyclone and more user-friendly, allowing a greater range of visualisations. Contour data, analytical tools, statistical summaries can all be generated. Some of these are shown in Figures 4.23 to 4.26.

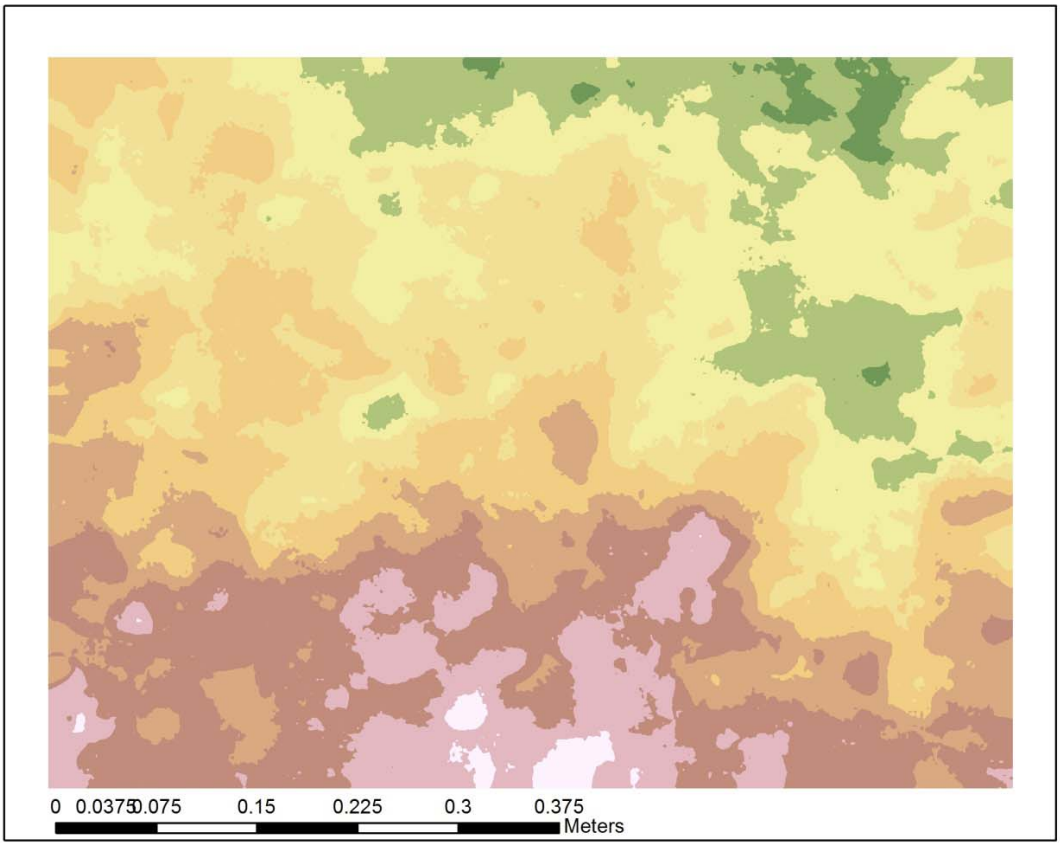

Figure 4.23 Point data shown in Figure 4.14 interpolated using Inverse Distance Weighting (considering 12 points surrounding each point) displayed using 9 classifications.

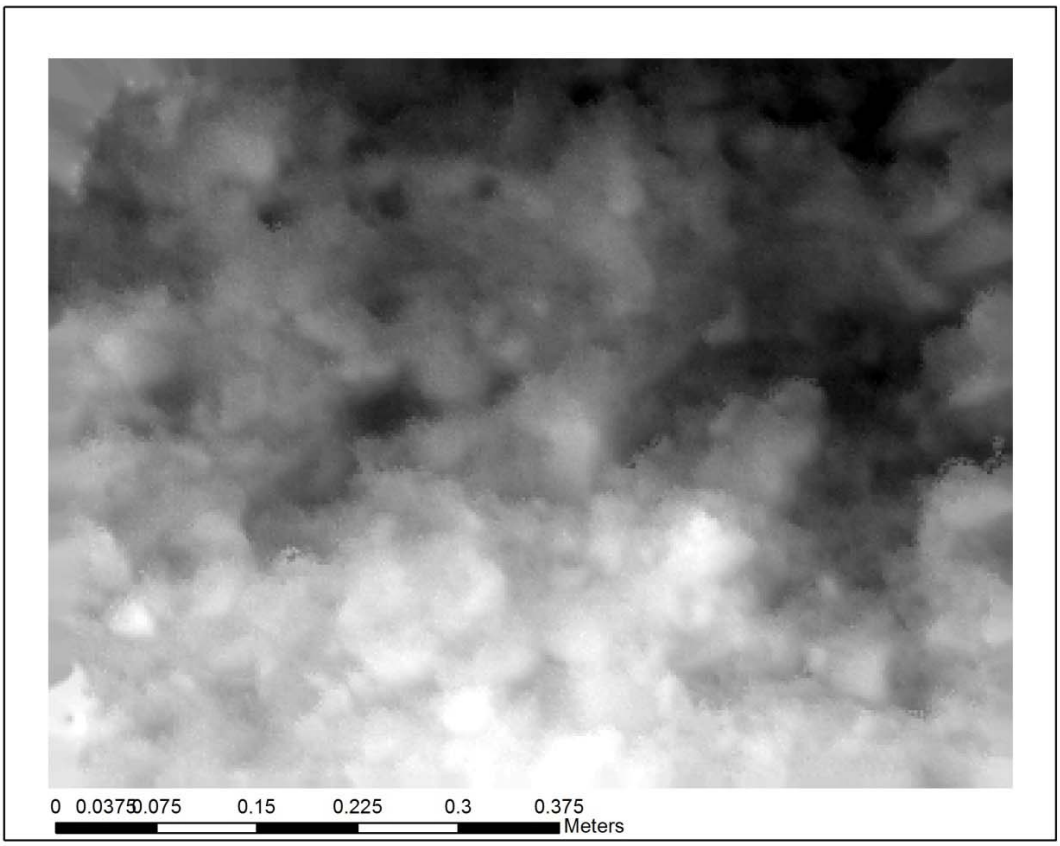

Legend

Idw_XYframep2

Value

High : 0.0289324

Low : -0.137531

Min: -0.13673131167888641
Max: 0.026773711666464806
Mean: -0.058255816138263125
StdDev: 0.034219158363130754

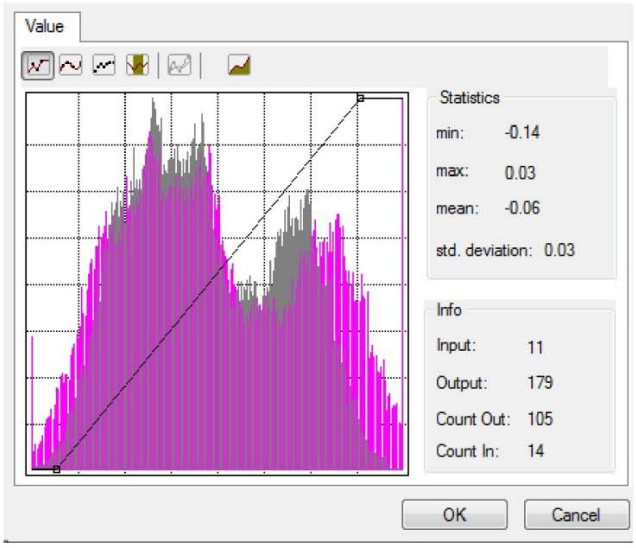

Figure 4.24 Point data displayed using stretched symbology, and with basic statistics and a histogram of values generated in ArcGIS.

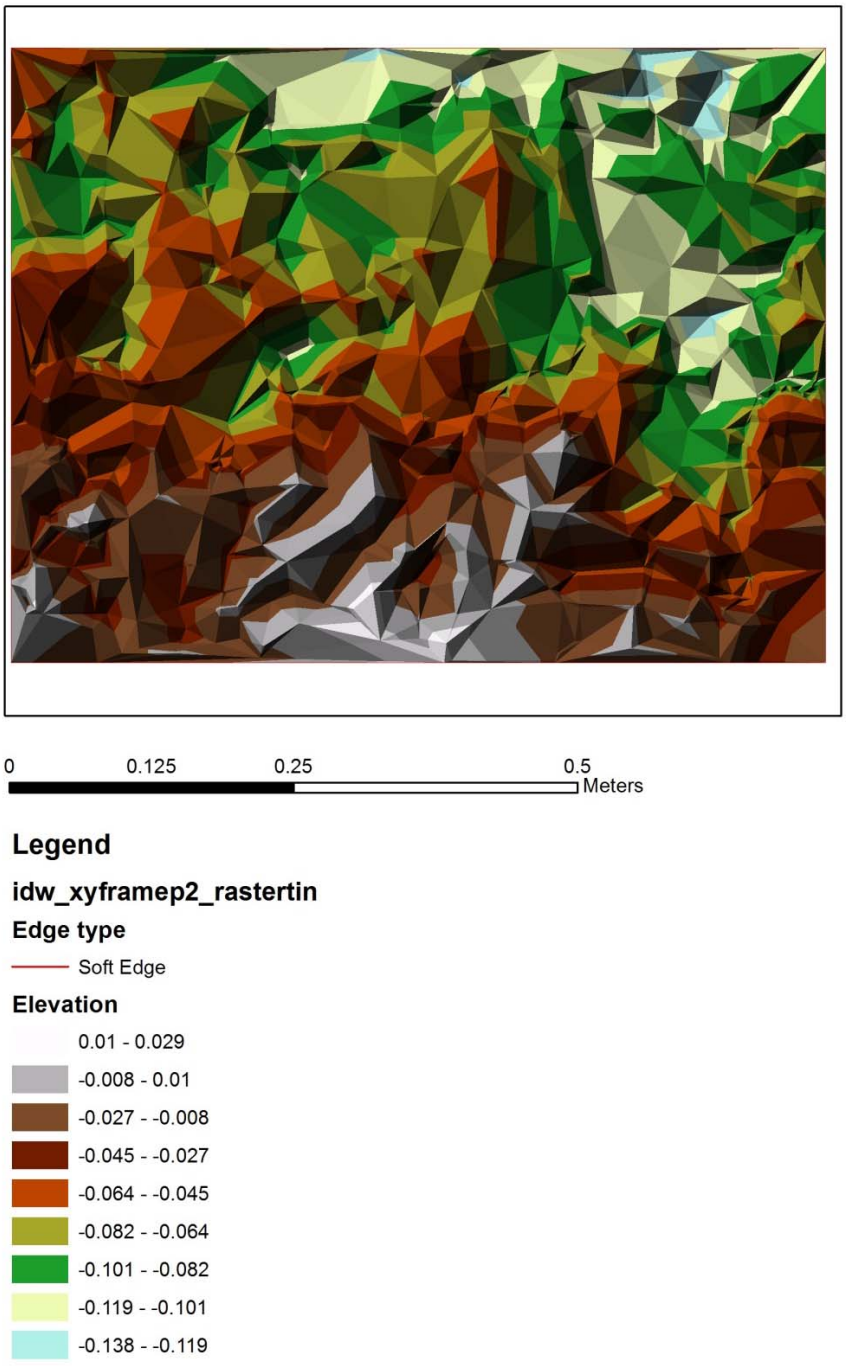

Figure 4.25 TIN of point data generated in ArcGIS. Note the display options are much better than in the Cyclone generated TIN as seen in Figure 4.20.

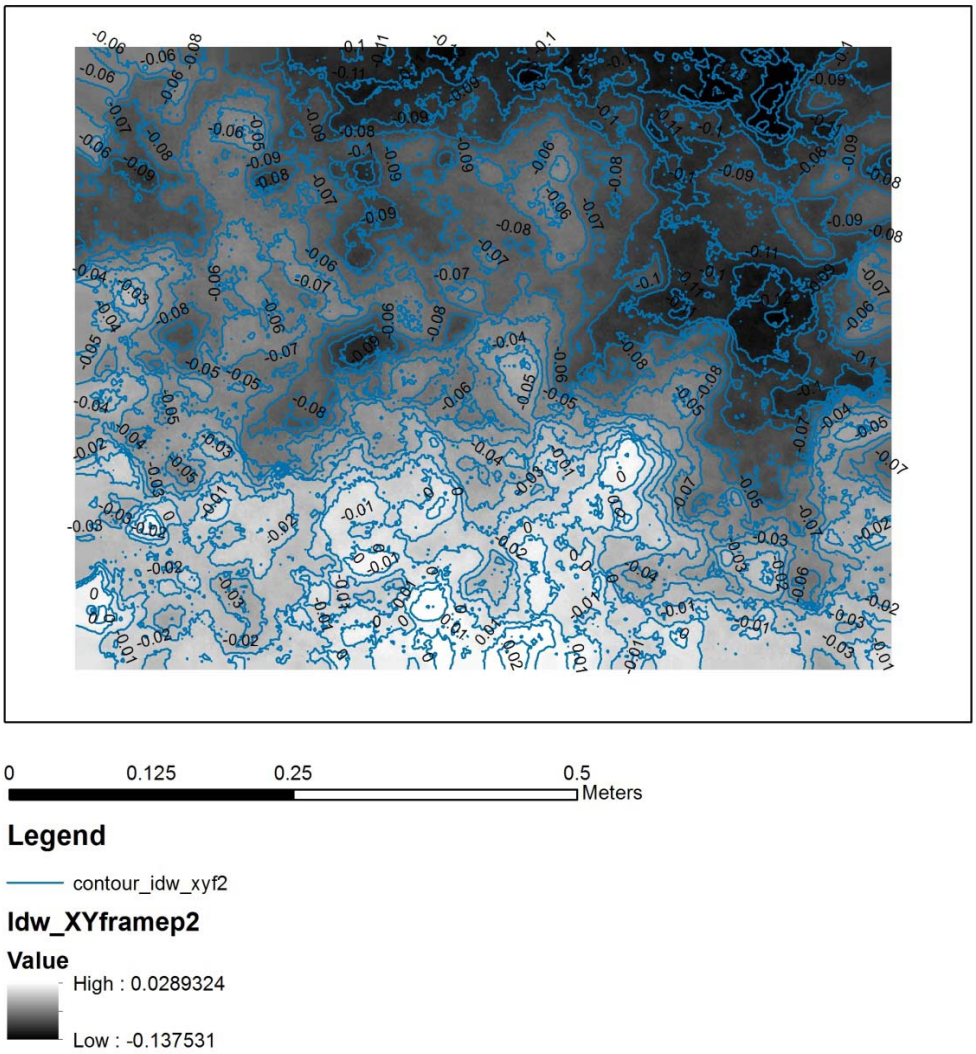

Figure 4.26 Inverse distance weighted interpolation of point data generated in ArcGIS, used to generate contours (blue lines) labelled with values.

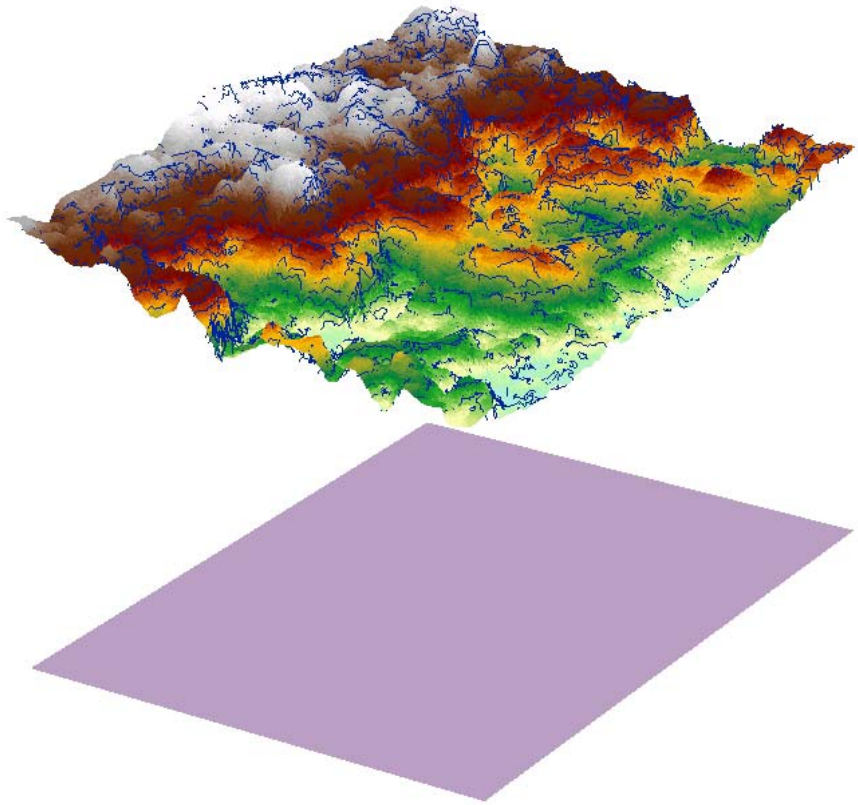

Figure 4.27 Data shown in Figure 4.17 modelled in ArcScene (white is high, blue/green is low) relative to an arbitrary plane.

It is also possible to generate volume and surface area values that act as a proxy for roughess within ArcMap. This is visualised in Figure 4.28 by displaying the data in ArcScene. Using the Terrain and TIN surface: Polygon Volume Tool, the volume between an arbitrary plane, set at a specific height and the TIN of the point cloud data can be calculated. I.e. the volume contained within the red lines, purple plane and green TIN shown in Figure 4.28. The surface area is also calculated, and both added to the attribute table of the plane polygon, as shown in Figure 2.29. Provided the height of the plane is constant relative to the points, it should be possible to generate measurements from the point cloud data of other frames and compare them. However, the third and most effective method trialled here, was to export the cleaned point cloud data from Cyclone keeping its real world co-ordinates. This data was then run through a programme designed by Dr Jo Neild to run in MatLab. This generates roughness plots quickly, at different scales (defined by the user) with excellent results. All the plot results below were run through 10 cm grids, as these were most appropriate to the size of the wooden frame used.

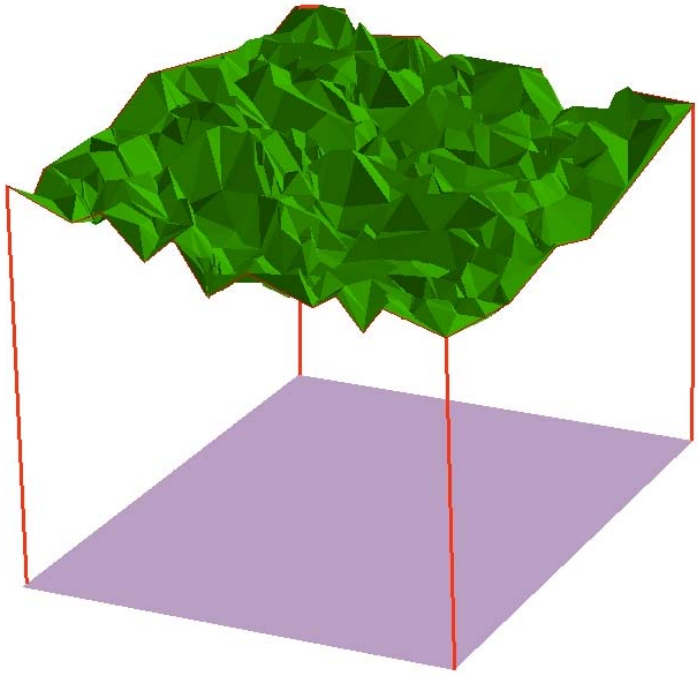

Figure 4.28 Visulisation of the principle behind calculating Volume and Surface area measurements relative to an arbitrary plane in ArcMap. This image was generated in ArcScene for illustration purposes only.

Table

Plane

OBJECTID *	SHAPE *	SHAPE_Length	SHAPE_Area	Height	Volume	SArea
1	Polygon Z	2.541088	0.39647	-1	0.365629	0.57415

Figure 4.29 Volume and Surface area calculations from Frame 3 against a plane set at an arbitrary height of -1.

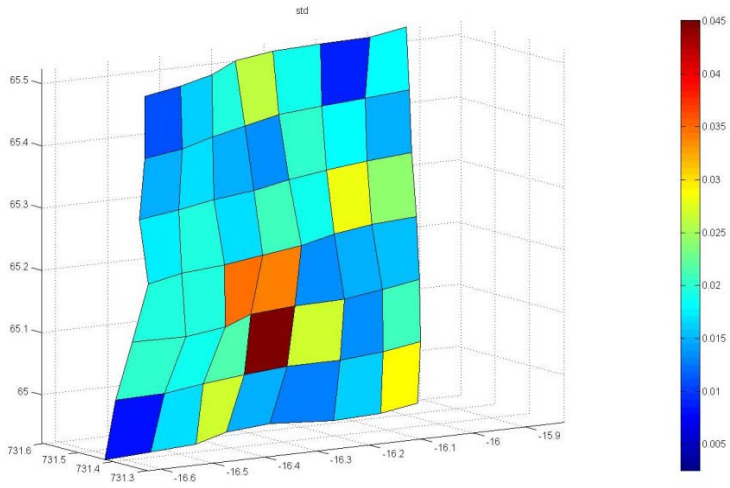

Figure 4.30 Roughness Frame 0 results using merged scan

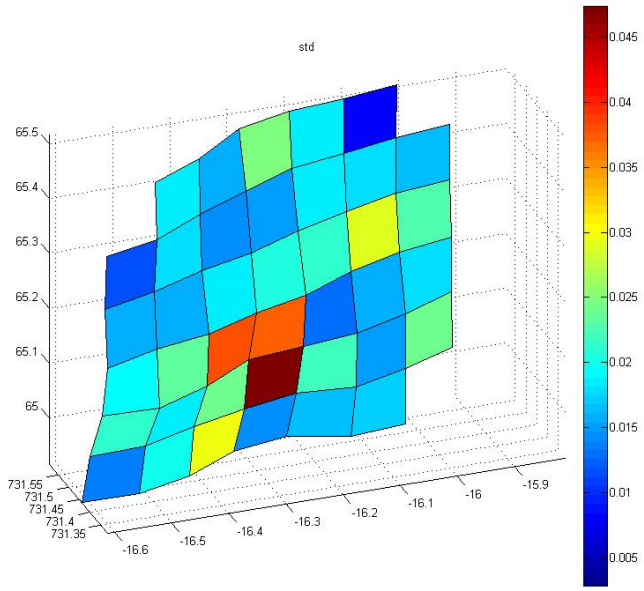

Figure 4.31 Roughness Frame 0 results using one scan

In Figures 4.30 and 4.31, the grid roughness is plotted from two merged scans and also for a single scan, (as discussed above and shown in Figure 4.13). As can be seen there is no significant difference between the two plots. The only difference is the missing corner squares, and this is related to holes in the data generated by the shadow of the frame.

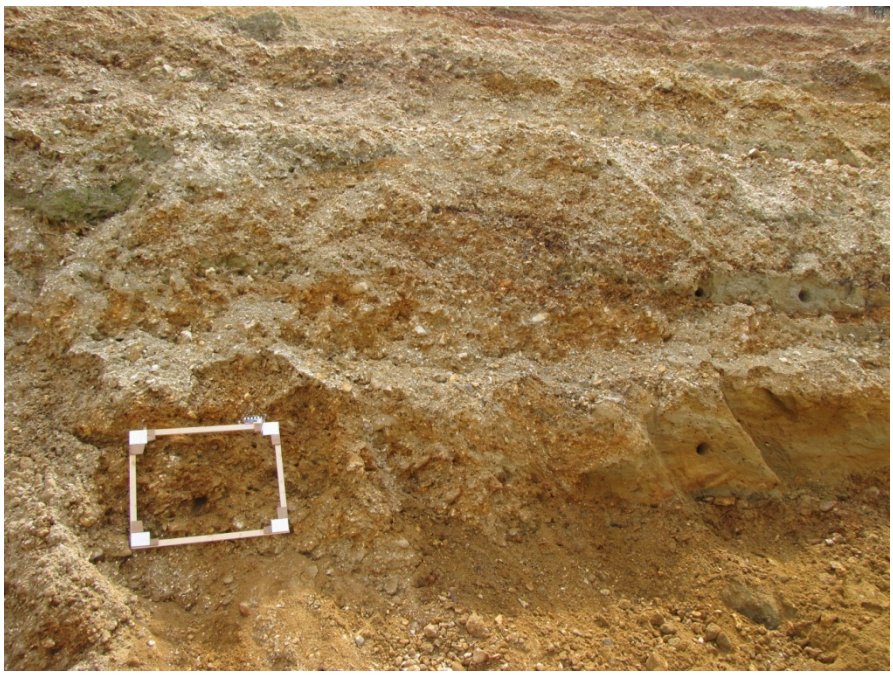

Figure 4.32 Frame 1 general location in Hodge Ditch 1

Figure 4.33 Frame 1

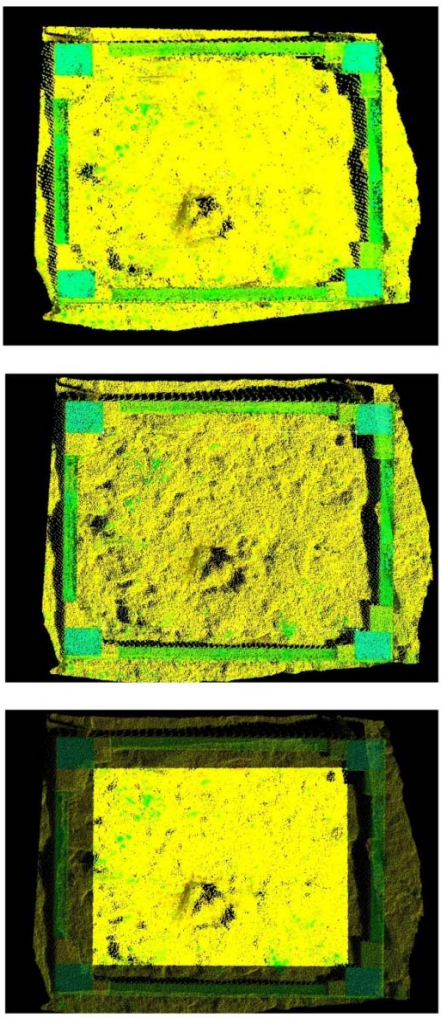

Figure 4.34 Frame 1 sequence of point cloud selection process using a single scan from one location nearly straight on to the face.

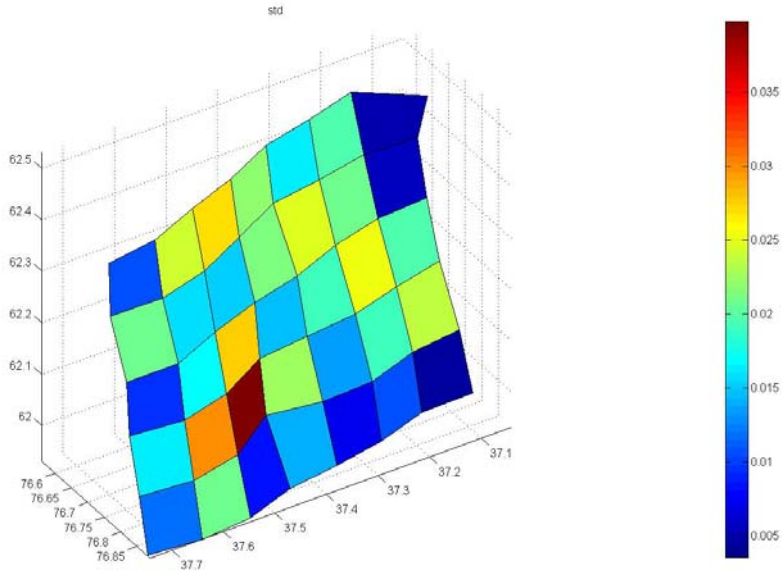

Figure 4.35 Roughness for Frame 1 generated in MatLab.

The process in coarse gravels can be followed from the frames in the field in Figures 4.32 and 4.33, through scanning and processing of the data (Figure 4.34) and the final calculation of grid roughness in Figure 4.35. Noticeable from this frame analysis is the high relative roughness values generated by a cluster of coarse grains which had fallen from the section.

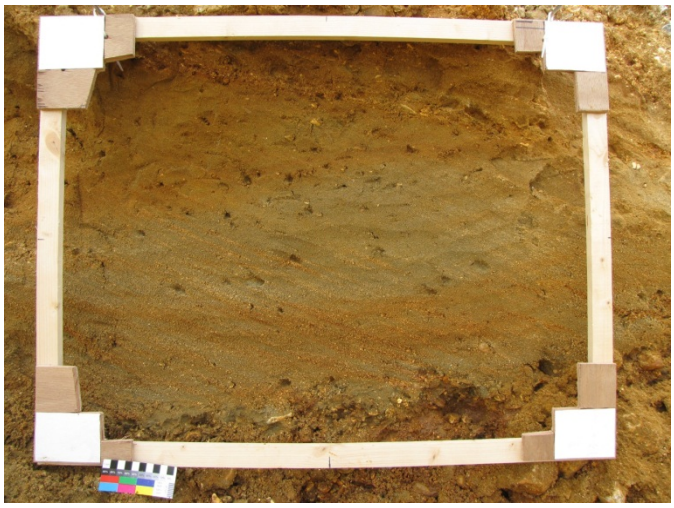

Figure 4.36: Frame 2 close up.

The process in sand and fine gravel can be followed the frames in the field in Figure 4.36, through scanning and processing of the data (Figure 4.37) and the final calculation of grid roughness in Figure 4.38. The uniform fine sediment grain size is reflected in the low relative roughness values in the majority of the grids. Also highly visible in the intensity values (colours) of the scanned data is the sub-horizontal bedding and the iron staining.

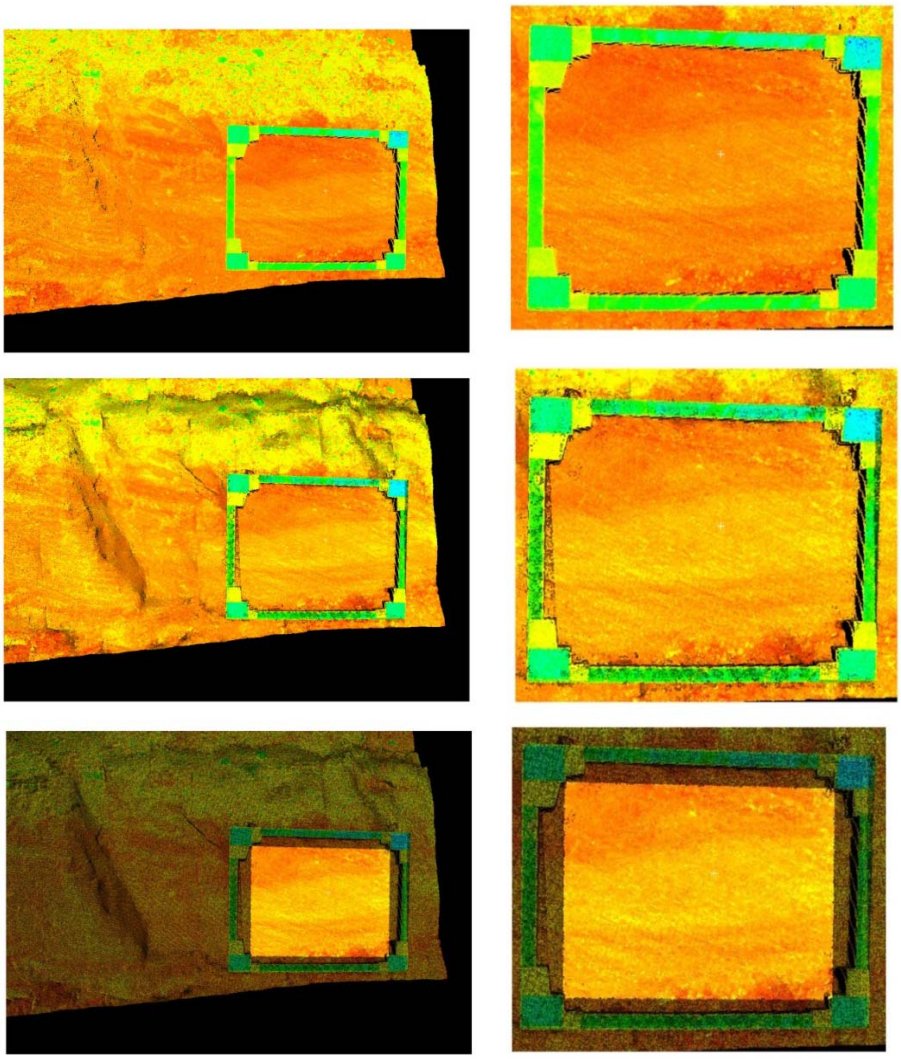

Figure 4.37 Frame 2 separate scans, merged shaded scans and selection of point cloud data.

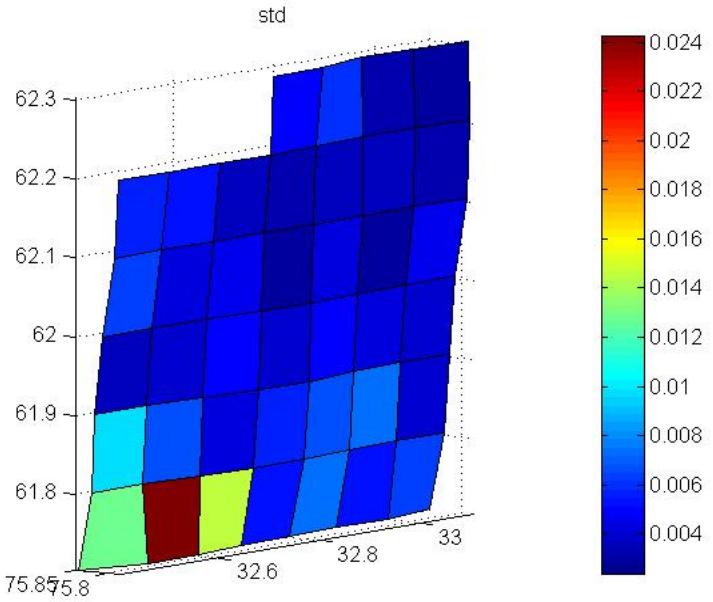

Figure 4.38 Frame 2 roughness generated in MatLab

The process can be followed for Frame 3, in Figures 4.39 and 4.40. This is a coarse, clast-supported, horizontally bedded gravel. The final calculation of grid roughness in shown in Figure 4.41. The bedding of the gravels in reflected in a vertical structure of the relative roughness data, shown in Figure 4.41.

Figure 4.39 Frame 3 close up.

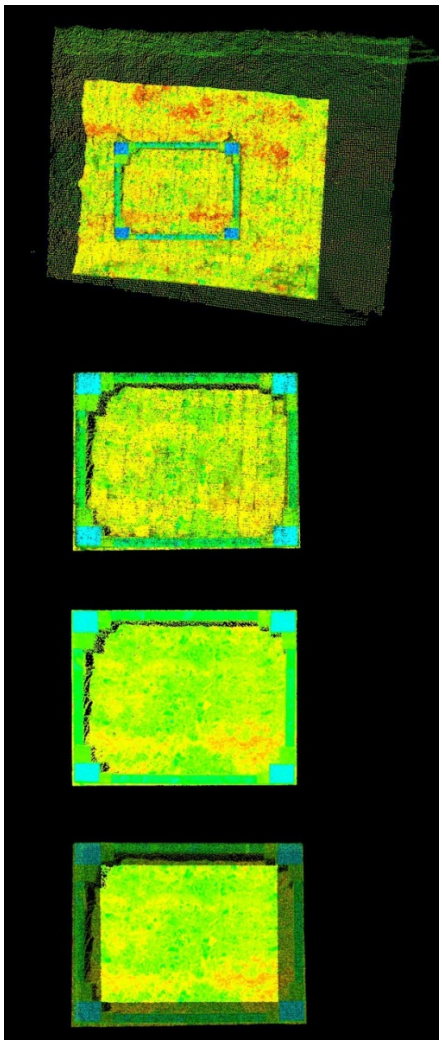

Figure 4.40 Frame 3 sequence of merged scans and point cloud selection

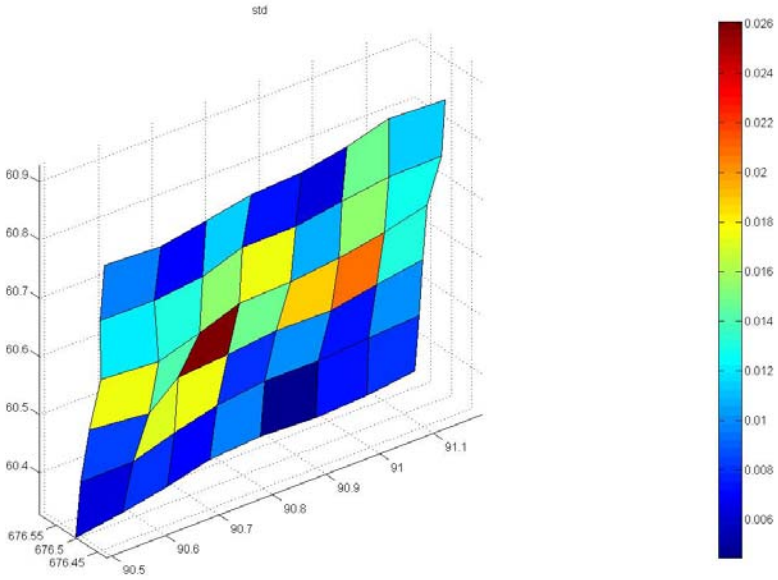

Figure 4.41 Roughness of unified scans for Frame 3

Figure 4.42: Frame 5 (upper steps frame)

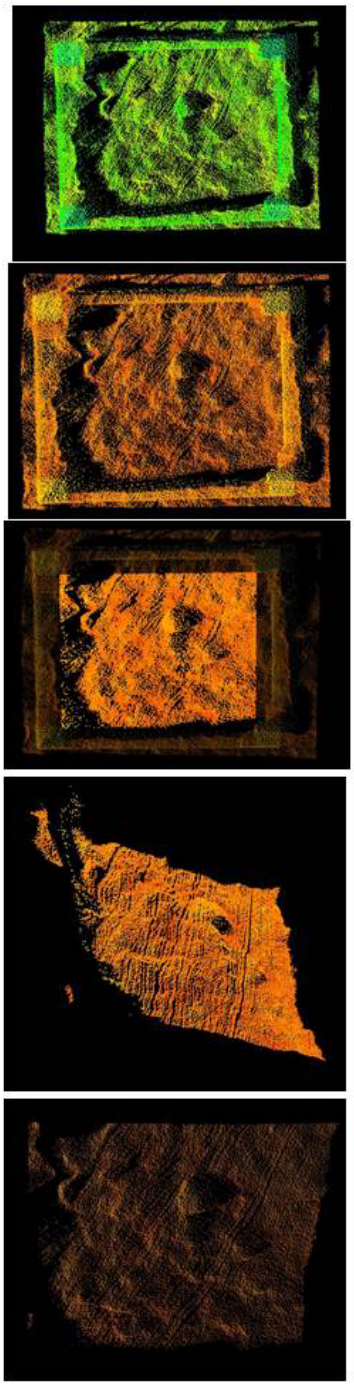

Figure 4.43 Frame 5 (upper steps frame) sequence.

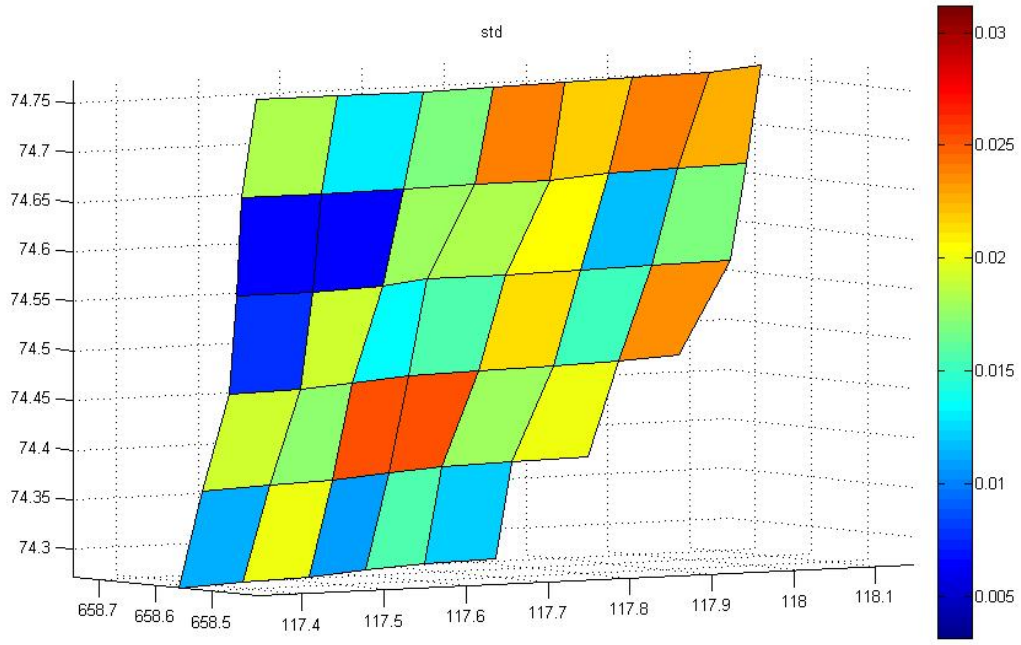

Figure 4.44 Roughness plot of Frame 5

The process can be followed for Frame 5, in Figures 4.42 to 4.44. This is a coarse, matrix supported, poorly sorted, gravel-rich diamicton. The final calculation of grid roughness in shown in Figure 4.44. The highly irregular surface of the diamicton is well expressed by the uniformly moderate to high roughness throughout the frame.

Scanned Stratigraphy

Numerous faces were scanned during Stage 2 of the project at Chard Junction. While the intensity data associated with scanned point clouds can show stratigraphic boundaries prior to merging scans and processing, there are various approaches which can be used to enhance the differentiation of strata. The first of these is simply merging multiple scans as the range of intensity values often increases which amplifies the differences. The second is to apply image analysis techniques to the photo drape as shown in Figure 4.45. If this is done, fine grained and uniform beds, are differentiated. Coarser beds are highlighted. However an effect of the colour of the gravel persists and this is grain size related.

The alternative approach is to use the intensity data (Figure 4.46). This can be classified and false colour images produced. With thresholding, this can highlight both coarse and fine units, and their boundaries. It is also particularly effective at highlighting iron staining and bedding related iron staining. It is impossible to completely remove the effects of face geometry by either method, however this face geometry (i.e. benches, overhangs etc.) is strongly grain size related and therefore part of a proxy stratigraphy.

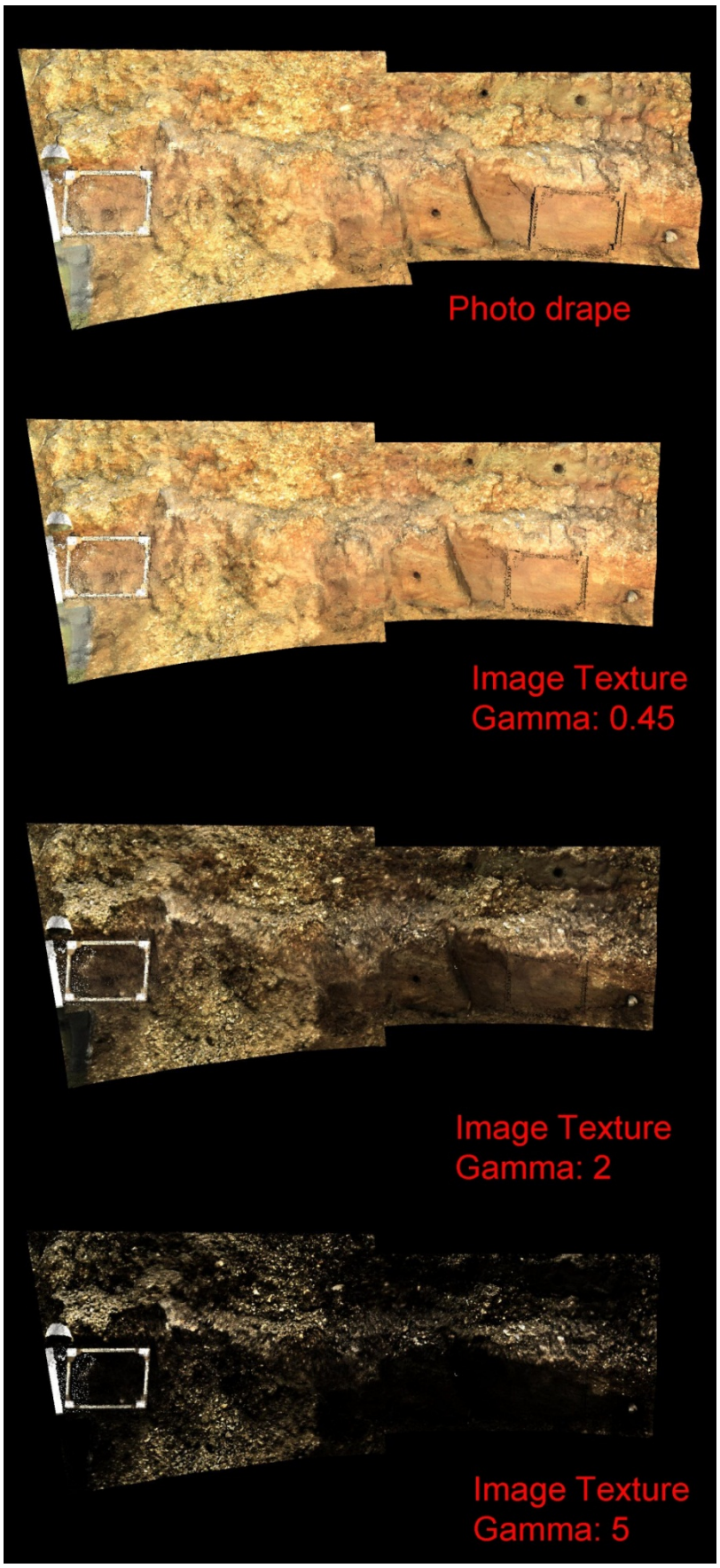

Figure 4.45 Scan data draped with photos taken using the ScanStation and then processed using different image texture settings.

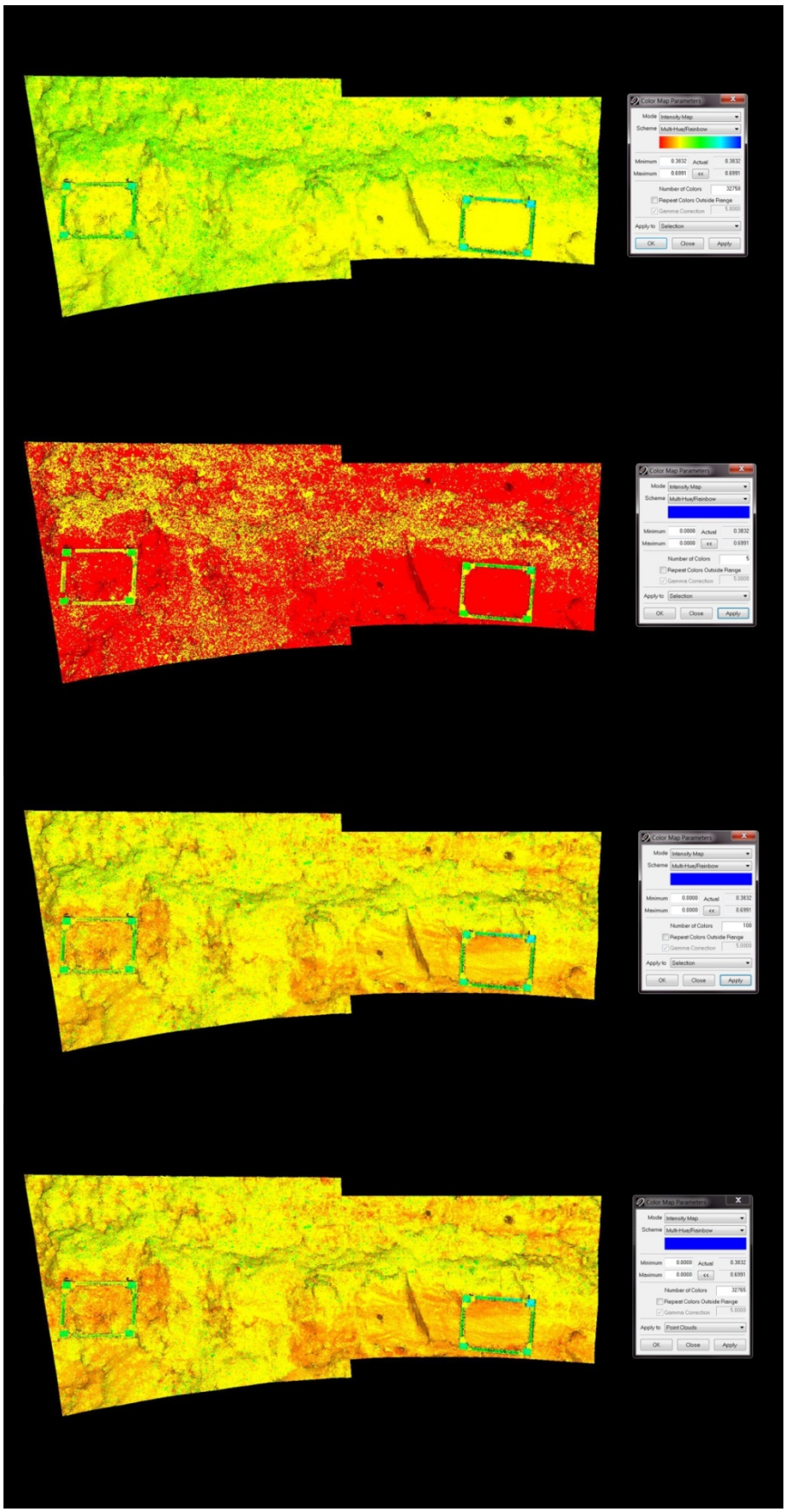

Figure 4.46 Altering the colour classification of the intensity map to highlight stratigraphic discontinuities and uniformities.

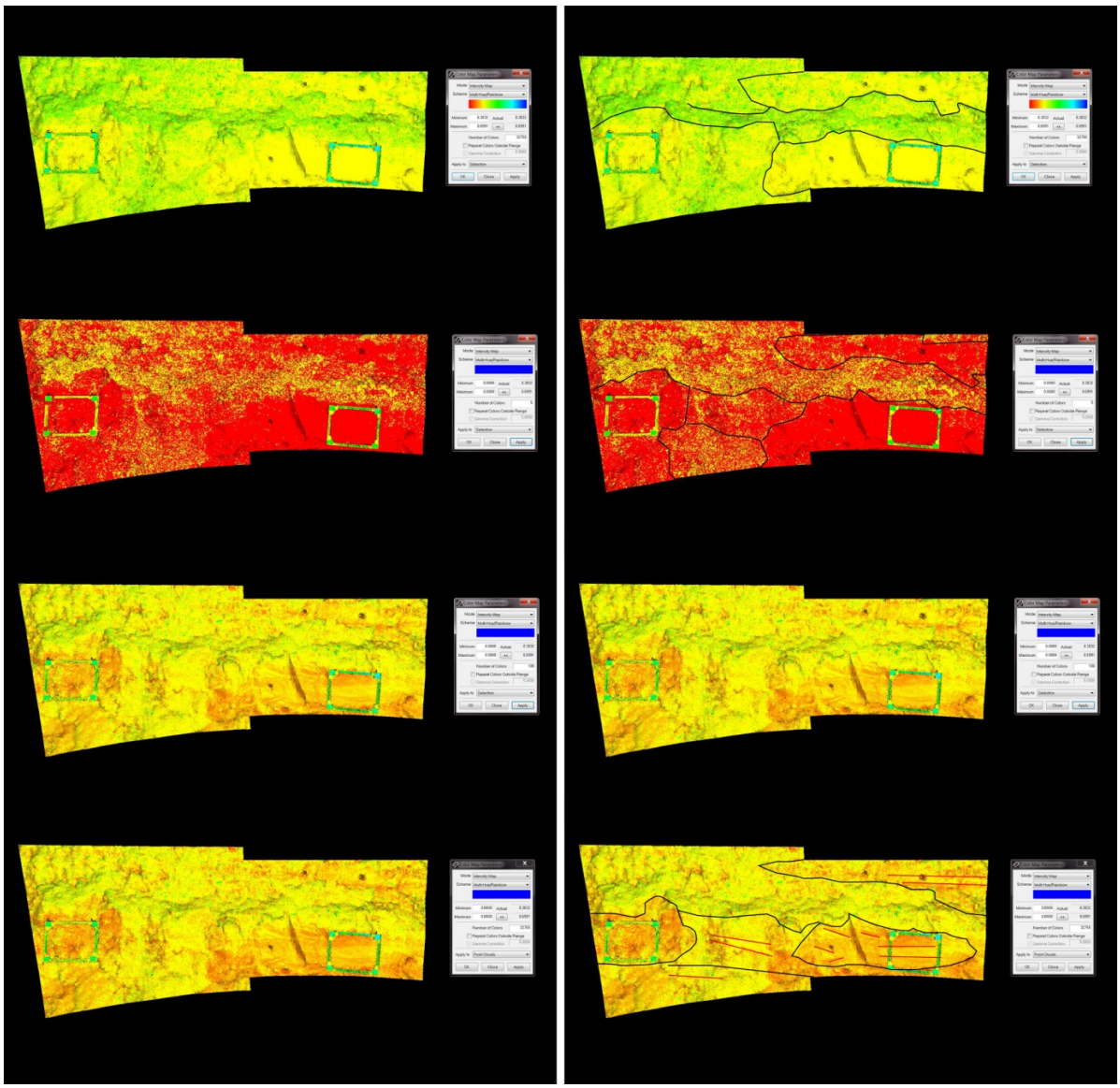

Figure 4.47 Manual classification of scan intensity images. Unit boundaries in black, and bedding trends in red. Image 3 was not annotated as it differs so little from Image 4.

The stratigraphy is highlighted manually in Figure 4.47, for each image independently, and it can be seen that there are differences in the interpretations by that the major vertical discontinuities persist. As these images show, there is complex but subtle stratigraphy in this face at Chard, and it is likely that for this reason and the coarse nature of the gravels which makes vertical plane faces extremely rare and impossible to create, that this represents a worse case-scenario. Indeed Figure 4.48 shows a planar excavated trench side, and the major stratigraphic discontinuity is immediately apparent.

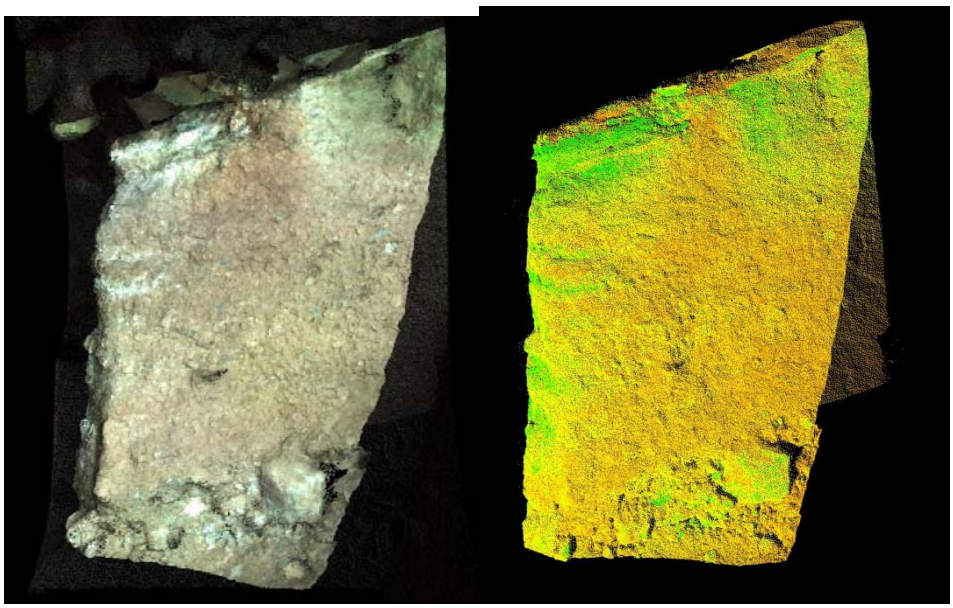

Figure 4.48 Scanned image of vertical face within excavations of a cave site at Ebbor Gorge, Somerset. Transitions of calcite floor through uniform angular gravel to a basal rubble are clearly seen in both the drape and scan intensity images.

4.4 Results

Based upon these results, we present the results of varying field parameters as specified in the UPD:

1. Number of viewing positions (1, 2..):
For a general situational coarse resolution scan, to create a "shell" into which data (e.g. OSL sample holes, artefacts etc.) may be inserted, at least 2 viewing positions are needed for a site the size of Hodge Ditch 1 and 2. Depending on the number of faces present at the time of the scan, more are likely to be necessary. This is discussed further under 3D modelling. The more scan locations can be obtained the fewer "holes" there will be in the data which could result in misleading interpolations between distant points. To obtain data that can then be analysed for roughness using a variety of different methodologies, if the scanner can be placed in front of the face, ideally between about 5 and 20 metres from the face, and the face is fairly flat, then one scan at 2mm resolution provides data that is perfectly good for looking at grain size. Using two scan locations, the situation is improved modelling in GIS, although analysis of roughness using the MatLab procedure does not appear to vary that much.

In summary, how many viewing positions are decided upon depends on several factors:
One scan at high resolution as parallel to the scan surface as possible, will enable a good estimation of grain size that may be easily compared with the sedimetrics photographic data if scanned close to the face. This is particularly effective on flat fine grained sediment. The advantage of one scan is that it is both quick and effective, and requires very little post-processing time. The disadvantage is that if the surface is unevenly excavated or the grain size is large and roughness is high, the scan may have large holes in it of no-data which will affect the overall calculation of grain size.

Two scans at high resolution will improve the overall quality of the scan, as there will be more points covering the surface, so that most of each clast surface exposed in the section will be covered by the scan. This method is recommended if the grain size is large

(gravel), and therefore has increased surface roughness; it is also advisable if the surface has been unevenly excavated. Ideally the scans should be at about 45 to 50 degrees.

2. Variation in range (distance from the face)

Over the course of the project, multiple ranges were used ranging from 2 metres from a face to 400 metres. Very close range, high resolution (2mm) scans resulted in image striping, and the scanned field was too small. The poor quality of the point clouds meant that these data were unsuitable for roughness analysis on any grain size combination. At very long ranges, point collection diminishes at all resolutions, time is increased and target collection becomes increasingly difficult as the density of points is not high enough to allow a fix on the centre of the target. Through trial and error, the optimum and most practical ranges are between 10 and 70 metres. This still allows the scanning of the vast majority of faces, even in a pit the size of Chard Junction Quarry. Within this range there are no detectable effects upon the processes applied to the data in this study. It is possible to extend the range up to 150 metres, without appreciable loss of quality, but other factors become increasingly important.

3. Resolution settings

Although the minimum theoretical resolution is 1.4mm it was found that striping and line dropout occurred between 2mm. Where possible, for detailed stratigraphic work and for grain size studies, 2mm to 5mm was preferred. However scanning at 5 to 10 mm provided excellent data for entire faces, and lower resolution scans proved valuable for the acquisition of data for the full quarry model, and relative positioning of faces within this. In fact coarse scanning provides a form of site survey which may prove to be one of the most valuable aspects of ground laser scanning. The relationship between resolution x range and scan-time, means that both range and resolution are an inevitable compromise for the time available and site size.

4. Angle and Geometry of the Face

For coarse resolution (e.g. 10 – 20 cm) angle of view has little effect on the overall model geometry. This is because internal shadow is not a significant issue. At higher resolution where the purpose of the scan is for grain size, the effect of increasing angle of view is to increase internal shadow. This is also dependent upon the grain size. However, the internal shadow is itself therefore a function of grain size and therefore, the angle of view has relatively little effect on the estimation of roughness from the point cloud (as used in MatLab) or DEMS created in GIS. A high angle of view does reduce the accuracy of the DEM derived from the point cloud. The geometry of the face, was found to have significant effects on both the DEM and more importantly on intensity and this can affect the interpretation of the intensity data. As discussed in Section 4.3, this effect is related to grain size and is difficult to avoid, but if not created artificially (e.g. by excavator) then tends to reflect the stratigraphy of the face.

5. Viewing/weather conditions

Four negative impacts of weather conditions were discovered during this project.

a) As is clear in all documentation of laser scanners, they cannot be operated during moderate to heavy rain. However, it was discovered that in the case of brief heavy showers, the scanner could be left running with a hood completely covering the

scanner until the shower had passed or the Scan station ran its internal calibration check. If the window is obscured this tended to cause the calibration check to fail, the scan had to be aborted and re-started.

b) By contrast, bright sunlight did not cause a problem with scanning, but made the photo mosaic acquisition difficult due to variations in contrast. This led to problems with photo drapes over scan data during processing.

c) When conditions were very overcast, or daylight began to fade, the acquisition of targets was hindered, particularly if they were at distances of >70 metres. Even using the Leica control targets with the highly reflective central circle, the cross hair positioning of the target centre was more frequently mis-aligned or the target could not be acquired at all.

d) Finally, high winds presented two problems. One is vibration of the scan unit especially when in exposed positions. The other is due to dust, which causes “false” points to be recorded (in the same way as light rain). This can be removed during processing, but is very time consuming.

4.5 Conclusions

The use of ground laser scanning has been shown to be extremely valuable at Chard Junction Quarry, for the rapid recoding of the location of faces, and the derivation of both proxy stratigraphic and proxy grain size data. A methodology is proposed that involves the establishment of a network of semi-permanent control points, distributed in such a manner that the whole site may be scanned from a minimum number of locations. These can then be integrated into a single site model (see section 9). More research is needed on the use of both the point cloud model and intensity for automated stratigraphic classification.

5 Clast analysis and burial dating sampling

Task 4. *As part of the clast lithological analysis we will select clasts that show evidence of having been sub-aerially weathered in the gravel (part patination) and others that have not from the same bed. Lithology must be kept constant so we will analyse a number of clasts and select suitable quartz-rich lithologies (sandstones). This will involve a clast lithology count which will benefit the whole project. As part of this task the samples will be selected for cosmogenic analysis. An application will be made to the NERC East Kilbride Cosmogenic Isotope Analysis Facility (CIAF) for burial dating of 4 samples initially. This will be made through the CIAF Committee with advice from the laboratory. The analyses requested will be ^{10}Be and ^{26}Al on two samples of clasts with evidence of subearial weathering and two without. If possible they will be from the same lithology.*

5.1 Introduction

The site at Chard Junction (Hodge Ditch) along with Broom and Kilmington have always presented a problem of interpretation. As more studies have been undertaken in southern England both to the west of the Axe catchment (Brown et al. 2010) and to the east (Briant et al. 2009) it has become clear that the stacked (or composite) sequence in the Axe valley is unique. Only two terrace levels can be seen in the valley, a lower terrace 1-3m above the Holocene floodplain (exposed at the Chard Junction crossing and downstream of Axminster) and a major terrace level of 5- 40 m above the floodplain which can be traced from Wayford, south of Crewkerne to the sea. In many places the surface of this terrace is sloping to the valley axis particularly where the valley changes direction such as at Chard Junction (Figure 5.1).

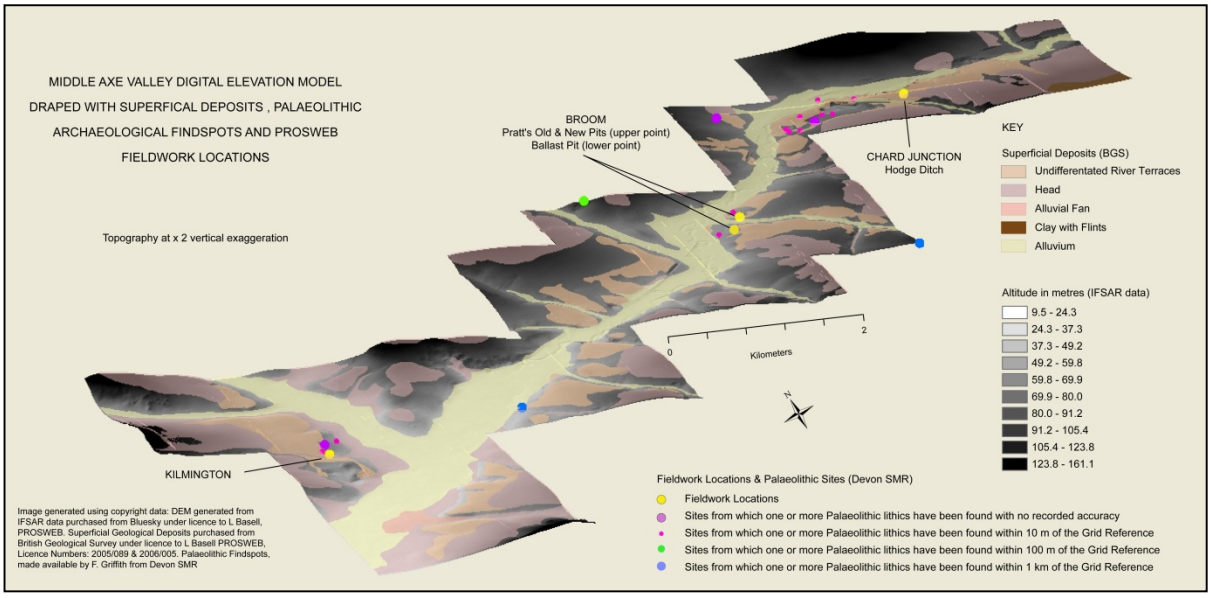

Figure 5.1: DEM draped with geology derived from IFSAR data.

This style of valley sedimentation has had important effects on the archaeological record and also the practical elements of assessing, evaluating and protecting the archaeological resource. It practice what it means is that the entire Palaeolithic record for the region could be contained in any deep quarry in the valley. This means that dating and understanding the sources for the gravels is critical to contextualising the archaeology to a greater extent than at typical Pleistocene aggregate sites. For this reason clast analyses have been

performed and an attempt is being made to augment the OSL dating with an experimental application of cosmogenic isotopes for dating the gravels.

5.2 Clast lithological analysis

Although the vast majority of the clasts that make up the gravels are chert from the local Greensand Chert beds other Lithologies are present and these may help identify other sources for not only the gravels but potentially transported artefacts and also indirectly help explain the sedimentary sequence in the valley. In order to accomplish this clast lithological analysis was conducted on samples taken for grain size analysis. Clast analysis was done visually on a clast by clast basis and on clasts greater than 11mm in diameter. In some cases such as Figure 5.2 roundness was also estimated using the standard Power's Roundness scale (Gardiner & Dackombe 1983). As can be seen from Figure 5.2 the results do vary significantly by grain-size fraction, except an increase in angular flint, and to a lesser extent chert, in the coarser fraction (31.5-45mm). This is probably due to the abrasion which naturally occurs with the shattering of flint into smaller clasts with transport and weathering. As can be seen from this example the representation of clasts is similar in the two size fractions but the rounding is not. On the basis of the data presented (Figure 5.3) here is not fractionated by grain size, however, the full fractionated results are given in Appendix C.

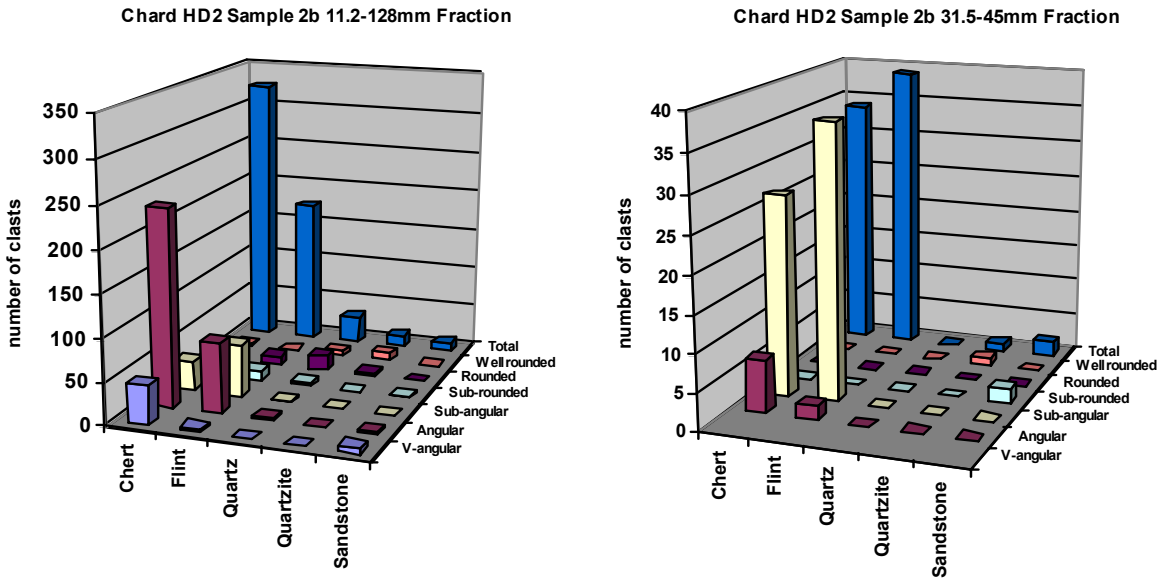

Figure 5.2 A comparison of clast type and lithology for two grain size fractions of sample

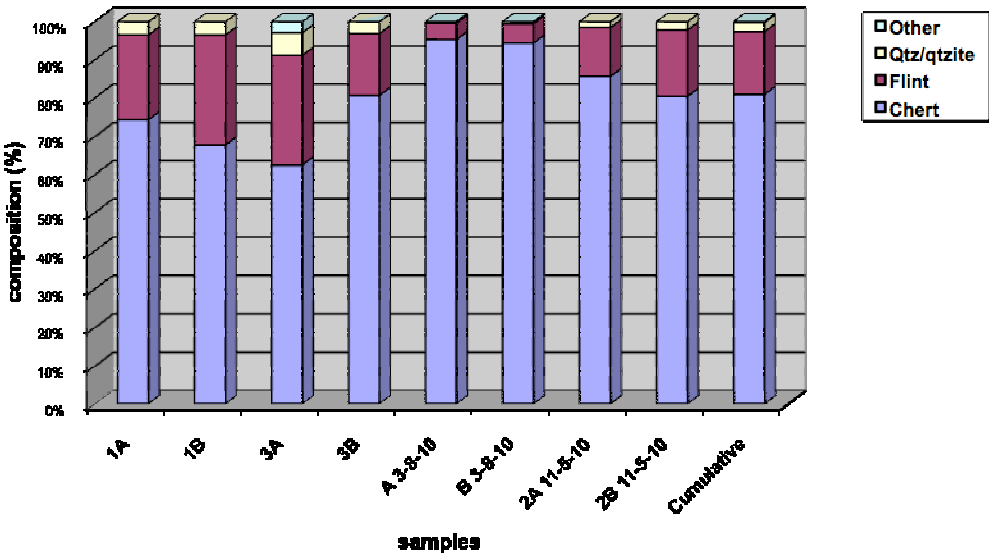

Figure 5.3 Clast lithological composition for large (>50 Kg) samples from Units B and C at Hodge Ditch II.

Figure 5.3 is based upon a total sample of 143 tons of gravel and so can be considered highly reliable in a statistical sense. The samples were all taken from visually homogenous gravel units. Although adjacent samples (A vs B samples) are generally similar there can be significant variation as for sample 3A and 3B and this probably represents a proxy grain-size effect (see section 3). The vast majority of the gravels clasts are composed of chert with a variable smaller component of flint and a trace of other Lithologies.

In all 6 lithologies have been identified (Table 5.1) and whilst the source for the chert, flint and sandstone is proximal and known the sources for the quartz, quartzites and rare Palaeozoic rocks is not. The sand matrix for the gravels is probably derived from the Upper Greensand and at least part of the matrix for the upper diamicton is derived from the Lower Lias as recorded by the Gcps values.

Lithology	Rank	Typical form	Sources & comments
chert	1	sub-angular to angular, all grain-sizes, typically tabular and of a triangular form. Contain bivalves in life positions and ripples.	The Upper Greensand (Late Albian, Cretaceous) Eggerton Grits. This formation forms the majority of the slopes at the valley sides & is composed of cherts & sandstones and is typically highly fractured.
flint	2	in all size fractions up to large pebble (rare) occurring both as nodules with cortex (rarely with horns intact), abraded nodules & shattered nodules. Some with chemical weathering pits	Ultimately the Middle Chalk (Cenomanian) but removed by weathering and erosion from most of the catchment only remaining as thin strata (<88m total thickness, Edwards & Gallois (2004)) cropping out on the upper valley-side slopes. Flints (abraded and shattered) can also be derived from the clay-with-flints that caps the plateau throughout the catchment and also from a residual fluvial gravel which is of Neogene or Pleistocene age (Isaac 1979; Edward and Freshney 1982).
quartz	3	generally milky quartz & always very well rounded	Not known but could be from the gravels on the plateau (see above) and/or ultimately from the Budleigh Salterton pebble beds the nearest crop out of which is to the west in the Sid & Otter catchments
quartzite	4	grey-brown always very well rounded some with chemical weathering pits/weathering rind	Not known but could be from the gravels on the plateau (see above) and/or ultimately from the Budleigh Salterton pebble beds the nearest crop out of which is to the west in the Sid & Otter catchments
sandstone	5	moderately rounded, weakly cemented	The Upper Greensand (Late Albian, Cretaceous) Eggerton Grits. This formation forms the majority of the slopes at the valley sides & is composed of cherts & sandstones and is typically highly fractured.
metamorphic rocks (Palaeozoic)	6 (rare)	very well rounded, some with chemical weathering pits/weathering rind	Not known but could be from the gravels on the plateau (see above) including a Tertiary weathering surface and/or from the Palaeozoic rocks of SW England probably via the Budleigh Salterton pebble beds the nearest crop out of which is to the west in the Sid & Otter catchments
sarsens	7 (rare)	large (up to 0.5m diameter) cemented sandstone, sub-angular to sub-rounded, some with chemical weathering pits (Figure 5.3)	Not known but probably a relict Tertiary surface related to the clay with flints and the Plateau gravels.

Table 5.1 Clast Lithologies at Hodge Ditch (I-III) and comments on provenance.

As Figure 5.2 shows the angularity-roundness of the clasts is highly lithology dependent and this reflects the clasts source rather than Pleistocene transport histories or distance from the source.

Sarsens in southwest England are commonly associated with terrace gravels (Scrivener et al. 2011) and it is commonly thought that they were created as silcretes through the weathering of sand-rich residual surfaces during the Tertiary. However, their anomalous

size for the gravels in which they are found, here and elsewhere, suggests that they have not been transported by normal fluvial transport. The most likely mechanism is via ice-rafting and so their presence in the gravels at several levels within Units A & B reinforces the fluvio-periglacial model of the formation of the gravels at Chard. Studies are underway to try and identify their original source.

Figure 5.3 Sarsens, Left from Hodge Ditch I (Unit B) and right Hodge Ditch III (Unit A)

5.3 Case for cosmogenic isotopes analyses

The burial dating of sediments uses the fact that sediment was exposed to cosmic (galactic) radiation prior to, and in the early stages of burial and individual cosmogenically-produced nuclides created by this exposure decay at a constant rate (Granger and Muzikar, 2001; Brown et al. 2009; Brown in press). It is an extension of exposure surface dating and has primarily been used for cave sediments (e.g. Anthony & Grainger, 2004). However, in the case of river gravels the decay ratio of the cosmogenic isotopes ^{26}Al and ^{10}Be which are abundant in quartz minerals (such as chert) can be used to calculate the time since the sediment was shielded from cosmogenic rays. The upper limit is about 5 Ma and adjustments have to be made for the progressive effect of burial and skyline shielding as described by Balco et al. (2008). The method has been applied to the terraces of the Utah river in the USA (Wolkowinsky and Grainger, 2004) and most recently on Rhine terraces (Dehnert, et al. 2006). In Britain the technique has been applied largely to late Pleistocene glaciated areas, particularly in Scotland (Ballantyne 2009; 2010), but also S Wales (Ballantyne et al. 2010) and more locally by Brown and others on the island of Lundy (Rolfe et al. in prep). It has not yet been attempted with Pleistocene fluvial sediments or archaeology-bearing sediments, and so, this first use in conjunction with archaeology in terrace sediments in the British Isles must be treated as experimental. However, there are three very strong reasons for attempting the procedure; firstly to augment the OSL record that we have for sites such as Chard Junction where no carbonate or biological methods are possible, and secondly to extend the time range of sediments that can be dated and thirdly to trial a method that might be used when there are no suitable sediments for OSL such as is the case in uniformly coarse gravels.

This site is problematic in terms of dating, as many are, because it is decalcified and so it is not possible to use mammalian biostratigraphy or amino-acid racemisation. Therefore other methods have to be found in order to gain reliable age estimates with as high a degree of confidence as possible. Method (in this case OSL) validation is only one aspect of this process – although one that has been rarely tried at such sites. However, even if the results were not significantly different then this only gives us confidence in the

reproducibility of the results. At sites of this antiquity and probably importance (pre-MIS 12 hominin activity) it is prudent to try all possible methods as soon as they become available.

Nearly all bifaces are in secondary context unless it can be shown that they were found where they were dropped or placed – a very few sites indeed (Boxgrove and Lynford being examples). So the vast majority of the British Palaeolithic record, including most cave finds, are from secondary contexts. However, the high concentrations of artefacts at some locations, the presence of debitage and/or fresh lithics with no edge damage, as at Broom and Hodge Ditch I) clearly indicates they have not travelled significant distances. The most likely source is a channel bank 'site' on either a gravel bar or the edge of the active floodplain. This has been termed a '*proximal secondary context*' by Brown (Brown et al. in prep). Of course OSL dating like any other sediment dating technique only provides a *terminus ante quem* if it is applied to the beds that contains the biface, or indeed overlies the biface context. In reality how close the biface is to where it was lying on a ground surface is probably very important as it can be assumed on geomorphological grounds that the further a biface has moved the greater the minimum time it will have taken to move that distance. So a biface reworked from one terrace into another is very different, to a biface which is washed off an adjacent gravel-bar surface into a pool. In one case the cosmogenic date should greatly exceed the burial date, in the other they should be similar. So we can define the relationship between our dates as;

burial age = creation age – use period – residuality

Since the use period can be assumed to be insignificant in geological terms this leads to a relationship between the OSL date and the cosmogenic date of the form;

$$t_{OSL} = t_c - t_b - t_r$$

It follows that the cosmogenic date (t_c) should exceed the burial date (t_{OSL}) in situations where the biface has been reworked from a older deposit or been residual (t_r) for a significant period or in conditions of slow burial ($t_{b)}$. Potentially we have data pertinent to these factors through variations in abrasion (highly abraded to mint condition) and the estimates of the rates of burial from sediments, leaving only the residuality. In this application we are seeking to date the clasts and not the biface but the same considerations apply and this work paves the way for a new the approach to the secondary contexts problem.

For the cosmogenic burial age to approximate the deposit age the clasts should be rapidly buried to several metres depth (2-5m) although this depends upon the density of the burying sediments. We believe this to be the case at Chard due to the sedimentology of the deposits. We can though factor in a burial rate and so try and model the range of ages with different burial rates. This is at the heart of recent approaches to burial dating which we will develop for Chard. The levels from which we will use clasts will be in excess of 100 ka and so these errors are likely to be less significant.

5.4 Cosmogenic isotopes sampling

In order to get as full as possible time-sequence of samples from Hodge Ditch the regarded stepped face at the SE corner of Hodge Ditch was sampled (Figure 5.4 – 5.6). This allowed a paired sample of a small cobble (64 - 256 mm) of an angular chert with a very well rounded quartzite cobble of a similar size at 10 levels from 71 m OD to 62 m OD. At two levels (4 & 5) no quartzite could be found and so a well rounded flint cobble

was collected. At all the levels the two cobbles were collected from the same stratigraphic unit (bed) and within 10m in lateral distance. As can be seen from Figure 5.4 two OSL samples were taken from the base of the sequence (CHAR 22 and 21). These clast samples have formed the basis of the application for cosmogenic dating which is being made to the C Isotope Analysis Facility (CIAF) at the Scottish Universities Environmental Research Centre (SUERC) and funded by NERC. Since this is a novel application of cosmogenic isotopes discussions have taken place with members of CIAF staff in particular Cassandra Fenton (now left), Christoph Schnabel and Angel Rodes. If all, or some of the dates are granted then the samples will be sent to SUERC at East Kilbride in October and undergo standard chemical preparation (digestion) before analysis of the nuclides using the AMS. The results when published would acknowledge the financial contribution of EH to this work.

Figure 5.4 The stepped face of Hodge Ditch I used for cosmogenic sampling. Note the bags at sample locations and the OSL holes at the base (CHAR 22 and CHAR 21).

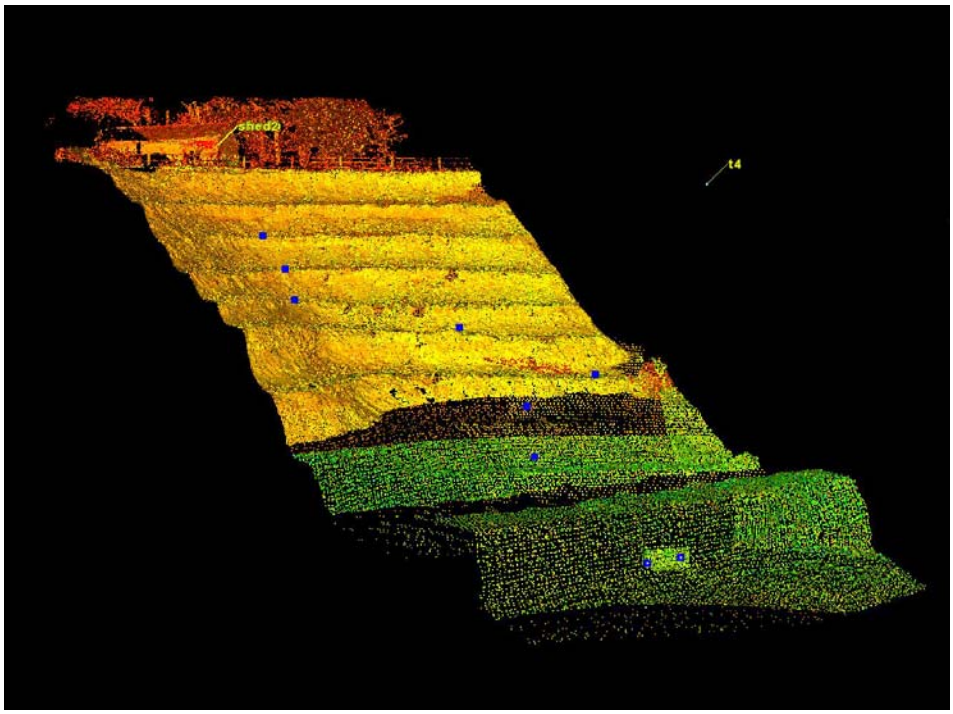

Figure 5.5: Stepped face of Hodge Ditch. Locations of cosmogenic samples are indicated by blue squares and correspond to bags on photo in Figure 5.4. The two basal blue squares with white dots in the middle indicate the location of OSL sample holes CHAR 22 and CHAR 21.

6 The OSL dating programme

Task 5. *Sample and analysis of further dates from sand lenses in faces as Hodge Ditch Phase II proceeds. Samples will be taken from the lower levels for single grain analyses. The analyses will be conducted at the University of Gloucestershire Geochronology Laboratories by Dr P. Toms, who will also supervise the sample collection and on-site dosimetry measurements.*

6.1 Introduction

The deposits of the proto-Axe at Chard Junction Quarry potentially contain evidence of the earliest hominin occupation of southwest Britain and represent one of the few sites that may span the Lower-Middle Palaeolithic. The aim of this report is to summarise and assess the reliability of the Optical chronology of the sediment sequence within the Hodge Ditch excavations. The analytical properties of the age estimates are evaluated, with intrinsic measures and a tri-laboratory inter-comparison conducted to assess reliability. The raw optical chronology is refined substantially by rejection of those age estimates accompanied by analytical caveats, driven principally by poor recycling ratios in the high, saturating region of dose response. One of two inter-laboratory samples produced a significantly different age by one laboratory, which may be forced by the differences in laboratory thermal treatment. The reliability of D_e:D_r plots may improve with increasing numbers of samples from equivalent stratigraphic units of divergent dosimetry, but having only two samples may lead to erroneous conclusions. Rapid sedimentation and deposition of artefacts between c. 15.2 and 4.5 m appears centred on a geometric mean age of 259±10 ka (MIS 7).There then followed relatively slow or pulsed sedimentation until 86 ka (MIS 5a) beyond which the deposits were incised to form the current course of the River Axe.

The deposits of the proto-Axe at Chard Junction Quarry are potentially of international significance. Optical dating of the upper 7m (out of 16 m) of sediments within Hodge Ditch 1, conducted previously under PRoSWEB (Toms et al., 2008), demonstrated intervals of deposition spanning 85 ka to 402 ka (Marine Isotope Stages (MIS) 5a to 11). With the subsequent discovery of two bifaces at a depth of c. 15 m in Hodge Ditch 1 (Brown and Basell, 2008), the deposits at Chard Junction may contain the oldest evidence of hominin occupation in at least southwest Britain. As such the lateral extension of aggregate extraction into Hodge Ditch 2 and 3 has been the subject of monitoring and further dating through the English Heritage Historic Environment Enabling Programme (Project Number 5695). The aim of this report is to summarise and assess the reliability of the Optical chronology of the Hodge Ditch sequence. The objectives are two-fold. Firstly, to assess the analytical validity of the optical age estimates. Secondly, to assess the accuracy of age estimates by intrinsic measures and inter-laboratory comparison between the Universities of Aberystwyth, Gloucestershire and Oxford.

6.2 Sampling

A total of 33 sediment samples were extracted from matrix-supported deposits within the Hodge Ditch excavations at Chard Junction Quarry. Triplicate samples of GL10001 and GL10002 were taken for the purposes of inter-laboratory comparison. Contained within opaque plastic tubing (100x45 mm) forced into each face, each sample was wrapped in cellophane and parcel tape in order to preserve moisture content and sample integrity until ready for laboratory preparation. For each sample, an additional c 100 g of sediment was collected for laboratory-based assessment of radioactive disequilibria.

6.3 Results

Taking the youngest and oldest age estimates (samples GL06011 and GL08047); the raw optical chronology for Hodge Ditch spans 86 to 544 ka (MIS 5a to 15; Appendix D Table 1 and Figure 1). There is a broad increase in age with depth to 274 ka (MIS 7) at c. 4.5 m. Beyond this level, there is an age plateau that appears to broaden with depth (169 to 544 ka at c. 15 m). The overall age-depth sequence is incompatible with Bayesian analysis, precluding a whole-site quantitative assessment of age consistency with relative stratigraphic position. In the absence of independent chronological control, intrinsic measures of reliability are the sole means by which to evaluate the accuracy of the age estimates.

A total of 17 samples failed one or more diagnostic elements; Appendix D Table 2 outlines the analytical caveats by sample. Five samples failed the Dose Recovery test (see 4.1.2), four samples exhibited varying levels of U disequilibrium (see 5.0), three samples produced D_e >600 Gy (see 4.1.3), one sample produced insufficient datable mass and one proved to have significant feldspar contamination. However the most common failure, in nine samples, was in the repeat dose ratio assessed as part of the D_e measurement (Murray and Wintle, 2000; 2003; see 4.1.4). Data within Table 1 indicates there is almost twice as much variation in the ratio for high doses (19%) than low (10%). The majority of samples yield D_e values in the high, saturating region of dose response. As such, estimates of D_e in this region are particularly sensitive to inaccuracies in the form of dose response forced by inaccurate correction of sensitivity change. Figure 1 highlights those samples with analytical caveats.

Samples obtained from the same or equivalent stratigraphic units whose ages converge but are based on divergent D_r values offer a powerful, though resource-intensive intrinsic assessment of reliability (Toms et al., 2005). Appendix D Figure 2 summarises the D_e: D_r plots for multiple age estimates obtained within stratigraphic units or between those at an equivalent stratigraphic level. Of the intra-unit assessments, samples GL10015/GL10016 and GL08043/GL08044 show convergent age estimates from statistically distinct D_r values (Appendix D Fig. 2c and 2d). At c.13 m (Appendix D Fig. 2e), this pattern is broadly true of the age estimates from units of equivalent depth within the sequence. However, this contrasts with those at c. 15 m (Appendix D Fig. 2f) where there is a marked variation in age. The concern evolved here is that the apparent convergence or divergence of age estimates may be dependent on the number of samples dated; Appendix D Figure 2f indicates at least two distinct age bands within which at least two samples with distinct D_r values appear to plot.

The full results and interpretation are given in Appendix D with a catalogue of all OSL sample locations in Appendix E.

6.4 The inter-laboratory comparison

Luminescence dating requires calibration, maintenance and monitoring of equipment involved in D_e and D_r evaluation. Though a rigorous methodology may be employed by a laboratory, in the absence of independent chronological control in a large study such as this inter-laboratory comparison is advisable to corroborate age estimates and thereby verify the accuracy of equipment calibration and function. In this study, the comparability of three procedural elements as well as age estimates was assessed from three Luminescence laboratories for two samples, GL10001 and GL10002 (Appendix D Table 3). Appendix D Figure 3a shows the outcome of the Dose recovery test for GL10001. Laboratory A recorded strong thermal dependence, Laboratory C slight and Laboratory B none. The origin of this variable response remains to be determined, but critically this decision-making process led to differences in preheat selection between laboratories. Appendix D Fig. 3a-e illustrate the outcome of the inter-comparison samples (Lab A, Lab B and Lab C). Inter-laboratory difference in γD_r is a maximum of 12±7%, whilst for βDr this climbs to 34±12%. The greater variation in βD_r may arise from differences in technology between laboratories. Appendix D Fig. 3d shows the age envelope of each sample based on the inter-laboratory range. The maximum difference in age is 29±18% for sample GL10001 between Laboratory B and C, 39±21% for GL10002 between Laboratory A and C. The principal driver behind these differences is D_e (43±18%, GL10001; 29±17%, GL10002), with laboratory C systematically lower than A and B. The divergence between laboratories in natural D_e value was further investigated by giving a precise 10 dose to three sets of three aliquots of bleached GL10001. Each laboratory then adopted the same measurement sequence and preheat temperature to estimate the dose applied. Appendix D Fig. 3e shows that the lower natural D_e value reported by Laboratory C is not rooted in source calibration, with statistically concordant doses recovered between laboratories. It is possible, therefore, that the inter-laboratory discrepancy in natural D_e originates from the choice of preheat temperature. For sample GL10002, where Laboratory A and B selected the same preheat temperature the natural D_e values are indistinguishable.

6.6 Age-depth modelling of Hodge Ditch Phases I & II

Figure 6.1: Summary of all date samples taken, their x,y,z co-ordinates, location in Hodge Ditch (HD), and ages, listed according to their GL laboratory code.

GL- LAB CODE	FIELD CODE	X	Y	Z	HODGE DITCH	AGE (ka)	ERROR (ka)	AGE & ERROR (ka)
6010	CHAR01	335149.215	104782.385	69.630	HD1	174	18	174±18
6011	CHAR02	335183.843	104748.680	72.042	HD1	94	9	94±9
6012	CHAR03	335146.241	104689.375	72.740	HD1	98	8	98±8
6013	CHAR04	334496.353	104761.158	59.830	Silt Ponds	274	25	274±25
6057	CHAR05	335035.405	104791.764	65.890	HD1	367	35	367±35
6058	CHAR06	335037.988	104789.819	65.890	HD1	284	36	284±26
8043	CHAR07	335058.120	104729.520	59.655	HD1	355	47	355±47
8044	CHAR08	335059.280	104729.780	59.800	HD1	292	37	292±37
8045	CHAR09	335045.360	104762.380	62.065	HD1	264	28	264±28
8046	CHAR10	335123.320	104749.780	60.035	HD1	334	36	334±36
8047	CHAR11	335084.060	104734.913	59.470	HD1	494	50	494±50
9029	CHAR12	334968.981	104663.731	71.650	HD2	124	9	124±9
9030	CHAR13	335012.036	104775.814	66.423	HD2	302	29	302±29
9031	CHAR14	335011.751	104775.684	67.966	HD2	294	30	294±30
9117	CHAR15	335132.737	104675.177	63.218	HD1	347	31	347±31
9118	CHAR16	335133.739	104675.303	63.300	HD1	230	17	230±17
9119	CHAR17	334974.134	104727.976	66.220	HD2	235	17	235±17
9120	CHAR18	334987.639	104733.167	64.286	HD2	475	53	475±53
10001	CHAR23	335123.417	104662.181	72.386	HD1	141	14	141±14
10002	CHAR24	335132.595	104675.735	61.929	HD1	268	25	268±25
10013	CHAR19	335131.881	104675.738	61.909	HD1	348	34	348±34
10014	CHAR20	335134.204	104676.055	62.055	HD1	313	42	313±42
10015	CHAR21	335086.726	104676.127	60.245	HD1	192	23	192±23
10016	CHAR22	335087.924	104676.198	60.213	HD1	208	21	208±21
10019	CHAR25	335026.249	104696.350	61.991	HD2	249	40	249±40
10020	CHAR26	335038.203	104698.350	60.857	HD 1 TO 2	281	34	281±34
10055	CHAR27	334964.195	104729.858	61.784	HD2	335	31	335±31
10063	CHAR28	334907.751	104710.584	62.443	HD2	320	31	320±31
10064	CHAR29	335027.140	104781.157	60.194	HD1 TO 2	212	17	212±17
10065	CHAR30	335040.292	104741.667	62.407	HD1 TO 2	226	20	226±20
10066	CHAR31	335058.257	104673.017	61.792	HD1 TO 2	336	42	336±42
10067	CHAR32	334927.125	104775.856	65.667	HD2	293	44	293±44
10084	CHAR33	334846.372	104722.779	70.607	HD3	126	11	126±11

FIELD CODE: CHAR-	LAB CODE: GL-	X	Y	Z	PIT LOCATION	AGE (ka)	ERROR (ka)	AGE & ERROR (ka)
1	6010	335149.215	104782.383	69.630	HD1	174	18	174±18
2	6011	335183.843	104748.680	72.042	HD1	94	9	94±9
3	6012	335146.241	104689.375	72.740	HD1	98	8	98±8
4	6013	334496.353	104761.158	59.830	Silt Ponds	274	25	274±25
5	6057	335035.405	104791.764	65.890	HD1	367	35	367±35
6	6058	335037.988	104789.819	65.890	HD1	284	36	284±26
7	8043	335058.120	104729.520	59.655	HD1	355	47	355±47
8	8044	335059.280	104729.780	59.800	HD1	292	37	292±37
9	8045	335045.360	104762.380	62.065	HD1	264	28	264±28
10	8046	335123.320	104749.780	60.035	HD1	334	36	334±36
11	8047	335084.060	104734.913	59.470	HD1	494	50	494±50
12	9029	334968.981	104663.731	71.650	HD2	124	9	124±9
13	9030	335012.036	104775.814	66.423	HD2	302	29	302±29
14	9031	335011.751	104775.684	67.966	HD2	294	30	294±30
15	9117	335132.737	104675.177	63.218	HD1	347	31	347±31
16	9118	335133.739	104675.303	63.300	HD1	230	17	230±17
17	9119	334974.134	104727.976	66.220	HD2	235	17	235±17
18	9120	334987.639	104733.167	64.286	HD2	475	53	475±53
19	10013	335131.881	104675.738	61.909	HD1	348	34	348±34
20	10014	335134.204	104676.055	62.055	HD1	313	42	313±42
21	10015	335086.726	104676.127	60.245	HD1	192	23	192±23
22	10016	335087.924	104676.198	60.213	HD1	208	21	208±21
23	10001	335123.417	104662.181	72.386	HD1	141	14	141±14
24	10002	335132.595	104675.735	61.929	HD1	268	25	268±25
25	10019	335026.249	104696.350	61.991	HD2	249	40	249±40
26	10020	335038.203	104698.350	60.857	HD 1 TO 2	281	34	281±34
27	10055	334964.195	104729.858	61.784	HD2	335	31	335±31
28	10063	334907.751	104710.584	62.443	HD2	32		320±31
29	10064	335027.140	104781.157	60.194	HD1 TO 2	212	17	212±17
30	10065	335040.292	104741.667	62.407	HD1 TO 2	226	20	226±20
31	10066	335058.257	104673.017	61.792	HD1 TO 2	336	42	336±42
32	10067	334927.125	104775.856	65.667	HD2	293	44	293±44
33	10084	334846.372	104722.779	70.607	HD3	126	11	126±11

Figure 6.2: Summary of all date samples taken, their x,y,z co-ordinates, location in Hodge Ditch (HD), and ages, listed according to their CHAR field code.

Excluding those samples with analytical caveats reduces the variability of the chronological sequence. The youngest unit of the site at 2.5 m in Hodge Ditch 1 (GL06011) suggests a minimum age of 86 ka (MIS 5a). The current data set suggests relatively slow or pulsed sedimentation back to c. 274 ka (MIS 7; c. 4.5 m, GL06013). This refined sequence then suggests rapid sedimentation and deposition of artefacts centred on a geometric mean age of 259±10 ka (MIS 7) between c. 4.5 and 15.2 m. Establishing the palaeogeography of sedimentation may develop this chronology further. This study has highlighted four areas for consideration in future application of Luminescence dating. Firstly, for Late and Middle Pleistocene samples, it is important to assess the success of correction for sensitivity change in the high dose region by repeat regenerative-dose ratio tests. Secondly, inter-laboratory methodological differences can lead to significant

differences in γ D_r, whereas the standard approach to measurement of g D_r produces equivalent values. Moreover and thirdly, a standardised approach to De acquisition can produce significant differences in this value between laboratories that may be forced by the choice of preheat temperature. Finally, targeting areas of divergent dosimetry in equivalent stratigraphic units and measuring the convergence of age estimates is not an infallible intrinsic measure of reliability. The quality of this metric improves with increasing numbers of samples from each unit; it is apparent that two samples per unit may lead to an erroneous conclusion on their reliability.

The additional samples in Hodge Ditch I brings the total number of OSL dates on the Phase to 13. These have been plotted in Figure 6.3 below.

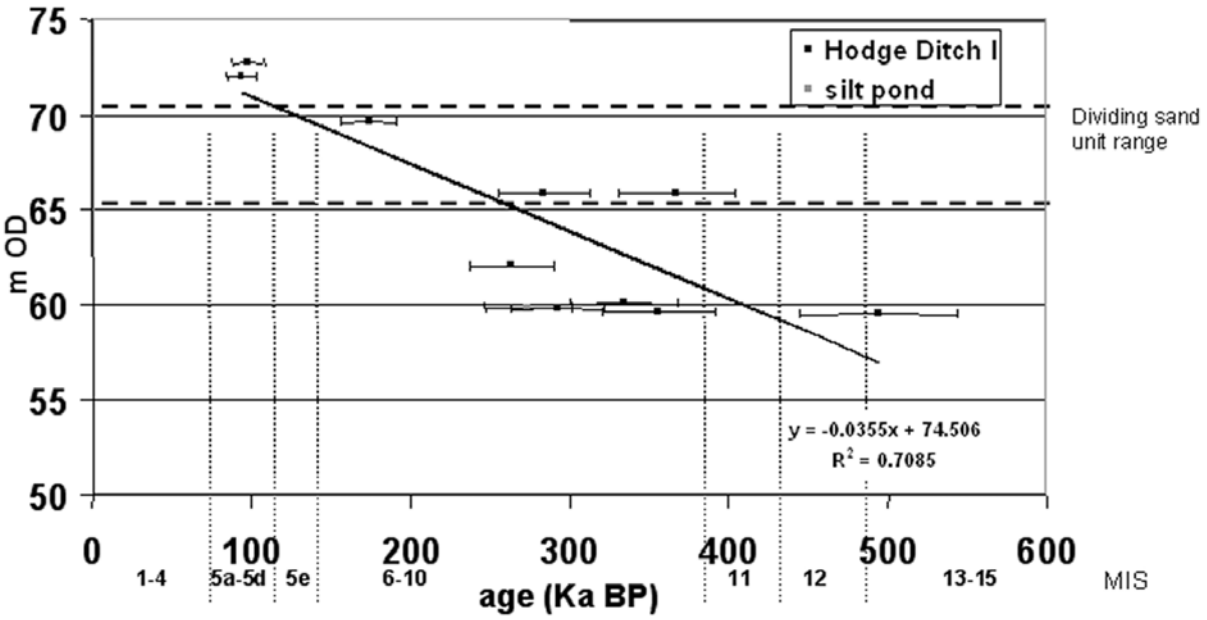

Figure 6.3: The raw age-depth model for the OSL dates at Chard Junction Hodge Ditch Phase I.

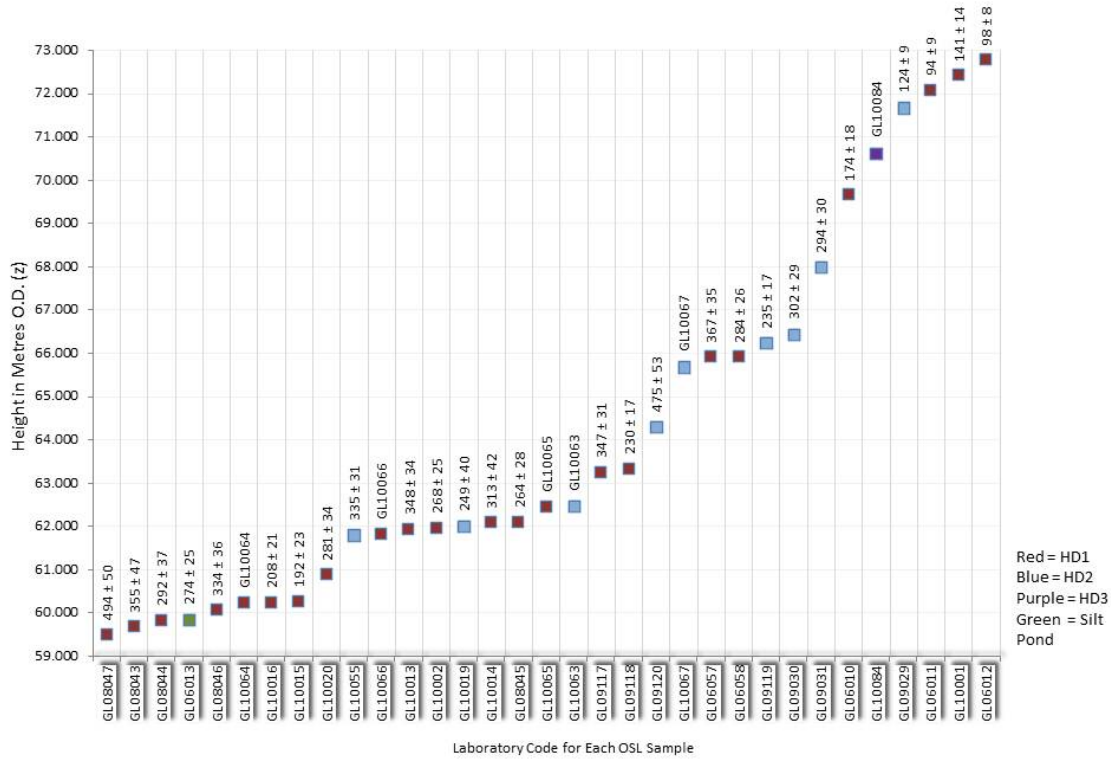

Figure 6.4: Chard OSL samples ordered according to height OD. Available dates shown are raw an unfiltered.

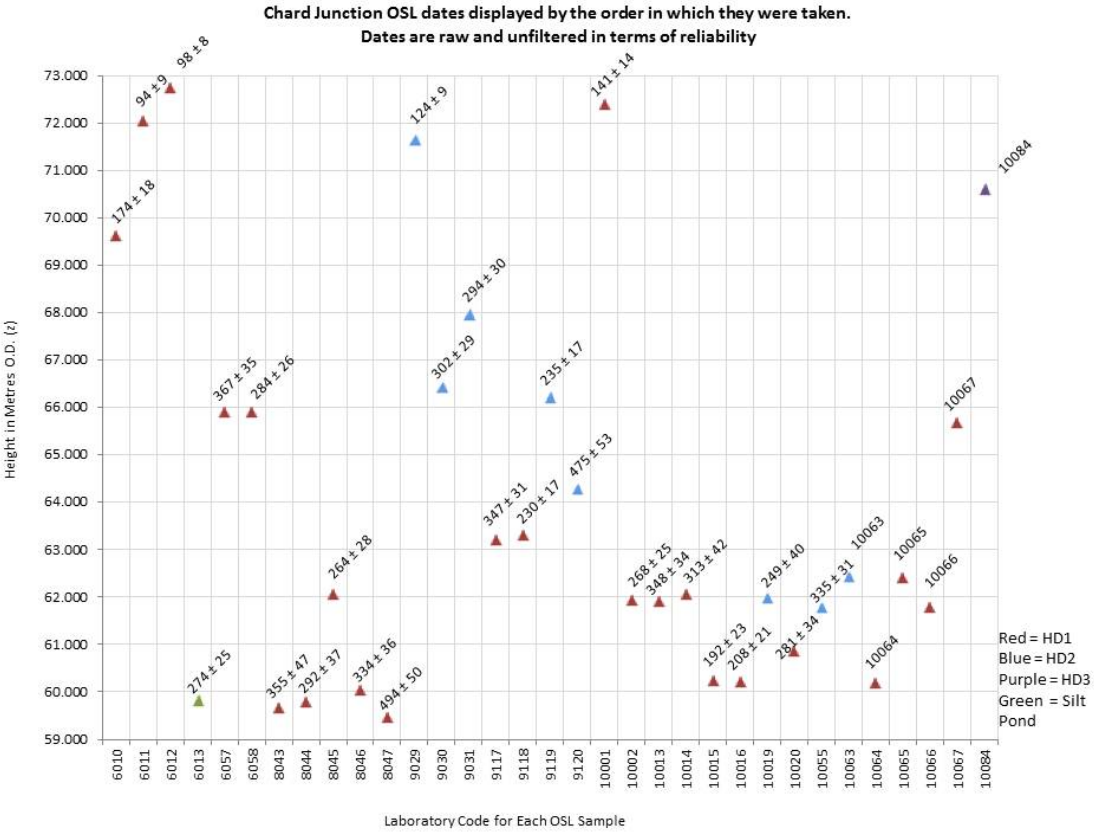

Figure 6.5: Chard OSL dates displayed by the order in which they were taken. Dates are raw and unfiltered in terms of reliability.

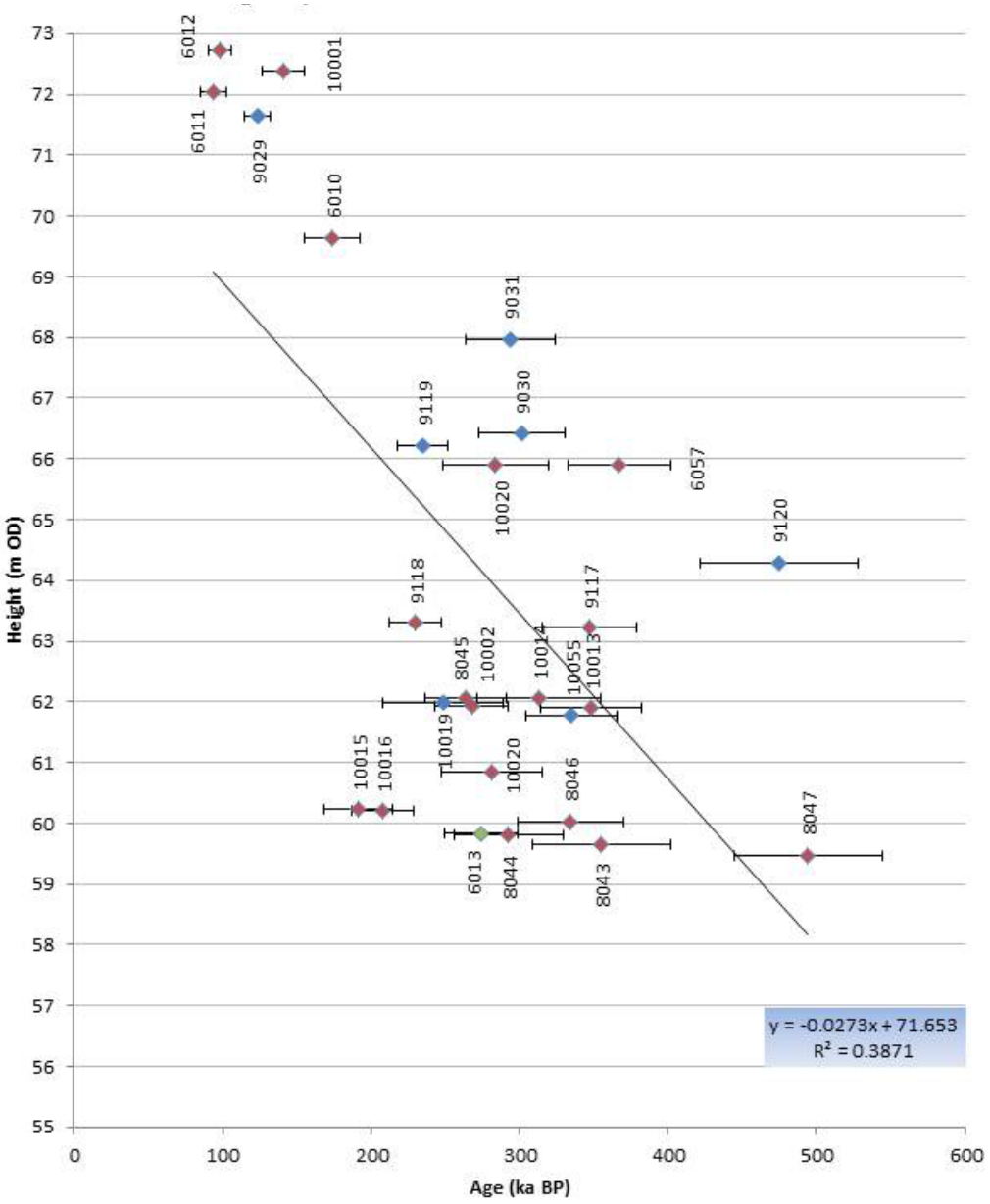

Figure 6.6: Raw age depth model for the OSL dates at Chard Junction. Red = HD1, Green = Silt Ponds and Blue = HD 2.

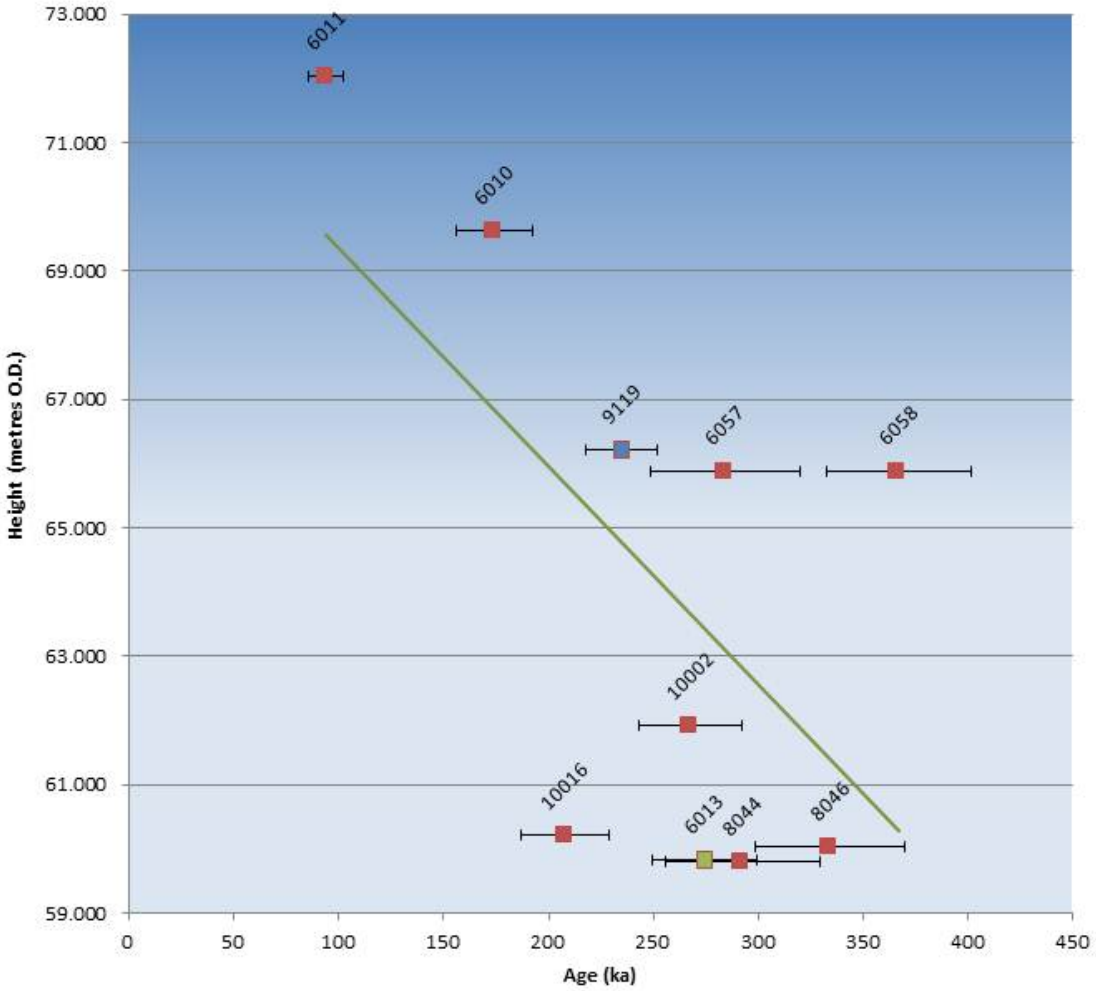

Red = HD1
Blue = HD2
Green = Silt Ponds

Numbers are GL Laboratory codes.

Linear trend line shown in green. R^2=0.3687

Height O.D.	Date	GL Lab Code	CHAR No
69.630	174 ± 18	6010	CHAR01
72.042	94 ± 9	6011	CHAR02
59.830	274 ± 25	6013	CHAR04
65.890	367 ± 35	6057	CHAR05
65.890	284 ± 26	6058	CHAR06
59.800	292 ± 37	8044	CHAR08
60.035	334 ± 36	8046	CHAR10
66.220	235 ± 17	9119	CHAR17
61.929	268 ± 25	10002	CHAR24
60.213	208 ± 21	10016	CHAR22

Figure 6.7: All analytically acceptable age estimates for Chard, plotted with standard deviation errors against height O.D.

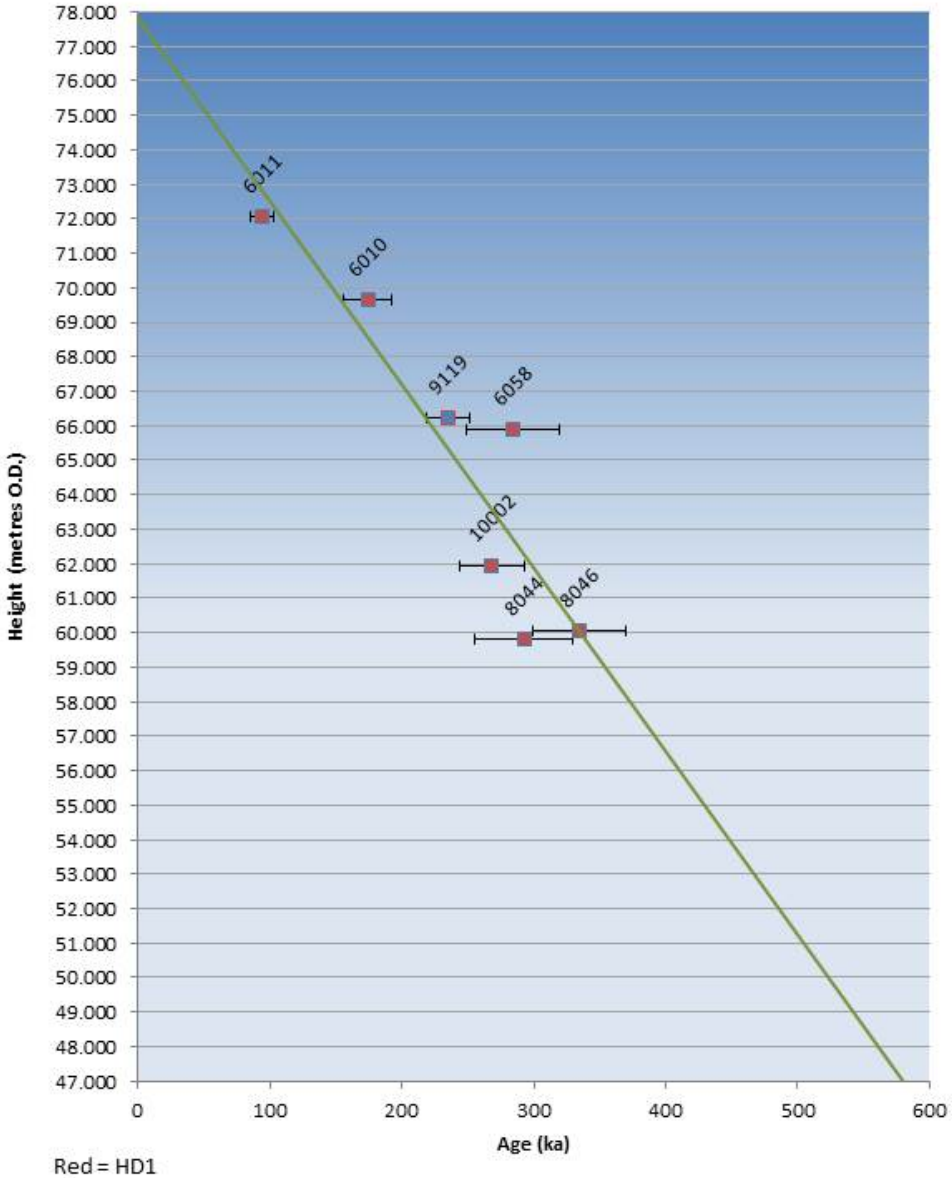

Figure 6.8: Filtered analytically acceptable age estimates for Chard, plotted with standard deviation errors against height O.D.

The raw age OSL data is shown in Figures 6.4 – 6.5 and plotted with height in 6.6. As can be seen from Figure 6.6, with all the OSL dates, both analytically acceptable and unacceptable, there is a wide age depth scatter and a low R^2 value. However, when only analytically acceptable age estimates are used, in Figure 6.7, there is an improved age-depth relationship although still a low R^2 value. Re-inspection of the individual ages and removal of the Silt Pond sample, which lies outside the Hodge Ditch Sequence, and two further outliers produced a much improved age depth relationship with a high R^2 value.

Further age-depth modelling will be undertaken when the full set of OSL dates are available.

In order to check that date variation was not due to stratigraphically unobserved lateral variation in the gravel body, dates are plotted against eastings and northings. This process after Phase 1 (Figure 6.9) appeared to produce some relationship between eastings/northings and age. However, using the expanded OSL dataset now available, there is seen to be little or no relationship between eastings, northings and age. We take this as provisional confirmation that the age depth modelling is representative of a stacked sedimentary sequence, and there is no evidence in this data for a major cut and fill discontinuity.

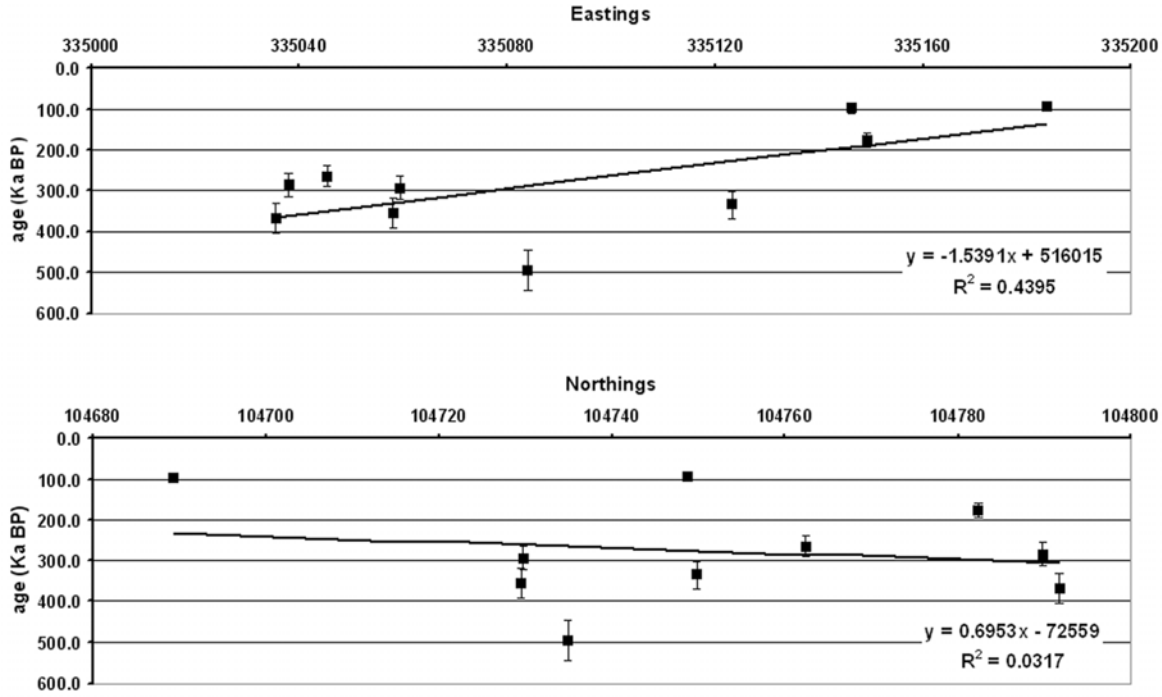

Figure 6.9: Hodge Ditch Phase I OSL dates regressed against eastings and northings.

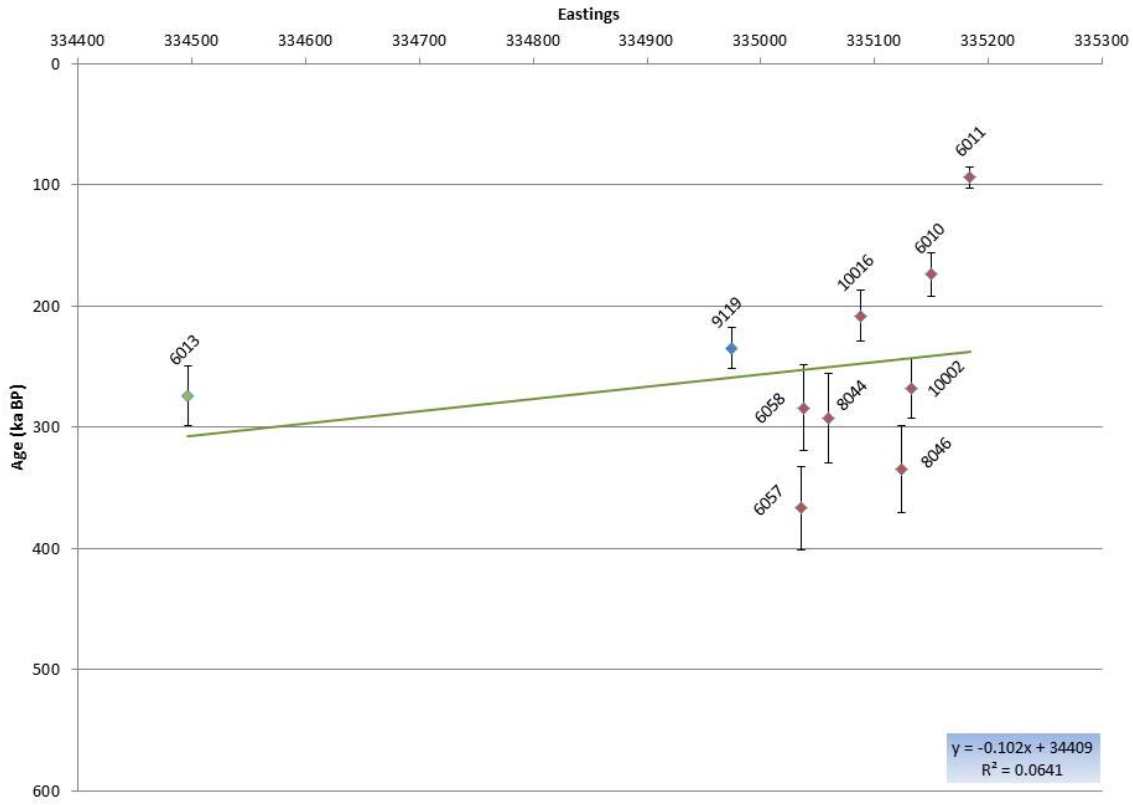

Figure 6.10: All analytically acceptable age estimates for Chard regressed against eastings.

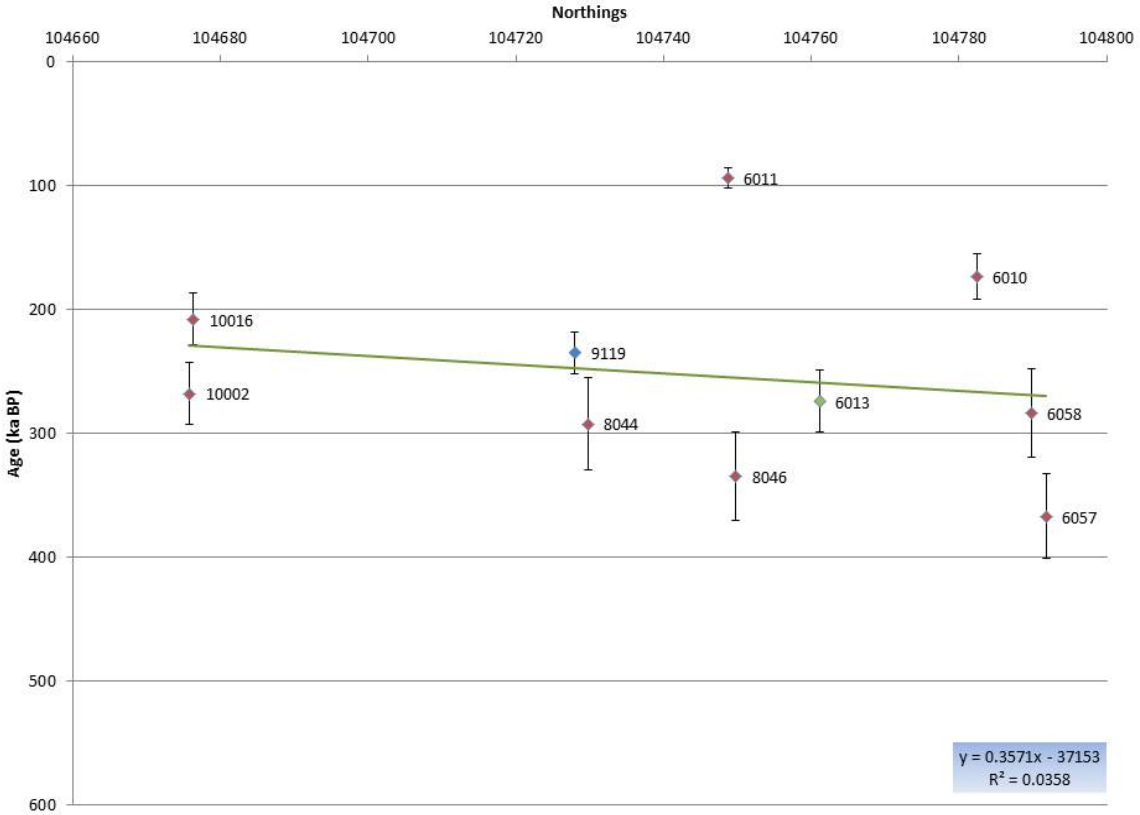

Figure 6.11: All analytically acceptable age estimates for Chard regressed against northings.

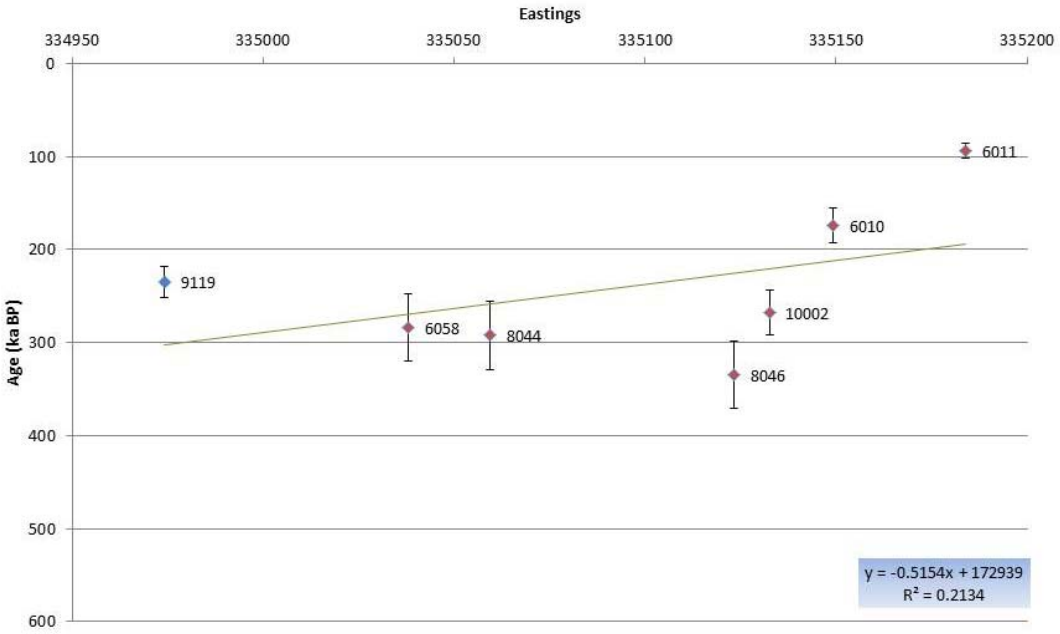

Figure 6.12: Filtered analytically acceptable age estimates for Chard regressed against eastings.

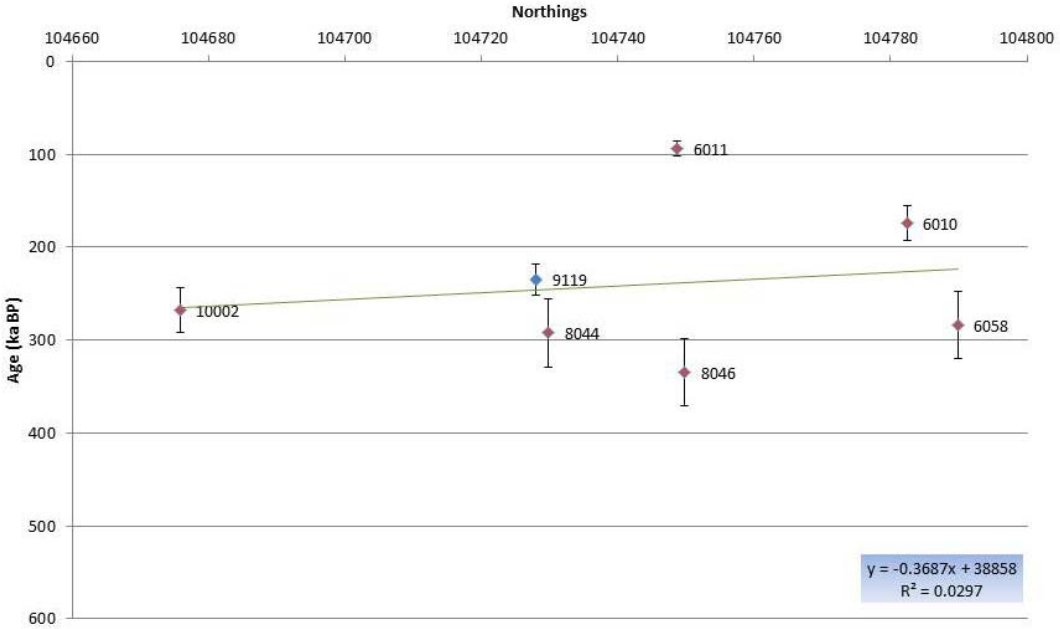

Figure 6.13: Filtered analytically acceptable age estimates for Chard regressed against northings.

7 Monitoring and mapping (Hodge Ditch Phase II)

Task 6. *This will be undertaken using standard methodologies of face survey (from the datum grid established in Stage 1), face logging, drawing and photography. We will also initiate a 3 weekly monitoring plan for this work. This is essential not only to monitor the pit and provide the data for the stratigraphic modelling but also provide the contextual data for the methodological studies. An additional element will be the geomorphological mapping of the full extent of the Chard Junction terrace at a scale of 1:5000. This will be done by stages during Stage 2.*

7.1 Monitoring Hodge Ditch Phase II

The methodological trials at the site also allowed monitoring of the quarry with an approximate frequency of 1-2 visit every 2 weeks. This produced a small number of new finds (a small broken biface, a core and a flake all of chert) as illustrated in Figure 7.1.

Chert biface

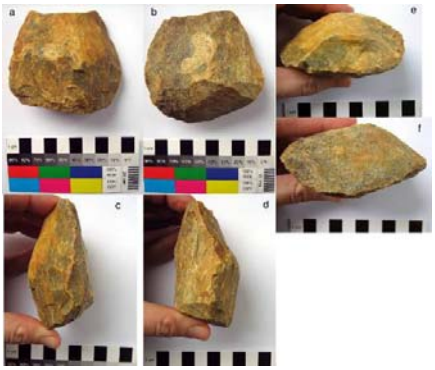

Flake from prepared core showing prior removal on dorsal side

Core/Core-scraper? Found next to

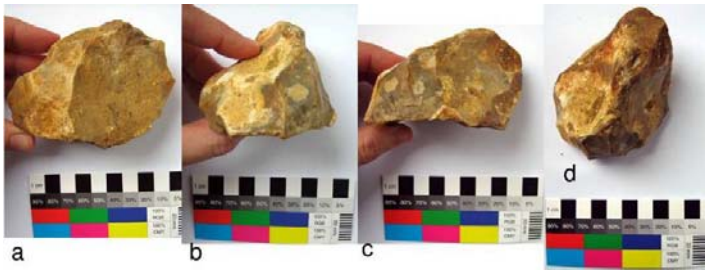

Figure 7.1: Lithic finds made by LSB during monitoring of Hodge Ditch II in 2010.

These finds are plotted on the GLS 3D model described in Section 9. Additionally the monitoring allowed a new generalised sedimentary profile of Hodge Ditch I and II to be produced (Figure 7.2).

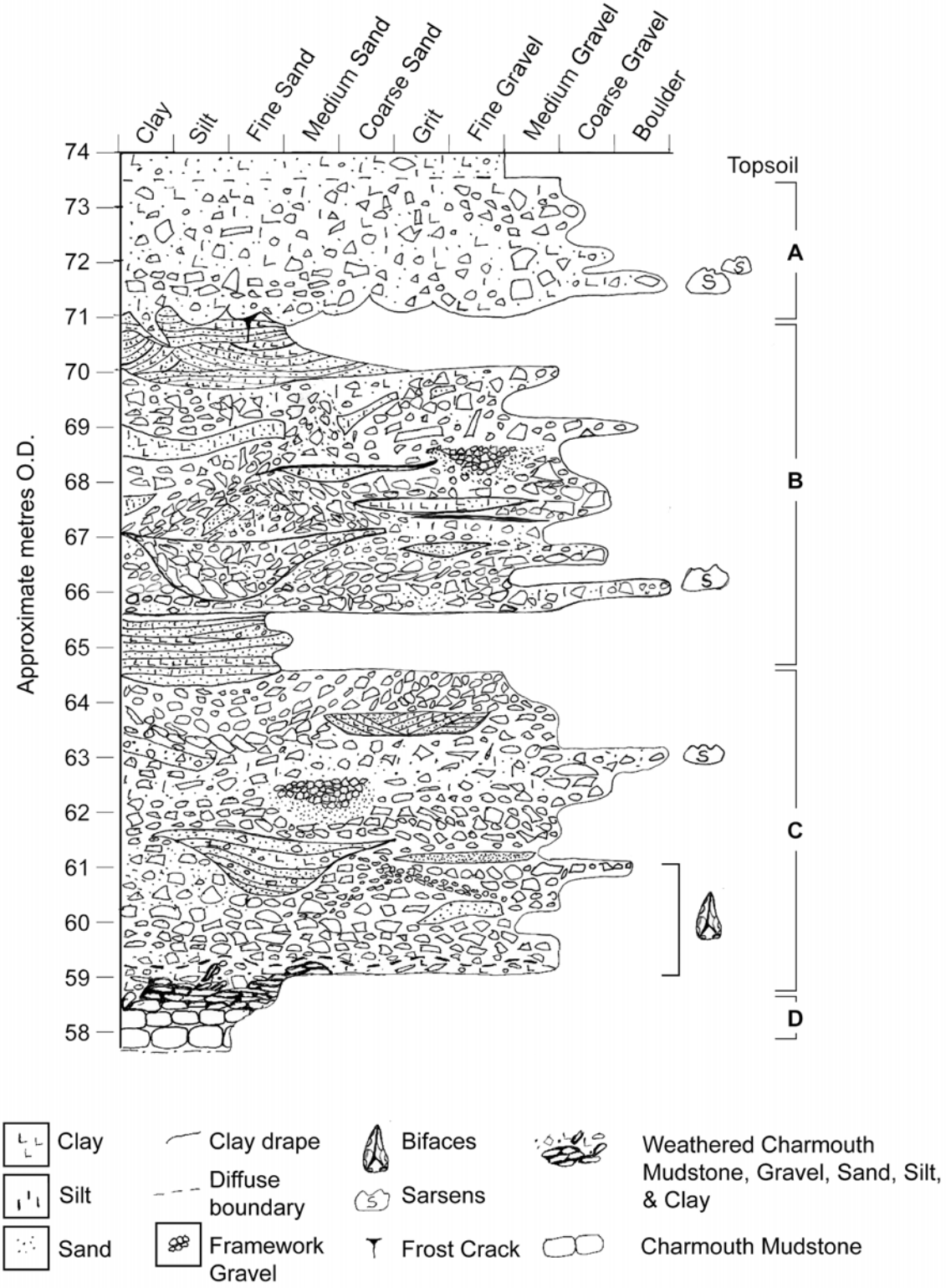

Figure 7.2: Generalised log of Hodge Ditch I and II

This log simplifies the complexity of the stratigraphy. A key factor in this complexity is that whilst the boundary between Unit A (upper diamicton) and Unit B is was seen throughout

the Hodge Ditch I & II (&III) the more subtle boundary between Unit B and C is neither always sharp or definable. There is, however, a general change from sub-angular chart matrix-rich gravels to more flint-rich and more frequently clast-supported chert and flint gravel often separated by discontinuous sand units. Whilst monitoring Hodge Ditch II we were also able to witness excavation of these gravels to below the water table. The weathered and brecciated bedrock head was only seen in Hodge Ditch I due to the greater depth of the gravels in Hodge Ditch II.

7.2 Geomorphological mapping

In order to try and assess the provenance of at least the upper diamicton unit and the pattern of surface finds of bifaces in the area, a programme of field geomorphological and geological mapping was undertaken. This was undertaken over 6km^2 upslope of Hodge Ditch Phase I and II (and indeed Phase 4 – Carter's Close). This was undertaken by mapping directly onto OS sheets at a scale of approximately 1:5000. The resulting maps (Figure 7.3-7.5) uses standard geomorphological symbols as recommended by the Geological Society Engineering Working Party (1972) and reproduced in Gardiner and Dackombe (1983).

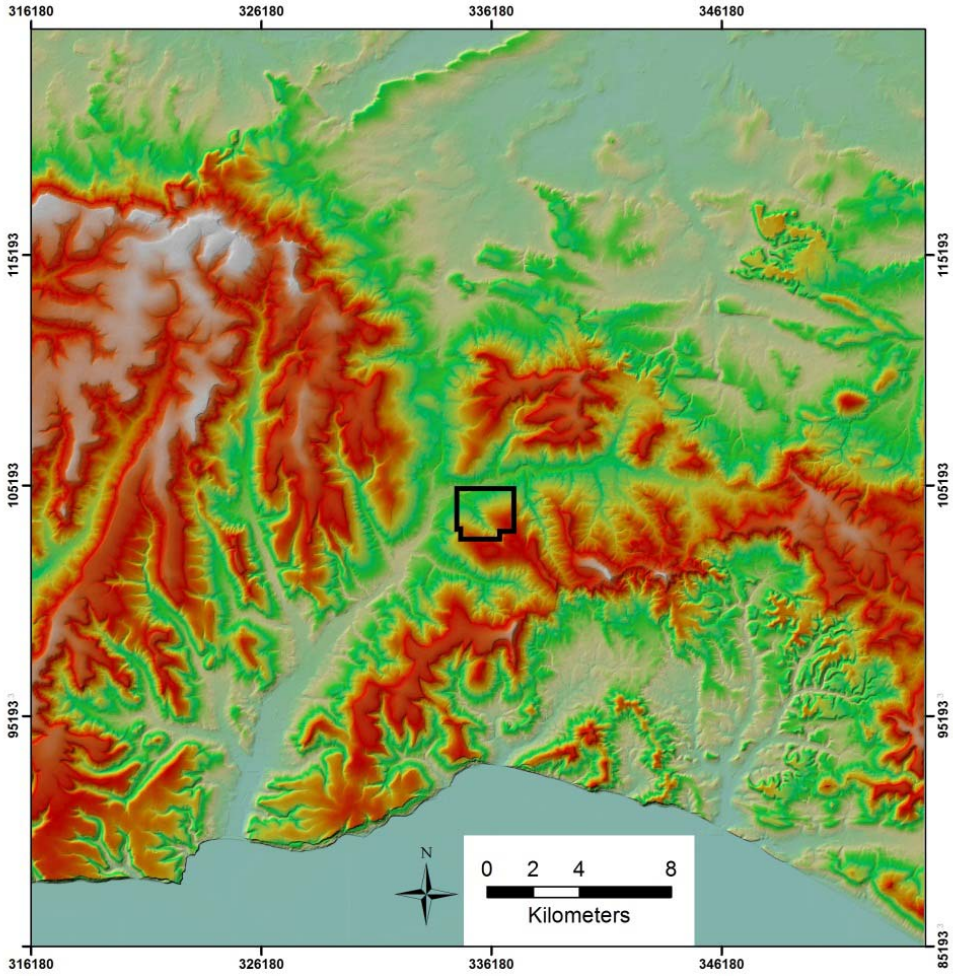

Figure 7.3 DEM of the Axe Valley and surrounding area generated from Digimap data under license to University of Southampton and modelled in ArcMap10. Black outline indicates area mapped.

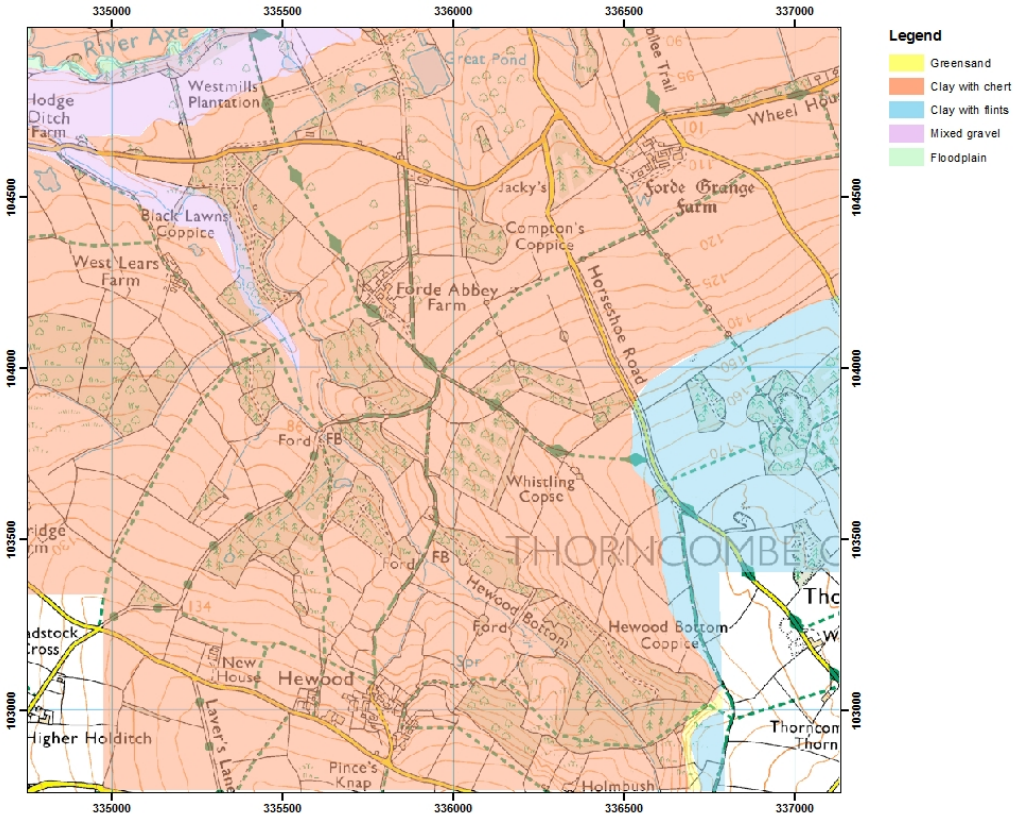

Figure 7.4 Geology mapped as part of this project of the slopes above Hodge Ditch I-III and Carter's Close, draped over 1:25,000 OS map from Digimap under license to University of Southampton

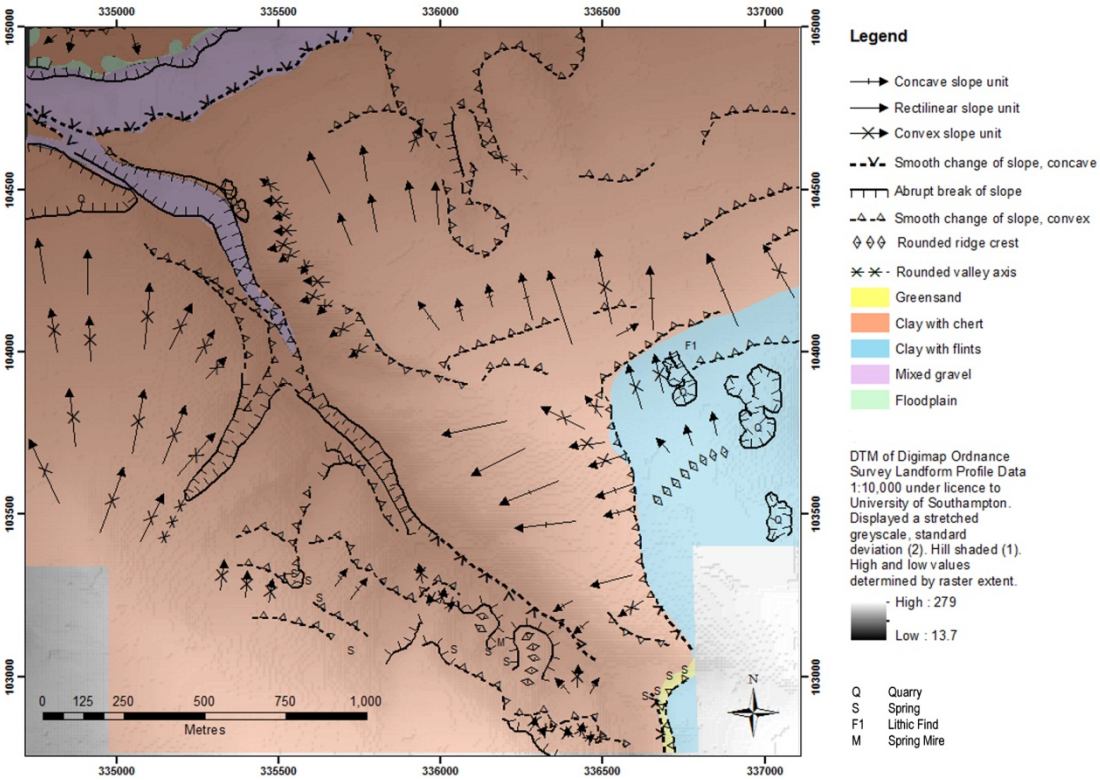

Figure 7.5 Geomorphological map and geology mapped during this project, of the slopes above Hodge Ditch I-III and Carter's Close.

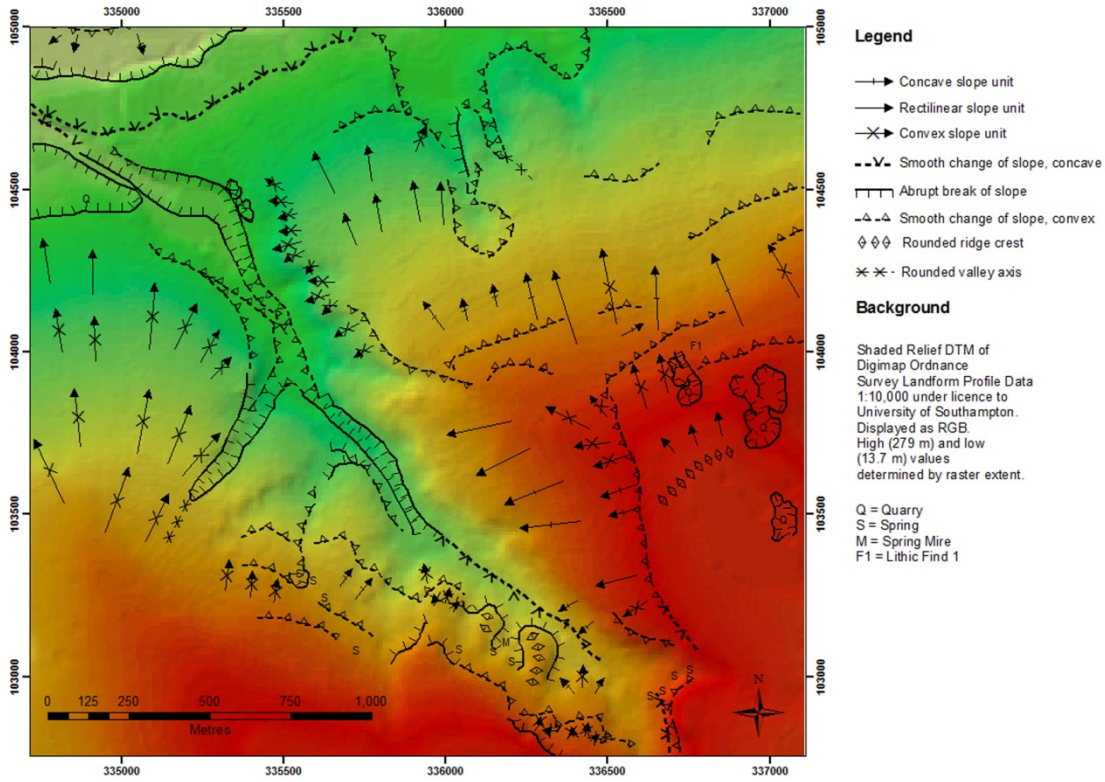

Figure 7.6 Geomorphological map of the slopes above Hodge Ditch I-III and Carter's Close draped on a DTM.

The surface of arable fields, animal burrows and small exposures were also used to determine the sub-surface lithology. The vast majority of the slopes to the south of Hodge Ditch was underlain by brown-red clay with chert (Figure 7.7). The chert was fractured and occasionally patinated but unabraded. This material is the source material for the uppermost diamicton unit at Hodge Ditch I & II. However, above 140 m OD on the plateau at Thorncombe the underlying lithology changed to a sandy clay-with-flint (Figure 7.8). The flint was generally small to medium sized shattered and nodular. Between these two Lithologies a yellow well-sorted fine to medium sand was exposed at Holmbush (Figure 7.8a).

Figure 7.7 The contrasting soils and subsurface lithology of the lower (left) and upper slopes (right) in the area mapped in Figure 7.4.

This sequence is interpreted as the chert and sandstone beds of the Eggerton Grit which is of Late Albian (Upper Greensand) age and deposited unconformably above it clay-with-flints which are regarded by the BGS as of Late Neogene (Tertiary) or early Pleistocene age (Edwards and Gallois 2004). There are abundant quarries into both units but all are overgrown. This boundary and the upper levels of the Upper Greensand controls the hydrogeology of the area with a very prominent spring line across the area and along the valley-side at between 130m OD and 140m OD. The slope above the quarry which has an average gradient of 40m per km (0.015) has a structurally controlled form reflecting the clay-with-flints, sandstone and chert, lithological stratigraphy with upper plateau, shallow ridges and convex slopes, and the lower chert slopes rectilinear or concave with alternating spurs and shallow valleys (Figure 7.9). Coming down from the springs along these valleys are a series of steep sided gullies many of which have pronounced concave headwalls at or below the springs.

Figure 7.8 (a) An exposure of Upper Greensand uncemented (weathered) sand at Holmbush, (b) the modified spring head at Hewood.

This mapping shows that whilst the source for the upper diamicton and the cherts at Hodge Ditch is the Upper Greensand cherts and sands from the valley slopes, the flint is derived from the plateau surface and from upstream. The surrounding slopes show very strong periglacial forms (gullies and amphitheatre-shaped gully heads, indicative of

periglacial weathering and mass movement (including solifluction) of the clay with chert. There is little doubt that the spring-line is of major importance in this processes as even today the discharges are high enough to feed perennial streams on the slopes, provide local water supply. In the Medieval period several of the springs (e.g. in Hewood Bottom Copse, Figure 7.8b) were exploited with shafts into the hillside and leets to supply the Great Pond at Forde Abbey. The abbey was founded in 1141-48 AD by Richard de Brioniis as a Cistercian Monastery and included a large watermill fed from the pond. The melting of both permafrost and annual snow on the Blackdown Hills plateau would have greatly increased the discharge of these springs supplying large quantities of water into and onto the slopes above Hodge Ditch and this is probably the process that created debris flows that deposited the upper diamicton at Hodge Ditch I and II during the Devensian.

Figure 7.9 The composite slope at Holmbush showing the upper break-of slope associated with the capping of clay-with-flints, the rectilinear slope and sharp spring-line (marked by brown Juncus sp.) formed by the upper sand unit and the lower convex slope formed by the chert.

Whilst mapping a grey chert flake with removals was discovered on the clay with flints (Figure 7.4) and although not truly diagnostic it is of typically Upper Palaeolithic form.

8 Palaeoenvironmental provision

Task 7. *This will only come into play if suitable sediments are recorded. It is therefore a floating task and will only be reported upon should it be undertaken.*

8.1 Discovery and sampling

Throughout the scanning and monitoring no organic sediments of recognisable land-surface was seen in any exposures in Hodge Ditch II. However, on the last visit to site on March 4th a red-purple disturbed and weathered horizon was noticed in Hodge Ditch III underlying gravels approximately 1.0 – 1.2 m below the junction with the upper diamicton unit (Figures 8.1 & 8.2). Hodge Ditch III is the small westerly extension of Hodge Ditch II with a continuation of the stratigraphy downstream and closer to the tributary junction that separates the Hodge Ditch sites from the old Chard Junction Quarry pits. The junction of the upper diamicton with the fluvial gravels had not been observed in Hodge Ditch II due to the infrequent (ad hoc) monitoring in the period between PRoSWEB work at Hodge Ditch I and the start of this project on Hodge Ditch II. As can be seen from Figures 8.1 and 8.2 the palaeosol horizon is undulating and discontinuous with lens-like pockets of organic clay separated by iron-stained gravels. There were also root channels with both sandy and organic-clay infillings. This suggests that the upper parts of the soil had been partially eroded leaving pockets of disturbed organic-rich clay. The form of these pockets is similar to the organic deposits found in tree-throw pits but the disturbance could equally be due to periglacial ground disturbance.

Figure 8.1 The palaeosol as exposed in the west face of Hodge Ditch III on March 4th 2008. The organic lens shown in Figure 8.2 is ringed in red.

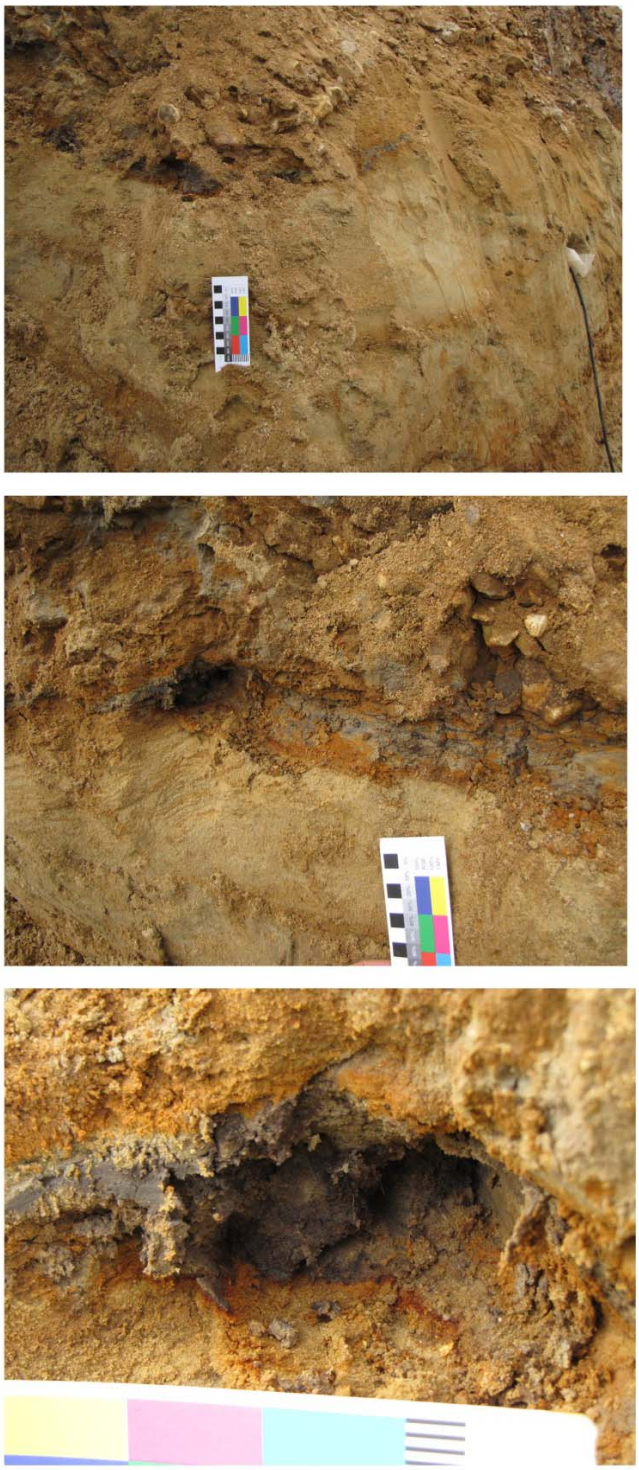

Figure 8.2 Photographs of the disturbed palaeosol horizon at Hodge Ditch II as seen and sampled on March 4th 2008. Note its undulating form and lens-like pockets of organic-rich clay.See Figure 8.1 for its location on the Hodge Ditch III face.

8.2 Sampling and Processing

The organic lens photographed in Figure 8.2 was removed and divided into an upper and lower sample each of 1cm in thickness. Two medium-sized samples (10g) were processed in order to test if pollen was present. The processing procedure used an in-house elutriation method (Scaife pres. comm.) followed by the standard chemical processing

procedures involving both hydrofluoric acid digestion and acetolysis (Moore et al. 1991). The elutriation method involves the swirling of the sample in a dish to separate the denser mineral grains from organic matter including pollen. Exotic spores (Lycopodium) in tablet form were added to a measured volume (10 g) in order to both aid pollen recovery (with low concentrations) and allow an assessment of pollen concentration. The tablets were added at the initial stage of processing (addition of NaOH). In order to evaluate the same sample for plant macrofossils and insect remains the sample was sieved at 1mm and 0.5mm intervals and the retained fraction inspected under a low-power binocular microscope.

8.3 Results

In this stage an evaluation was undertaking by counting two small sub-sample slides (10x10mm) from each preparation. Pollen was found to be present in both sub-samples but at low concentrations (see Table 8.1). However, the pollen was in good condition and if concentrated by processing larger samples (e.g. 100g) then could provide a single-level pollen spectra from the palaeosol.

Type	**CHD3A**	**CHD3B**
Trees		
Betula	1	
Pinus	1	
Corylus	1	1
Quercus	1	1
Alnus	4	7
Fraxinus	1	
Taxus	1	
Total Trees	*10*	*9*
Shrubs		
Salix	1	
Herbs		
Poaceae	2	4
Cyperaceae	1	1
Centaurea cyanus		1
Plantago lanc.		1
Sanguisorba	1	
Total herbs	*4*	*7*
Spores		
Polypodium		1
Unid.	*1*	*1*
Charcoal	*trace*	*trace*
Exotics	*381*	*752*
Total land pollen	**15**	**16**
Total pollen + spores (TPS)	**16**	**17**
TPC conc. gr.cm^{-3}	**462**	**249**

Table 8.1 Assessment sub-sample pollen from the Hodge Ditch III palaeosol.

Despite the low sample count it is clear that both are dominated by tree pollen and particularly *Alnus*. The presence of *Alnus* and other thermophilious trees (*Quercus*, *Fraxinus* and *Corylus*) clearly indicates that this is from an interglacial rather than an interstadial. Given this, the presence of *Taxus* and the sedimentary context below the upper diamicton unit the most likely ascription is to sometime in MIS5. If funded further work will produce a full pollen spectra and investigate the nature and environment of the

palaeosol from its geochemistry and micromorphology. This discovery provides for the first time some independent check on the OSL dating of the site.

The retained fraction from sieving produced very little organic residue. No insect (coleoptera, diptera or chironomid) remains were found. The plant material consisted only of unidentified fine root or stem material probably of monocotyledonous origin, black humic matter and very small lignified fragments of stem or bark. Some small fragments of charcoal were present (under 2mm) and material, including a few whole leaves of bryophytes. Comparison with type material and reference to Smith (2004) showed them to be typical of *Sphagnum* sp.

From this analysis it is suggested that only the pollen has the potential to reveal both palaeoenvironmental and chronological data if a full analysis is undertaken (see Stage 3 request). A full analysis of the pollen would allow comparison with the nearby late-Pleistocene spectra from Broom (Hosfield et al. 2011) and the Honiton by-pass site (Turner 2011).

9 3D modelling

Task 8. *This will be undertaken in the final 3 months of this stage of the project. See methodology for details.*

9.1 Introduction and methodology

As per the UPD detailed consideration was given to two approaches. The first was the use of a 3D bespoke Geographical Information System GSI3D (British Geological Survey). This has been developed by the British Geological Survey and uses routines derived from GOCAD. It holds data in depth-related structured database allowing the plotting of bounding surfaces in 3D enabling the production of 'exploded views'. The second was a commercially available package, Rockworks©, which has been used for fluvial sediments by Bennett (2005) and others. However, both were designed for projects based upon borehole records. This was clearly possible from the data supplied to the project by Bardon Ltd., however, the lack of any differentiation by the drillers of the gravels below the upper matrix-rich (dirty) gravels (i.e. diamicton) would have provided no internal stratigraphic differentiation and forced the use of proxy data for this purpose. This is both impractical and for the effort required would not have produced much of an advantage over a combination of logging and spatially-referenced location of finds. Instead it was decided to develop a 3D model using ground laser scanning of the entire area of Hodge Ditch I & II.

9.2 Results

The models presented below are the results of combining as many scans as possible at a particular time during the excavation of this constantly changing quarry. The models presented are obviously 2D representations of 3D models, and in suitable software can be rotated and viewed from different perspectives. Figure 9.1 shows unmerged scans of HD1 and 2 prior to the start of excavations in HD3. It also illustrates the problem of shadow created by talus and dumping which can be remedied by increasing the number of scan locations used. Also visible is the shadow under a scan location in HD2, and a segment covered by only one scan. The distal portions of some scans have also incorporated the surrounding vegetation – predominantly trees.

The full extent of the present extraction area can be seen in Figure 9.2, as well as many of the faces. This is a model because it contains faces that no longer exist and would have obscured other faces within the model. The data have not been cleaned, so in the middle of HD 2 it is possible to see a dark hooked feature which is the mechanical excavator. The yellow annotations mark the control points. Figure 9.3 shows the same data but with the point clouds rendered using the Silhouette tool in Cyclone. This rendering mode makes some of the cloud points in the model space view transparent, and highlights the excavated faces that were scanned during the project. This rendering is particularly valuable as it highlights the vertical and horizontal levels.

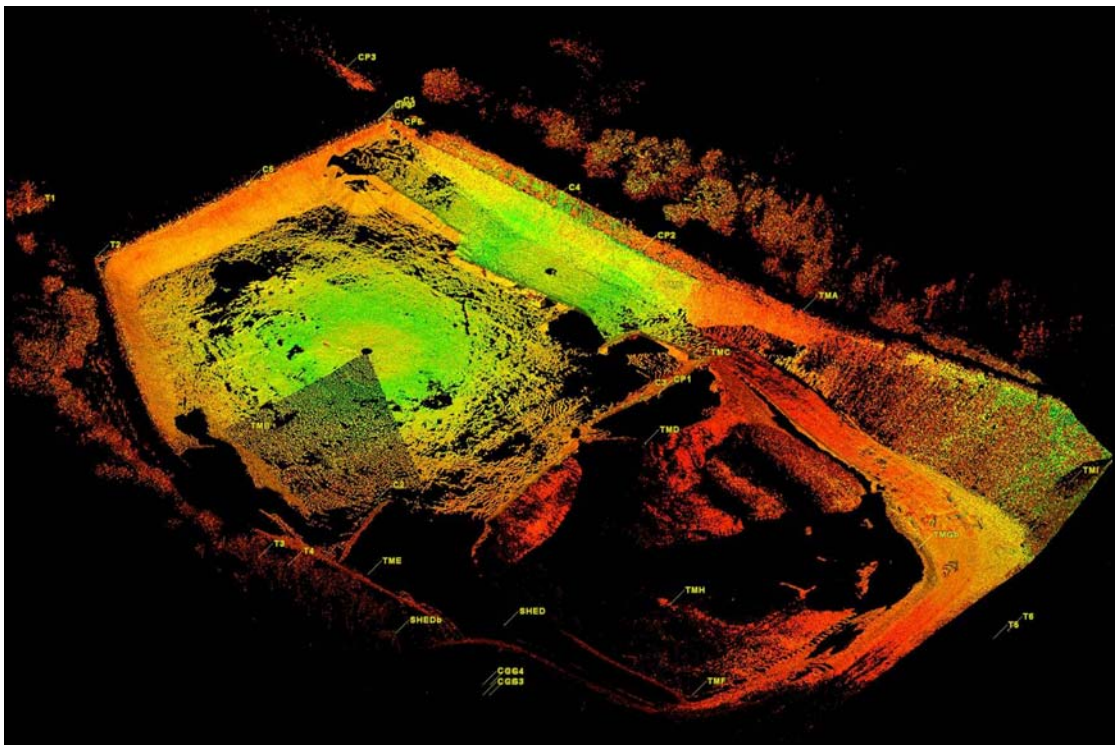

Figure 9.1 Partial 3D Model of Hodge Ditch I & II produced by sequential laser scanning 2010.

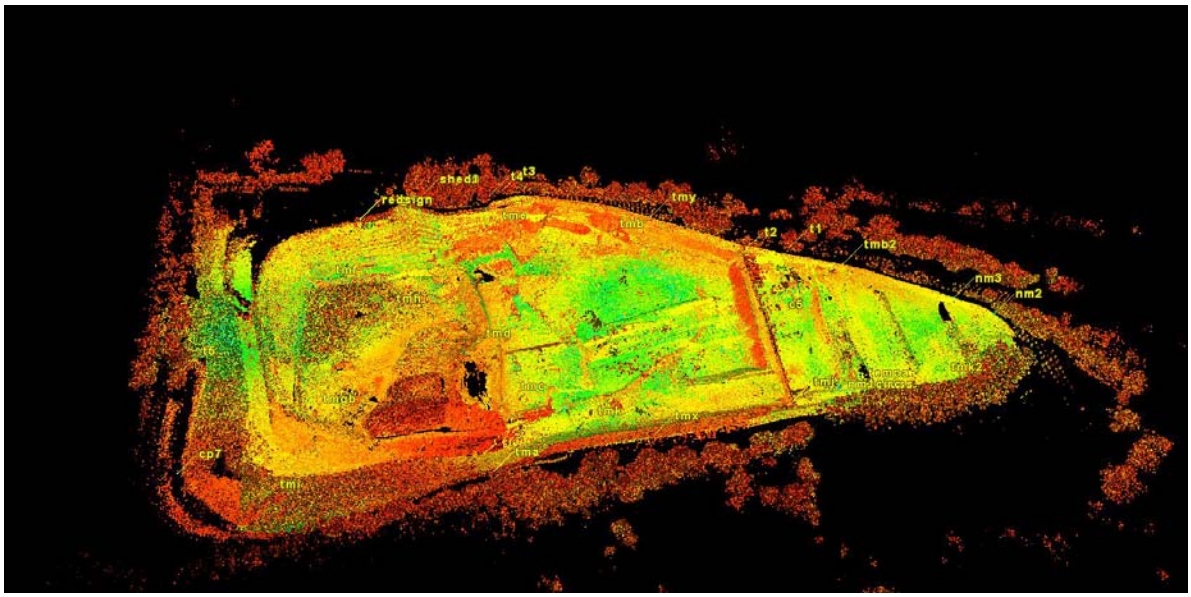

Figure 9.2 All unmerged and 'uncleaned' scans of HD1, HD2 and HD3: 2010 - 2011

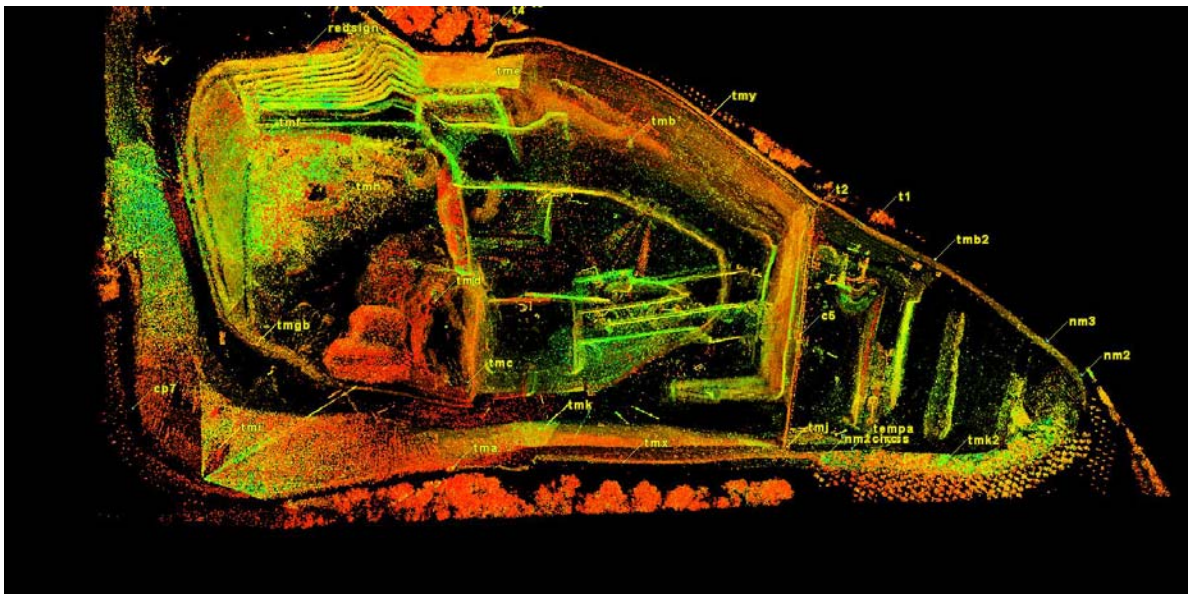

Figure 9.3 Silhouette rendering of all unmerged and 'uncleaned' scans of HD1, HD2 and HD3: 2010 - 2011

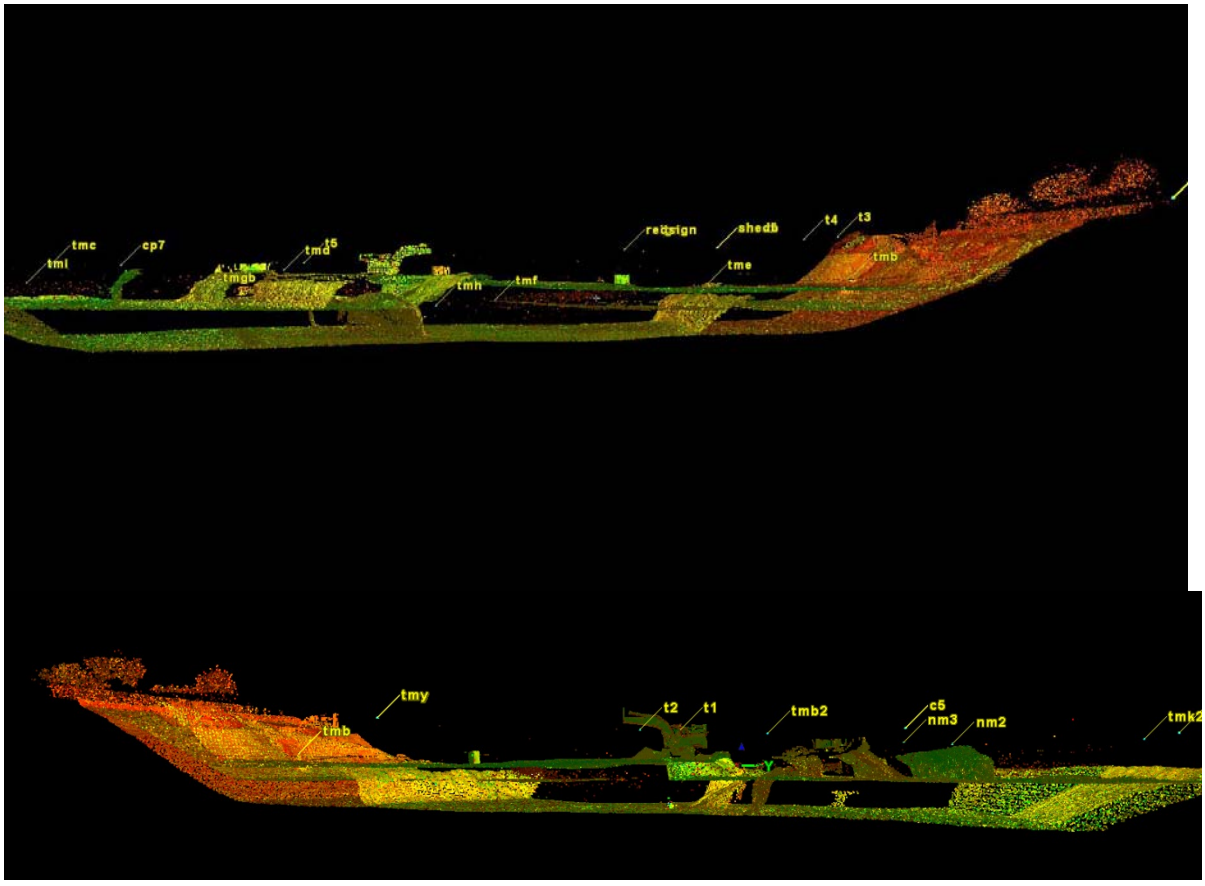

Figure 9.4 Left and right images of North –South slice through HD2. Unmerged, partially cleaned cross sections.

Figure 9.4 shows the data in Figures 9.2 – 9.3 partially cleaned (but with mechanical excavator left in for scale) where selected components of point clouds have been deleted manually from the west and east of the slice to allow a view of faces excavated and scanned over time. The cross sectional geometry of the excavations is also clear. In order to create a shell, it is necessary to merge point clouds and to select the points that are deepest in the pit, i.e. parts of clouds that are not required in the final model, have to be removed at this stage. Usually it is easiest to clean the data first, and then to merge the point clouds. As millions of points are generated during scanning (for the model shown in 9.2, there were over 479 point clouds and >207 million individual scanned points) any further manipulation requires software that can handle such large data sets, or a reduction in the density of points. Usually, once a scan has been cleaned and merged, then a decimation process can be run to reduce the points to the required density. However, during this project, an upgrade to a newer version of Cyclone meant that this tool was temporarily disabled which meant a work-around had to be implemented in order to reduce point cloud density.

The process used is described below. The result is very similar to the more normal decimation process; the main difference being that the “Tinning” interpolation procedure in Cyclone adds an additional statistically interpretative element, that would not be necessary under normal circumstances. In Figure 9.5 the difference between the full density scans of HD1 and HD2 may be contrasted with the “decimated” scan data for HD3 (far right) where the cleaned scan data have been sampled at a 2m grid spacing across the area.

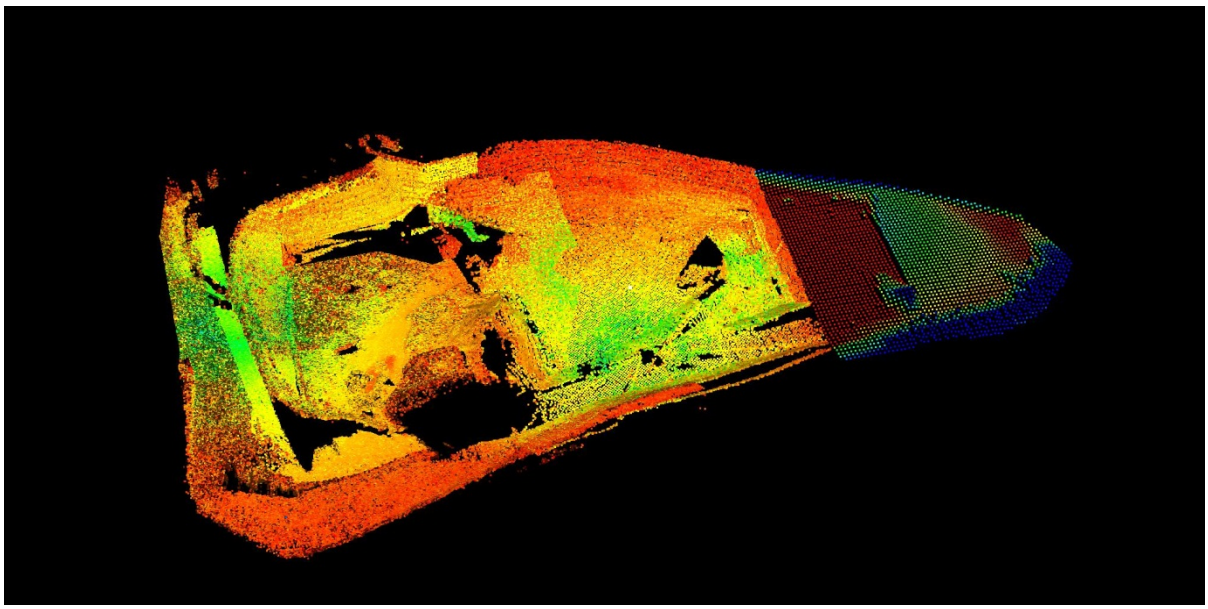

Figure 9.5: Partially cleaned and merged point clouds in HD1 and HD2. HD3 point cloud has also been “decimated”.

Because of the temporary loss of decimation functionality after an upgrade, the following method was employed to generate a solid model of the pit. Firstly, the data were “cleaned” (i.e. faces from high levels in the pit, excavators, large areas of peripheral vegetation etc.) as much as possible and merged. Then all the points were meshed together using a triangulated interpolation network (Tin) as shown in in Figure 9.6. This is itself a solid model, but because of the density of points, vegetation and stray points which had not been deleted during the cleaing process can be seen as spikes in the pit. Some of these

are “real” features. For example the cluster in the bottom right hand corner of Figure 9.6 represent the trees and vegetation in this corner of the pit. In the centre of the image there are several stray peaks and clusters of peaks, which represent dust or rain droplets, or moments when the dumper truck passed in front of the scanner which were not picked up during the initial cleaning process. One way of dealining with this would be to go back to the individual scan point clouds and clean these out. A quicker way however, is to reduce the density of the point cloud data, and many of these “aberrant” points are then automatically removed. Having meshed the merged point clouds, a new point cloud was generated from the Tin using a 2 metre spacing. This can be seen in Figures 9.7 and 9.8.

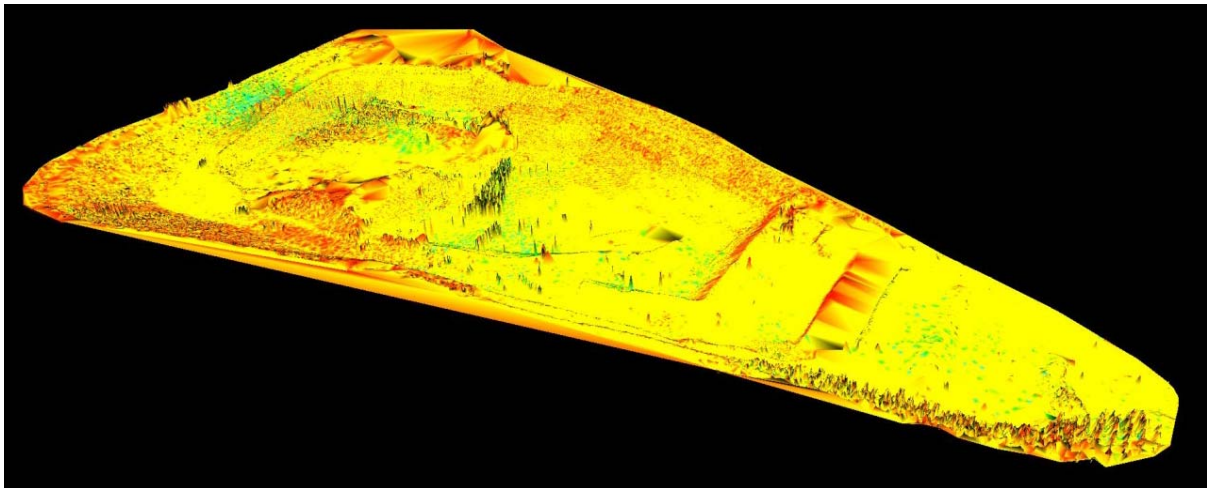

Figure 9.6 Tin colour mesh of cleaned scan data for HD 1, 2, and 3.

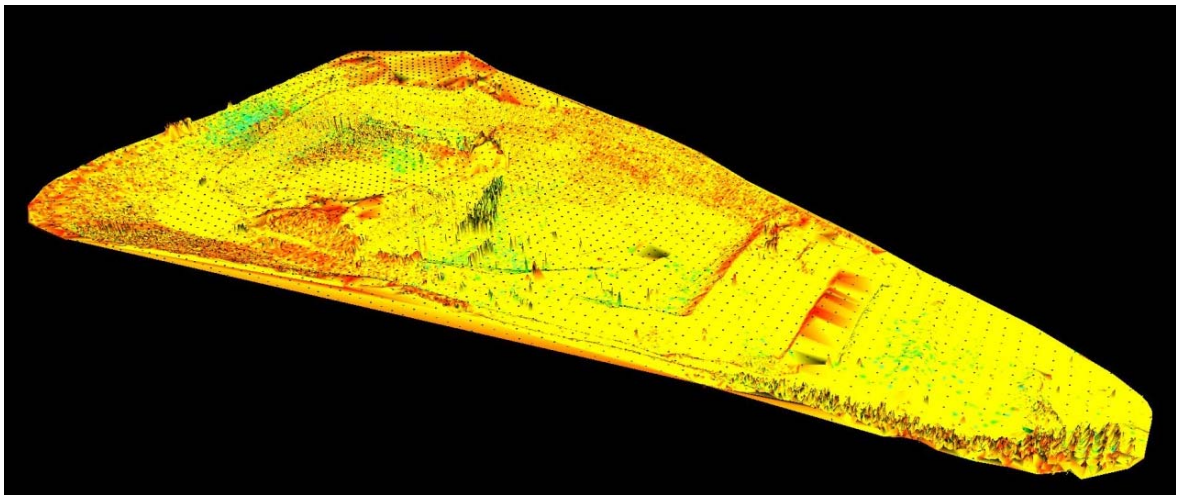

Figure 9.7 Grid (2 metre spacing) generated from Tin colour mesh of cleaned scan data for HD 1, 2, and 3. Tin also visible

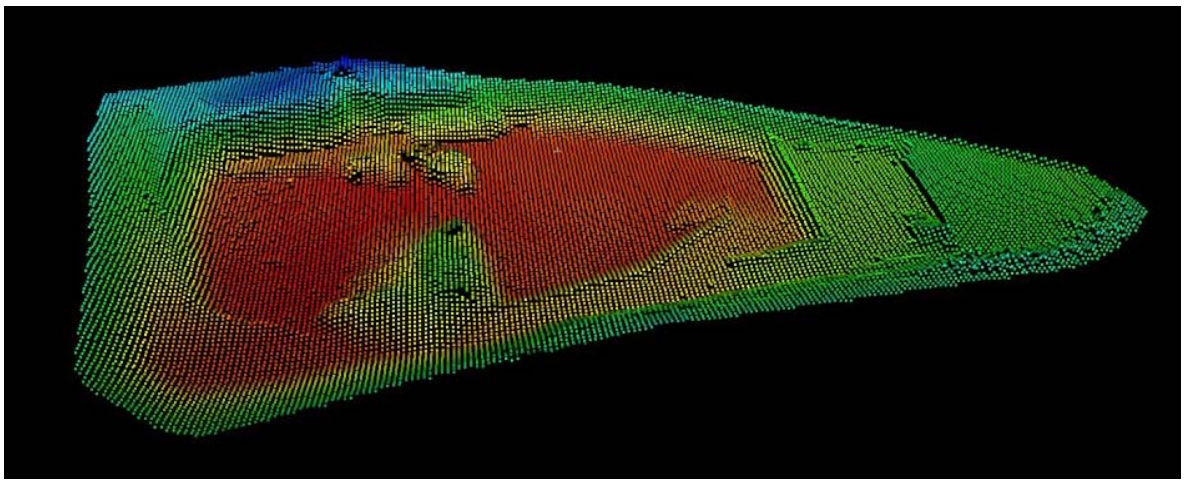

Figure 9.8 Grid (2 metre spacing) generated from Tin colour mesh of cleaned scan data for HD 1, 2, and 3.

Once reduced, the points could be easily exported, and modelled within ArcMap 10 to produce a pseudo 3D quarry model as shown in Figure 9.9. The vegetation in the top left corner on the banks of HD3 can be seen as a series of bobbles, as well as the vegetation in the bottom of HD1 which have developed over the course of the last year. Spoil heaps, and some large unexcavated gravel bodies can be seen between HD1 and HD2. One of these, topped with yellow, appears to spread into the vehicular access track. Re-examination of the data showed that this is the result of a gap in scan data in this area and is a “creation” of the interpolation method. Similarly the very high (white) values along the southern edge seem rather too high compared to Digimap spot height data on the road outside the pit, and data recorded using differential GPS, and this is probably because some scan points of trees and buildings were not removed during the cleaning process. In principal an algorithm such as those used to process airborne Lidar to remove vegetation could be applied. However, given the range of different sources of error, (i.e. it is not just vegetation causing the bobbles, and not all inconsistencies are represented in the same way) in practice it is far more sensible in this case to resolve such issues by going back to the original scan data and performing a second cleaning and correction process.

The 3D model of the same low density point cloud may be seen in Figure 9.10. The display tools in ArcMap and ArcScene allow a greater range of interpolation methods and visualisations. Having created a “shell” other data generated over the last 5 years by a range of different methods can be situated and integrated within the model. Some examples of this are presented below in Figures 9.11-9.16.

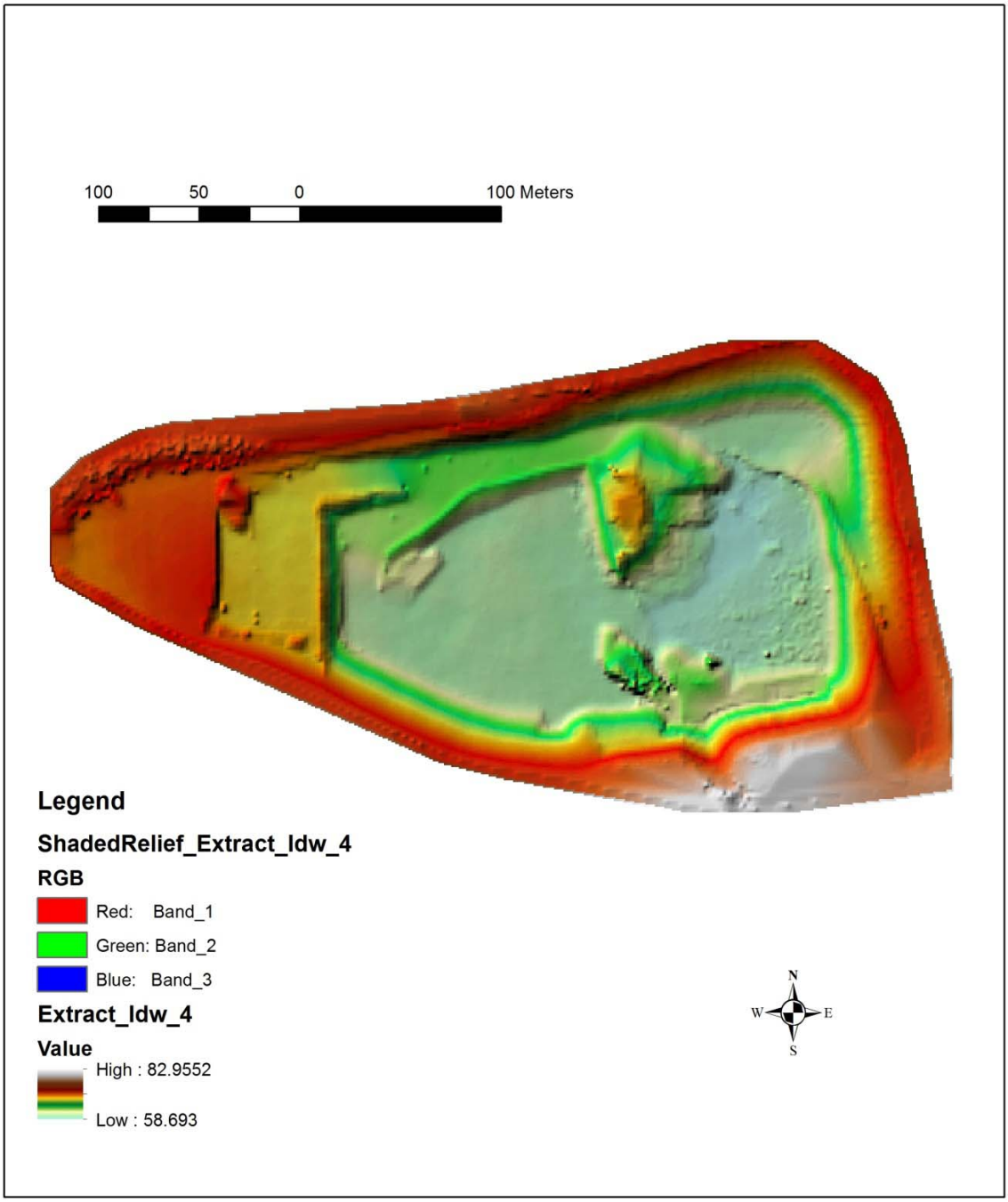

Figure 9.9: HD 1, 2 and 3 point data interpolated in ArcMap 10 using inverse distance weighting and displayed using height colour values. Displayed in ArcMap (2D) using a shaded relief rendering of to produce a pseudo-3D image.

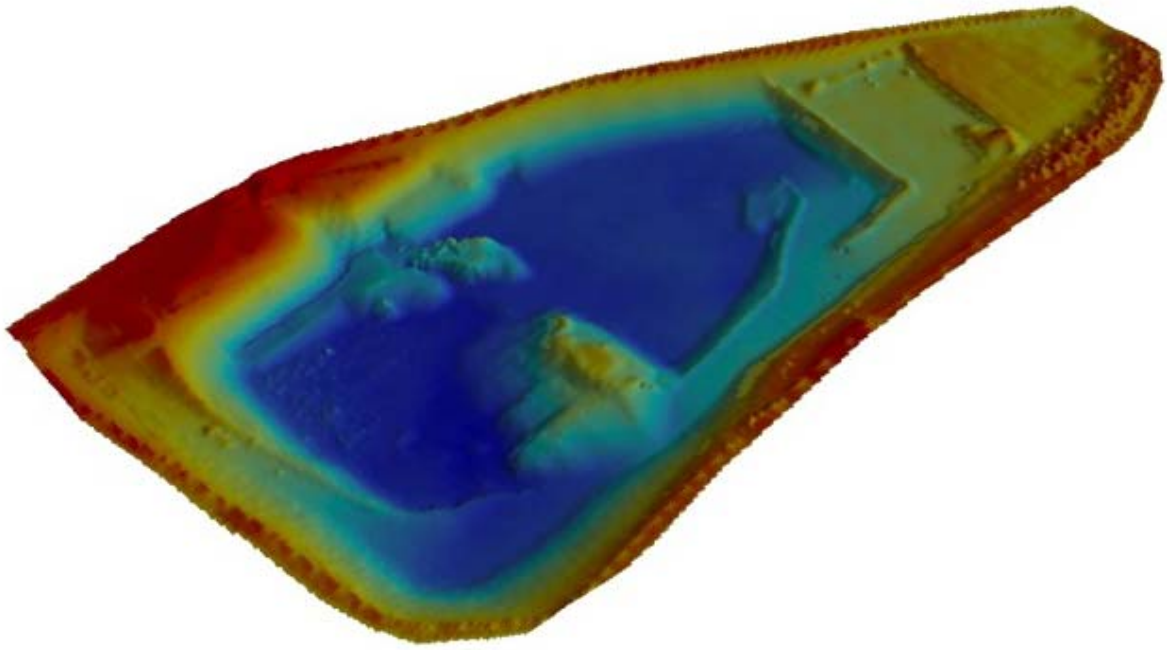

Figure 9.10 HD 1, 2 and 3 point data interpolated in ArcMap 10 using inverse distance weighting and displayed in ArcScene in 3D using height values. Red = high and blue = low. HD 3 top right, HD1, left.

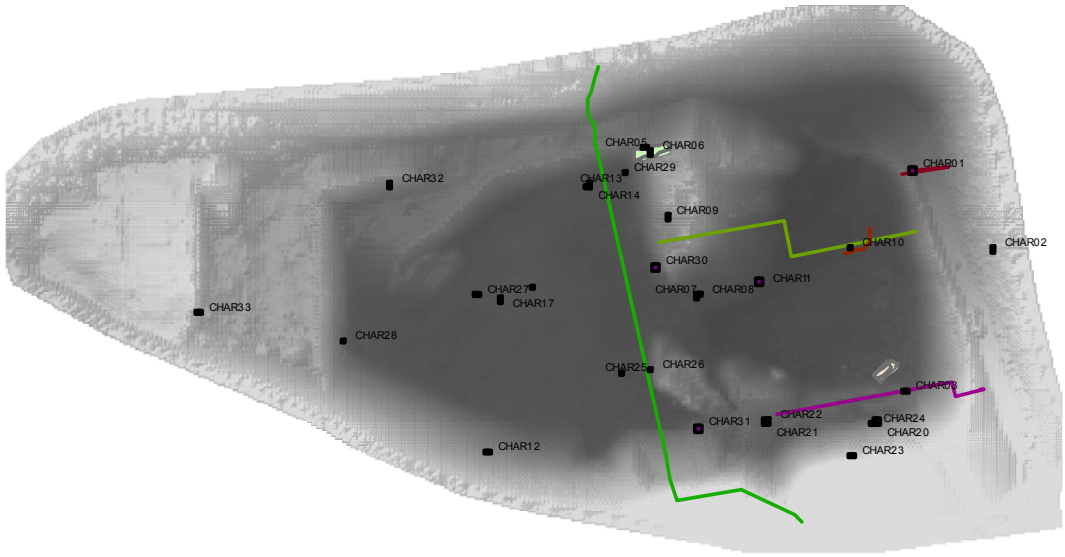

Figure 9.11 HD 1, 2 and 3 point data interpolated in ArcMap 10 using inverse distance weighting. Selected sections recorded prior to laser scanning marked by red, pale green and pink lines. Recorded using during previous work at HD using total station/tapes/dumpy levels. Pale green solid and beige solid shapes represent trenches exavated during previous work at HD to take OSL samples prior to the application of laser scanning. Dark green line marks old fence line between HD1 and HD2 recorded using differential GPS. CHAR points are OSL lcoations.

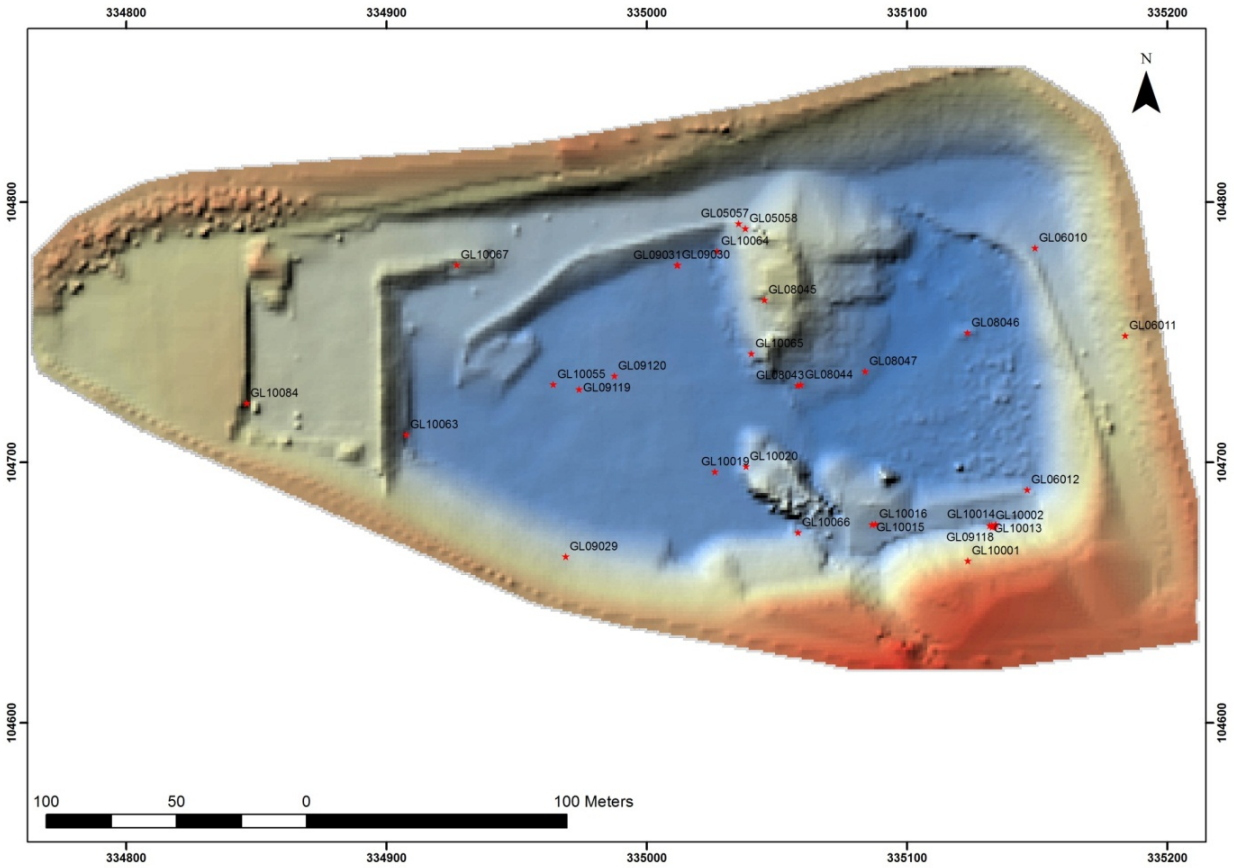

Figure 9.12 HD 1, 2 and 3 point data interpolated in ArcMap 10 using inverse distance weighting and displayed using height colour values. Displayed in ArcMap (2D) using a shaded relief rendering of to produce a pseudo-3D image. Red high, blue low. Red points show distribution of OSL sample locations labelled according to GL-number.

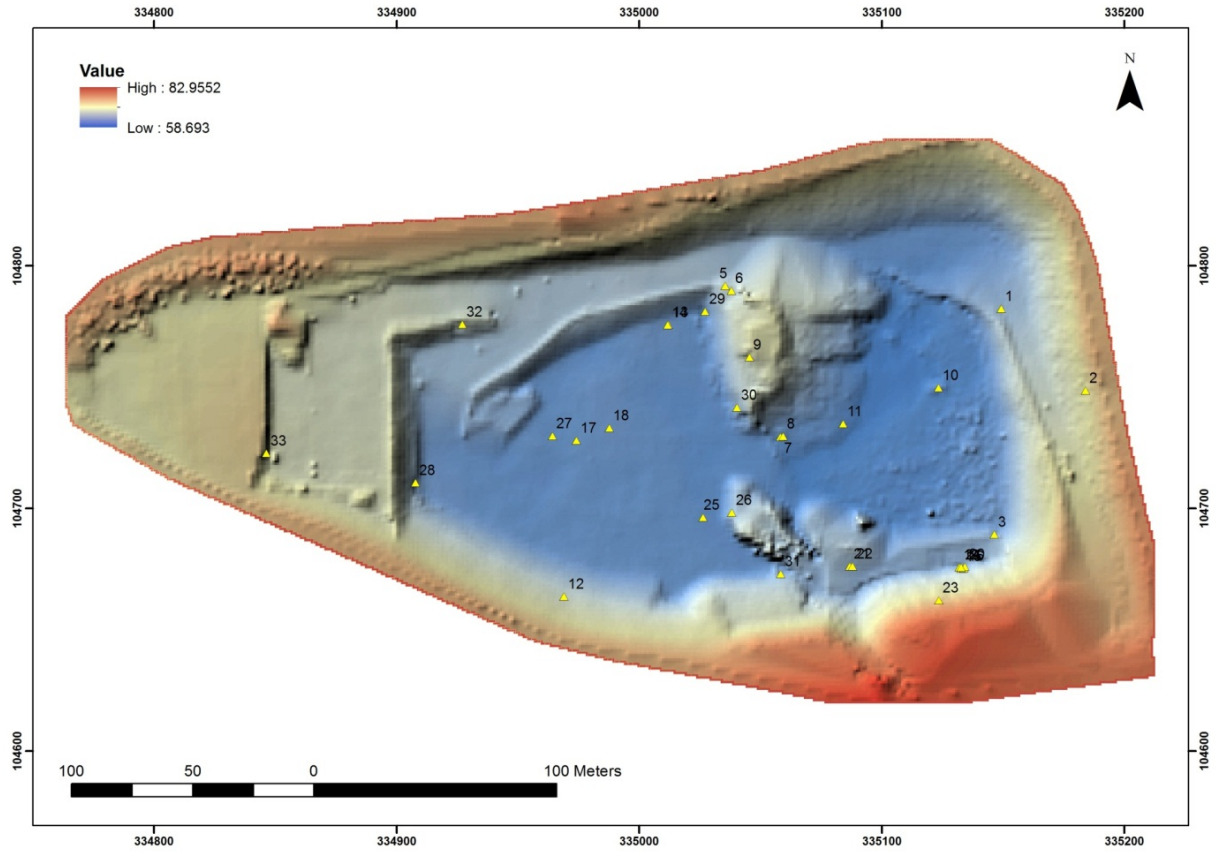

Figure 9.13 HD 1, 2 and 3 point data interpolated in ArcMap 10 using inverse distance weighting and displayed using height colour values. Displayed in ArcMap (2D) using a shaded relief rendering of to produce a pseudo-3D image. Red high, blue low. Yellow points show lateral distribution of OSL sample locations labelled according to CHAR number. Close up of points that overlap at this scale are shown in Figures 9.13 – 9.15.

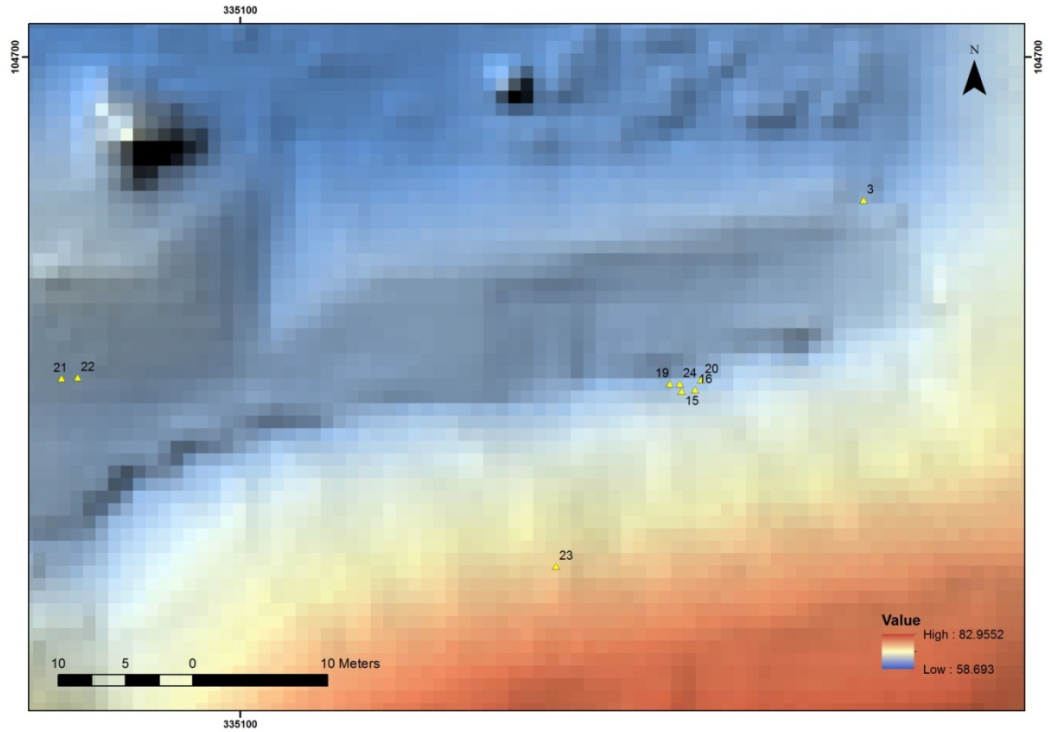

Figure 9.14 Selected area of Figure 9.12. Close up of OSL location cluster A.

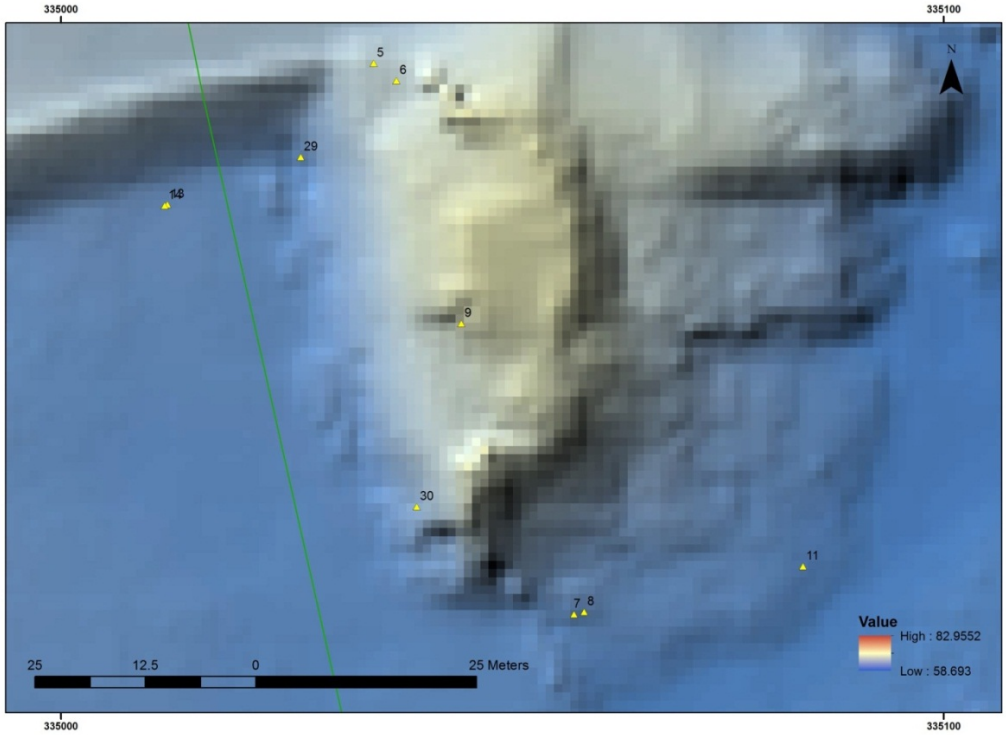

Figure 9.15: Selected area of Figure 9.12. Close up of OSL location cluster B.

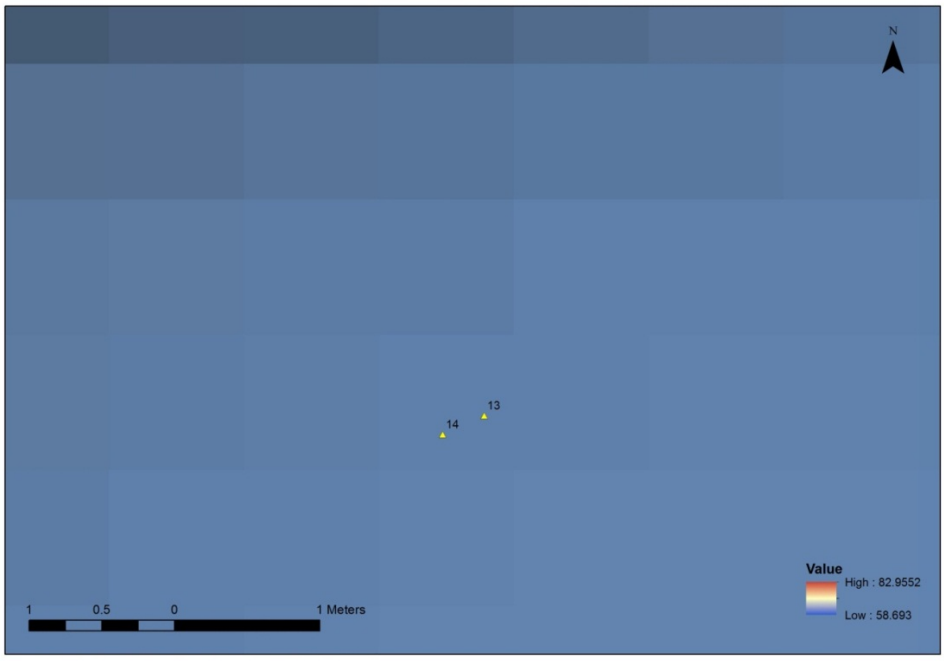

Figure 9.16 Selected area of Figure 9.12. Close up of OSL location cluster C.

ArcScene allows the 3D visualisation of integrated HD data from a range of sources to be rotated, exaggerated and examined from multiple angles. Fly-throughs are possible in Cyclone, but were found to be quite jerky. Smoother fly-throughs were possible in ArcScene. Figure 9.17 shows the HD model generated from scan data (as shown in Figure

9.9) viewed from the side with no vertical exaggeration. It is integrated with two grey layers generated by interpolating between points recorded in bore-hole data of the top of bedrock and the diamicton.

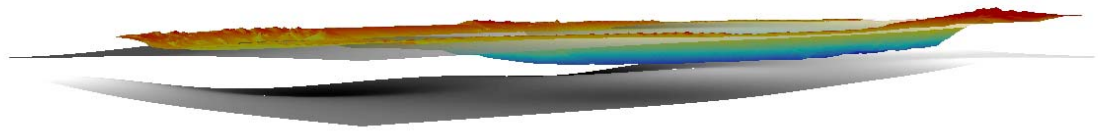

Figure 9.17 Side view of HD data shown in Figure 9.9 (red high, blue low) with no vertical exagerration displayed in ArcScene. Grey layers are top: diamicton and base: top of bedrock, generated by interpolatingn bore hole data. HD 3 on the left, HD 1 on the right

Due to the lack of natural vertical exaggeration compared to the horizontal area covered, it is difficult to examine the relationships between these layers. Figure 9.18 shows the same data rotated and with a vertical exaggeration scale of 5. Different colour scales have been used for the three different layers, and this allows the relationship between them to be seen far more easily. The undulations in the bedrock and the diamicton can be seen, although it should be emphasised that these layers were generated by the interpolation (again using IDW) of only nine data points for each layer, with variable spatial distribution (compared to hundreds of data points with even distribution for the quarry model). The height of bedrock and the diamicton in HD 3 for example, is based on only one bore hole record in this area and this is discussed further below. The proximity of the base of HD1 with the bedrock junction is well illustrated. This was also “ground truthed” by a test pit where the gravel/bedrock junction was seen during earlier research at Chard.

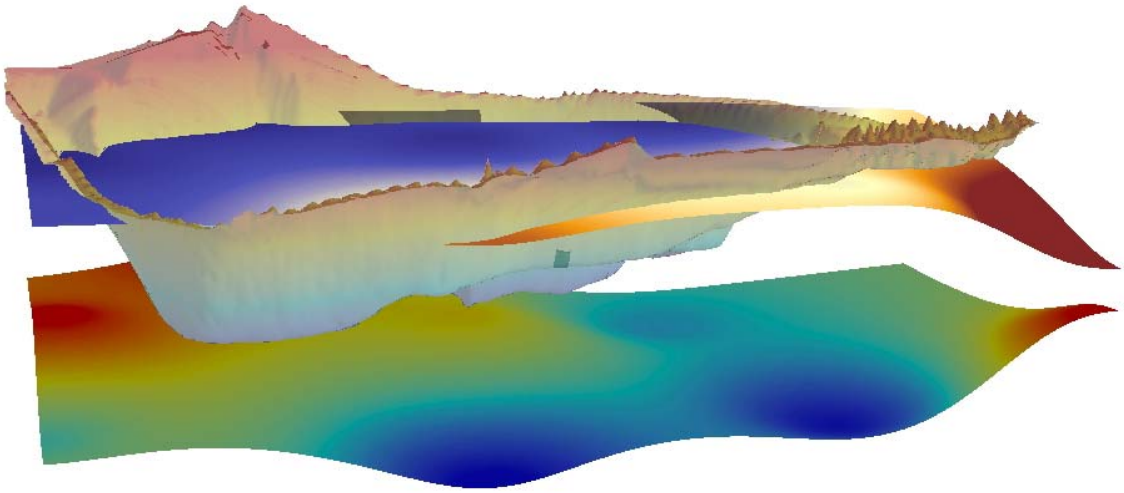

Figure 9.18 Quarry model generated from scan data displayed in ArcScene integrated with diamicton layer (purple high, brown low) and bedrock top layer (red high, blue low) both generated from bore-hole data. Displayed at 5 x normal vertical exaggeration.

Further 3D models of the excavated area of the quarry, which contain in real space co-ordinates the sand unit data, OSL sample locations and find locations within the 3D model of the gravels are shown in Figures 9.19 to 9.24. This allows manipulation and rotation of the model of the gravel body to inspect the spatial relationships between these entities. In addition discrepancies between the data sources can be examined. For example, the effect of the low resolution of the bore hole data in HD 3 can be seen in Figure 9.20. The position of the diamicton layer in this part of the pit modelled from the bore hole data is too low, as this boundary is known from observation during extraction and scaned data to occur above the sand unit and the overlying palaeosol the centre of the image.

As the extraction of stratigraphic and sedimentological information improves and with a simpler quarry, this procedure will allow 3D modelling of the stratigraphy and sedimentology of the gravel body. This will be a step towards a fully automated 3D model of gravel body stratigraphy produced directly from laser scanning.

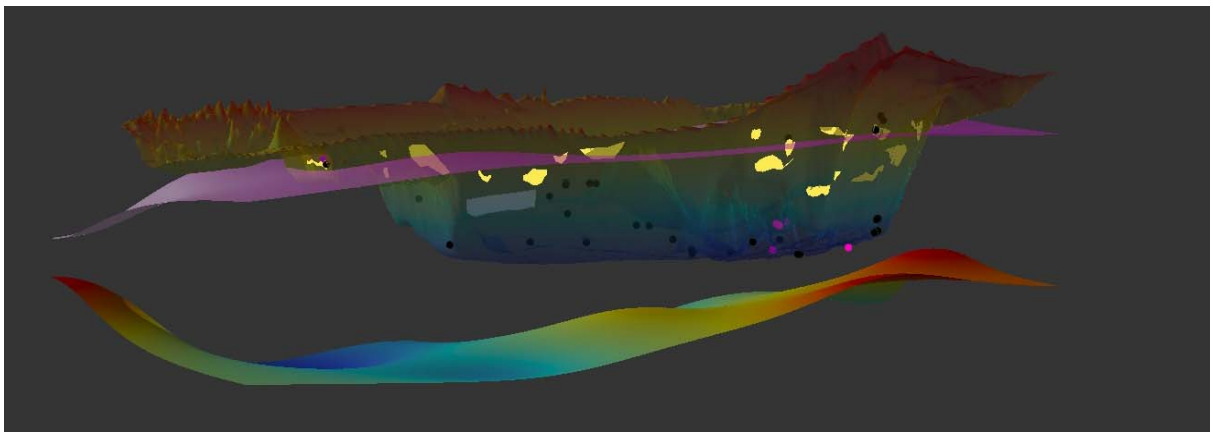

Figure 9.19: Quarry model (red high, blue low) generated from scan data displayed semi-transparently in ArcScene and integrated with diamicton layer (dark pink high, pale pink low) and bedrock top layer (red high, blue low) both generated from bore-hole data. Displayed at 5 x normal vertical exaggeration. Major sand units observed and recorded from

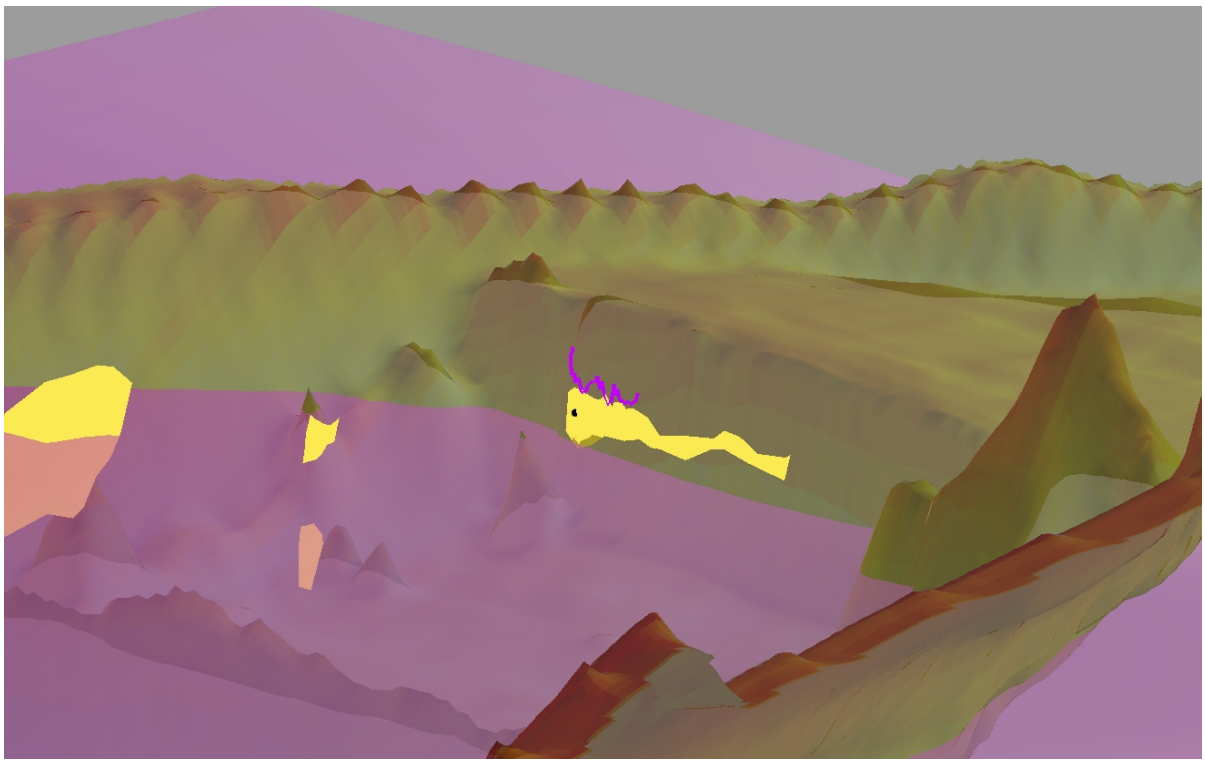

Figure 9.20 Close up of sand lens sampled for OSL (hole shown in black) and palaeosol (bright pink line) in "shell" of HD3 gravels derived from scan data. Diamicton boundary in HD3 shown as semi-transparent pink layer is clearly too low. See text for further explanation.

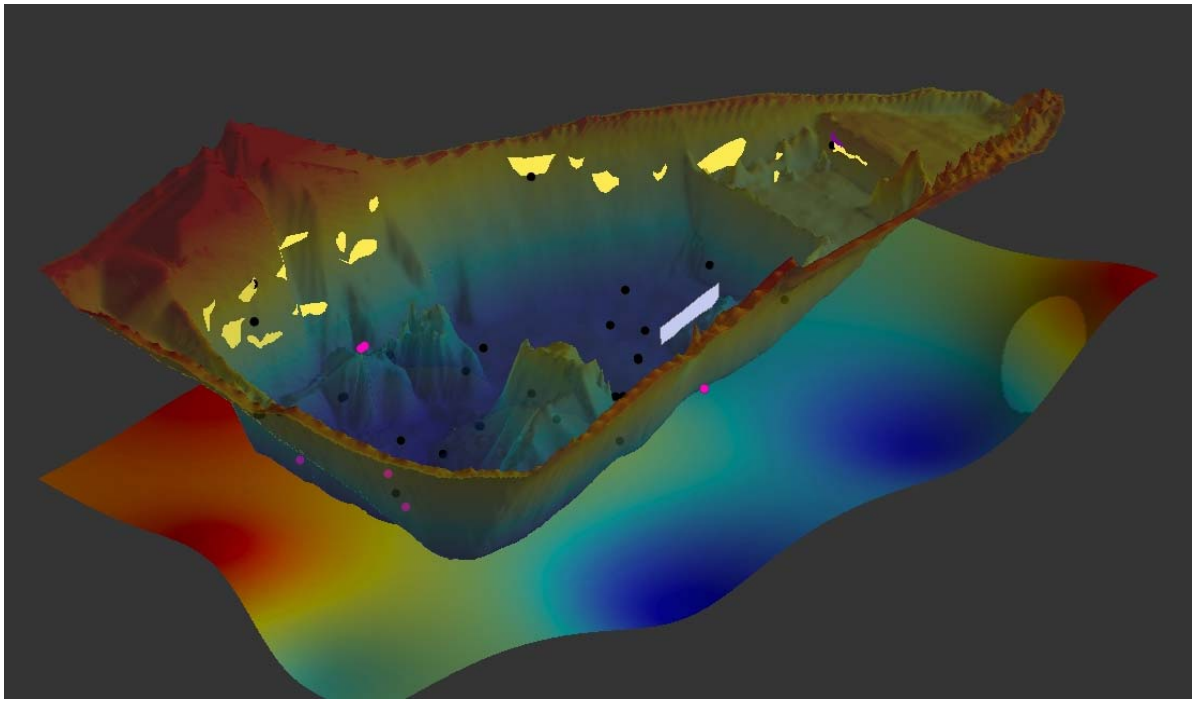

Figure 9.21: Model with OSL sample locations (black), bedrock from bore hole data, location of one of the scanned faces (pale mauve) inserted from scanned grid co-ordinates as an example, palaeosol (bright pink line in HD3) and location of major sand units derived from scan data and photographs. Artefact locations are shown in bright pink. The apparent position of some of the OSL sample locations within mounds of gravel is because some of the mounds are spoil heaps that were dumped in areas previously worked for gravel and sampled during the gravel extraction process. 5 x vertical exaggeration.

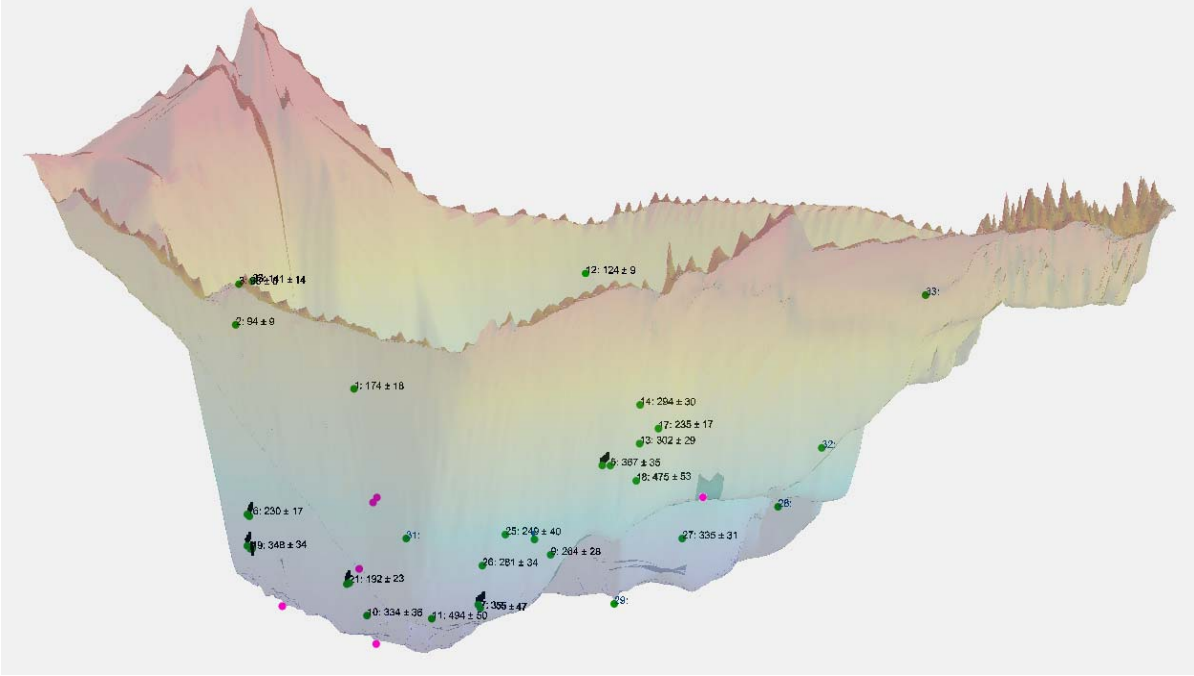

Figure 9.22: Model with OSL sample locations (green), and OSL CHAR numbers, dates and errors inserted individually for each point within ArcScene using 3D text. Pink dots are find locations. 10 x vertical exaggeration.

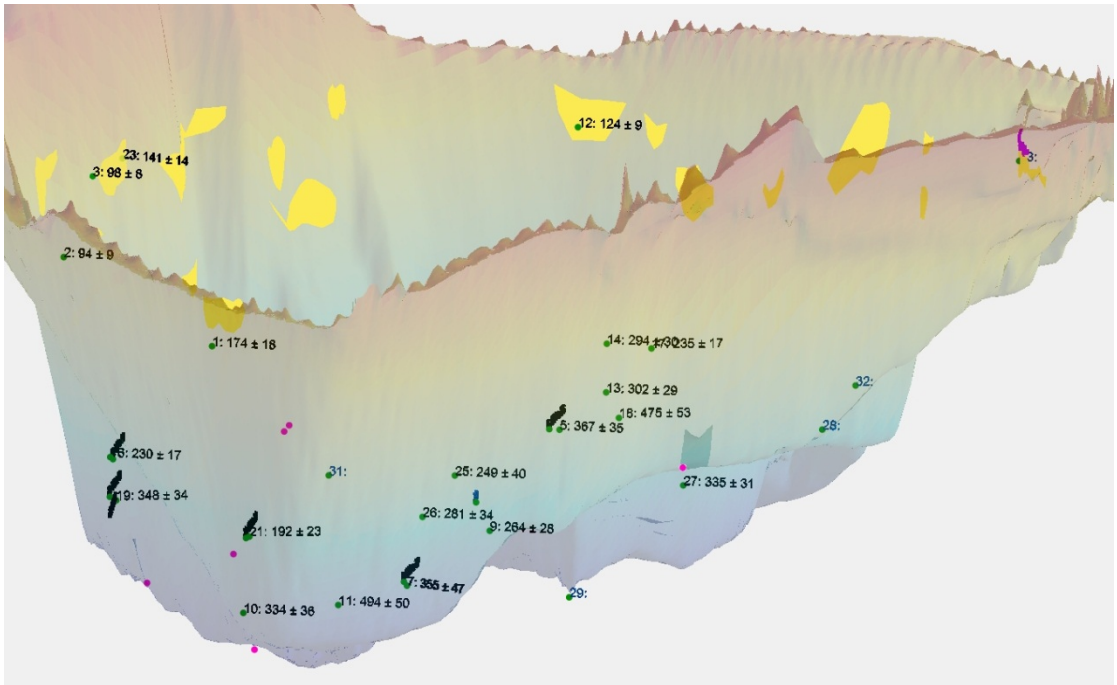

Figure 9.23 Model with OSL sample locations (green), and OSL CHAR numbers, dates and errors inserted individually for each point within ArcScene using 3D text. Pink dots are find locations. 10 x vertical exaggeration. Palaeosol (bright pink line in HD3) and location of major sand units derived from scan data and photographs are also shown. Where no dates are available, just the CHAR number is shown in blue.

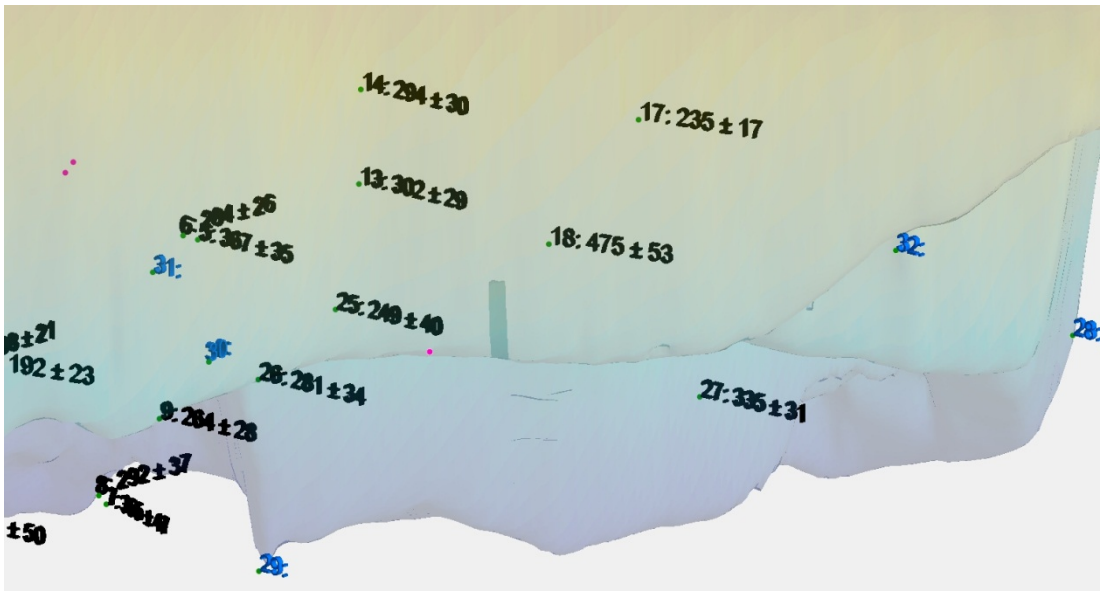

Figure 9.24 Model with OSL sample locations (green), and OSL CHAR numbers, dates and errors inserted individually for each point within ArcScene using 3D text. Pink dots are find locations. 10 x vertical exaggeration. Where no dates are available, just the CHAR number is shown in blue. Where OSL sample locations are close together, dates have to be displayed at different angles, and can be viewed when the scene is rotated. This can highlight dating discrepancies. E.g. CHAR 5 and 6 to the left of the image.

9.3 Implications of 3D Modelling, Stratigraphy and Clast Lithological Studies

It is now possible to combine the results into a lithostratigraphical model of deposition in the Axe valley from the studies described here and additional information from Broom and Kilmington. Both the mapping and IFSAR drape confirm that as mapped by BGS the Axe valley contains only two morphological terraces. The lower terrace is only well preserved at the junction of the River Coly with the River Axe at Colyford but a small area was also mapped at Chard Junction just to the west of the area shown in Figure 7.4. This has not been investigated as part of this project and no archaeology is known from it. The upper 'terrace' unit was mapped by BGS as 'undifferentiated' due to its sloping surface and lack of clear terrace form. At one location, Ash House (just north of Maidenhayne, Nr. Musbury) BGS also recognised an 'alluvial fan: gravel & sand' issuing from a small tributary. This is unusual; and again reflects problems encountered trying to fit the pattern, form and distribution of aggregate deposits in the valley into the normal terrace-type model applicable elsewhere in England. The data presented here and comparisons with work by PRoSWEB to the west (Brown et al. 2009 & 2010) and studies in the Solent system to the east (Wenban-Smith and Hosfield 2001; Briant et al. 2009) allow a tentative resolution to this problem.

The Axe valley is a relatively small and steep (Figure 9.25) headwater tributary of the Exe System draining into the English Channel. Its relative depth is comparable with the valleys to the east and the west at 100-120m. It grades to present sea level and although not investigated probably has a buried valley under its present mouth which is graded to Pleistocene low sea levels. Although the lower course of the valley is fault controlled (Gallois 2006) it is not a graben (or half-graben) and cannot have been a centre of subsidence during the late Pleistocene. However, as the mapping highlights the entire Axe valley is cut into the Upper Greensand (UGS) and from at least Chard Junction

downstream it was excavated through the Greensand strata into the underlying Lias rocks (Charmouth Mudstone). Indeed we believe that this is the only catchment in England to be entirely developed within the bedrock zone where UGS lies unconformably on Lias as to the east the Jurassic appears and thickens and to the west the UGS is entirely removed until the outlier of the Haldon Hills which lie on Permian Breccias (Hamblin 2011). As the boreholes and 3D model show at Chard Junction there is up to 28m of gravel and sands with a locally highly variable stratigraphy dominated by gravel and sand deposition by shallow channels and capped by a diamicton. The local presence of a thick sand body in Hodge Ditch I and running across Hodge Ditch II from east to west and close to the southern edge of the palaeo-floodplain suggests that this is an in-filled channel of the River Axe abandoned by avulsion. It is of critical importance that this feature, and other sand-lenses do not extend across the entire quarry and do not form a cut-and fill unit. This is further supported by the absence of this sand unit at Kilmington and the majority of the exposures at Broom. That the Middle Silts & Sand named the Broom Member Member by Hosfield et al. (2011) seen at the ballast Pit at Broom is likely to be a local channel filling of either the Blackwater tributary or a marginal Axe Channel. The sedimentology indicates abundant local erosion and transport into the valley of the surrounding chert derived from the UGS. This chert is angular or sub-angular (never rounded) and as the majority of the gravels are clast supported locks together forming a sediment body resistant to erosion but with a relatively high hyporheic potential (ability to conduct sub-surface water) and so forming an open aquifer. It is proposed that the result was that after head-ward erosion of the initial valley through

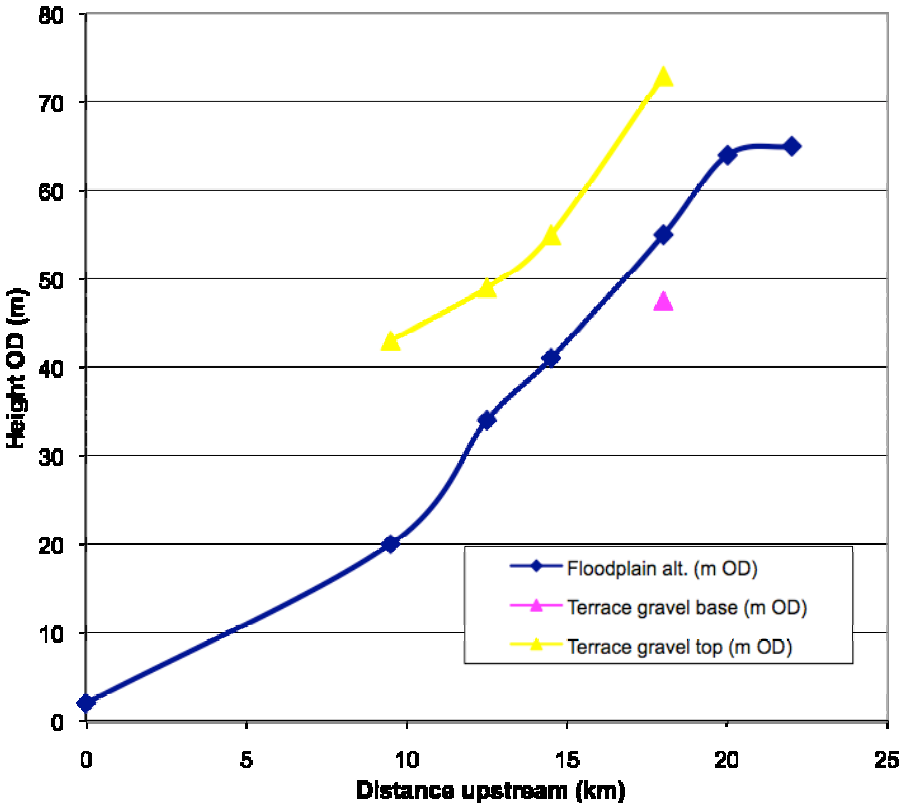

Figure 9.25 Slope of the gravels and the floodplain of the Axe from Chard Junction to the sea. Note the nick-points in the modern m floodplain surface at Axminster (13 km) and at Forde Abbey (20 km)

the clay-with flints into the UGS to the junction of the UGS with the Lias. Subsequently valley widening and periglacial conditions produced large quantities of shattered chert which was deposited in a combination of alluvial fans, shallow sheet-flow and braided

periglacial rivers. This occurred in pulses during cold stages of the Middle to late Pleistocene and they may be associated with the nick-points of the Axe valley floodplain at Axminster and Forde Abbey (Shakesby pers. comm.., Shakesby and Stephens 1984, Figure 9.25).It is postulated that, due to the interlocking nature of the chert clasts (due to their sub-angularity) and high porosity (an aquifer) channel flows did not have high enough shear stresses to incision into their beds. Therefore the channel or channels were not able to cut through the deposits of each cold-cycle sediment pulse with the result that the valley floor continued to aggrade. This process continued producing a vertically aggraded stack of gravels until the last glacial cycle when large areas of the valley floor were covered by lobes of soliflucted gravels. This constrained the valley floor and promoted incision leading to the creation of the terrace and an inset floodplain into which terrace 1 was deposited. The dating strongly suggests that the deposition of this diamicton was in MIS 3 or 2. Why this did not occur in other cold stages is a valid question, and the most probable reason is the extreme nature of the LGM which is believed to be the most extreme cold stage since MIS 12. The special factor in this case is the nature of the UGS. Both BGS mapping and the mapping around Chard reveal that the chert is unevenly distributed through the UGS and that the UGS is decalcified in this area. The BGS (Edwards and Gallois 2004) divide the UGS into three units; at the base the Foxmould Member which is sand, the Whitecliffe Chert Member and the upper Bindon Sandstone Member which is decalcified yellow sand underlying the clay-with-flints which is of early Tertiary age. As the mapping reveals the Bindon Sandstone member once decalcifies acts as a confined aquifer producing strong springs on the valley sides. During periglacial conditions the sand cropping out on the valley sides would have been part of the active layer and become saturated producing high pore-water pressures both above and below the Whitecliffe Chert which is a partial aquiclude. The result would have been collapse and slumping of the valley-sides with fractured chert being carried into the valley floor by debris flows and solifluction creep.

This is a variant of the cascade model recently proposed by Brown et al (2008, 2010) and illustrates the variation in aggregate depositional style that can occur due to local conditions. It is an extreme case but similarities exist with other valleys draining the UGS including the Upper Culm and Tone system, both of which also have poorly differentiated terrace systems and on a smaller scale similar processes may also explain the last-cold cycle stacked terrace within at Doniford (Basell in prep.). This model of aggregate deposition has three important archaeological implications;

a) The valley floor would have remained of low relief and constrained during the Late Pleistocene concentrating human activity into a relatively narrow strip of valley floor.

b) Terraces, as such, would not have existed only upstanding gravel channel edges and bars within the floodplain.

c) Areas of deposition would have had only minimal post-depositional disturbance by channel migration and would have then been buried by gravels during the next cold-pulse of sedimentation.

The last of these implications also implies that the artefacts as well as the gravels are in a time-series from lowest/oldest to highest/youngest and testing this proposition is one of the aims of the cosmogenic isotope analyses.

10 Outreach

Task 9. *This will be undertaken early in the Stage 2 period but the exact dates will be dependent upon Forde Abbey and Bardon Aggregates. Two "Open Days" have been planned and two posters are planned.*

The outreach activities and outputs from Stage II are listed below;

a) IFA: A paper at the IFA on methodological aspects of the study has been offered for the meeting in 2012 as the 2011 meeting (13th-15th April at Reading) is too close to our completion deadline.

Outreach: Outreach activities to date have included;

b) Attendance at the Aggregate Industries open day (on 16th February 2011) the Carter's Close extension and presentation of a poster on the project at this meeting.

c) Presentation at the EH Training Meeting at St Anne's College on16th February, Oxford.

d) Presentation at the Centre for Human Origins Anniversary Conference at the University of Southampton, 27th-29th January 2011.

e) Insertion of references to the project and implications for Palaeolithic archaeology in the region at the South West Archaeological Framework Meeting, Taunton 10th February 2011.

f) Presentation of the results and a visit to Chard Junction Quarry (Hodge Ditch I-III) as part of the Quaternary Research Associations' Annual Fieldmeeting to the Exe valley and Adjoining areas being run by Prof. Brown, Dr Basell and Dr Toms (4th-7th April 2011). This also includes the preparation of a fieldguide with a chapter on Chard Junction Quarry and full acknowledgements to EH throughout. At present there are 50 registered for the fieldmeeting including representatives from BGS, CBA, the Independent sector and several Universities. This has also involved the production of a Fieldguide (Basell et al. 2011) which will be distributed through the Quaternary Research Association.

g) Agreement to present on the project to;

1) Devonshire Association Conference, Axminster 4th June 2011
2) Bath Geological Society, 3rd November 2011

h) Agreement to give an open lecture to tourists and locals at Forde Abbey at a date to be arranged by Forde Abbey.

11 Project design for Phase III

Task 10. *To provide an updated Project Design for Stage 3.*

Stage 3: Extension, Dissemination and Outreach

11.1 Palaeoenvironmental Extension*:* As sediments were discovered in the later stages of the Main Project Stage 2 project palaeoenvironmental work will be undertaken. The nature of the deposits, organic-rich palaeosol dictates the techniques that can be used. This will be pollen, wood/macrofossils, insects, geochemistry and soil micromorphology. The sediments will be compared with beds of finer sand and silt which are more common at both Broom and Kilmington and which have yielded pollen in the past (work at Broom by R. Scaife, and at Kilmington by James Scourse back in the 1970s). The newly exposed sediments at Hodge Ditch III will be analysed with the use of large volume sampling (1 Kg) for microfossil analysis (pollen and spores) in order to increase the concentration to countable levels. As a trained palynologist I am aware that we long-ago gave up trying to date Pleistocene sites using pollen analysis, however, the changes in the UK flora from the early to and mid to late Pleistocene are large enough to allow us to use it to provide confirming (or consistent) data with the OSL dates, or not. Additionally the assessment already performed clearly indicates that the sediment were deposited in an interglacial rather than an interstadial.

A full methods statement will be produced for all palaeoenvironmental as suitable sediments have been revealed. In addition in this stage a seminar will be held jointly with the excavators of other sites in the area (e.g. Rob Hosfield) to try and draw together the methodological findings from the Main Project, implications for the Axe Valley and the regional picture for the Blackdown Hills. This stage will also include a final assessment and analysis, collation, dissemination and review of the contribution of Chard Junction Quarry to the British Palaeolithic. More detail on this stage will be given in the Main Stage project design.

11.2 Dissemination: At this stage copies of the project archive will be placed with both local authorities and the ADS. We would also give a paper at a suitable archaeological conference on the project (such as the IFA).

11.3 Outreach - Methodological Feedback to Industry: This will be undertaken through the workshop that has been planned for Stage 3, although the data upon which it will be based will be included in the report on Stage 2. The purpose will be to provide feedback to the industry on the resultant improved information base and the benefits that this will provide in Minerals Planning and fieldwork methodologies. Support for the workshop will be sought from both the Quarry Products Association (QPR) and the Minerals Industry Research Organisation (MIRO).

11.4 Status of Disused Quarries in the Axe Valley: We will undertake a review of the status of other disused quarries in the area to determine their archaeological potential, inform county archaeologists of that potential so as to inform PPG16 considerations. There are a number of sites, generally small, but which were into the “100 ft” terrace as it was known which have produced bifaces. These will be visited and where possible the stratigraphy recorded and a report produced on their archaeological potential. These sites are under threat and so this information will be valuable to the planning authorities in all

three counties. This aspect has been discussed with Steve Wallis of Dorset County Council and Bob Croft of Somerset County Council.

11.5 Budget

For a breakdown of the budget see Appendix F. But the total cost of the Stage 3 extension is £26,950

12 Concluding Comments

This project has advanced methodologies applicable to the study of Pleistocene aggregate sites with the aim of maximising their heritage potential. Sites such as Chard Junction are difficult to handle from an assessment and curatorial angle, however, they have some of the oldest remains of human occupation of the British Isles and are thus of crucial importance in NW European archaeology.

The work has shown how Gamma cps records can be of value in the pre-excavation assessment of the stratigraphy of such sites and guidance is given on both the theory underlying the technique and practical aspects of interpretation. The use of digital photography for the grain-size characterisation of gravels has been evaluated and found to produce a reliable relative proxy for true grain size variations which makes it a cost effective method for archaeologists. The use of easily constructed and cheap frames is recommended in order to allow easy demarcation of a suitable area of quarry face for analysis. With the increasing quality of digital cameras at a reasonable cost this technique may become even more applicable and could in future be used to map variations in sedimentology across working faces. The ground laser scanning of working faces was found to be both practical and of archaeological value. Its practicality lies in no, or minimal, disruption to quarrying activities and its archaeological value lies in the real-space location of quarry faces thus replacing far more time consuming total station or differential GPS survey. Stratigraphy is also visible from quarry face scans both through the variations in the DEM and through the relative intensity values. Intensity of laser return is a complex variable and appears at this site to be related to both grain size (sand vs gravel) and iron staining. This may partly be through variations in water-content and this aspect of scanning requires more research. Using the micro-topographic information provided by very high resolution scanning (2mm) of panels and frames and spatial analysis of the sampled point cloud it has been shown that roughness can be used as a proxy for variations in sedimentology. Practical recommendations are made for the set up of such surveys including the target framework, scan ranges, locations and the need for multiple scans of single faces in order to reduce internal shadow. There is little doubt that as the cost of laser scanners falls in relative terms the technique will become increasingly used due not to its visualisation of sites, but far more because of its high-resolution multiple-survey capability.

The project simultaneously applied a number of established techniques to the site as part of its monitoring. Clast lithological analysis was undertaken on both a bulk and size-fraction basis. It highlighted potential erratics and clasts which had clearly had a different geomorphological/geological history. Whilst the bulk of the clasts and matrix at Hodge Ditch I-III is of local origin from the Upper Greensand cherts and the plateau clay-with-flint, there are indications of other sources. These include sarsens and very rounded and weathered flints from probable Tertiary weathering surfaces on the Blackdown Hills and Palaeozoic pebbles probably derived from the Triassic pebble beds to the west. Samples have been taken for cosmogenic isotope analysis and discussions are presently underway with the Cosmogenic Isotope Analytical Facility at East Kilbride over this aspect of the project. OSL sampling and dating of the site has been continued with a further 15 dates sampled and 33 results currently available from Hodge Ditch II & III. The results show that we have a vertically accreted sediment body from at least MIS 8/7 but probably up to the late Pleistocene. Taking into consideration the full depth of gravels, (see Figure 9.19) and the age depth modelling and the full suite of dates (Appendix D) this suggests the initiation of gravel accumulation was between 600 and 400 ka BP and probably during MIS10, raising the distinct possibility that the erosion of the valley floor and initiation of this

sedimentary sequence was associated with MIS12. However, two older outlier dates do raise the possibility that the initiation could be MIS14-13.

In addition to development of the intrinsic-reliability testing approach an inter-laboratory comparison has also been undertaken. On 3rd August 2010 Toms, Duller and Schwenninger all sampled the same sediments from two levels in Hodge Ditch I. All efforts were made to both standardise the methodology each laboratory employed and also to assess the causes of variance in the analytical steps of the procedures. This process has highlighted areas that will be important in future applications of Luminescence dating.

The continued monitoring of the site has yielded three further lithics and further sedimentological information. Late-on in the process organic sediments were discovered in Hodge Ditch III and preliminary assessment suggests they are the disturbed remains of a Late Pleistocene interglacial alluvial soil. This work will be continued subsequent to funding under the Palaeoenvironmental Provision of Stage 3. Consideration of 3D modelling techniques given the depth and lack of internal stratigraphy of the site lead the authors to develop a laser scanning-based 3D model of both Hodge Ditch II & III. This has the great advantage that it; stores any finds and dating data in true co-ordinates, stores all the scanned face data, provides a complete digital survey of the quarry and can be updated over time. This is clearly an area that requires further research but as this study shows it has the potential to unify both survey and many aspects of recording into a semi-permanent 3D model compatible with other data storage approaches and particular GIS.

13 References

Anthony, D. M. & Granger, D. E. 2004. A late Tertiary origin for multi-level caves along the western escarpment of the Cumberland Plateau, Tennessee and Kentucky using ^{26}AL and ^{10}Be. *Journal of Cave and Karst Studies* 66, 46-55.

Ayers, H. 2011. GNSS (GPS and GLONASS) Positioning used in Land Surveying and Engineering. Presented at the Joint AMLS/APEGM Professional Development Seminar on GPS Best Practices Workshop Winnipeg, Manitoba, Canada, January 18th 2011. Published online by Leica Geosystems Ltd. Downloaded from
http://www.apegm.mb.ca/pdf/PD_Papers/GNSSPositioning.pdf
Accessed March 2011.

Balco, G., Stone, J.O., Nathaniel A. Lifton, N. A., Dunai, T. J. 2008. A complete and easily accessible means of calculating surface exposure ages or erosion rates from 10Be and 26Al measurements. *Quaternary Geochronology* 3, 174–195

Ballantyne C.K. 2010. Extent and deglacial chronology of the last British-Irish Ice Sheet: implications of exposure dating using cosmogenic isotopes. *Journal of Quaternary Science*, 25, 515-534.

Ballantyne C.K, Schnabel C and Xu S. 2009. Readvance of the last British-Irish Ice Sheet during Greenland Interstade 1 (GI-1): the Wester Ross Readvance, NW Scotland. *Quaternary Science Reviews*, 28, 783-789.

Basell, L. S., Brown, A. G. and Toms, P. S. 2011. *The Quaternary of the Exe valley and Adjoining Areas. Field Guide*. Quaternary Research Association, London 163p.

McCarroll D, Stone J.O, Ballantyne C.K, Scourse J.D, Fifield LK, Evans D.J.A and Hiemstra J.F 2010. Exposure age constraints on the extent, timing and rate of retreat of the last Irish Sea ice stream. *Quaternary Science Reviews*, 29, 1844-1852.

Barrash, W. & Morin, R. H. 1997 Recognition of units in coarse, unconsolidated braided-stream deposits from geophysical log data with principal components analysis. *Geology* 25, 687-690

Bennett, J. A. 2005 *Late Pleistocene and Holocene fluvial geomorphology of te river Exe, Devon, UK.* Unpub. Phd Thesis University of Exeter.

Blott, S. J. and Pye, K. 2001 GRADISTAT: A grain size distribution and statistics package for the analysis of unconsolidated sediments. *Earth Surface Processes and Landforms Earth Surf. Process. Landforms* 26, 1237–1248

Briant, R. M., bates, M. R., Hosfield, R. T. and Wenban-Smith, F. F. 2009 *The Quaternary of the Solent Basin and West Sussex Raised Beaches Field Guide.* Quaternary Research Association, London.

Brown, A. G. 1997. *Alluvial Environments: Geoarchaeology and Environmental Change*. Cambridge University Press, Cambridge.

Brown, A. G. 2010. The geomorphology and environment of the Hemington reach. In L. Cooper and S. Ripper (Eds.) *The Hemington Bridges; The excavation of three medieval bridges at Hemington Quarry, Castle Donington, Leicestershire*. University of Leicester Archaeological Services, Leicester, 142-173.

Brown, A. G. In Press. Dating Surfaces and Sediments. In K. J. Gregory, A. Goudie and B. Gomez (Eds.) *Handbook of Geomorphology*, Oxford University Press.

Brown, A.G. and Basell, L.S. 2008. New Lower Palaeolithic Finds from the Axe Valley, Dorset. *PAST*, 60, 1-4.

Brown, A. G.,.Basell, L.S, Toms, P.S., Bennett, J., Hosfield, R.T. and Scrivener, R.C. 2010. Late Pleistocene Evolution of the Exe Valley. A Chronostratigraphic Model of Terrace Formation and its Implications for Palaeolithic Archaeology. *Quaternary Science Reviews* 29, 897-912.

Brown, A. G., Carey. C., Erkens, G., Fuchs, M., Hoffman, T., Macaire, J-J., Moldenhauer, K-M. and D. E. Walling. 2009. From Sedimentary Records to Sediment Budgets: Multiple Approaches to Catchment Sediment Flux. *Geomorphology* 108, 35-47.

Buckley, S. J., Howell, J. A., Enge, H. D. and Kurz, T. H. 2008. Terrestrial; laser scanning in geology: data acquisition, processing and accuracy. *Journal of the Geological Society of London 165, 625-638.*

Butler, J. B., S. N. Lane, and J. H. Chandler. 2001. Automated extraction of grain-size data from gravel surfaces using digital image processing. *Journal of Hydraulic Research* 39, 519-529.

Canti, M. 2007 *Geoarchaeology: using earth sciences to understand the archaeological record*. English Heritage, London.

Cripps, A. C. and McCann, D. M. 2000 The use of the natural gamma log in engineering geological investigations. *Engineering Geology* 55, 313-324.

Dehnert, A., Akcar, N., Kemna, H.A., Kubik, P., Preusser, F. & Schlüchter, C. 2006. Burial dating of fluvial sediments from the Lower Rhine Embayment, Germany. *Terra Nostra* 2006, 2, 87.

Edwards, R. A. and Freshney, E. C. 1982 The Tertiary sedimentary rock. In Durrance, E. M. and Lamming, D. J. C. (Eds.) *The Geology of Devon*, Exeter University Press, Exeter, 204-237

Edwards, R.A. and Gallois, R. W. 2004. *A brief description of the geology of the Sidmouth district.* British Geological Survey Sheet Explanation. Sheets 326/340 (England and Wales)

Ellis, D.V., 1987. *Well logging for earth scientists.* Elsevier, Amsterdam.

English Heritage 2006. *Advice and guidance to users on laser scanning in archaeology and architecture.*

Ferrari, S., Piuri, V. and Scotti, F. 2008. Image processing for granulometry ana;ysis via neural networks. *Institute of EEE, International Conference on Intelligence for Measuring Systems and Applications*, 1-5.

Franciskovic ´ -Bilinski, S., Bilinski, H., Neda Vdovic´ N., Balagurunathan, Y., Edward R. Dougherty, E. R. 2003. Application of image-based granulometry to siliceous and calcareous estuarine and marine sediments. *Estuarine, Coastal and Shelf Science* 58, 227–239.

Gardiner, V. and Dackombe, R. 1983. *Geomorphological Field Manual.* George Allen & Unwin, London.

Geological Society Engineering Working Party 1972 The preparation of maps and plans in terms of engineering geology. Quarterly. *Journal of Engineering Geology* 5, 295-382.

Goldberg, P. and Macphail, R. I. 2006. *Practical and Theoretical Geoarchaeology.* Blackwell Publishing, Oxford.

Graham, D. J., Reid, I. and Rice, S. P. 2005a. Automated Sizing of Coarse-Grained Sediments: Image-Processing Procedures. *Mathematical Geology, 37, 1-28.*

Graham, D. J., Rice, S. P. and Reid, I. 2005b A transferable method for the automated grain sizing of river gravels. *Water Resources Research* 41, 1-12.

Granger, D. E. and Muziker, P. F. 2001. Dating sediment burial with cosmogenic nuclides: Theory, techniques and limitations. *Earth and Planetary Science Letters* 188, 269-281.

Hamblin, R. 2011. The Haldon Hills gravels. In L. S. Basell, A. G. Brown and P. S. Toms (Eds.) *The Quaternary of the Exe Valley and Adjoining Areas: Field Guide*, Quaternary Research Association, London, 47-66.

Hosfield, R.T., Green, C. P., Toms, P. S., Scourse, J., Scaife, R. and Chambers, J. C. 2011. The Middle Pleistocene deposits and archaeology at Broom. In L. S. Basell, A. G. Brown and P. S. Toms (Eds.) *The Quaternary of the Exe Valley and Adjoining Areas: Field Guide*, Quaternary Research Association, London, 103-127.

Isaac, K. P. 1979 Tertiary silcretes of the Sidmouth area, east Devon. *Proceedings of the Ussher Society* 4, 341-354.

Millane R.P., Weir, M.I. and Smart, G.M. 2006. Automated Analysis of Imbrication and Flow Direction in Alluvial Sediments Using Laser-Scan Data. *Journal of Sedimentary Research* 76, 1049-1055.

Moore, P.D., Webb, J.A., Collinson, M.E. 1991. *Pollen Analysis* (2nd ed) Blackwells, Oxford.

Murray, A.S. and Wintle, A.G. 2000. Luminescence dating of quartz using an improved single-aliquot regenerative-dose protocol. *Radiation Measurements*, 32, 57-73.

Murray, A.S. and Wintle, A.G. 2003. The single aliquot regenerative dose protocol: potential for improvements in reliability. *Radiation Measurements*, 37, 377-381.

Pain CF, 2008 *Field Guide for Describing Regolith and Landforms.* CRC LEME c/o CSIRO Exploration and Mining, Bentley, Western Australia.

Rolfe, C.J., Hughes, P.D., Fenton C.R., Xu, S. and Brown, A.G. In Prep. New evidence for the maximum extent and timing of glaciation in NW Europe during the last glacial cycle.

Schlumberger. 1974 *Log Interpretation Manual/Application. Vol. II.* Houston, Schlumberger Well Services Inc.

Scrivner R. C. Basell, L. S. Brown A. G. 2011 Terrace gravels and sarcens on the Exe-Creedy Interfluve. In L. S. Basell, A. G. Brown and P. S. Toms (Eds.) *The Quaternary of the Exe Basin and Adjoining Areas*, Quaternary Research Association, London.

Shakesby, R. A. and Stephens, N. 1984. The Pleistocene gravels of the Axe valley, Devon. *Report of the Transactions of the Devon Association for the Advancement of Science* 116, 77-88.

Slatt, R. M., Jordan, D. W., D'Agostino, A. E. & Gillespie, R. H. 1992 Outcrop gamma-ray logging to improve understanding of subsurface well log correlations. *Geological Society, London, Special Publications* 65, 3-19.

Smith, A. J. E. 2004. *The Moss Flora of Britain and Ireland. Second Edition*. Cambridge University Press, Cambridge.

Strom, K. B., Kuhns, R. D. & Lucas, H. J. 2010. Comparison of automated image-based grain sizing to standard pebble-counting. *Journal of Hydraulic Engineering* 136, 461-474.

Toms, P.S., Hosfield, R.T., Chambers, J.C., Green, C.P. and Marshall, P. 2005. *Optical dating of the Broom Palaeolithic sites, Devon and Dorset.* English Heritage Centre for Archaeology Report 16/2005.

Turner, C. 2011. Honiton By-pass Hippopotamus site. In L. S. Basell, A. G. Brown and P. S. Toms (Eds.) *The Quaternary of the Exe Valley and Adjoining Areas: Field Guide*, Quaternary Research Association, London,133-138.

Wenban-Smith, F. F. and Hosfield, R. T. (Eds.) 2001. *Palaeolithic Archaeology of the Solent River*. Lithic Studies Occasional paper 7, Lithic Studies, London.

Whitman, M. S., E. H. Moran, and Ourso, R. T. 2003. Photographic techniques for characterizing streambed particle sizes. *Transactions of the American Fisheries Society* 132, 605-610.

Wolkowinsky, A. J. and Granger, D. E. 2004. early Pleistocene incision of the San Juan River Utah dated with ^{36}AL and ^{10}Be. *Geology* 32, 749-752.

APPENDICES

Appendix A. Guidesheets

The interpretation of Gamma cps Data for Archaeological Assessment & Evaluation

This guidesheet is to assist any in the archaeology and/or planning fields who need to assess or evaluate sites using data supplied by industry. Gamma cps (gamma radiation in counts per second) is recorded by a gamma detector that is lowered down the borehole at incremental depths. It has for some time now been a standard procedure in the drilling industry and site-investigations industry and is commonly supplied with or alongside driller's log sheets (as supplied by commercial drilling companies). For further information on the technique see Brown et al. (2011). Below is a short set of notes that can be used to interpret the Gcps data;

1. The data is relative normally on a scale of 0-50 or 0-75 so look to see if there are any significant variations through the deposit of interest (such as the gravels) and into the underlying bedrock. If there is not then the data will be of little value. However, if there is:

2. You need to establish the end-members of the Gcps data that you have. In most cases this will be the bedrock and either pure sand or pure gravels and the bedrock. Typical value ranges are given in Table 1 *but it must be remembered that the data from the drillers log will be relative and adjusted to maximum variation*.

3. Assess how a mixture between these end-members could have caused the variation in the Gcps data.

4. Use variations in the Gcps trace to identify additional boundaries in the borehole stratigraphy and provide a short likely explanation (e.g. Unit 2b is a mixture of low Gcps flint gravel with high Gcps matrix derived from the underlying Mercia Mudstone).

5. Use these additional boundaries along with other stratigraphic information to identify likely and unlikely archaeology-bearing sediments (e.g. Unit 1 is a debris flow or diamicton and not likely to contain valuable archaeology, whereas unit 2a is a clean fluvial gravel which could contain lithics and unit 3 is a palaeosol which could contain in-situ artefacts and might warrant particular archaeological attention).

Rock/sediment type	Typical Gcps values	Comments
sand & sandstones	low (0-1/15)	depending upon the non-quartz component
clay (lake or marine)	high (30-70)	will vary depending upon the clay mineralogy
mixed gravels	mod (20-35)	depending upon the source of the clasts and the matrix
diamicton & debris flows	mod to high (20-60)	depending upon the source of the matrix and the ratio of quartz to clay
chert or flint	low to very low	increased by presence of non-quartz minerals and matrix
Palaeosol or landsurface	elevated above surrounding values	elevation can be caused by weathering but highly lithology dependent
metamorphic & igneous rocks	mod to high (20-60)	dependent upon the chemistry (acidic-basic) and the degree of alteration

Table 1 Typical value ranges of Gcps for common lithologies

References

Brown, A. G., Basell, L. S. & Toms, P. 2011. *Monitoring and modelling of the Palaeolithic resource at Chard Junction Quarry, Hodge Ditch Phases II & III. Assessment Stage II.* PNUM 5695, Historic Environment & Enabling Project, Prepared for English Heritage, Palaeoenvironmental Laboratory University of Southampton (PLUS).

Ellis, D.V., 1987. *Well logging for earth scientists.* Elsevier, Amsterdam.

The Use of Digital Granulometry for Archaeological Assessment & Evaluation

This guidesheet describes the method of measuring grain size using digital photographs and the Sedimetrics© software system. Users are referred to both on-line and support instructions and the papers by Graham et al. 2005a (see below) and the evaluation contained in Brown et al. 2011.

Requirements
a) As high quality digital camera as possible (10+ MPX)
b) A computer capable of running Sedimetrics© software
c) The Sedimetrics© software currently £500
c) Some means of demarcating the sampling dimensions of known area (e.g. a frame or tags)

The Sampling Area
a) There must be four markers in each image in the corner of a rectangle of known dimensions. A shape ratio of 4:3 is usual.
b) The sampling area must be small enough so that the diameter of the smallest grain of interest (i.e. smallest measurable grain) is 23 pixels in the image.
c) The area must be marked by four corner control markers with distances apart measured as accurately as possible. A frame can be used or clasts marked with high-contrast spots (e.g. using Tipp-ex).

Photography
a) Nothing other than the control markers should appear in the image.
b) All grains that intersect the boundary of the sampling area should be completely within the image – so the image must be bigger than the sampling area. Alternatively the sampling area must be reduced in size within the image.
c) Do not use a wide angle lens and adjust distance from the frame rather than using the zoom.
d) Shade the sampling area from direct sunlight
e) Set flash to on and if possible use a camera-mounted external flash to increase the overhead light intensity.
f) Try and ensure even illumination and try and take the photograph at 90 degrees from the face
g) Set the camera to maximum pixel resolution and store the images as JPEGs with no compression.

Processing
a) After downloading do not modify the JPEGs at all.
b) Run the Sedimetrics© software and follow the instructions in order to load the JPEGs.

References
Brown, A. G., Basell, L. S. & Toms, P. 2011. *Monitoring and modelling of the Palaeolithic resource at Chard Junction Quarry, Hodge Ditch Phases II & III. Assessment Stage II.* PNUM 5695, Historic Environment & Enabling Project, Prepared for English Heritage, Palaeoenvironmental Laboratory University of Southampton (PLUS).

Graham, D. J., Reid, I. and Rice, S. P. 2005a. Automated Sizing of Coarse-Grained Sediments: Image-Processing Procedures. *Mathematical Geology, 37, 1-28.*

Sedimetrics software Available from: University of Loughborough, UK

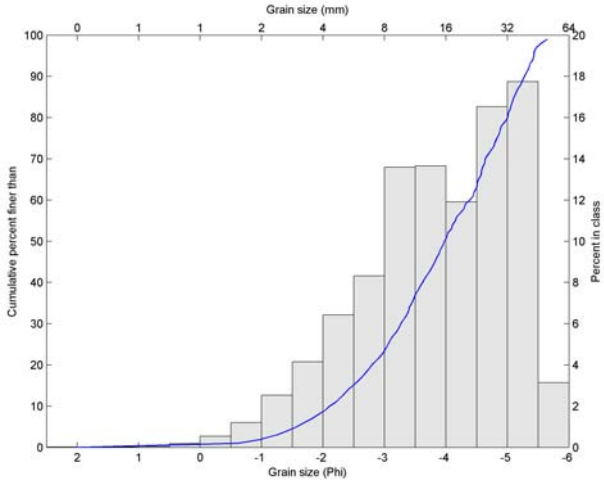

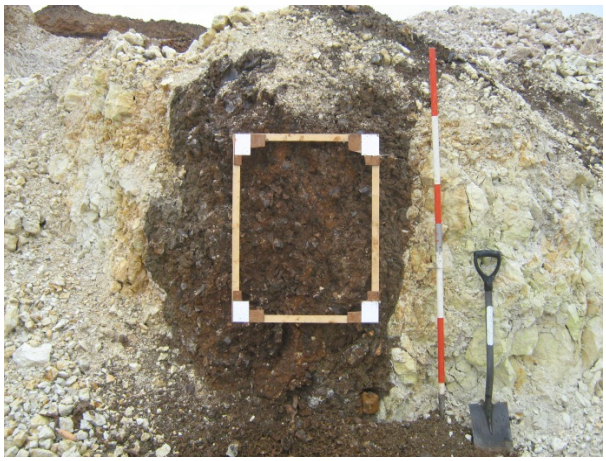

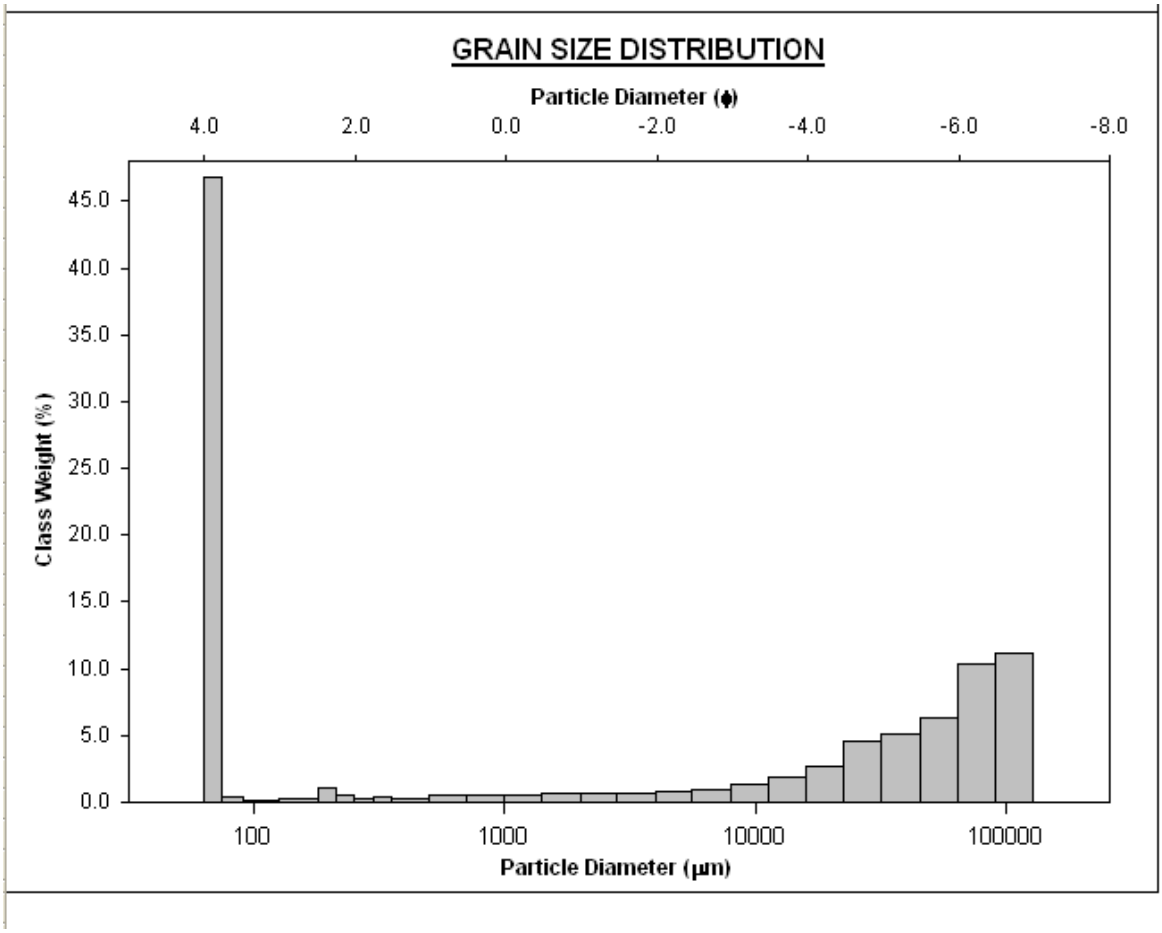

Lower red-brown clay-with-flints. Sedimetrics (above) and sieve results (below). Note how the Sedimetrics can only resolve the coarser (over 63 micron) fraction in this case (as represented by the bar at 63 microns in the sieve results).

Sedimetrics results from Black Hill

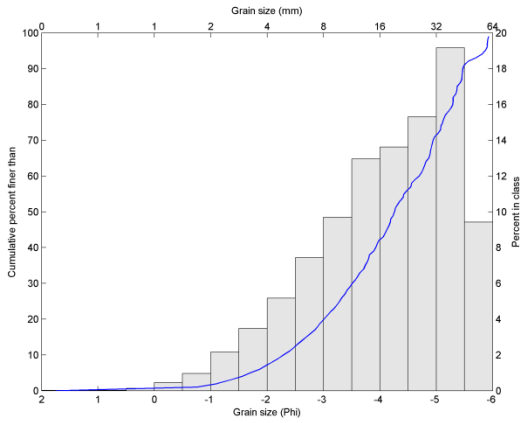

BH1

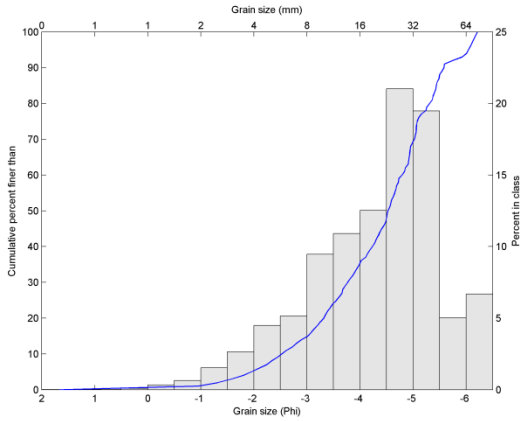

BH2

Sedimetrics results from Clifton (on Severn)

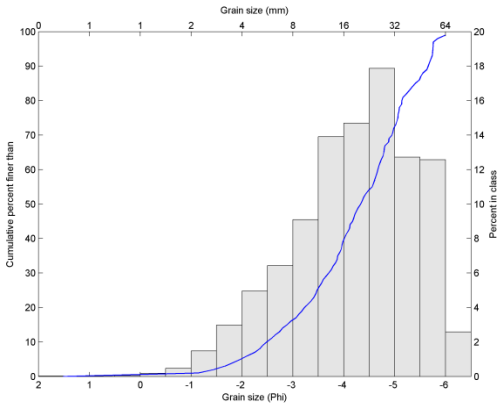

Clifton Gravels

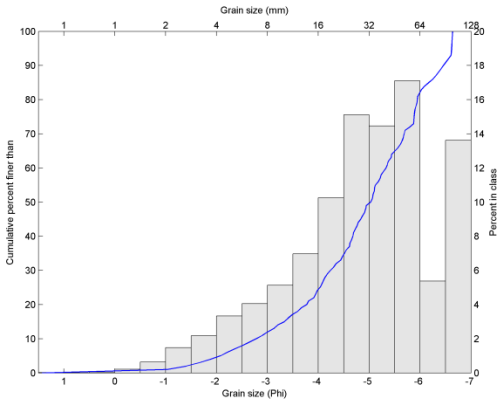

Clifton sand with gravel

Sedimetrics results from Frampton-on-Severn

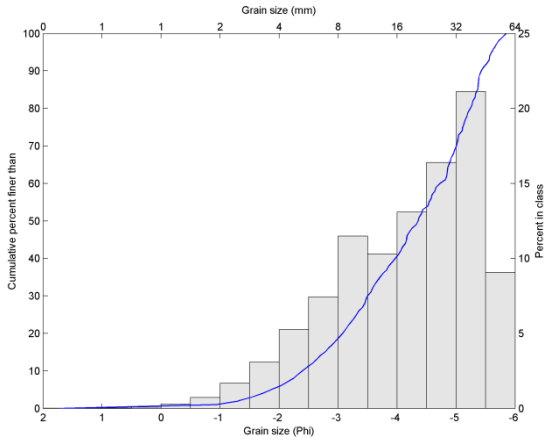

Gravels above OSL sampling location

Appendix C Clast Lithological Data

1A 22-7-10		Chert		Flint		Quartz/Quartzite		Total
phi	mm/µm	g	%	g	%	g	%	g
-7	128	0.00	0.00	0.00	0.00	0.00	0.00	-
-6.5	90.5	0.00	0.00	0.00	0.00	0.00	0.00	-
-6	64	924.84	100.00	0.00	0.00	0.00	0.00	924.84
-5.5	45	3747.45	93.48	261.31	6.52	0.00	0.00	4008.76
-5	31.5	1323.15	82.18	286.98	17.82	0.00	0.00	1610.13
-4.5	22.4	1001.99	57.59	682.36	39.22	55.66	3.20	1740.01
-4	16	666.45	52.73	505.40	39.98	92.13	7.29	1263.98
-3.5	11.2	587.45	51.73	461.06	40.60	87.02	7.66	1135.53
-3	8	600.01	59.93	295.86	29.55	105.36	10.52	1001.23
-2.5	5.6	402.34	52.86	271.52	35.67	87.32	11.47	761.18
-2	4	-	-	-	-	-	-	594.86
-1.5	2.8	-	-	-	-	-	-	588.71
-1	2	-	-	-	-	-	-	537.01
-0.5	1.4	-	-	-	-	-	-	577.28
0	1	-	-	-	-	-	-	604.3
0.5	710	-	-	-	-	-	-	459.56
1	500	-	-	-	-	-	-	256.18
1.5	355	-	-	-	-	-	-	-
1.75	300	-	-	-	-	-	-	-
2	250	-	-	-	-	-	-	-
2.25	212	-	-	-	-	-	-	-
2.5	180	-	-	-	-	-	-	-
3	125	-	-	-	-	-	-	-
3.5	90	-	-	-	-	-	-	-
3.735	75	-	-	-	-	-	-	-
4	63	-	-	-	-	-	-	-
	0							274.65
		9253.68		**2764.49**		**427.49**		**16338.21**

1B 22-7-10		Chert		Flint		Quartz/Quartzite		Total
phi	mm/µm	g	%	g	%	g	%	g
-7	128	0.00	0.00	0.00	0.00	0.00	0.00	-
-6.5	90.5	0.00	0.00	0.00	0.00	0.00	0.00	-
-6	64	2362.07	100.00	0.00	0.00	0.00	0.00	2362.07
-5.5	45	2110.34	70.38	888.26	29.62	0.00	0.00	2998.6
-5	31.5	1013.45	59.30	695.49	40.70	0.00	0.00	1708.94
-4.5	22.4	832.87	47.15	877.78	49.70	55.66	3.15	1766.31
-4	16	807.51	56.30	534.77	37.28	92.13	6.42	1434.41
-3.5	11.2	596.76	65.18	231.75	25.31	87.02	9.50	915.53
-3	8	376.42	56.83	180.56	27.26	105.36	15.91	662.34
-2.5	5.6	287.90	54.46	153.45	29.03	87.32	16.52	528.67
-2	4	-	-	-	-	-	-	447.26
-1.5	2.8	-	-	-	-	-	-	377.46
-1	2	-	-	-	-	-	-	443.08
-0.5	1.4	-	-	-	-	-	-	579.79
0	1	-	-	-	-	-	-	385.06
0.5	710	-	-	-	-	-	-	595.56
1	500	-	-	-	-	-	-	582.41
1.5	355	-	-	-	-	-	-	380.12
1.75	300	-	-	-	-	-	-	91.51
2	250	-	-	-	-	-	-	-
2.25	212	-	-	-	-	-	-	-
2.5	180	-	-	-	-	-	-	-
3	125	-	-	-	-	-	-	-
3.5	90	-	-	-	-	-	-	-
3.735	75	-	-	-	-	-	-	-
4	63	-	-	-	-	-	-	-
	0							112.11
		8387.32		**3562.06**		**427.49**		**16371.23**

3A 22-7-10		Chert		Flint		Sandstone		Quartz/Quartzite		Total
phi	mm/µm	g	%	g	%	g	%	g	%	g
-7	128	-	-	-	-	-	-	-	-	-
-6.5	90.5	923.14	100.00	0.00	0.00	0.00	0.00	0.00	0.00	923.14
-6	64	1369.21	76.82	413.15	23.18	0.00	0.00	0.00	0.00	1782.36
-5.5	45	997.88	67.76	474.73	32.24	0.00	0.00	0.00	0.00	1472.61
-5	31.5	748.05	68.63	341.88	31.37	0.00	0.00	0.00	0.00	1089.93
-4.5	22.4	543.65	49.12	491.54	44.41	0.00	0.00	71.53	6.46	1106.72
-4	16	341.34	43.32	266.20	33.78	145.61	18.48	34.83	4.42	787.98
-3.5	11.2	245.09	41.19	222.71	37.43	56.76	9.54	70.45	11.84	595.01
-3	8	267.87	47.80	222.29	39.67	28.45	5.08	41.80	7.46	560.41
-2.5	5.6	198.31	48.00	151.78	36.73	23.21	5.62	39.88	9.65	413.18
-2	4	-	-	-	-	-	-	-	-	284.82
-1.5	2.8	-	-	-	-	-	-	-	-	337.50
-1	2	-	-	-	-	-	-	-	-	307.37
-0.5	1.4	-	-	-	-	-	-	-	-	314.58
0	1	-	-	-	-	-	-	-	-	499.30
0.5	710	-	-	-	-	-	-	-	-	560.66
1	500	-	-	-	-	-	-	-	-	489.69
1.5	355	-	-	-	-	-	-	-	-	252.53
1.75	300	-	-	-	-	-	-	-	-	147.22
2	250	-	-	-	-	-	-	-	-	128.41
2.25	212	-	-	-	-	-	-	-	-	71.01
2.5	180	-	-	-	-	-	-	-	-	145.08
3	125	-	-	-	-	-	-	-	-	195.81
3.5	90	-	-	-	-	-	-	-	-	-
3.735	75	-	-	-	-	-	-	-	-	-
4	63	-	-	-	-	-	-	-	-	-
	0									111.38
		5634.54		**2584.28**		**532.84**		**258.49**		**12576.70**

3B 3-8-10		Chert		Flint		Quartz/Quartzite		Total
phi	mm/µm	g	%	g	%	g	%	g
-7	128	0.00	0.00	0.00	0.00	0.00	0.00	-
-6.5	90.5							
-6	64	2188.99	100.00	0.00	0.00	0.00	0.00	2188.99
-5.5	45	3106.05	100.00	0.00	0.00	0.00	0.00	3106.05
-5	31.5	1986.54	81.34	455.70	18.66	88.20	3.61	2442.24
-4.5	22.4	1675.11	74.20	531.55	23.54	50.95	2.26	2257.61
-4	16	1345.78	68.45	540.24	27.48	79.99	4.07	1966.01
-3.5	11.2	808.65	62.19	428.46	32.95	63.08	4.85	1300.19
-3	8	628.33	59.53	303.17	28.72	123.95	11.74	1055.45
-2.5	5.6	451.43	64.17	190.48	27.08	61.60	8.76	703.51
-2	4	-	-	-	-	-	-	468.04
-1.5	2.8	-	-	-	-	-	-	451.86
-1	2	-	-	-	-	-	-	438.92
-0.5	1.4	-	-	-	-	-	-	503.25
0	1	-	-	-	-	-	-	657.01
0.5	710	-	-	-	-	-	-	470.02
1	500	-	-	-	-	-	-	296.59
1.5	355	-	-	-	-	-	-	108.01
1.75	300	-	-	-	-	-	-	84.13
2	250	-	-	-	-	-	-	-
2.25	212	-	-	-	-	-	-	-
2.5	180	-	-	-	-	-	-	-
3	125	-	-	-	-	-	-	-
3.5	90	-	-	-	-	-	-	-
3.735	75	-	-	-	-	-	-	-
4	63	-	-	-	-	-	-	-
	0							76.08
		12190.9		**2449.60**		**467.77**		**18573.96**

B 11-5-10		Chert		Flint		Quartz/Quartzite		Total
phi	mm/µm	g	%	g	%	g	%	g
-7	128	-	-	-	-	-	-	-
-6.5	90.5	3707.45	0.00	0.00	0.00	0.00	0.00	3707.45
-6	64	3101.56	100.00	0.00	0.00	0.00	0.00	3101.56
-5.5	45	1855.19	100.00	0.00	0.00	0.00	0.00	1855.19
-5	31.5	1067.30	96.60	37.61	3.40	0.00	0.00	1104.91
-4.5	22.4	945.02	90.80	95.79	9.20	0.00	0.00	1040.81
-4	16	880.13	90.70	77.87	8.02	12.35	1.27	970.35
-3.5	11.2	876.54	78.51	221.47	19.84	18.39	1.65	1116.40
-3	8	513.77	82.74	96.20	15.49	10.98	1.77	620.95
-2.5	5.6	328.02	81.04	64.79	16.01	11.96	2.95	404.77
-2	4	-	-	-	-	-	-	332.14
-1.5	2.8	-	-	-	-	-	-	517.02
-1	2	-	-	-	-	-	-	429.25
-0.5	1.4	-	-	-	-	-	-	380.38
0	1	-	-	-	-	-	-	375.28
0.5	710	-	-	-	-	-	-	331.37
1	500	-	-	-	-	-	-	312.32
1.5	355	-	-	-	-	-	-	235.61
1.75	300	-	-	-	-	-	-	103.30
2	250	-	-	-	-	-	-	99.89
2.25	212	-	-	-	-	-	-	71.22
2.5	180	-	-	-	-	-	-	139.55
3	125	-	-	-	-	-	-	196.37
3.5	90	-	-	-	-	-	-	-
3.735	75	-	-	-	-	-	-	-
4	63	-	-	-	-	-	-	-
	0							277.08
		13274.98		**593.73**		**53.68**		**17723.17**

B 3-8-10		Chert		Flint		Quartz/Quartzite		Total
phi	mm/µm	g	%	g	%	g	%	g
-7	128	0.00	0.00	0.00	0.00	0.00	0.00	0.00
-6.5	90.5	-	-	-	-	-	-	-
-6	64	2168.50	100.00	0.00	0.00	0.00	0.00	2168.50
-5.5	45	2387.11	100.00	0.00	0.00	0.00	0.00	2387.11
-5	31.5	1012.84	100.00	37.61	3.71	0.00	0.00	1012.84
-4.5	22.4	1078.34	91.03	106.29	8.97	0.00	0.00	1184.63
-4	16	613.42	86.94	77.87	11.04	12.96	1.84	705.58
-3.5	11.2	498.62	84.20	76.35	12.89	17.22	2.91	592.19
-3	8	412.99	77.74	106.55	20.06	11.68	2.20	531.22
-2.5	5.6	345.65	85.49	50.75	12.55	7.90	1.95	404.30
-2	4	-	-	-	-	-	-	483.13
-1.5	2.8	-	-	-	-	-	-	463.78
-1	2	-	-	-	-	-	-	437.37
-0.5	1.4	-	-	-	-	-	-	372.33
0	1	-	-	-	-	-	-	333.68
0.5	710	-	-	-	-	-	-	301.50
1	500	-	-	-	-	-	-	284.90
1.5	355	-	-	-	-	-	-	200.11
1.75	300	-	-	-	-	-	-	87.33
2	250	-	-	-	-	-	-	100.25
2.25	212	-	-	-	-	-	-	53.43
2.5	180	-	-	-	-	-	-	98.81
3	125	-	-	-	-	-	-	179.64
3.5	90	-	-	-	-	-	-	114.32
3.735	75	-	-	-	-	-	-	-
4	63	-	-	-	-	-	-	-
	0							158.58
		8517.47		**455.42**		**49.76**		**12496.95**

2A 11-5-10		Chert		Flint		Quartz/Quartzite		Total
phi	mm/µm	g	%	g	%	g	%	g
-7	128	-	-	-	-	-	-	-
-6.5	90.5	705.05	0.00	0.00	0.00	0.00	0.00	705.05
-6	64	4500.01	79.80	1138.92	20.20	0.00	0.00	5638.93
-5.5	45	5463.38	87.36	790.55	12.64	0.00	0.00	6253.93
-5	31.5	3863.64	92.08	332.52	7.92	0.00	0.00	4196.16
-4.5	22.4	1533.01	84.60	262.12	14.46	16.97	0.94	1812.10
-4	16	1223.71	86.33	77.87	5.49	67.28	4.75	1417.45
-3.5	11.2	624.05	77.10	61.74	7.63	123.66	15.28	809.45
-3	8	384.01	76.69	57.30	11.44	59.45	11.87	500.76
-2.5	5.6	304.82	70.91	66.27	15.42	58.76	13.67	429.85
-2	4	-	-	-	-	-	-	507.21
-1.5	2.8	-	-	-	-	-	-	499.01
-1	2	-	-	-	-	-	-	356.43
-0.5	1.4	-	-	-	-	-	-	429.61
0	1	-	-	-	-	-	-	391.91
0.5	710	-	-	-	-	-	-	401.77
1	500	-	-	-	-	-	-	387.43
1.5	355	-	-	-	-	-	-	-
1.75	300	-	-	-	-	-	-	-
2	250	-	-	-	-	-	-	-
2.25	212	-	-	-	-	-	-	-
2.5	180	-	-	-	-	-	-	-
3	125	-	-	-	-	-	-	-
3.5	90	-	-	-	-	-	-	-
3.735	75	-	-	-	-	-	-	-
4	63	-	-	-	-	-	-	-
	0							312.45
		18601.68		**2787.29**		**326.12**		**25049.50**

2B 11-5-10		Chert		Flint		Quartz/Quartzite		Total
phi	mm/µm	g	%	g	%	g	%	g
-7	128	-	-	-	-	-	-	-
-6.5	90.5	3575.00	100.00	0.00	0.00	0.00	0.00	3575.00
-6	64	3425.00	100.00	1138.92	33.25	0.00	0.00	3425.00
-5.5	45	2600.00	70.27	1100.00	29.73	0.00	0.00	3700.00
-5	31.5	2654.31	78.65	332.52	9.85	192.33	5.70	3375.00
-4.5	22.4	1239.76	70.84	510.24	29.16	0.00	0.00	1750.00
-4	16	1345.98	76.91	77.87	4.45	18.74	1.07	1750.00
-3.5	11.2	856.12	71.34	259.71	21.64	84.17	7.01	1200.00
-3	8	727.71	74.64	156.36	16.04	90.93	9.33	975.00
-2.5	5.6	500.23	76.96	81.36	12.52	68.41	10.52	650.00
-2	4	-	-	-	-	-	-	500.00
-1.5	2.8	-	-	-	-	-	-	504.80
-1	2	-	-	-	-	-	-	485.30
-0.5	1.4	-	-	-	-	-	-	425.80
0	1	-	-	-	-	-	-	440.16
0.5	710	-	-	-	-	-	-	428.00
1	500	-	-	-	-	-	-	289.00
1.5	355	-	-	-	-	-	-	-
1.75	300	-	-	-	-	-	-	-
2	250	-	-	-	-	-	-	-
2.25	212	-	-	-	-	-	-	-
2.5	180	-	-	-	-	-	-	-
3	125	-	-	-	-	-	-	-
3.5	90	-	-	-	-	-	-	-
3.735	75	-	-	-	-	-	-	-
4	63	-	-	-	-	-	-	-
	0							510.00
		16924.11		**3656.98**		**454.58**		**23983.06**

University of Gloucestershire

Geochronology Laboratories

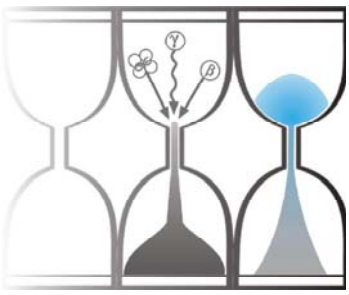

Optical dating of deposits of the proto-Axe at Chard Junction Quarry, Somerset

to

Prof. A.G. Brown, University of Southampton

Prepared by Dr P.S. Toms, 23 May 2011

Optical dating of deposits of the proto-Axe at Chard Junction Quarry, Somerset

Dr P.S. Toms[1], Prof. A.G. Brown[2], Dr L.S. Basell[2], Prof. G.A. Duller[3], Dr J-L. Schwenninger[4]

Abstract

The deposits of the proto-Axe at Chard Junction Quarry potentially contain evidence of the earliest hominin occupation of southwest Britain and, along with Broom and Kilmington, represent one of the longest terrestrial records of Palaeolithic occupation. The aim of this report is to summarise and assess the reliability of the Optical chronology of the sediment sequence within the Hodge Ditch excavations. The analytical properties of the age estimates are evaluated, with intrinsic measures and a tri-laboratory inter-comparison conducted to assess reliability. The raw optical chronology is refined substantially by rejection of those age estimates accompanied by analytical caveats, driven principally by poor recycling ratios in the high, saturating region of dose response. One of two inter-laboratory samples produced a significantly different age by one laboratory, which may be forced by the differences in laboratory thermal treatment. The reliability of D_e:D_r plots may improve with increasing numbers of samples from equivalent stratigraphic units of divergent dosimetry, but having only two samples may lead to erroneous conclusions. Rapid sedimentation and deposition of artefacts between c. 15.2 and 4.5 m appears centred on a geometric mean age of 259±10 ka (MIS 7).There then followed relatively slow or pulsed sedimentation until 86 ka (MIS 5a) beyond which the deposits were incised to form the current course of the River Axe.

[1]Geochronology Laboratories, Department of Natural & Social Sciences, University of Gloucestershire, Swindon Road, Cheltenham GL50 4AZ. Tel: 01242 714708. Email: ptoms@glos.ac.uk

[2]School of Geography, University of Southampton, Highfield, Southampton SO17 1BJ

[3]Institute of Geography & Earth Sciences, Aberystwyth University, Penglais Campus, Aberystwyth SY23 3DB

[4]Research Laboratory for Archaeology and the History of Art, Dyson Perrins Building, South Parks Road, Oxford OX1 3QY

1.0 Introduction

The deposits of the proto-Axe at Chard Junction Quarry are potentially of international significance. Optical dating of the upper 7m (out of 16 m) of sediments within Hodge Ditch 1, conducted previously under PRoSWEB (Toms et al., 2008), demonstrated intervals of deposition spanning 85 ka to 402 ka (Marine Isotope Stages (MIS) 5a to 11). With the subsequent discovery of two bifaces at a depth of c. 15 m in Hodge Ditch 1 (Brown and Basell, 2008), the deposits at Chard Junction may contain the oldest evidence of hominin occupation in at least southwest Britain and may represent one of the longest terrestrial sequences of Palaeolithic occupation. As such the lateral extension of aggregate extraction into Hodge Ditch 2 and 3 has been the subject of monitoring and further dating through the English Heritage Historic Environment Enabling Programme (Project Number 5695).

The aim of this report is to summarise and assess the reliability of the Optical chronology of the Hodge Ditch sequence. The objectives are two-fold. Firstly, to assess the analytical validity of the optical age estimates. Secondly, to assess the accuracy of age estimates by intrinsic measures and inter-laboratory comparison between the Universities of Aberystwyth, Gloucestershire and Oxford.

2.0 Mechanisms and principles

Upon exposure to ionising radiation, electrons within the crystal lattice of insulating minerals are displaced from their atomic orbits. Whilst this dislocation is momentary for most electrons, a portion of charge is redistributed to meta-stable sites (traps) within the crystal lattice. In the absence of significant optical and thermal stimuli, this charge can be stored for extensive periods. The quantity of charge relocation and storage relates to the magnitude and period of irradiation. When the lattice is optically or thermally stimulated, charge is evicted from traps and may return to a vacant orbit position (hole). Upon recombination with a hole, an electron's energy can be dissipated in the form of light generating crystal luminescence providing a measure of dose absorption.

Quartz is the most commonly used mineral in Luminescence dating. The utility of this minerogenic dosimeter lies in the stability of its datable signal over the mid to late Quaternary period, predicted through isothermal decay studies (e.g. Smith *et al*., 1990; retention lifetime 630 Ma at 20°C) and evidenced by optical age estimates concordant with independent chronological controls (e.g. Murray and Olley, 2002).

Optical age estimates of sedimentation (Huntley *et al*., 1985) are premised upon reduction of the minerogenic time-dependent signal (Optically Stimulated Luminescence, OSL) to zero through exposure to sunlight and, once buried, signal reformulation by absorption of litho- and cosmogenic radiation. The signal accumulated post burial acts as a dosimeter recording total dose absorption, converting to a chronometer by estimating the rate of dose absorption quantified through the assay of radioactivity in the surrounding lithology and streaming from the cosmos.

$$\text{Age} = \frac{\text{Mean Equivalent Dose } (D_e, \text{Gy})}{\text{Mean Dose Rate } (D_r, \text{Gy.ka}^{-1})}$$

Aitken (1998) and Bøtter-Jensen et al. (2003) offer a detailed review of optical dating.

3.0 Sample Collection and Preparation

3.1 Sample Collection

A total of 33 sediment samples were extracted from matrix-supported deposits within the Hodge Ditch excavations at Chard Junction Quarry. Triplicate samples of GL10001 and GL10002 were taken for the purposes of inter-laboratory comparison. Contained within opaque plastic tubing (100x45 mm) forced into each face, each sample was wrapped in cellophane and parcel tape in order to preserve moisture content and sample integrity until ready for laboratory preparation. For each sample, an additional c 100 g of sediment was collected for laboratory-based assessment of radioactive disequilibrium.

3.2 Sample preparation

To preclude optical erosion of the datable signal prior to measurement, all samples were prepared under controlled laboratory illumination. To isolate that material potentially exposed to daylight during sampling, sediment located within 20 mm of each tube-end was removed.

The remaining sample was dried. The triplicates of samples GL10001 and GL10002 were then mixed at Gloucestershire and equal masses sent to Aberystwyth and Oxford in light-tight parcels. Quartz within the fine sand (125-180 or 180-250 μm) or fine silt (5-15 μm) fraction was then segregated (Table 1). Samples were subjected to acid and alkaline digestion (10% HCl, 15% H_2O_2) to attain removal of carbonate and organic components respectively.

For fine sand fractions, a further acid digestion in HF (40%, 60 mins) was used to etch the outer 10-15 μm layer affected by α radiation and degrade each samples' feldspar content. During HF treatment, continuous magnetic stirring was used to effect isotropic etching of grains. 10% HCl was then added to remove acid soluble fluorides. Each sample was dried, resieved and quartz isolated from the remaining heavy mineral fraction using a sodium polytungstate density separation at 2.68g.cm^{-3}. Multi-grain aliquots (*c*. 3-6 mg) of quartz from each sample were then mounted on aluminium discs for diagnostics and determination of D_e values.

Fine silt sized quartz, along with other mineral grains of varying density and size, was extracted by sample sedimentation in acetone (<15 μm in 2 min 20 s, >5 μm in 21 mins at 20ºC). Feldspars and amorphous silica were then removed from this fraction through acid digestion (35% H_2SiF_6 for 2 weeks, Jackson *et al*., 1976; Berger *et al*., 1980). Following addition of 10% HCl to remove acid soluble fluorides, grains degraded to <5 μm as a result of acid treatment were removed by acetone sedimentation. Multi-grain aliquots (*c*. 1.5 mg) were then mounted on aluminium discs for diagnostics and D_e evaluation.

All drying was conducted at 40°C to prevent thermal erosion of the signal. All acids and alkalis were Analar grade. All dilutions (removing toxic-corrosive and non-minerogenic luminescence-bearing substances) were conducted with distilled water to prevent signal contamination by extraneous particles.

4.0 Acquisition and accuracy of D_e value

All minerals naturally exhibit marked inter-sample variability in luminescence per unit dose (sensitivity). Therefore, the estimation of D_e acquired since burial requires calibration of the natural signal using known amounts of laboratory dose. D_e values were quantified using a single-aliquot regenerative-dose (SAR) protocol (Murray and Wintle 2000; 2003), facilitated by a Risø TL-DA-15 irradiation-stimulation-detection system (Markey *et al*., 1997; Bøtter-Jensen *et al*., 1999) and standardised for inter-laboratory comparison. Within this apparatus and for the majority of samples, optical signal

stimulation was provided by a 150 W tungsten halogen lamp, filtered to a broad blue-green light, 420-560 nm (2.21-2.95 eV) conveying 16 $mWcm^{-2}$, using three 2 mm Schott GG420 and a broadband interference filter. For the inter-laboratory comparison, optical stimulation was conducted by an assembly of blue diodes (5 packs of 6 Nichia NSPB500S), filtered to 470±80 nm conveying 15 $mW.cm^{-2}$ using a 3 mm Schott GG420 positioned in front of each diode pack. Infrared stimulation, provided by 13 IR diodes (Telefunken TSHA 6203) stimulating at 875±80nm delivering ~5 $mWcm^{-2}$, was used to indicate the presence of contaminant feldspars (Hütt *et al*., 1988). Stimulated photon emissions from quartz aliquots are in the ultraviolet (UV) range and were filtered from stimulating photons by 7.5 mm HOYA U-340 glass and detected by an EMI 9235QA photomultiplier fitted with a blue-green sensitive bialkali photocathode. Aliquot irradiation was conducted using γ-calibrated 1.48 GBq $^{90}Sr/^{90}Y$ β sources.

SAR by definition evaluates D_e through measuring the natural signal (Appendices 1-27, Fig. i) of a single aliquot and then regenerating that aliquot's signal by using known laboratory doses to enable calibration. For each aliquot, up to 5 different regenerative-doses were administered so as to image dose response. D_e values for each aliquot were then interpolated, and associated counting and fitting errors calculated, by way of exponential plus linear regression (Appendices 1-27, Fig. i) using Analyst v3.24 (Duller, 2007). Weighted (geometric) mean D_e values were calculated from 12 aliquots using the central age model outlined by Galbraith *et al*. (1999) and are quoted at 1σ confidence. Owing to limited sample mass, only 6 aliquots of GL09120 were used for D_e measurement. The accuracy with which D_e equates to total absorbed dose and that dose absorbed since burial was assessed. The former can be considered a function of laboratory factors, the latter, one of environmental issues. Diagnostics were deployed to estimate the influence of these factors and criteria instituted to optimise the accuracy of D_e values.

4.1 Laboratory Factors

4.1.1 Feldspar contamination

The propensity of feldspar signals to fade and underestimate age, coupled with their higher sensitivity relative to quartz makes it imperative to quantify feldspar contamination. At room temperature, feldspars generate a signal (IRSL) upon exposure to IR whereas quartz does not. The signal from feldspars contributing to OSL can be depleted by prior exposure to IR. For all aliquots the contribution of any remaining feldspars was estimated from the OSL IR depletion ratio (Duller, 2003). If the addition to OSL by feldspars is insignificant, then the repeat dose ratio of OSL to post-IR OSL should be statistically consistent with unity (Appendices 1-27, Fig. i and v). Significant feldspar contamination was noted for only one sample, GL06012.

4.1.2 Preheating

Preheating aliquots between irradiation and optical stimulation is necessary to ensure comparability between natural and laboratory-induced signals. However, the multiple irradiation and preheating steps that are required to define single-aliquot regenerative-dose response leads to signal sensitisation, rendering calibration of the natural signal inaccurate. The SAR protocol (Murray and Wintle, 2000; 2003) enables this sensitisation to be monitored and corrected using a test dose, set in this study at c. 5 Gy, to track signal sensitivity between irradiation-preheat steps. However, the accuracy of sensitisation correction for both natural and laboratory signals can be preheat dependent. Two diagnostics were used to assess the optimal preheat temperature for accurate correction and calibration.

D_e preheat dependence quantifies the combined effects of thermal transfer and sensitisation on the natural signal. Insignificant adjustment in D_e values in response to differing preheats may reflect limited influence of these effects. Samples generating D_e values <10Gy and exhibiting a systematic, statistically significant adjustment in D_e value with increasing preheat temperature may indicate the presence of significant thermal transfer; in such instances low temperature (<220°C) preheats provide the apposite measure of D_e. A total of 18 aliquots were divided into sets of 3;

each set was assigned a 10 s preheat between 180°C and 280°C and the D_e value from each aliquot was then assessed.

The Dose Recovery test (Appendices 1-27, Fig. ii) attempts to replicate the above diagnostic, yet provide improved resolution of thermal effects through removal of variability induced by heterogeneous dose absorption in the environment, using a precise lab dose to simulate natural dose. The ratio between the applied dose and recovered D_e value should be statistically concordant with unity. For this diagnostic, a further 6 aliquots were each assigned a 10 s preheat between 180°C and 280°C. In the case of the inter-laboratory comparison, this test used 18 aliquots divided into sets of 3; each set was assigned a 10 s preheat between 180°C and 280°C.

Measures of D_e preheat dependence were used exclusively within Hodge Ditch 1 early in the site's study by Toms et al. (2008). There were limited instances where D_e thermal dependence occurred. When observed the Dose Recovery test also demonstrated thermal dependence, hence for samples GL09030 the effect of preheating was monitored by this test only. That preheat treatment fulfilling the criteria of accuracy for thermal diagnostics was selected to refine the final D_e value from 12 aliquots.

Further thermal treatments, prescribed by Murray and Wintle (2000; 2003), were applied to optimise accuracy and precision. Optical stimulation occurred at 125ºC in order to minimise effects associated with photo-transferred thermoluminescence and maximise signal to noise ratios. Inter-cycle optical stimulation was conducted at 280°C to minimise recuperation.

4.1.3 Irradiation

For all samples having D_e values in excess of 100 Gy, matters of signal saturation and laboratory irradiation effects are of concern. With regards the former, the rate of signal accumulation generally adheres to a saturating exponential form and it is this that limits the precision and accuracy of D_e values for samples having absorbed large doses. For such samples, the functional range of D_e interpolation by SAR has been verified up to 600 Gy by Pawley *et al*. (2010). Age estimates based on D_e values exceeding this value should be accepted tentatively.

4.1.4 Internal consistency

Quasi-radial plots (Appendices 1-27, Figs iii to v; *cf* Galbraith, 1990) are used to illustrate inter-aliquot D_e variability for natural and repeated regeneration of low and high laboratory doses. D_e values are standardised relative to the central D_e value for natural signals and applied dose for regenerated signals. D_e values are described as overdispersed when >5% lie beyond $\pm 2\sigma$ of the standardising value; resulting from a heterogeneous absorption of burial dose and/or response to the SAR protocol. For multi-grain aliquots, overdispersion for natural signals does not necessarily imply inaccuracy. However where overdispersion is observed for regenerated signals, the age estimate from that sample should be accepted tentatively. The majority of sensitivity corrected signals from repeated regeneration doses appear overdispersed. This measure of SAR protocol success at Gloucestershire differs and is more stringent than that prescribed by Murray and Wintle (2000; 2003). They suggest repeat dose ratios (Table 1) should be concordant with the range 0.9-1.1; this filter has been applied in this study (Table 2).

4.2 Environmental factors

4.2.1 Incomplete zeroing

Post-burial OSL signals residual of pre-burial dose absorption can result where pre-burial sunlight exposure is limited in spectrum, intensity and/or period, leading to age overestimation. This effect is particularly acute for material eroded and redeposited sub-aqueously (Olley *et al*., 1998, 1999; Wallinga, 2002) and exposed to a burial dose of <20 Gy (e.g. Olley *et al*., 2004), has some influence in sub-aerial contexts but is rarely of consequence where aerial transport has occurred.

Given the D_e values recorded for the Hodge Ditch sequence (Table 1), partial bleaching is unlikely to impact on age estimates but was nevertheless evaluated for each sample by signal analysis (Appendices 1-27, Fig. vi; Bailey *et al*., 2003). Systematic increase in D_e (t), testifying to partial bleaching, was observed only for sample GL09029.

4.2.2 Pedoturbation

The accuracy of sedimentation ages can further be controlled by post-burial trans-strata grain movements forced by pedo- or cryoturbation (Berger, 2003; Singhvi et al., 2001; Bateman et al., 2003). Within the Hodge Ditch sequences there is no evidence of *in situ* palaeosols. Cryoturbation was observed in number of locations; inaccuracy created by such forces by may be bidirectional, heaving older material upwards or drawing younger material downwards into the level to be dated. Areas of cryogenic deformation of matrix-supported material were avoided.

5.0 Acquisition and accuracy of D_r value

Lithogenic D_r values were defined through measurement of U, Th and K radionuclide concentration and conversion of these quantities into β and γ D_r values (Table 1). β contributions were estimated from sub-samples at Gloucestershire by laboratory-based γ spectrometry using an Ortec GEM-S high purity Ge coaxial detector system, calibrated using certified reference materials supplied by CANMET. For the inter-laboratory samples, each laboratory used their standard approach (β counting at Aberystwyth and ICP-MS at Oxford; Table 3). γ dose rates were estimated from *in situ* NaI gamma spectrometry using an EG&G μNomad portable NaI gamma spectrometer (calibrated using the block standards at RLAHA); these reduce uncertainty relating to potential heterogeneity in the γ dose field surrounding each sample. For the inter-laboratory samples, each laboratory measured the same position with their portable spectrometer (Table 3). The level of U disequilibrium was estimated by laboratory-based Ge γ spectrometry. Estimates of radionuclide concentration were converted into D_r values (Adamiec and Aitken, 1998), accounting for D_r modulation forced by grain size (Mejdahl, 1979), present moisture content (Zimmerman, 1971). Cosmogenic D_r values were calculated on the basis of sample depth, geographical position and matrix density (Prescott and Hutton, 1994).

The spatiotemporal validity of D_r values can be considered as four variables. Firstly, disequilibrium can force temporal instability in U and Th emissions. The impact of this infrequent phenomenon (Olley et al., 1996) upon age estimates is usually insignificant given their associated margins of error. However, for samples where this effect is pronounced (>50% disequilibrium between ^{238}U and ^{226}Ra; Appendices 1-27, Fig. vii), the resulting age estimates should be accepted tentatively. Secondly, pedogenically-induced variations in matrix composition of B and C-horizons, such as radionuclide and/or mineral remobilisation, may alter the rate of energy emission and/or absorption. Thirdly, spatiotemporal detractions from present moisture content are difficult to assess directly, requiring knowledge of the magnitude and timing of differing contents. However, the maximum influence of moisture content variations can be delimited by recalculating D_r for minimum (zero) and maximum (saturation) content. Finally, temporal alteration in the thickness of overburden alters cosmic D_r values. Cosmic D_r often forms a negligible portion of total D_r. It is possible to quantify the maximum influence of overburden flux by recalculating D_r for minimum (zero) and maximum (surface sample) cosmic D_r.

6.0 Estimation of Age

The ages reported in Table 1 provide an estimate of sediment burial period based on mean D_e and D_r values and their associated analytical uncertainties. Uncertainty in age estimates is reported as a product of systematic and experimental errors, with the magnitude of experimental errors alone shown in parenthesis (Table 1). Probability distributions indicate the inter-aliquot variability in age (Appendices 1-27, Figs iii and viii). The maximum influence of temporal variations in D_r

forced by minima-maxima variation in moisture content and overburden thickness is illustrated in Fig. viii, Appendices 1-27. Where uncertainty in these parameters exists this age range may prove instructive, however the combined extremes represented should not be construed as preferred age estimates. The analytical validity of each sample is presented in Table 2.

7.0 Analytical uncertainty

All errors are based upon analytical uncertainty and quoted at 1σ confidence. Error calculations account for the propagation of systematic and/or experimental (random) errors associated with D_e and D_r values.

For D_e values, systematic errors are confined to laboratory β source calibration. Uncertainty in this respect is that combined from the delivery of the calibrating γ dose (1.2%; NPL, pers. comm.), the conversion of this dose for SiO_2 using the respective mass energy-absorption coefficient (2%; Hubbell, 1982) and experimental error, totalling 3.5%. Mass attenuation and bremsstrahlung losses during γ dose delivery are considered negligible. Experimental errors relate to D_e interpolation using sensitisation corrected dose responses. Natural and regenerated sensitisation corrected dose points (S_i) are quantified by,

$$S_i = (D_i - x.L_i) / (d_i - x.L_i) \qquad \textbf{Eq.1}$$

where D_i = Natural or regenerated OSL, initial 0.2 s
L_i = Background natural or regenerated OSL, final 5 s
d_i = Test dose OSL, initial 0.2 s
x = Scaling factor, 0.08

The error on each signal parameter is based on counting statistics, reflected by the square-root of measured values. The propagation of these errors within Eq. 1 generating σS_i follows the general formula given in Eq. 2. σS_i are then used to define fitting and interpolation errors within exponential plus linear regressions performed by Analyst 3.24 (Duller, 2007).

For D_r values, systematic errors accommodate uncertainty in radionuclide conversion factors (5%), β attenuation coefficients (5%), a-value (4%; derived from a systematic α source uncertainty of 3.5% and experimental error), matrix density (0.20 $g.cm^{-3}$), vertical thickness of sampled section (specific to sample collection device), saturation moisture content (3%), moisture content attenuation (2%), burial moisture content (25% relative, unless direct evidence exists of the magnitude and period of differing content) and NaI gamma spectrometer calibration (3%). Experimental errors are associated with radionuclide quantification for each sample by NaI and Ge gamma spectrometry.

The propagation of these errors through to age calculation is quantified using the expression,

$$\sigma y\,(\delta y/\delta x) = (\Sigma\,((\delta y/\delta x_n).\sigma x_n)^2)^{1/2} \qquad \textbf{Eq. 2}$$

where y is a value equivalent to that function comprising terms x_n and where σy and σx_n are associated uncertainties.

Errors on age estimates are presented as combined systematic and experimental errors and experimental errors alone. The former (combined) error should be considered when comparing luminescence ages herein with independent chronometric controls. The latter assumes systematic errors are common to luminescence age estimates generated by means equal to those detailed herein and enable direct comparison with those estimates.

8.0 Discussion

Taking the youngest and oldest age estimates (samples GL06011 and GL08047); the raw optical chronology for Hodge Ditch spans 86 to 544 ka (MIS 5a to 15; Table 1 and Fig. 1). There is a broad increase in age with depth to 274 ka (MIS 7) at c. 4.5 m. Beyond this level, there is an age plateau that appears to broaden with depth (169 to 544ka at c. 15 m). The overall age-depth sequence is incompatible with Bayesian analysis, precluding a whole-site quantitative assessment of age consistency with relative stratigraphic position. In the absence of independent chronological control, intrinsic measures of reliability are the sole means by which to evaluate the accuracy of the age estimates.

8.1 Analytical validity

A total of 23 samples failed one or more diagnostic elements; Table 2 outlines the analytical caveats by sample. Five samples failed the Dose Recovery test (see 4.1.2), five samples exhibited varying levels of U disequilibrium (see 5.0), four samples produced D_e >600 Gy (see 4.1.3), one sample produced insufficient datable mass and one proved to have significant feldspar contamination. However the most common failure, in thirteen samples, was in the repeat dose ratio assessed as part of the D_e measurement (Murray and Wintle, 2000; 2003; see 4.1.4). Data within Table 1 indicates there is 70% more variation in the ratio for high doses (17%) than low (10%). The majority of samples yield D_e values in the high, saturating region of dose response. As such, estimates of D_e in this region are particularly sensitive to inaccuracies in the form of dose response forced by inaccurate correction of sensitivity change. Figure 1 highlights those samples with analytical caveats.

8.2 D_e:D_r plots

Samples obtained from the same or equivalent stratigraphic units whose ages converge but are based on divergent D_r values offer a powerful, though resource-intensive intrinsic assessment of reliability (Toms et al., 2005). Figure 2 summarises the D_e:D_r plots for multiple age estimates obtained within stratigraphic units or between those at an equivalent stratigraphic level. Of the intra-unit assessments, samples GL10015/GL10016 and GL08043/GL08044 show convergent age estimates from statistically distinct D_r values (Fig. 2c and 2d). At c.13 m (Fig. 2e), this pattern is broadly true of the age estimates from units of equivalent depth within the sequence. However, this contrasts with those at c. 15 m (Fig. 2f) where there is a marked variation in age. The concern evolved here is that the apparent convergence or divergence of age estimates may be dependent on the number of samples dated; Figure 2f indicates at least two distinct age bands within which at least two samples with distinct D_r values appear to plot.

8.3 Inter-laboratory comparison

Luminescence dating requires calibration, maintenance and monitoring of equipment involved in D_e and D_r evaluation. Though a rigorous methodology may be employed by a laboratory, in the absence of independent chronological control in a large study such as this inter-laboratory comparison is advisable to corroborate age estimates and thereby verify the accuracy of equipment calibration and function. In this study, the comparability of three procedural elements as well as age estimates was assessed from three Luminescence laboratories for two samples, GL10001 and GL10002 (Table 3; Fig. 3; Appendices 17-18).

Figure 3a shows the outcome of the Dose recovery test for GL10001. Laboratory A recorded strong thermal dependence, Laboratory C slight and Laboratory B none. The origin of this variable response remains to be determined, but critically this decision-making process led to differences in preheat selection between laboratories. For GL10002, Laboratory B and C elected a preheat temperature based on extrapolation from their respective Dose Recovery tests on GL10001. Laboratory A conducted a separate Dose Recovery test on GL10002. Extrapolation of preheat temperature

using Dose Recovery tests conducted on a sub-set of samples is not uncommon in Luminescence dating. Figures 3b and 3c illustrate the outcome of β and γ D_r assessment. Inter-laboratory difference in γ D_r is a maximum of 12±7%, whilst for β D_r this climbs to 34±12%. The greater variation in β D_r may arise from differences in technology between laboratories. Fig. 3d shows the age envelope of each sample based on the inter-laboratory range. The maximum difference in age is 29±18% for sample GL10001 between Laboratory B and C, 39±21% for GL10002 between Laboratory A and C. The principal driver behind these differences is D_e (43±18%, GL10001; 29±17%, GL10002), with laboratory C systematically lower than A and B. The divergence between laboratories in natural D_e value was further investigated by giving a precise dose to three sets of three aliquots of bleached GL10001. Each laboratory then adopted the same measurement sequence and preheat temperature to estimate the dose applied. Fig. 3e shows that the lower natural D_e value reported by Laboratory C is not rooted in source calibration, with statistically concordant doses recovered between laboratories. It is possible, therefore, that the inter-laboratory discrepancy in natural D_e originates from the choice of preheat temperature. For sample GL10002, where Laboratory A and B selected the same preheat temperature the natural D_e values are indistinguishable. Sources of differential thermal dependence of inter-laboratory Dose Recovery tests should form the focus of future work. It is possible that application of this test to some rather than all samples from a site may affect the choice of preheat temperature.

9.0 Synopsis

Excluding those samples with analytical caveats reduces the variability of the chronological sequence. The youngest unit of the site at 2.5 m in Hodge Ditch 1 (GL06011) suggests a minimum age of 86 ka (MIS 5a). The current data set suggests relatively slow or pulsed sedimentation back to c. 274 ka (MIS 7; c. 4.5 m, GL06013). This refined sequence then suggests rapid sedimentation and deposition of artefacts centred on a geometric mean age of 259±10 ka (MIS 7) between c. 4.5 and 15.2 m.

This study has highlighted four areas for consideration in future application of Luminescence dating. Firstly, for Late and Middle Pleistocene samples, it is important to assess the success of correction for sensitivity change in the high dose region by repeat regenerative-dose ratio tests. Secondly, inter-laboratory methodological differences can lead to significant differences in β D_r, whereas the standard approach to measurement of γ D_r produces equivalent values. Moreover and thirdly, a standardised approach to D_e acquisition can produce significant differences in this value between laboratories that may be forced by the choice of preheat temperature. Finally, targeting areas of divergent dosimetry in equivalent stratigraphic units and measuring the convergence of age estimates is not an infallible intrinsic measure of reliability. The quality of this metric improves with increasing numbers of samples from each unit; it is apparent that two samples per unit may lead to an erroneous conclusion on their reliability.

Field Code	Lab Code	Overburden (m)	Grain size (µm)	Moisture content (%)	NaI γ-spectrometry (in situ)			γ D_r (Gy.ka^{-1})	Ge γ-spectrometry (lab based)			α D_r (Gy.ka^{-1})	β D_r			Cosmic D_r (Gy.ka^{-1})	Total D_r (Gy.ka^{-1})			
					K (%)	Th (ppm)	U (ppm)		K (%)	Th (ppm)	U (ppm)									
CHAR01	GL06010	4.3	125-180	16 ± 4	0.36 ± 0.01	2.28 ± 0.12	1.29 ± 0.08	0.34 ± 0.02	1.27 ± 0.06	6.86 ± 0.29	2.08 ± 0.10	-	1.09 ± 0.10	0.11 ± 0.01	1.54 ± 0.10	240	0.98 ± 0.03	-	268.5 ± 22.0	174 ± 18 (16)
CHAR02	GL06011	2.5	125-180	13 ± 3	0.30 ± 0.01	2.12 ± 0.10	1.01 ± 0.07	0.29 ± 0.01	0.60 ± 0.03	3.10 ± 0.15	0.95 ± 0.06	-	0.53 ± 0.04	0.14 ± 0.01	0.96 ± 0.05	260	1.00 ± 0.02	-	90.2 ± 6.8	94 ± 9 (7)
CHAR03	GL06012	1.7	125-180	14 ± 3	0.68 ± 0.02	3.85 ± 0.17	1.62 ± 0.11	0.53 ± 0.02	1.53 ± 0.07	7.23 ± 0.31	1.90 ± 0.09	-	1.28 ± 0.11	0.16 ± 0.02	1.97 ± 0.11	260	0.96 ± 0.03	-	193.7 ± 11.0	98 ± 9 (6)
CHAR04	GL06013	4.5	125-180	15 ± 4	0.36 ± 0.02	1.82 ± 0.13	0.79 ± 0.08	0.26 ± 0.01	0.99 ± 0.05	2.71 ± 0.13	0.65 ± 0.05	-	0.72 ± 0.07	0.10 ± 0.01	1.09 ± 0.07	240	0.99 ± 0.03	-	298.6 ± 19.2	274 ± 25 (20)
CHAR05	GL06057	6.7	125-180	16 ± 4	0.18 ± 0.01	1.32 ± 0.08	0.82 ± 0.06	0.20 ± 0.01	0.87 ± 0.04	5.30 ± 0.21	1.30 ± 0.05	-	0.75 ± 0.07	0.08 ± 0.01	1.02 ± 0.07	240	0.99 ± 0.03	-	375.3 ± 24.6	367 ± 35 (29)
CHAR06	GL06058	7.0	125-180	15 ± 4	0.23 ± 0.01	1.55 ± 0.10	0.67 ± 0.07	0.21 ± 0.01	1.09 ± 0.05	3.90 ± 0.16	1.00 ± 0.04	-	0.84 ± 0.08	0.07 ± 0.01	1.12 ± 0.08	280	1.00 ± 0.04	-	318.3 ± 33.3	284 ± 36 (32)
CHAR07	GL08043	15.3	125-180	17 ± 4	0.28 ± 0.01	1.39 ± 0.10	0.81 ± 0.07	0.22 ± 0.01	0.68 ± 0.04	3.33 ± 0.34	0.78 ± 0.06	-	0.54 ± 0.05	0.03 ± 0.00	0.80 ± 0.6	280	-	1.25 ± 0.02	284.9 ± 31.9	355 ± 47 (43)
CHAR08	GL08044	15.2	125-180	21 ± 5	0.48 ± 0.01	2.68 ± 0.11	1.20 ± 0.07	0.38 ± 0.02	1.66 ± 0.08	9.41 ± 0.55	1.45 ± 0.09	-	1.22 ± 0.13	0.03 ± 0.00	1.63 ± 0.14	280	-	0.89 ± 0.02	477.2 ± 45.1	292 ± 37 (33)
CHAR09	GL08045	12.9	125-180	17 ± 4	0.27 ± 0.01	2.01 ± 0.13	0.86 ± 0.08	0.26 ± 0.01	1.21 ± 0.06	6.59 ± 0.46	1.36 ± 0.08	-	0.97 ± 0.09	0.03 ± 0.00	1.26 ± 0.10	280	-	1.35 ± 0.03	332.7 ± 23.8	264 ± 28 (23)
CHAR10	GL08046	15.0	125-180	20 ± 5	0.48 ± 0.02	3.29 ± 0.16	1.83 ± 0.11	0.48 ± 0.02	1.34 ± 0.06	8.00 ± 0.51	1.51 ± 0.09	-	1.04 ± 0.11	0.03 ± 0.00	1.56 ± 0.11	260	-	1.07 ± 0.03	521.4 ± 41.5	334 ± 36 (31)
CHAR11	GL08047	15.5	125-180	20 ± 5	0.46 ± 0.02	3.22 ± 0.13	1.39 ± 0.09	0.42 ± 0.02	1.23 ± 0.06	9.24 ± 0.55	1.82 ± 0.10	-	1.03 ± 0.11	0.03 ± 0.00	1.49 ± 0.11	280	-	0.76 ± 0.02	736.8 ± 51.7	494 ± 50 (43)
CHAR12	GL09029	3.3	125-180	13 ± 3	0.32 ± 0.01	2.84 ± 0.11	0.76 ± 0.08	0.41 ± 0.02	0.54± 0.03	4.65 ± 0.37	1.03 ± 0.07	-	0.54 ± 0.05	0.12 ± 0.01	1.07 ± 0.05	260	1.06 ± 0.18	-	132.1 ± 7.0	124 ± 9 (7)
CHAR13	GL09030	8.1	125-180	13 ± 3	0.26 ± 0.01	1.54 ± 0.11	0.76 ± 0.08	0.22 ± 0.01	0.63 ± 0.04	3.63 ± 0.33	0.68 ± 0.06	-	0.53 ± 0.05	0.06 ± 0.01	0.82 ± 1.43	250	0.79 ± 0.02	0.86 ± 0.04	247.4 ± 18.9	302 ± 29 (25)
CHAR14	GL09031	9.6	125-180	15 ± 4	0.28 ± 0.02	1.86 ± 0.13	1.14 ± 0.09	0.28 ± 0.01	1.28 ± 0.06	8.21 ± 0.52	1.61 ± 0.10	-	1.09 ± 0.10	0.05 ± 0.01	1.43 ± 0.10	230	0.76 ± 0.04	1.00 ± 0.07	419.8 ± 31.7	294 ± 30 (26)
CHAR15	GL09117	11.8	5-15	21 ± 5	1.00 ± 0.03	5.62 ± 0.21	2.68 ± 0.14	0.81 ± 0.03	1.72 ± 0.08	9.96 ± 0.58	2.02 ± 0.11	0.38 ± 0.04	1.44 ± 0.14	0.04 ± 0.00	2.67 ± 0.15	210	1.02 ± 0.04	0.99 ± 0.08	928.1 ± 64.8	347 ± 31 (28)
CHAR16	GL09118	11.7	5-15	19 ± 5	1.01 ± 0.02	5.33 ± 0.18	2.57 ± 0.12	0.79 ± 0.03	1.79 ± 0.08	9.30 ± 0.56	1.76 ± 0.10	0.35 ± 0.04	1.48 ± 0.14	0.04 ± 0.00	2.67 ± 0.15	250	1.01 ± 0.04	1.11 ± 0.09	614.0 ± 30.6	230 ± 17 (14)
CHAR17	GL09119	8.8	5-15	19 ± 5	0.72 ± 0.02	4.53 ± 0.16	1.98 ± 0.10	0.61 ± 0.02	1.37 ± 0.06	9.03 ± 0.55	1.87 ± 0.10	0.35 ± 0.04	1.23 ± 0.12	0.06 ± 0.01	2.26 ± 0.12	260	1.06 ± 0.03	0.98 ± 0.04	529.9 ± 24.5	235 ± 17 (14)
CHAR18	GL09120	10.7	125-180	8 ± 2	0.31 ± 0.02	1.74 ± 0.13	0.73 ± 0.09	0.24 ± 0.01	0.61 ± 0.04	3.41 ± 0.35	1.03 ± 0.07	-	0.59 ± 0.04	0.05 ± 0.00	0.88 ± 0.05	240	0.82 ± 0.06	1.18 ± 0.18	419.1 ± 41.5	475 ± 53 (48)
CHAR19	GL10013	13.1	125-180	21 ± 5	0.35 ± 0.01	1.90 ± 0.11	0.81 ± 0.07	0.27 ± 0.01	0.73 ± 0.04	2.52 ± 0.25	0.56 ± 0.06	-	0.50 ± 0.05	0.04 ± 0.00	0.80 ± 0.06	240	1.04 ± 0.06	1.54 ± 0.28	279.4 ± 18.0	348 ± 34 (14)
CHAR20	GL10014	12.9	125-180	12 ± 3	0.39 ± 0.02	2.07 ± 0.15	1.01 ± 0.10	0.31 ± 0.02	0.70 ± 0.04	4.46 ± 0.34	0.53 ± 0.06	-	0.56 ± 0.05	0.04 ± 0.00	0.91 ± 0.05	260	-	-	284.4 ± 34.1	313 ± 42 (21)
CHAR21	GL10015	14.7	125-180	16 ± 4	0.66 ± 0.02	2.99 ± 0.16	1.79 ± 0.11	0.50 ± 0.02	1.29 ± 0.06	7.29 ± 0.48	1.18 ± 0.08	-	1.02 ± 0.10	0.03 ± 0.00	1.55 ± 0.10	260	0.97 ± 0.05	1.12 ± 0.1	298.3 ± 30.2	192 ± 23 (40)
CHAR22	GL10016	14.8	125-180	18 ± 4	0.43 ± 0.02	2.58 ± 0.13	1.23 ± 0.09	0.37 ± 0.02	1.04 ± 0.05	6.06 ± 0.43	1.27 ± 0.08	-	0.84 ± 0.08	0.03 ± 0.00	1.24 ± 0.09	260	1.08 ± 0.05	0.90 ± 0.08	267.7 ± 19.0	208 ± 21 (44)

Table 1 D_r, D_e and Age data of samples from Chard Junction (51°N, 3°W, 75 m O.D.). Samples CHAR01 to CHAR06 from Toms *et al*. (2008) Uncertainties in age are quoted at 1σ confidence, are based on analytical errors and reflect combined systematic and experimental variability and (in parenthesis) experimental variability alone (see 7.0). Blue indicates samples with analytically-acceptable age estimates, red, age estimates with analytical caveats (see Table 2). All ages are expressed in thousands of years before 2010.

Field Code	Lab Code	Sample specific considerations
CHAR01	GL06010	
CHAR02	GL06011	
CHAR03	GL06012	Significant feldspar contamination Failed Dose Recovery test
CHAR04	GL06013	
CHAR05	GL06057	
CHAR06	GL06058	
CHAR07	GL08043	Failed Repeat Dose Ratio test
CHAR08	GL08044	
CHAR09	GL08045	Failed Repeat Dose Ratio test
CHAR10	GL08046	
CHAR11	GL08047	D_e exceeds 600 Gy Failed Repeat Dose Ratio test
CHAR12	GL09029	Potential partial bleaching
CHAR13	GL09030	Failed Repeat Dose Ratio test
CHAR14	GL09031	Failed Repeat Dose Ratio test
CHAR15	GL09117	D_e exceeds 600 Gy Minor to moderate U disequilibrium
CHAR16	GL09118	D_e exceeds 600 Gy Minor to moderate U disequilibrium
CHAR17	GL09119	
CHAR18	GL09120	Limited sample mass
CHAR19	GL10013	Failed Repeat Dose Ratio test
CHAR20	GL10014	Failed Dose Recovery test
CHAR21	GL10015	Failed Dose Recovery test Minor U disequilibirum
CHAR22	GL10016	
CHAR23	GL10001	Failed Repeat Dose Ratio test Minor U disequilibirum
CHAR24	GL10002	
CHAR25	GL10019	Failed Repeat Dose Ratio test
CHAR26	GL10020	Failed Dose Recovery test Failed Repeat Dose Ratio test
CHAR27	GL10055	Failed Dose Recovery test
CHAR28	GL10063	Failed Repeat Dose Ratio test
CHAR29	GL10064	Failed Repeat Dose Ratio test
CHAR30	GL10065	Failed Repeat Dose Ratio test

CHAR31	GL10066	Significant feldspar contamination D_e exceeds 600 Gy Minor U disequilibrium
CHAR32	GL10067	Failed Repeat Dose Ratio test
CHAR33	GL10084	Significant feldspar contamination

Table 2 Analytical validity of sample suite age estimates and caveats for consideration.

Sample	Laboratory	γ D_r (Gy.ka^{-1})	β D_r (Gy.ka^{-1})	Total D_r (Gy.ka^{-1})	1.1.1.1.1.1.9 (°C for 10s)	1.1.1.1.1.1.10 (Gy)	1.1.1.1.1.1.1 (ka)
GL10001	A	0.46 ± 0.02	0.57 ± 0.04	1.17 ± 0.05	280	164.9 ± 15.6	141 ± 14
	B	0.48 ± 0.02	0.66 ± 0.04	1.24 ± 0.05	240	195.4 ± 15.5	158 ± 14
	C	0.44 ± 0.02	0.49 ± 0.03	1.12 ± 0.06	260	136.6 ± 13.4	122 ± 14
GL10002	A	0.31 ± 0.02	0.51 ± 0.05	0.86 ± 0.05	240	229.4 ± 16.2	268 ± 25
	B	0.34 ± 0.02	0.58 ± 0.04	0.92 ± 0.04	240	212.2 ± 15.4	231 ± 20
	C	0.30 ± 0.01	0.54 ± 0.04	0.92 ± 0.05	260	177.7 ± 19.8	193 ± 24

Table 3 Anonymised inter-laboratory results for samples GL10001 and GL10002. γ D_r acquired by each laboratory's NaI γ spectrometer. β D_r determined by each laboratories standard method. Preheat selected by each laboratory based on their dose recover tests.

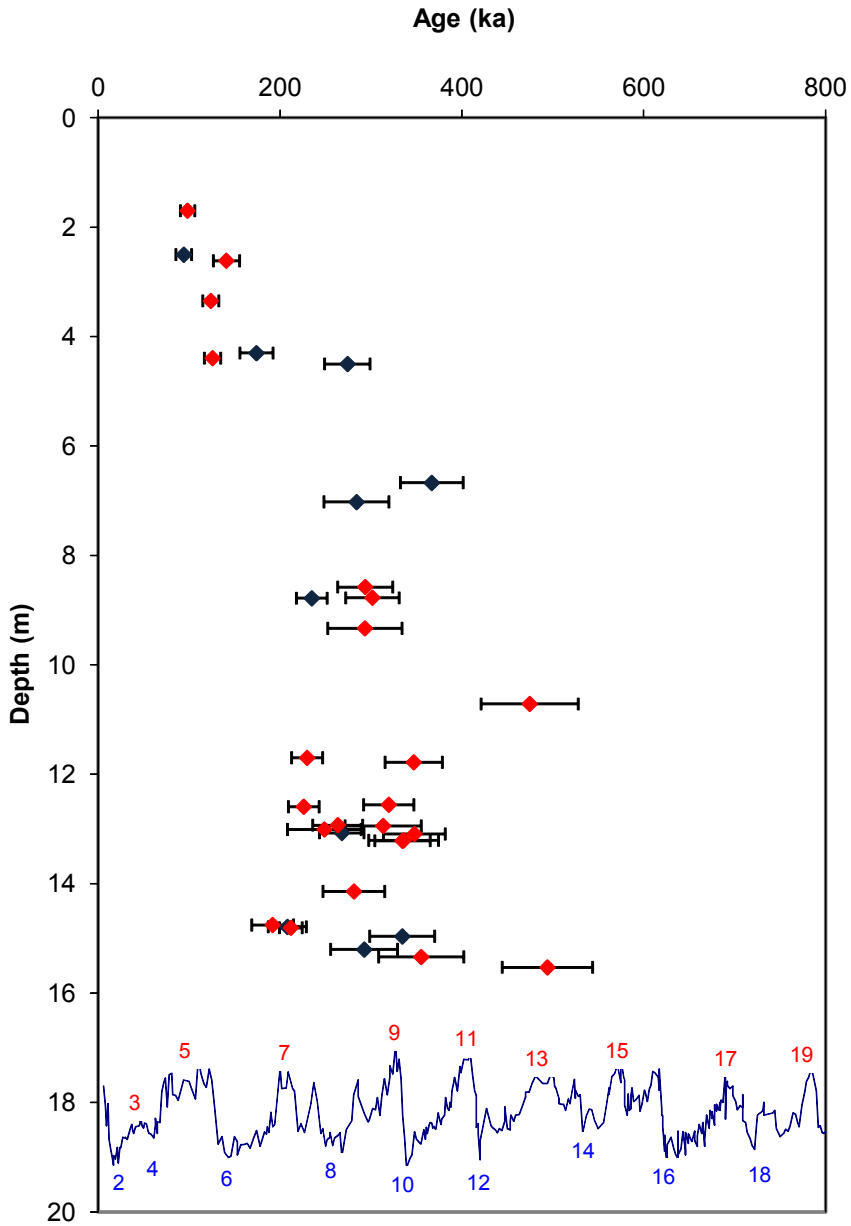

Figure 1 Age-depth plot for Chard Junction Quarry optical dating samples analysed at Gloucestershire. Red fill indicates those samples with analytical caveats. The blue line shows the oxygen isotope curve from ODP 677 along with temperate (red numbered) and cool (blue numbered) MIS.

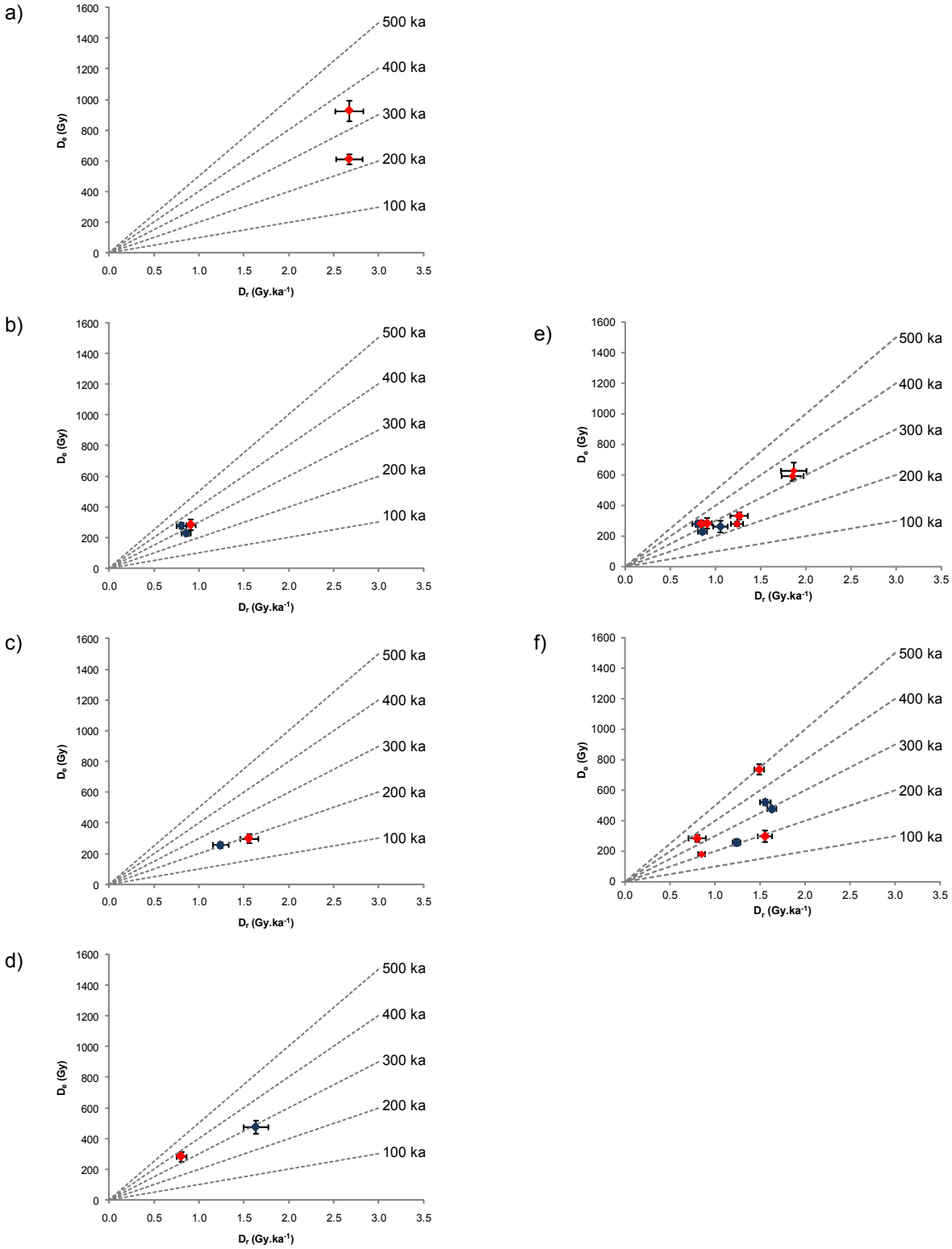

Figure 2 D_e:D_r plots for samples within the same unit; a) GL09117 and GL09118 (11.7 m depth), b) GL10002, GL10013, GL10014 (13m depth), c) GL10015 and GL10016 (14.7 m depth), d) GL08043 and GL08044 (15.2 m depth) and from units at equivalent depth within the sequence; e) GL08045, GL10002, GL10013, GL10014,

GI10019, GL10055, GL10063, GL10065, GL10066 (13m depth) and f) GL08043, GL08044, GL08046, GL08047, GL10015, GL10016, GL10064 (15 m depth). Red fill indicates samples with analytical caveats. The gradient of dashed lines represents age, which increases with slope.

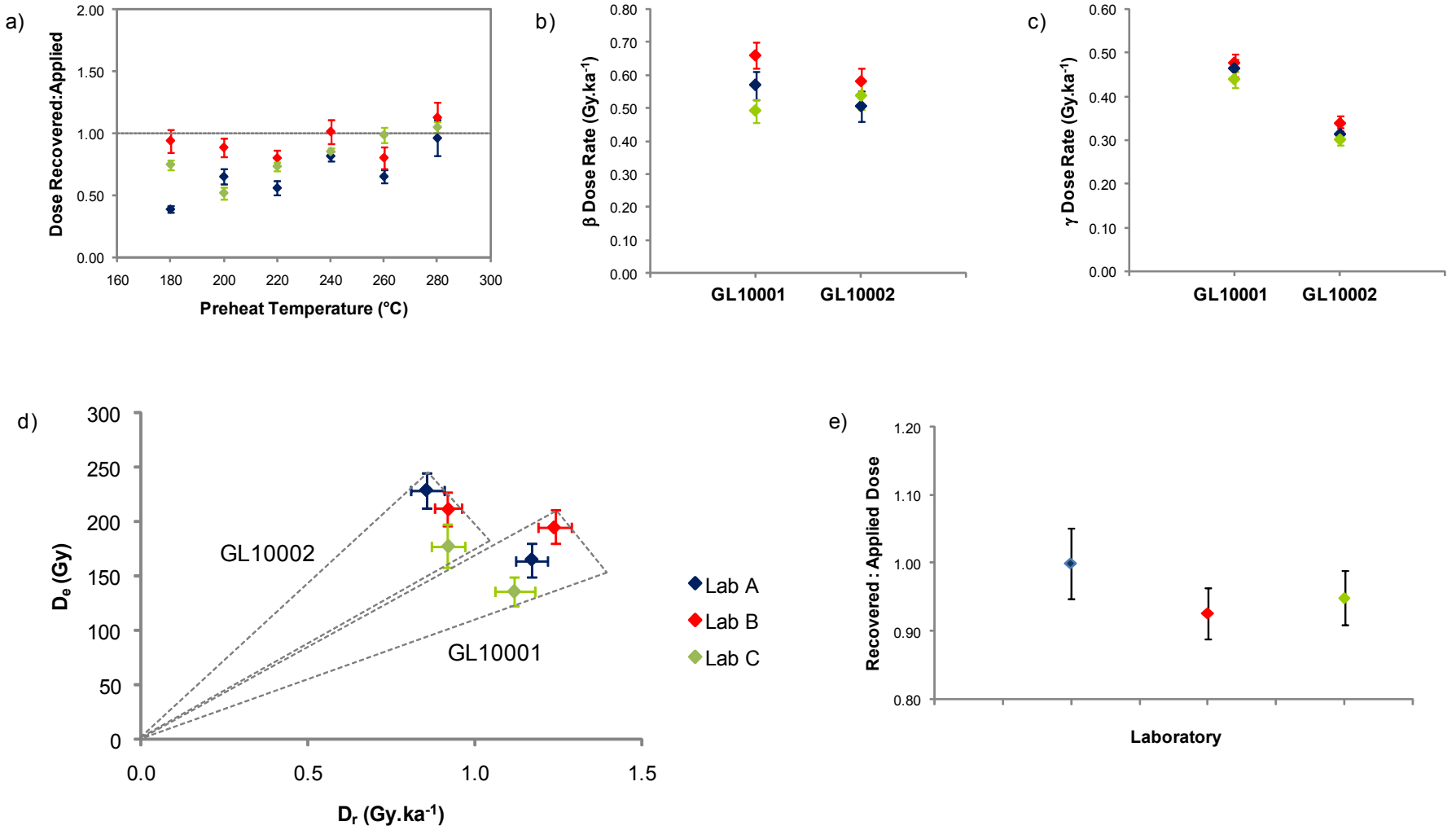

Figure 3 Summary of inter-comparison for samples GL10001 and GL10002 between Laboratory A, B and C in blue, red and green fill respectively; a) dose recovery test, b) β Dr assessment, c) γ Dr assessment, d) age envelopes and e) dose recovery test of source calibration centred on that dose recovered from Laboratory A.

Appendix

(excluding data reported in Toms et al. (2008))

Fig. i Signal Calibration

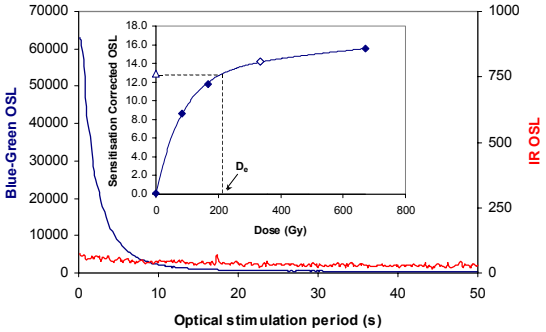

OSL signals. Detectable IR signal decays are diagnostic of feldspar contamination. Inset, the natural blue OSL signal (open triangle) of each aliquot is calibrated against known laboratoy doses to yield equivalent dose (D_e) values. Repeats of low and high doses (open diamonds) illustate the success of sensitivity correction.

Fig. ii Dose Recovery The acquisition of D_e values is necessarily predicated upon thermal treatment of aliquots succeeding environmental and laboratoy irradiation. The Dose Recovery test quantifies the combined effects of thermal transfer and sensitisation on the natural signal using a precise lab dose to simulate natural dose. Based on this an appropriate thermal treatment is selected to generate the final D_e value.

Fig. iii Inter-aliquot D_e distribution Provides a measure of inter-aliquot statistical concordance in D_e values derived from **natural** irradiation. Discordant data (those points lying beyond ±2 standardised ln D_e) reflects heterogeneous dose absorption and/or inaccuracies in calibration.

Fig. iv Low and High Repeat Regenerative-dose Ratio Measures the statistical concordance of signals from repeated **low** and **high** regenerative-doses. Discordant data (those points lying beyond ±2 standardised ln D_e) indicate inaccurate sensitivity correction.

Fig. v OSL to Post-IR OSL Ratio Measures the statistical concordance of OSL and post-IR OSL responses to the same regenerative-dose. Discordant, underestimating data (those points lying below -2 standardised ln D_e) highlight the presence of significant feldspar contamination.

Fig.viSignal Analysis Statistically significant increase in **natural** D_e value with signal stimulation period is indicative of a partially-bleached signal, provided a significant increase in D_e results from **simulated partial bleaching** followed by insignificant adjustment in D_e for simulated **zero** and **full bleach** conditions. Ages from such samples are considered maximum estimates. In the absence of a significant rise in D_e with stimulation time, simulated partial bleaching and zero/full bleach tests are not assessed.

Fig. vii U Activity Statistical concordance (equilibrium) in the activities of the daughter radioisotope ^{226}Ra with its parent ^{238}U may signify the temporal stability of D_r emissions from these chains. Significant differences (disequilibrium; >50%) in activity indicate addition or removal of isotopes creating a time-dependent shift in D_r values and increased uncertainty in the accuracy of age estimates. A 20% disequilibrium marker is also shown.

Fig. viii Age Range The **mean age range** provides an estimate of sediment burial period based on mean D_e and D_r values with associated analytical uncertainties. The probability distribution indicates the inter-aliquot variability in age. The maximum influence of temporal variations in D_r forced by minima-maxima variation in moisture content and overburden thickness may prove instructive where there is uncertainty in these parameters, however the combined extremes represented should not be construed as preferred age estimates.

Fig.ii Dose Recovery

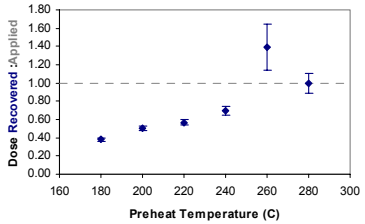

Fig. iii and iv (combined) Inter-aliquot D_e distribution

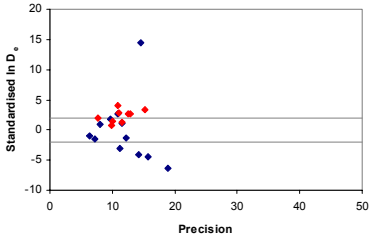

Fig. v OSL to Post-IR OSL Ratio

Not available

Appendix 1
Sample: GL08043

Fig. vi Signal Analysis

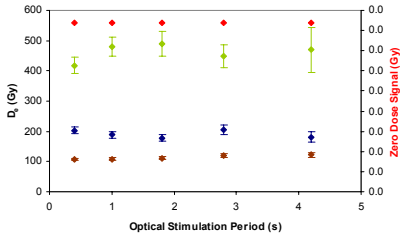

Fig. vii U Decay Activity

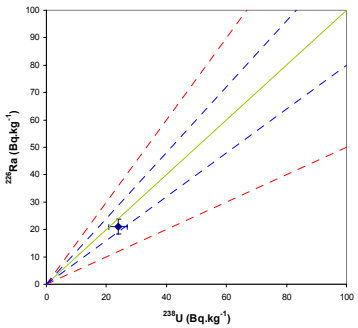

Fig. viii Age Range

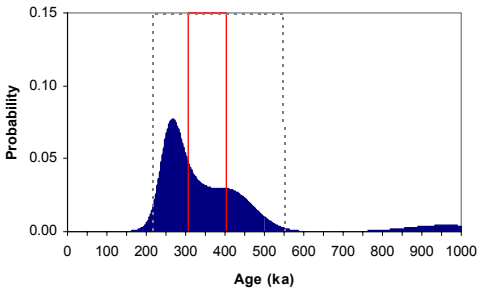

Fig. i Signal Calibration

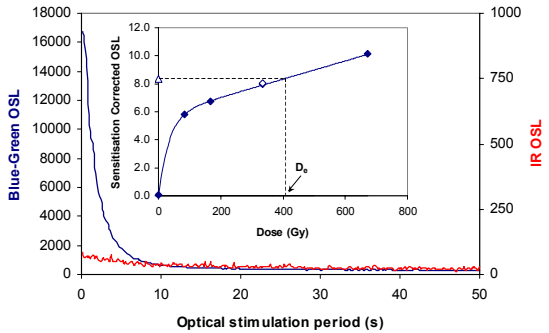

OSL signals. Detectable IR signal decays are diagnostic of feldspar contamination. Inset, the natural blue OSL signal (open triangle) of each aliquot is calibrated against known laboratory doses to yield equivalent dose (D_e) values. Repeats of low and high doses (open diamonds) illustrate the success of sensitivity correction.

Fig. ii Dose Recovery The acquisition of D_e values is necessarily predicated upon thermal treatment of aliquots succeeding environmental and laboratory irradiation. The Dose Recovery test quantifies the combined effects of thermal transfer and sensitisation on the natural signal using a precise lab dose to simulate natural dose. Based on this an appropriate thermal treatment is selected to generate the final D_e value.

Fig. iii Inter-aliquot D_e distribution Provides a measure of inter-aliquot statistical concordance in D_e values derived from **natural** irradiation. Discordant data (those points lying beyond ±2 standardised ln D_e) reflects heterogeneous dose absorption and/or inaccuracies in calibration.

Fig. iv Low and High Repeat Regenerative-dose Ratio Measures the statistical concordance of signals from repeated **low** and **high** regenerative-doses. Discordant data (those points lying beyond ±2 standardised ln D_e) indicate inaccurate sensitivity correction.

Fig. v OSL to Post-IR OSL Ratio Measures the statistical concordance of OSL and post-IR OSL responses to the same regenerative-dose. Discordant, underestimating data (those points lying below -2 standardised ln D_e) highlight the presence of significant feldspar contamination.

Fig.viSignal Analysis Statistically significant increase in **natural** D_e value with signal stimulation period is indicative of a partially-bleached signal, provided a significant increase in D_e results from **simulated partial bleaching** followed by insignificant adjustment in D_e for simulated **zero** and **full bleach** conditions. Ages from such samples are considered maximum estimates. In the absence of a significant rise in D_e with stimulation time, simulated partial bleaching and zero/full bleach tests are not assessed.

Fig. vii U Activity Statistical concordance (equilibrium) in the activities of the daughter radioisotope ^{226}Ra with its parent ^{238}U may signify the temporal stability of D_r emissions from these chains. Significant differences (disequilibrium: >50%) in activity indicate addition or removal of isotopes creating a time-dependent shift in D_r values and increased uncertainty in the accuracy of age estimates. A 20% disequilibrium marker is also shown.

Fig. viii Age Range The **mean age range** provides an estimate of sediment burial period based on mean D_e and D_r values with associated analytical uncertainties. The probability distribution indicates the inter-aliquot variability in age. The maximum influence of temporal variations in D_r forced by minima-maxima variation in moisture content and overburden thickness may prove instructive where there is uncertainty in these parameters, however the combined extremes represented should not be construed as preferred age estimates.

Fig.ii Dose Recovery

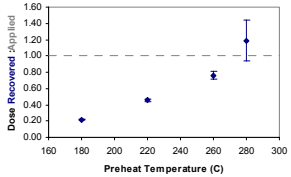

Fig. iii and iv (combined) Inter-aliquot D_e distribution

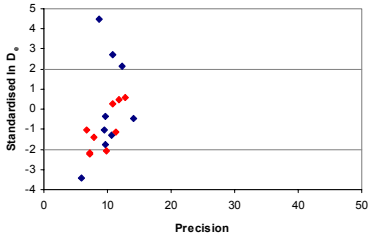

Fig. v OSL to Post-IR OSL Ratio

Not available

Appendix 2
Sample: GL08044

Fig. vi Signal Analysis

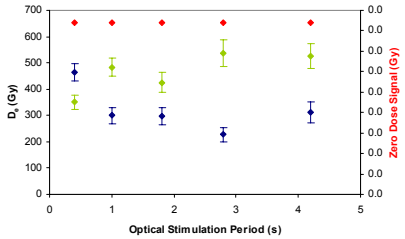

Fig. vii U Decay Activity

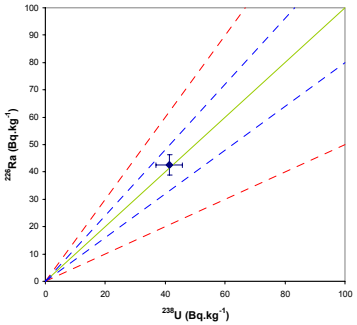

Fig. viii Age Range

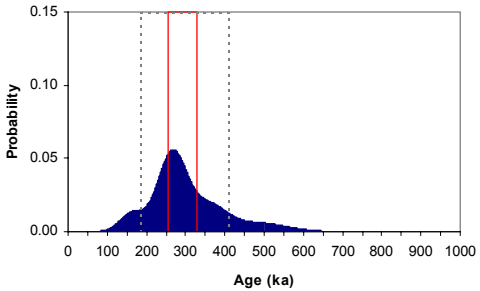

Fig. i Signal Calibration

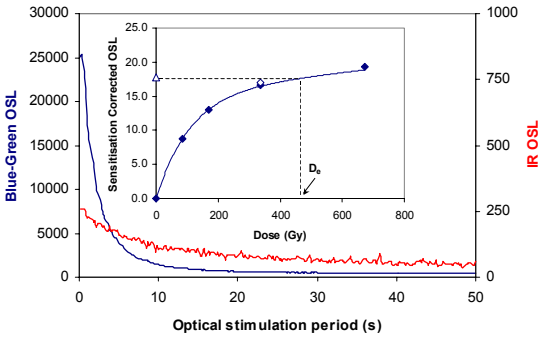

OSL signals. Detectable IR signal decays are diagnostic of feldspar contamination. Inset, the natural blue OSL signal (open triangle) of each aliquot is calibrated against known laboratory doses to yield equivalent dose (D_e) values. Repeats of low and high doses (open diamonds) illustrate the success of sensitivity correction.

Fig. ii Dose Recovery The acquisition of D_e values is necessarily predicated upon thermal treatment of aliquots succeeding environmental and laboratory irradiation. The Dose Recovery test quantifies the combined effects of thermal transfer and sensitisation on the natural signal using a precise lab dose to simulate natural dose. Based on this an appropriate thermal treatment is selected to generate the final D_e value.

Fig. iii Inter-aliquot D_e distribution Provides a measure of inter-aliquot statistical concordance in D_e values derived from **natural** irradiation. Discordant data (those points lying beyond **±2 standardised ln D_e**) reflects heterogeneous dose absorption and/or inaccuracies in calibration.

Fig. iv Low and High Repeat Regenerative-dose Ratio Measures the statistical concordance of signals from repeated **low** and **high** regenerative-doses. Discordant data (those points lying beyond **±2 standardised ln D_e**) indicate inaccurate sensitivity correction.

Fig. v OSL to Post-IR OSL Ratio Measures the statistical concordance of OSL and post-IR OSL responses to the same regenerative-dose. Discordant, underestimating data (those points lying below **-2 standardised ln D_e**) highlight the presence of significant feldspar contamination.

Fig.viSignal Analysis Statistically significant increase in **natural** D_e value with signal stimulation period is indicative of a partially-bleached signal, provided a significant increase in D_e results from **simulated partial bleaching** followed by insignificant adjustment in D_e for simulated **zero** and **full bleach** conditions. Ages from such samples are considered maximum estimates. In the absence of a significant rise in D_e with stimulation time, simulated partial bleaching and zero/full bleach tests are not assessed.

Fig. vii U Activity Statistical concordance (**equilibrium**) in the activities of the daughter radioisotope ^{226}Ra with its parent ^{238}U may signify the temporal stability of D_r emissions from these chains. Significant differences (disequilibrium: **>50%**) in activity indicate addition or removal of isotopes creating a time-dependent shift in D_r values and increased uncertainty in the accuracy of age estimates. A **20%** disequilibrium marker is also shown.

Fig. viii Age Range The **mean age range** provides an estimate of sediment burial period based on mean D_e and D_r values with associated analytical uncertainties. The **probability distribution** indicates the inter-aliquot variability in age. The **maximum influence** of temporal variations in D_r forced by minima-maxima variation in moisture content and overburden thickness may prove instructive where there is uncertainty in these parameters, however the combined extremes represented should not be construed as preferred age estimates.

Fig.ii Dose Recovery

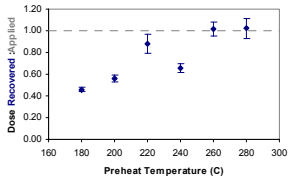

Fig. iii and iv (combined) Inter-aliquot D_e distribution

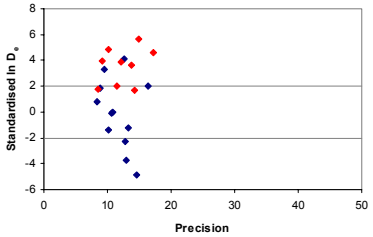

Fig. v OSL to Post-IR OSL Ratio

Not available

Appendix 3
Sample: GL08045

Fig. vi Signal Analysis

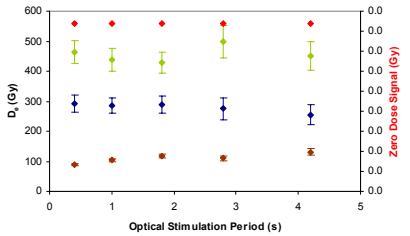

Fig. vii U Decay Activity

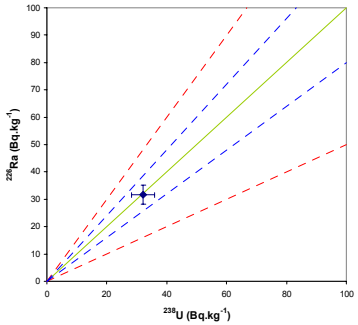

Fig. viii Age Range

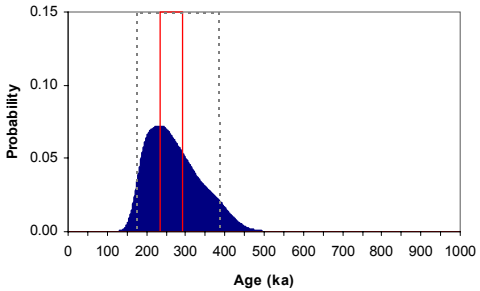

Fig. i Signal Calibration

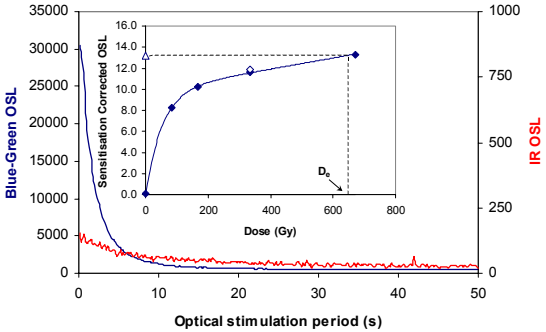

OSL signals. Detectable IR signal decays are diagnostic of feldspar contamination. Inset, the natural blue OSL signal (open triangle) of each aliquot is calibrated against known laboratory doses to yield equivalent dose (D_e) values. Repeats of low and high doses (open diamonds) illustrate the success of sensitivity correction.

Fig. ii Dose Recovery The acquisition of D_e values is necessarily predicated upon thermal treatment of aliquots succeeding environmental and laboratory irradiation. The Dose Recovery test quantifies the combined effects of thermal transfer and sensitisation on the natural signal using a precise lab dose to simulate natural dose. Based on this an appropriate thermal treatment is selected to generate the final D_e value.

Fig. iii Inter-aliquot D_e distribution Provides a measure of inter-aliquot statistical concordance in D_e values derived from **natural** irradiation. Discordant data (those points lying beyond ±2 standardised ln D_e) reflects heterogeneous dose absorption and/or inaccuracies in calibration.

Fig. iv Low and High Repeat Regenerative-dose Ratio Measures the statistical concordance of signals from repeated **low** and **high** regenerative-doses. Discordant data (those points lying beyond ±2 standardised ln D_e) indicate inaccurate sensitivity correction.

Fig. v OSL to Post-IR OSL Ratio Measures the statistical concordance of OSL and post-IR OSL responses to the same regenerative-dose. Discordant, underestimating data (those points lying below -2 standardised ln D_e) highlight the presence of significant feldspar contamination.

Fig.viSignal Analysis Statistically significant increase in **natural** D_e value with signal stimulation period is indicative of a partially-bleached signal, provided a significant increase in D_e results from **simulated partial bleaching** followed by insignificant adjustment in D_e for simulated **zero** and **full bleach** conditions. Ages from such samples are considered maximum estimates. In the absence of a significant rise in D_e with stimulation time, simulated partial bleaching and zero/full bleach tests are not assessed.

Fig. vii U Activity Statistical concordance (equilibrium) in the activities of the daughter radioisotope ^{226}Ra with its parent ^{238}U may signify the temporal stability of D_r emissions from these chains. Significant differences (disequilibrium; >50%) in activity indicate addition or removal of isotopes creating a time-dependent shift in D_r values and increased uncertainty in the accuracy of age estimates. A 20% disequilibrium marker is also shown.

Fig. viii Age Range The **mean age range** provides an estimate of sediment burial period based on mean D_e and D_r values with associated analytical uncertainties. The probability distribution indicates the inter-aliquot variability in age. The maximum influence of temporal variations in D_r forced by minima-maxima variation in moisture content and overburden thickness may prove instructive where there is uncertainty in these parameters, however the combined extremes represented should not be construed as preferred age estimates.

Fig.ii Dose Recovery

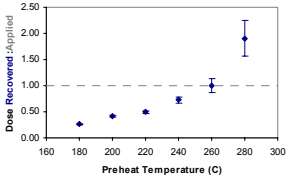

Fig. iii and iv (combined) Inter-aliquot D_e distribution

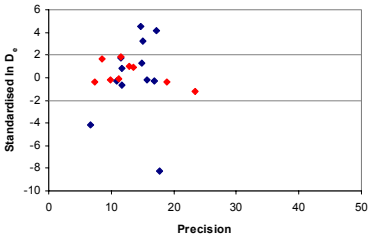

Fig. v OSL to Post-IR OSL Ratio

Not available

Appendix 4
Sample: GL08046

Fig. vi Signal Analysis

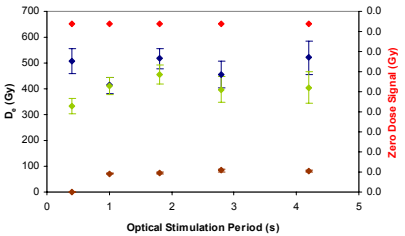

Fig. vii U Decay Activity

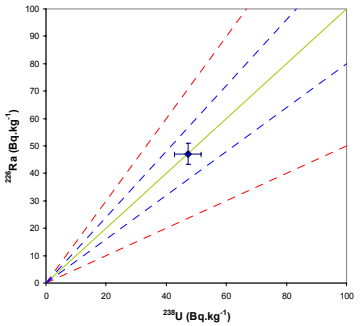

Fig. viii Age Range

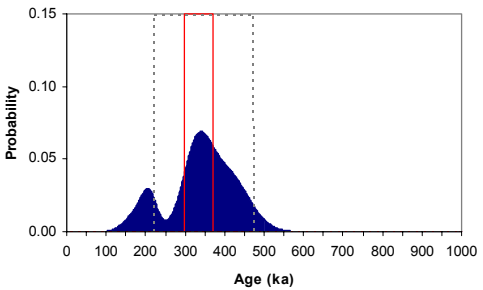

Fig. i Signal Calibration

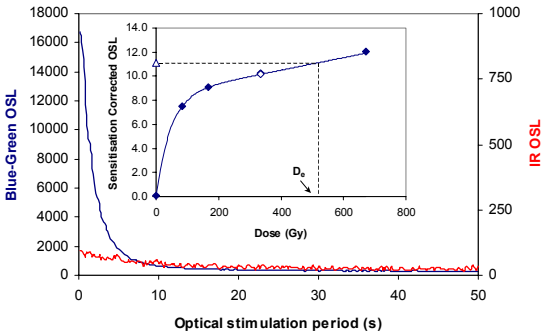

OSL signals. Detectable IR signal decays are diagnostic of feldspar contamination. Inset, the natural blue OSL signal (open triangle) of each aliquot is calibrated against known laboratory doses to yield equivalent dose (D_e) values. Repeats of low and high doses (open diamonds) illustate the success of sensitivity correction.

Fig. ii Dose Recovery The acquisition of D_e values is necessarily predicated upon thermal treatment of aliquots succeeding environmental and laboratory irradiation. The Dose Recovery test quantifies the combined effects of thermal transfer and sensitisation on the natural signal using a precise lab dose to simulate natural dose. Based on this an appropriate thermal treatment is selected to generate the final D_e value.

Fig. iii Inter-aliquot D_e distribution Provides a measure of inter-aliquot statistical concordance in D_e values derived from **natural** irradiation. Discordant data (those points lying beyond ±2 standardised ln D_e) reflects heterogeneous dose absorption and/or inaccuracies in calibration.

Fig. iv Low and High Repeat Regenerative-dose Ratio Measures the statistical concordance of signals from repeated **low** and **high** regenerative-doses. Discordant data (those points lying beyond ±2 standardised ln D_e) indicate inaccurate sensitivity correction.

Fig. v OSL to Post-IR OSL Ratio Measures the statistical concordance of OSL and post-IR OSL responses to the same regenerative-dose. Discordant, underestimating data (those points lying below -2 standardised ln D_e) highlight the presence of significant feldspar contamination.

Fig.viSignal Analysis Statistically significant increase in **natural** D_e value with signal stimulation period is indicative of a partially-bleached signal, provided a significant increase in D_e results from **simulated partial bleaching** followed by insignificant adjustment in D_e for simulated **zero** and **full bleach** conditions. Ages from such samples are considered maximum estimates. In the absence of a significant rise in D_e with stimulation time, simulated partial bleaching and zero/full bleach tests are not assessed.

Fig. vii U Activity Statistical concordance (equilibrium) in the activities of the daughter radioisotope ^{226}Ra with its parent ^{238}U may signify the temporal stability of D_r emissions from these chains. Significant differences (disequilibrium; >50%) in activity indicate addition or removal of isotopes creating a time-dependent shift in D_r values and increased uncertainty in the accuracy of age estimates. A 20% disequilibrium marker is also shown.

Fig. viii Age Range The **mean age range** provides an estimate of sediment burial period based on mean D_e and D_r values with associated analytical uncertainties. The probability distribution indicates the inter-aliquot variability in age. The maximum influence of temporal variations in D_r forced by minima-maxima variation in moisture content and overburden thickness may prove instructive where there is uncertainty in these parameters, however the combined extremes represented should not be construed as preferred age estimates.

Fig.ii Dose Recovery

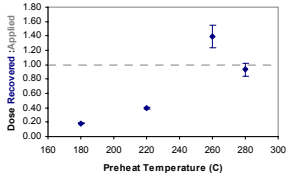

Fig. iii and iv (combined) Inter-aliquot D_e distribution

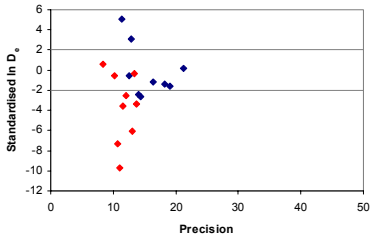

Fig. v OSL to Post-IR OSL Ratio

Not available

Appendix 5
Sample: GL08047

Fig. vi Signal Analysis

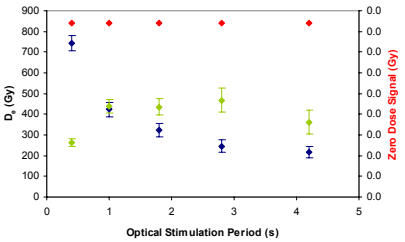

Fig. vii U Decay Activity

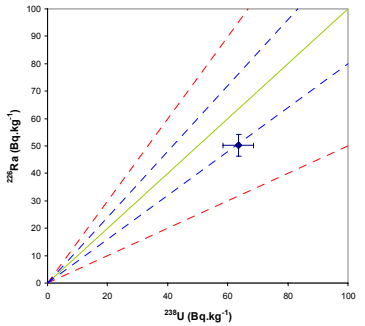

Fig. viii Age Range

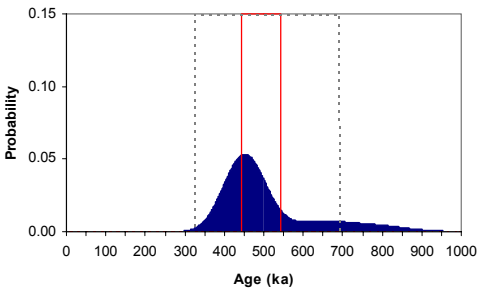

Fig. i Signal Calibration

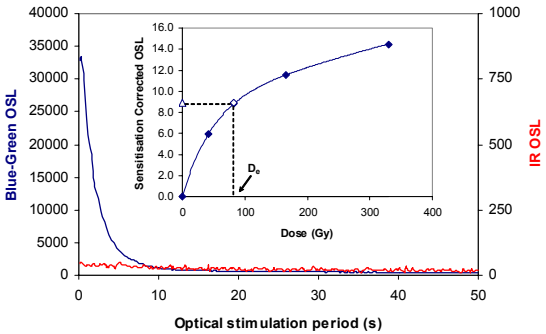

OSL signals. Detectable IR signal decays are diagnostic of feldspar contamination. Inset, the natural blue OSL signal (open triangle) of each aliquot is calibrated against known laboratory doses to yield equivalent dose (D_e) values. Repeats of low and high doses (open diamonds) illustate the success of sensitivity correction.

Fig. ii Dose Recovery The acquisition of D_e values is necessarily predicated upon thermal treatment of aliquots succeeding environmental and laboratory irradiation. The Dose Recovery test quantifies the combined effects of thermal transfer and sensitisation on the natural signal using a precise lab dose to simulate natural dose. Based on this an appropriate thermal treatment is selected to generate the final D_e value.

Fig. iii Inter-aliquot D_e distribution Provides a measure of inter-aliquot statistical concordance in D_e values derived from **natural** irradiation. Discordant data (those points lying beyond ±2 standardised ln D_e) reflects heterogeneous dose absorption and/or inaccuracies in calibration.

Fig. iv Low and High Repeat Regenerative-dose Ratio Measures the statistical concordance of signals from repeated **low** and **high** regenerative-doses. Discordant data (those points lying beyond ±2 standardised ln D_e) indicate inaccurate sensitivity correction.

Fig. v OSL to Post-IR OSL Ratio Measures the statistical concordance of OSL and post-IR OSL responses to the same regenerative-dose. Discordant, underestimating data (those points lying below -2 standardised ln D_e) highlight the presence of significant feldspar contamination.

Fig.viSignal Analysis Statistically significant increase in **natural** D_e value with signal stimulation period is indicative of a partially-bleached signal, provided a significant increase in D_e results from **simulated partial bleaching** followed by insignificant adjustment in D_e for simulated **zero** and **full bleach** conditions. Ages from such samples are considered maximum estimates. In the absence of a significant rise in D_e with stimulation time, simulated partial bleaching and zero/full bleach tests are not assessed.

Fig. vii U Activity Statistical concordance (equilibrium) in the activities of the daughter radioisotope ^{226}Ra with its parent ^{238}U may signify the temporal stability of D_r emissions from these chains. Significant differences (disequilibrium; >50%) in activity indicate addition or removal of isotopes creating a time-dependent shift in D_r values and increased uncertainty in the accuracy of age estimates. A 20% disequilibrium marker is also shown.

Fig. viii Age Range The **mean age range** provides an estimate of sediment burial period based on mean D_e and D_r values with associated analytical uncertainties. The probability distribution indicates the inter-aliquot variability in age. The maximum influence of temporal variations in D_r forced by minima-maxima variation in moisture content and overburden thickness may prove instructive where there is uncertainty in these parameters, however the combined extremes represented should not be construed as preferred age estimates.

Fig.ii Dose Recovery

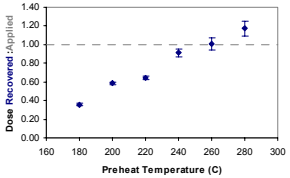

Fig. iii and iv (combined) Inter-aliquot D_e distribution

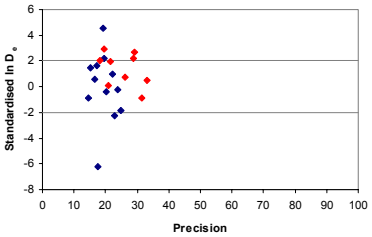

Fig. v OSL to Post-IR OSL Ratio

Not available

Appendix 6
Sample: GL09029

Fig. vi Signal Analysis

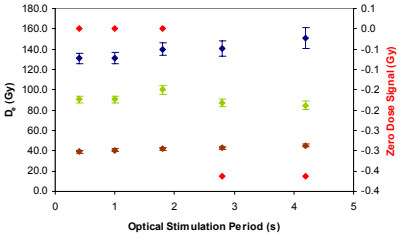

Fig. vii U Decay Activity

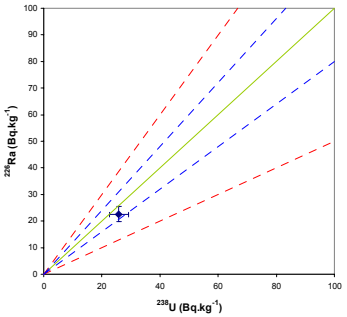

Fig. viii Age Range

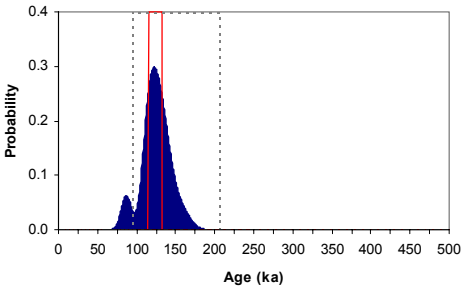

Fig. i Signal Calibration

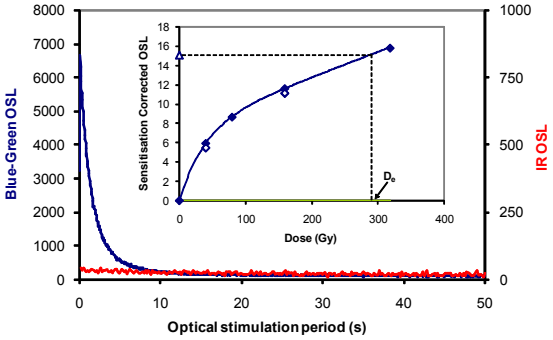

Fig. i Signal Calibration Natural blue and laboratory-induced infrared (IR) OSL signals. Detectable IR signal decays are diagnostic of feldspar contamination. Inset, the natural blue OSL signal (open triangle) of each aliquot is calibrated against known laboratory doses to yield equivalent dose (D_e) values. Repeats of low and high doses (open diamonds) illustrate the success of sensitivity correction.

Fig. ii Dose Recovery The acquisition of D_e values is necessarily predicated upon thermal treatment of aliquots succeeding environmental and laboratory irradiation. The Dose Recovery test quantifies the combined effects of thermal transfer and sensitisation on the natural signal using a precise lab dose to simulate natural dose. Based on this an appropriate thermal treatment is selected to generate the final D_e value.

Fig. iii Inter-aliquot D_e distribution Provides a measure of inter-aliquot statistical concordance in D_e values derived from **natural** irradiation. Discordant data (those points lying beyond **±2 standardised ln D_e**) reflects heterogeneous dose absorption and/or inaccuracies in calibration.

Fig. iv Low and High Repeat Regenerative-dose Ratio Measures the statistical concordance of signals from repeated **low** and **high** regenerative-doses. Discordant data (those points lying beyond **±2 standardised ln D_e**) indicate inaccurate sensitivity correction.

Fig. v OSL to Post-IR OSL Ratio Measures the statistical concordance of OSL and post-IR OSL responses to the same regenerative-dose. Discordant, underestimating data (those points lying below **-2 standardised ln D_e**) highlight the presence of significant feldspar contamination.

Fig.viSignal Analysis Statistically significant increase in **natural** D_e value with signal stimulation period is indicative of a partially-bleached signal, provided a significant increase in D_e results from **simulated partial bleaching** followed by insignificant adjustment in D_e for simulated **zero** and **full bleach** conditions. Ages from such samples are considered maximum estimates. In the absence of a significant rise in D_e with stimulation time, simulated partial bleaching and zero/full bleach tests are not assessed.

Fig. vii U Activity Statistical concordance (equilibrium) in the activities of the daughter radioisotope ^{226}Ra with its parent ^{238}U may signify the temporal stability of D_r emissions from these chains. Significant differences (disequilibrium; >50%) in activity indicate addition or removal of isotopes creating a time-dependent shift in D_r values and increased uncertainty in the accuracy of age estimates. A 20% disequilibrium marker is also shown.

Fig. viii Age Range The **mean age range** provides an estimate of sediment burial period based on mean D_e and D_r values with associated analytical uncertainties. The probability distribution indicates the inter-aliquot variability in age. The maximum influence of temporal variations in D_r forced by minima-maxima variation in moisture content and overburden thickness may prove instructive where there is uncertainty in these parameters, however the combined extremes represented should not be construed as preferred age estimates.

Fig.ii Dose Recovery

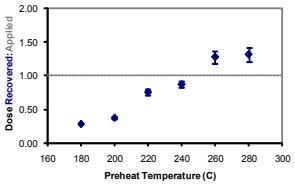

Fig. iii Inter-aliquot D_e distribution

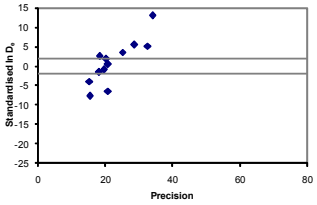

Fig. iv Low and High Repeat Regenerative-dose Ratio

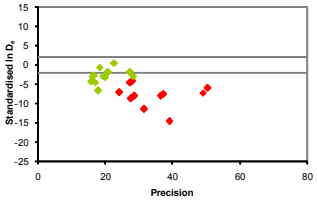

Fig. v OSL to Post-IR OSL Ratio

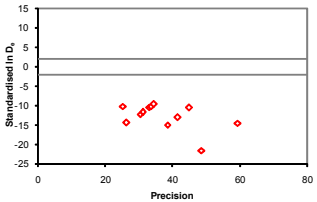

Appendix 7
Sample: GL09030

Fig. vi Signal Analysis

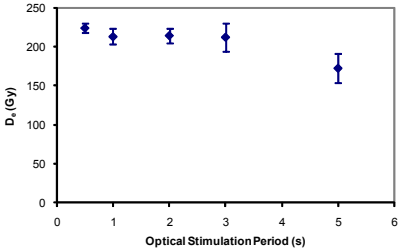

Fig. vii U Decay Activity

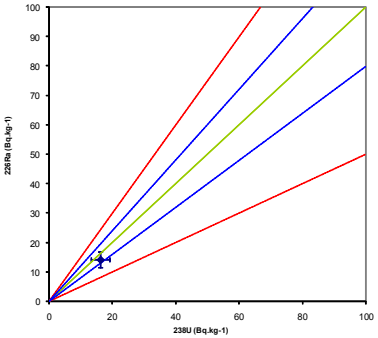

Fig. viii Age Range

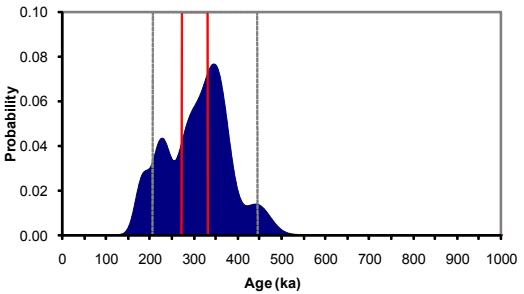

Fig. i Signal Calibration

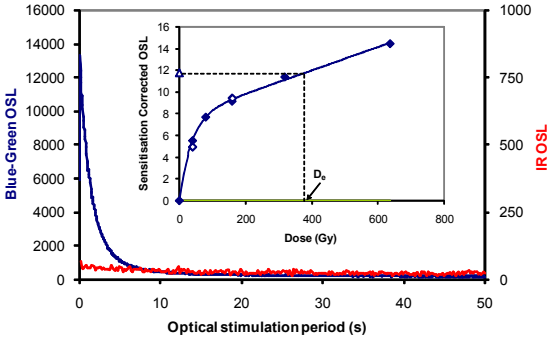

Fig. i Signal Calibration Natural blue and laboratory-induced infrared (IR) OSL signals. Detectable IR signal decays are diagnostic of feldspar contamination. Inset, the natural blue OSL signal (open triangle) of each aliquot is calibrated against known laboratory doses to yield equivalent dose (D_e) values. Repeats of low and high doses (open diamonds) illustrate the success of sensitivity correction.

Fig. ii Dose Recovery The acquisition of D_e values is necessarily predicated upon thermal treatment of aliquots succeeding environmental and laboratory irradiation. The Dose Recovery test quantifies the combined effects of thermal transfer and sensitisation on the natural signal using a precise lab dose to simulate natural dose. Based on this an appropriate thermal treatment is selected to generate the final D_e value.

Fig. iii Inter-aliquot D_e distribution Provides a measure of inter-aliquot statistical concordance in D_e values derived from **natural** irradiation. Discordant data (those points lying beyond **±2 standardised ln D_e**) reflects heterogeneous dose absorption and/or inaccuracies in calibration.

Fig. iv Low and High Repeat Regenerative-dose Ratio Measures the statistical concordance of signals from repeated **low** and **high** regenerative-doses. Discordant data (those points lying beyond **±2 standardised ln D_e**) indicate inaccurate sensitivity correction.

Fig. v OSL to Post-IR OSL Ratio Measures the statistical concordance of OSL and post-IR OSL responses to the same regenerative-dose. Discordant, underestimating data (those points lying below **-2 standardised ln D_e**) highlight the presence of significant feldspar contamination.

Fig.viSignal Analysis Statistically significant increase in **natural** D_e value with signal stimulation period is indicative of a partially-bleached signal, provided a significant increase in D_e results from **simulated partial bleaching** followed by insignificant adjustment in D_e for simulated **zero** and **full bleach** conditions. Ages from such samples are considered maximum estimates. In the absence of a significant rise in D_e with stimulation time, simulated partial bleaching and zero/full bleach tests are not assessed.

Fig. vii U Activity Statistical concordance (equilibrium) in the activities of the daughter radioisotope ^{226}Ra with its parent ^{238}U may signify the temporal stability of D_r emissions from these chains. Significant differences (disequilibrium; >50%) in activity indicate addition or removal of isotopes creating a time-dependent shift in D_r values and increased uncertainty in the accuracy of age estimates. A 20% disequilibrium marker is also shown.

Fig. viii Age Range The **mean age range** provides an estimate of sediment burial period based on mean D_e and D_r values with associated analytical uncertainties. The probability distribution indicates the inter-aliquot variability in age. The **maximum influence** of temporal variations in D_r forced by minima-maxima variation in moisture content and overburden thickness may prove instructive where there is uncertainty in these parameters, however the combined extremes represented should not be construed as preferred age estimates.

Fig.ii Dose Recovery

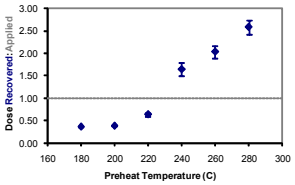

Fig. iii Inter-aliquot D_e distribution

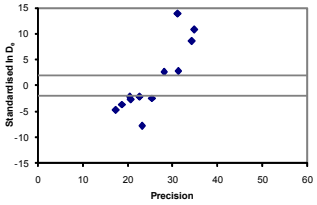

Fig. iv Low and High Repeat Regenerative-dose Ratio

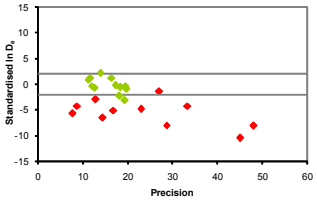

Fig. v OSL to Post-IR OSL Ratio

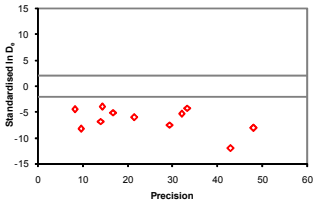

Fig. vi Signal Analysis

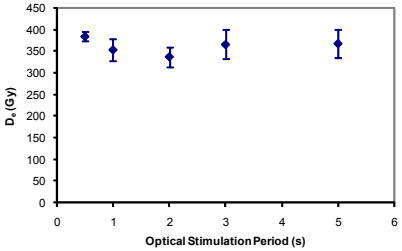

Fig. vii U Decay Activity

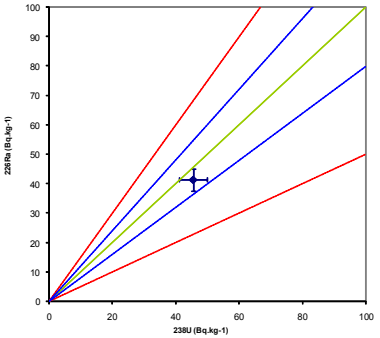

Fig. viii Age Range

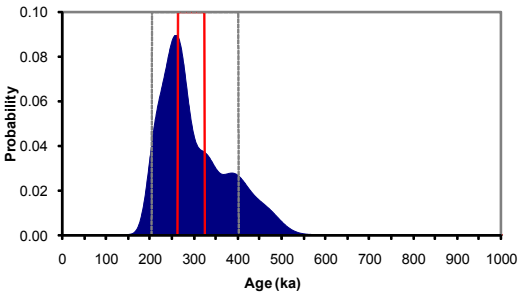

Appendix 8
Sample: GL09031

Fig. i Signal Calibration

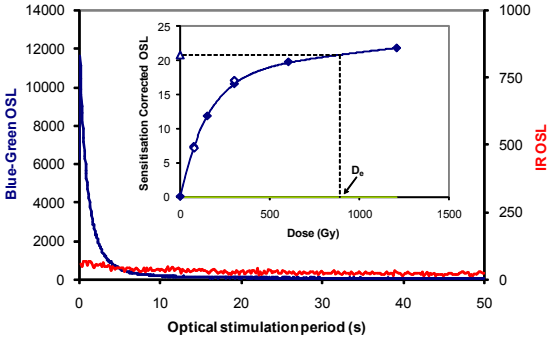

Fig. i Signal Calibration Natural blue and laboratory-induced infrared (IR) OSL signals. Detectable IR signal decays are diagnostic of feldspar contamination. Inset, the natural blue OSL signal (open triangle) of each aliquot is calibrated against known laboratory doses to yield equivalent dose (D_e) values. Repeats of low and high doses (open diamonds) illustrate the success of sensitivity correction.

Fig. ii Dose Recovery The acquisition of D_e values is necessarily predicated upon thermal treatment of aliquots succeeding environmental and laboratory irradiation. The Dose Recovery test quantifies the combined effects of thermal transfer and sensitisation on the natural signal using a precise lab dose to simulate natural dose. Based on this an appropriate thermal treatment is selected to generate the final D_e value.

Fig. iii Inter-aliquot D_e distribution Provides a measure of inter-aliquot statistical concordance in D_e values derived from **natural** irradiation. Discordant data (those points lying beyond **±2 standardised ln D_e**) reflects heterogeneous dose absorption and/or inaccuracies in calibration.

Fig. iv Low and High Repeat Regenerative-dose Ratio Measures the statistical concordance of signals from repeated **low** and **high** regenerative-doses. Discordant data (those points lying beyond **±2 standardised ln D_e**) indicate inaccurate sensitivity correction.

Fig. v OSL to Post-IR OSL Ratio Measures the statistical concordance of OSL and post-IR OSL responses to the same regenerative-dose. Discordant, underestimating data (those points lying below **-2 standardised ln D_e**) highlight the presence of significant feldspar contamination.

Fig.viSignal Analysis Statistically significant increase in **natural** D_e value with signal stimulation period is indicative of a partially-bleached signal, provided a significant increase in D_e results from **simulated partial bleaching** followed by insignificant adjustment in D_e for simulated **zero** and **full bleach** conditions. Ages from such samples are considered maximum estimates. In the absence of a significant rise in D_e with stimulation time, simulated partial bleaching and zero/full bleach tests are not assessed.

Fig. vii U Activity Statistical concordance (equilibrium) in the activities of the daughter radioisotope ^{226}Ra with its parent ^{238}U may signify the temporal stability of D_r emissions from these chains. Significant differences (disequilibrium; >50%) in activity indicate addition or removal of isotopes creating a time-dependent shift in D_r values and increased uncertainty in the accuracy of age estimates. A 20% disequilibrium marker is also shown.

Fig. viii Age Range The **mean age range** provides an estimate of sediment burial period based on mean D_e and D_r values with associated analytical uncertainties. The probability distribution indicates the inter-aliquot variability in age. The **maximum influence** of temporal variations in D_r forced by minima-maxima variation in moisture content and overburden thickness may prove instructive where there is uncertainty in these parameters, however the combined extremes represented should not be construed as preferred age estimates.

Fig.ii Dose Recovery

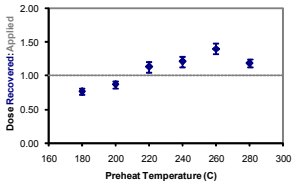

Fig. iii Inter-aliquot D_e distribution

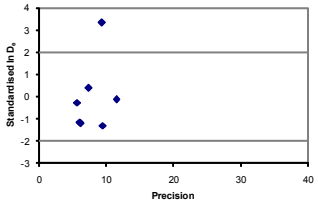

Fig. iv Low and High Repeat Regenerative-dose Ratio

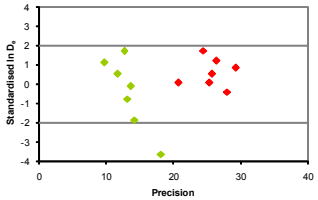

Fig. v OSL to Post-IR OSL Ratio

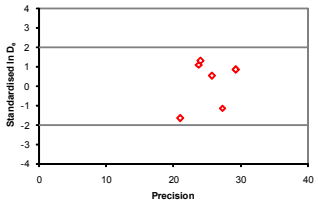

Appendix 9
Sample: GL09117

Fig. vi Signal Analysis

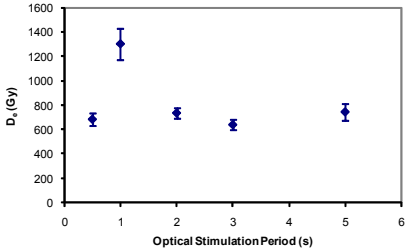

Fig. vii U Decay Activity

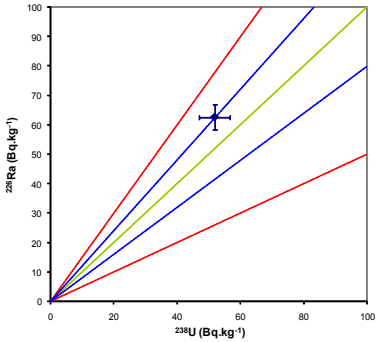

Fig. viii Age Range

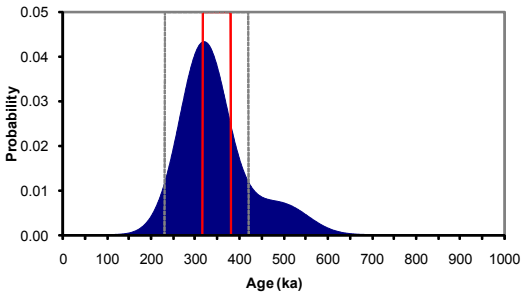

Fig. i Signal Calibration

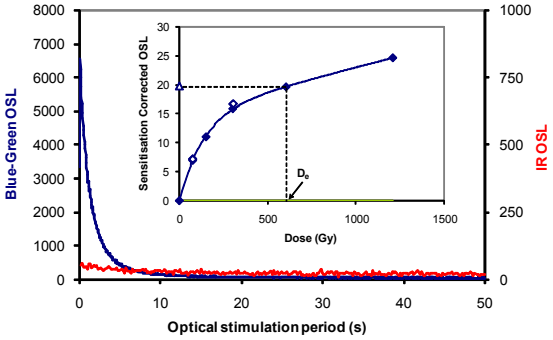

Fig. i Signal Calibration Natural blue and laboratory-induced infrared (IR) OSL signals. Detectable IR signal decays are diagnostic of feldspar contamination. Inset, the natural blue OSL signal (open triangle) of each aliquot is calibrated against known laboratory doses to yield equivalent dose (D_e) values. Repeats of low and high doses (open diamonds) illustrate the success of sensitivity correction.

Fig. ii Dose Recovery The acquisition of D_e values is necessarily predicated upon thermal treatment of aliquots succeeding environmental and laboratory irradiation. The Dose Recovery test quantifies the combined effects of thermal transfer and sensitisation on the natural signal using a precise lab dose to simulate natural dose. Based on this an appropriate thermal treatment is selected to generate the final D_e value.

Fig. iii Inter-aliquot D_e distribution Provides a measure of inter-aliquot statistical concordance in D_e values derived from **natural** irradiation. Discordant data (those points lying beyond **±2 standardised ln D_e**) reflects heterogeneous dose absorption and/or inaccuracies in calibration.

Fig. iv Low and High Repeat Regenerative-dose Ratio Measures the statistical concordance of signals from repeated **low** and **high** regenerative-doses. Discordant data (those points lying beyond **±2 standardised ln D_e**) indicate inaccurate sensitivity correction.

Fig. v OSL to Post-IR OSL Ratio Measures the statistical concordance of OSL and post-IR OSL responses to the same regenerative-dose. Discordant, underestimating data (those points lying below **-2 standardised ln D_e**) highlight the presence of significant feldspar contamination.

Fig.viSignal Analysis Statistically significant increase in **natural** D_e value with signal stimulation period is indicative of a partially-bleached signal, provided a significant increase in D_e results from **simulated partial bleaching** followed by insignificant adjustment in D_e for simulated **zero** and **full bleach** conditions. Ages from such samples are considered maximum estimates. In the absence of a significant rise in D_e with stimulation time, simulated partial bleaching and zero/full bleach tests are not assessed.

Fig. vii U Activity Statistical concordance (equilibrium) in the activities of the daughter radioisotope ^{226}Ra with its parent ^{238}U may signify the temporal stability of D_r emissions from these chains. Significant differences (disequilibrium; >50%) in activity indicate addition or removal of isotopes creating a time-dependent shift in D_r values and increased uncertainty in the accuracy of age estimates. A 20% disequilibrium marker is also shown.

Fig. viii Age Range The **mean age range** provides an estimate of sediment burial period based on mean D_e and D_r values with associated analytical uncertainties. The probability distribution indicates the inter-aliquot variability in age. The **maximum influence** of temporal variations in D_r forced by minima-maxima variation in moisture content and overburden thickness may prove instructive where there is uncertainty in these parameters, however the combined extremes represented should not be construed as preferred age estimates.

Fig.ii Dose Recovery

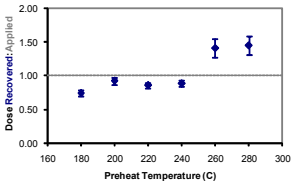

Fig. iii Inter-aliquot D_e distribution

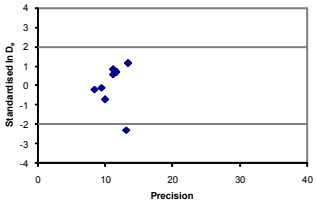

Fig. iv Low and High Repeat Regenerative-dose Ratio

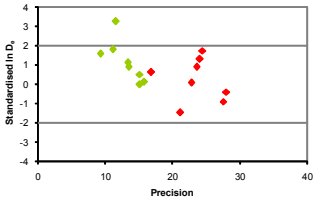

Fig. v OSL to Post-IR OSL Ratio

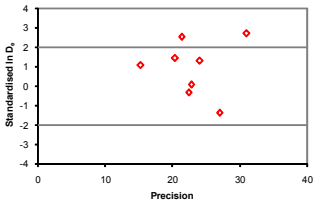

Appendix 10
Sample: GL09118

Fig. vi Signal Analysis

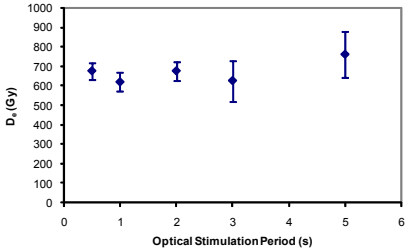

Fig. vii U Decay Activity

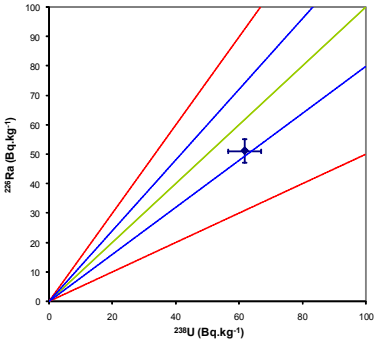

Fig. viii Age Range

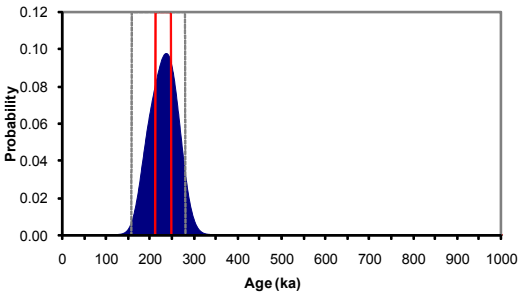

Fig. i Signal Calibration

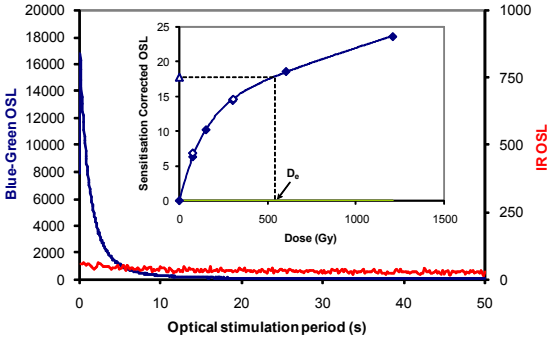

Fig. i Signal Calibration Natural blue and laboratory-induced infrared (IR) OSL signals. Detectable IR signal decays are diagnostic of feldspar contamination. Inset, the natural blue OSL signal (open triangle) of each aliquot is calibrated against known laboratory doses to yield equivalent dose (D_e) values. Repeats of low and high doses (open diamonds) illustrate the success of sensitivity correction.

Fig. ii Dose Recovery The acquisition of D_e values is necessarily predicated upon thermal treatment of aliquots succeeding environmental and laboratory irradiation. The Dose Recovery test quantifies the combined effects of thermal transfer and sensitisation on the natural signal using a precise lab dose to simulate natural dose. Based on this an appropriate thermal treatment is selected to generate the final D_e value.

Fig. iii Inter-aliquot D_e distribution Provides a measure of inter-aliquot statistical concordance in D_e values derived from **natural** irradiation. Discordant data (those points lying beyond **±2 standardised ln D_e**) reflects heterogeneous dose absorption and/or inaccuracies in calibration.

Fig. iv Low and High Repeat Regenerative-dose Ratio Measures the statistical concordance of signals from repeated **low** and **high** regenerative-doses. Discordant data (those points lying beyond **±2 standardised ln D_e**) indicate inaccurate sensitivity correction.

Fig. v OSL to Post-IR OSL Ratio Measures the statistical concordance of OSL and post-IR OSL responses to the same regenerative-dose. Discordant, underestimating data (those points lying below **-2 standardised ln D_e**) highlight the presence of significant feldspar contamination.

Fig.viSignal Analysis Statistically significant increase in **natural** D_e value with signal stimulation period is indicative of a partially-bleached signal, provided a significant increase in D_e results from **simulated partial bleaching** followed by insignificant adjustment in D_e for simulated **zero** and **full bleach** conditions. Ages from such samples are considered maximum estimates. In the absence of a significant rise in D_e with stimulation time, simulated partial bleaching and zero/full bleach tests are not assessed.

Fig. vii U Activity Statistical concordance (equilibrium) in the activities of the daughter radioisotope ^{226}Ra with its parent ^{238}U may signify the temporal stability of D_r emissions from these chains. Significant differences (disequilibrium; >50%) in activity indicate addition or removal of isotopes creating a time-dependent shift in D_r values and increased uncertainty in the accuracy of age estimates. A 20% disequilibrium marker is also shown.

Fig. viii Age Range The **mean age range** provides an estimate of sediment burial period based on mean D_e and D_r values with associated analytical uncertainties. The probability distribution indicates the inter-aliquot variability in age. The **maximum influence** of temporal variations in D_r forced by minima-maxima variation in moisture content and overburden thickness may prove instructive where there is uncertainty in these parameters, however the combined extremes represented should not be construed as preferred age estimates.

Fig.ii Dose Recovery

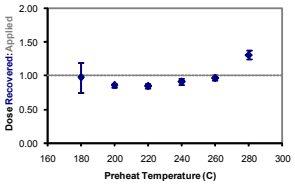

Fig. iii Inter-aliquot D_e distribution

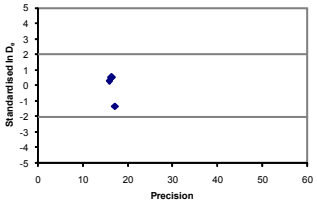

Fig. iv Low and High Repeat Regenerative-dose Ratio

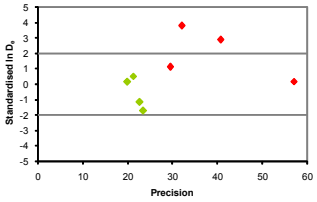

Fig. v OSL to Post-IR OSL Ratio

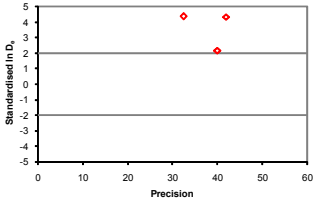

Appendix 11
Sample: GL09119

Fig. vi Signal Analysis

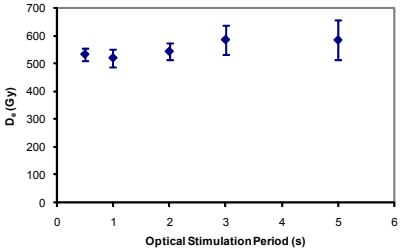

Fig. vii U Decay Activity

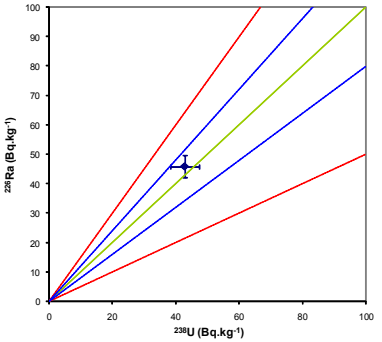

Fig. viii Age Range

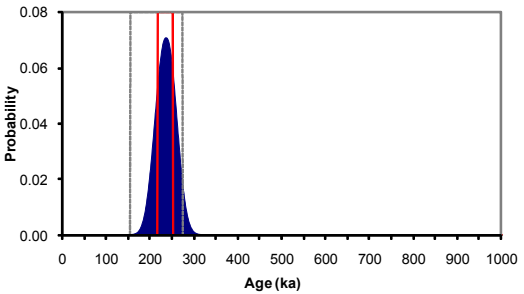

Fig. i Signal Calibration

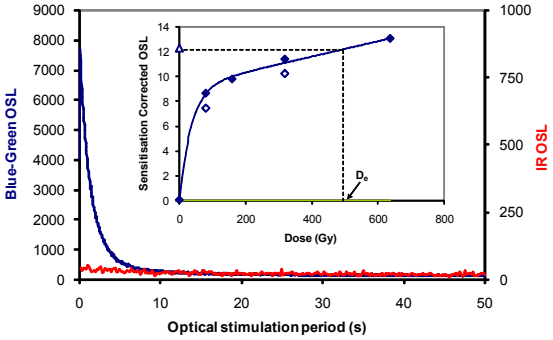

Fig. i Signal Calibration Natural blue and laboratory-induced infrared (IR) OSL signals. Detectable IR signal decays are diagnostic of feldspar contamination. Inset, the natural blue OSL signal (open triangle) of each aliquot is calibrated against known laboratory doses to yield equivalent dose (D_e) values. Repeats of low and high doses (open diamonds) illustrate the success of sensitivity correction.

Fig. ii Dose Recovery The acquisition of D_e values is necessarily predicated upon thermal treatment of aliquots succeeding environmental and laboratory irradiation. The Dose Recovery test quantifies the combined effects of thermal transfer and sensitisation on the natural signal using a precise lab dose to simulate natural dose. Based on this an appropriate thermal treatment is selected to generate the final D_e value.

Fig. iii Inter-aliquot D_e distribution Provides a measure of inter-aliquot statistical concordance in D_e values derived from **natural** irradiation. Discordant data (those points lying beyond **±2 standardised ln D_e**) reflects heterogeneous dose absorption and/or inaccuracies in calibration.

Fig. iv Low and High Repeat Regenerative-dose Ratio Measures the statistical concordance of signals from repeated **low** and **high** regenerative-doses. Discordant data (those points lying beyond **±2 standardised ln D_e**) indicate inaccurate sensitivity correction.

Fig. v OSL to Post-IR OSL Ratio Measures the statistical concordance of OSL and post-IR OSL responses to the same regenerative-dose. Discordant, underestimating data (those points lying below **-2 standardised ln D_e**) highlight the presence of significant feldspar contamination.

Fig.viSignal Analysis Statistically significant increase in **natural** D_e value with signal stimulation period is indicative of a partially-bleached signal, provided a significant increase in D_e results from **simulated partial bleaching** followed by insignificant adjustment in D_e for simulated **zero** and **full bleach** conditions. Ages from such samples are considered maximum estimates. In the absence of a significant rise in D_e with stimulation time, simulated partial bleaching and zero/full bleach tests are not assessed.

Fig. vii U Activity Statistical concordance (equilibrium) in the activities of the daughter radioisotope ^{226}Ra with its parent ^{238}U may signify the temporal stability of D_r emissions from these chains. Significant differences (disequilibrium; >50%) in activity indicate addition or removal of isotopes creating a time-dependent shift in D_r values and increased uncertainty in the accuracy of age estimates. A 20% disequilibrium marker is also shown.

Fig. viii Age Range The **mean age range** provides an estimate of sediment burial period based on mean D_e and D_r values with associated analytical uncertainties. The probability distribution indicates the inter-aliquot variability in age. The **maximum influence** of temporal variations in D_r forced by minima-maxima variation in moisture content and overburden thickness may prove instructive where there is uncertainty in these parameters, however the combined extremes represented should not be construed as preferred age estimates.

Fig.ii Dose Recovery

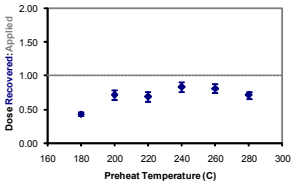

Fig. iii Inter-aliquot D_e distribution

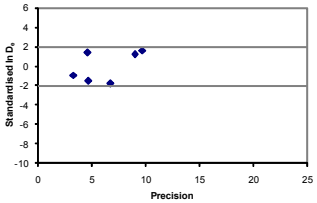

Fig. iv Low and High Repeat Regenerative-dose Ratio

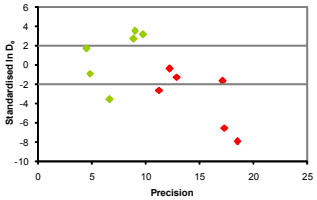

Fig. v OSL to Post-IR OSL Ratio

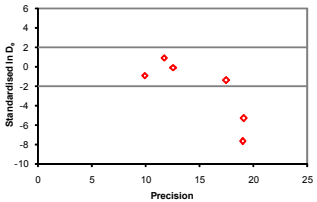

Appendix 12
Sample: GL09120

Fig. vi Signal Analysis

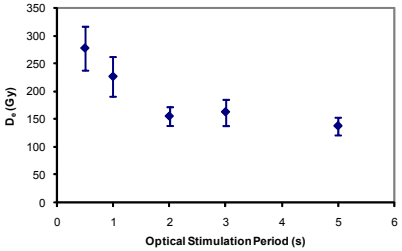

Fig. vii U Decay Activity

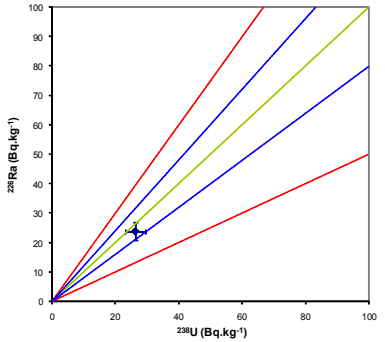

Fig. viii Age Range

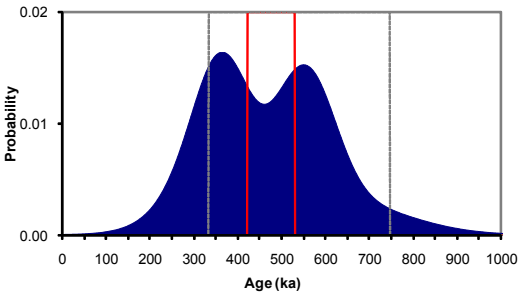

Fig. i Signal Calibration

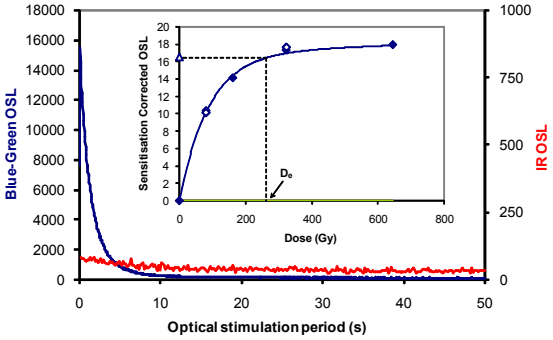

Fig. i Signal Calibration Natural blue and laboratory-induced infrared (IR) OSL signals. Detectable IR signal decays are diagnostic of feldspar contamination. Inset, the natural blue OSL signal (open triangle) of each aliquot is calibrated against known laboratory doses to yield equivalent dose (D_e) values. Repeats of low and high doses (open diamonds) illustrate the success of sensitivity correction.

Fig. ii Dose Recovery The acquisition of D_e values is necessarily predicated upon thermal treatment of aliquots succeeding environmental and laboratory irradiation. The Dose Recovery test quantifies the combined effects of thermal transfer and sensitisation on the natural signal using a precise lab dose to simulate natural dose. Based on this an appropriate thermal treatment is selected to generate the final D_e value.

Fig. iii Inter-aliquot D_e distribution Provides a measure of inter-aliquot statistical concordance in D_e values derived from **natural** irradiation. Discordant data (those points lying beyond **±2 standardised ln D_e**) reflects heterogeneous dose absorption and/or inaccuracies in calibration.

Fig. iv Low and High Repeat Regenerative-dose Ratio Measures the statistical concordance of signals from repeated **low** and **high** regenerative-doses. Discordant data (those points lying beyond **±2 standardised ln D_e**) indicate inaccurate sensitivity correction.

Fig. v OSL to Post-IR OSL Ratio Measures the statistical concordance of OSL and post-IR OSL responses to the same regenerative-dose. Discordant, underestimating data (those points lying below **-2 standardised ln D_e**) highlight the presence of significant feldspar contamination.

Fig.viSignal Analysis Statistically significant increase in **natural** D_e value with signal stimulation period is indicative of a partially-bleached signal, provided a significant increase in D_e results from **simulated partial bleaching** followed by insignificant adjustment in D_e for simulated **zero** and **full bleach** conditions. Ages from such samples are considered maximum estimates. In the absence of a significant rise in D_e with stimulation time, simulated partial bleaching and zero/full bleach tests are not assessed.

Fig. vii U Activity Statistical concordance (equilibrium) in the activities of the daughter radioisotope ^{226}Ra with its parent ^{238}U may signify the temporal stability of D_r emissions from these chains. Significant differences (disequilibrium; >50%) in activity indicate addition or removal of isotopes creating a time-dependent shift in D_r values and increased uncertainty in the accuracy of age estimates. A 20% disequilibrium marker is also shown.

Fig. viii Age Range The **mean age range** provides an estimate of sediment burial period based on mean D_e and D_r values with associated analytical uncertainties. The probability distribution indicates the inter-aliquot variability in age. The maximum influence of temporal variations in D_r forced by minima-maxima variation in moisture content and overburden thickness may prove instructive where there is uncertainty in these parameters, however the combined extremes represented should not be construed as preferred age estimates.

Fig.ii Dose Recovery

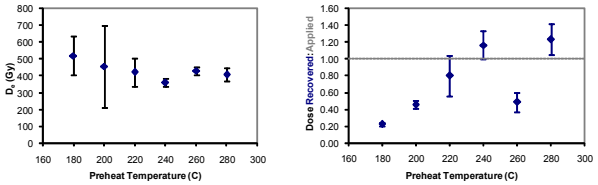

Fig. iii Inter-aliquot D_e distribution

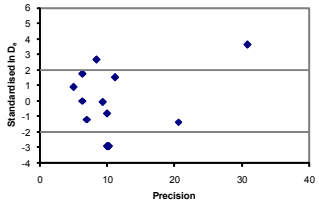

Fig. iv Low and High Repeat Regenerative-dose Ratio

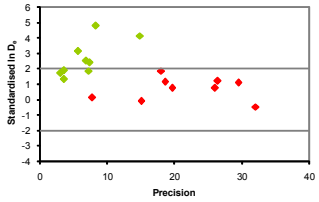

Fig. v OSL to Post-IR OSL Ratio

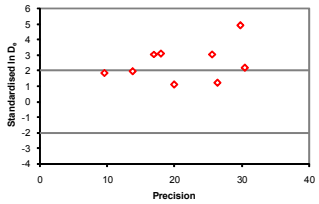

Appendix 13
Sample: GL10013

Fig. vi Signal Analysis

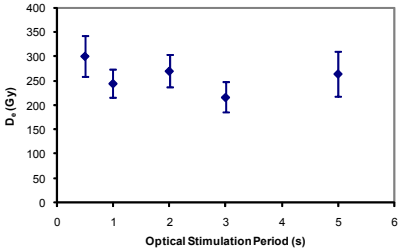

Fig. vii U Decay Activity

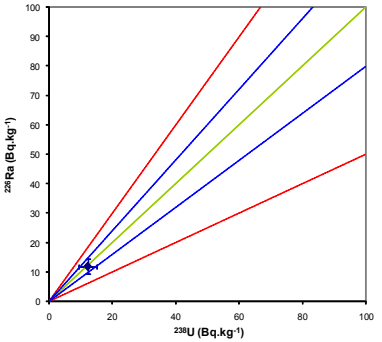

Fig. viii Age Range

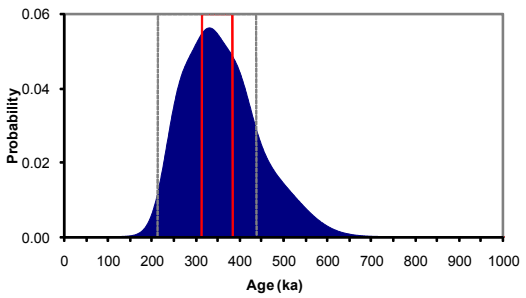

Fig. i Signal Calibration

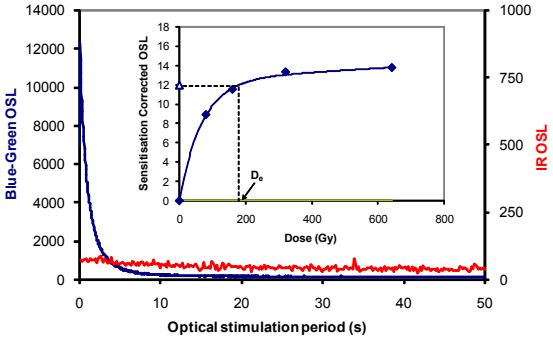

Fig. i Signal Calibration Natural blue and laboratory-induced infrared (IR) OSL signals. Detectable IR signal decays are diagnostic of feldspar contamination. Inset, the natural blue OSL signal (open triangle) of each aliquot is calibrated against known laboratory doses to yield equivalent dose (D_e) values. Repeats of low and high doses (open diamonds) illustrate the success of sensitivity correction.

Fig. ii Dose Recovery The acquisition of D_e values is necessarily predicated upon thermal treatment of aliquots succeeding environmental and laboratory irradiation. The Dose Recovery test quantifies the combined effects of thermal transfer and sensitisation on the natural signal using a precise lab dose to simulate natural dose. Based on this an appropriate thermal treatment is selected to generate the final D_t value.

Fig. iii Inter-aliquot D_e distribution Provides a measure of inter-aliquot statistical concordance in D_e values derived from **natural** irradiation. Discordant data (those points lying beyond **±2 standardised ln D_e**) reflects heterogeneous dose absorption and/or inaccuracies in calibration.

Fig. iv Low and High Repeat Regenerative-dose Ratio Measures the statistical concordance of signals from repeated **low** and **high** regenerative-doses. Discordant data (those points lying beyond **±2 standardised ln D_e**) indicate inaccurate sensitivity correction.

Fig. v OSL to Post-IR OSL Ratio Measures the statistical concordance of OSL and post-IR OSL responses to the same regenerative-dose. Discordant, underestimating data (those points lying below **-2 standardised ln D_e**) highlight the presence of significant feldspar contamination.

Fig.viSignal Analysis Statistically significant increase in **natural** D_e value with signal stimulation period is indicative of a partially-bleached signal, provided a significant increase in D_e results from **simulated partial bleaching** followed by insignificant adjustment in D_e for simulated **zero** and **full bleach** conditions. Ages from such samples are considered maximum estimates. In the absence of a significant rise in D_e with stimulation time, simulated partial bleaching and zero/full bleach tests are not assessed.

Fig. vii U Activity Statistical concordance (equilibrium) in the activities of the daughter radioisotope ^{226}Ra with its parent ^{238}U may signify the temporal stability of D_r emissions from these chains. Significant differences (disequilibrium; >50%) in activity indicate addition or removal of isotopes creating a time-dependent shift in D_r values and increased uncertainty in the accuracy of age estimates. A 20% disequilibrium marker is also shown.

Fig. viii Age Range The **mean age range** provides an estimate of sediment burial period based on mean D_e and D_r values with associated analytical uncertainties. The probability distribution indicates the inter-aliquot variability in age. The **maximum influence** of temporal variations in D_r forced by minima-maxima variation in moisture content and overburden thickness may prove instructive where there is uncertainty in these parameters, however the combined extremes represented should not be construed as preferred age estimates.

Fig.ii Dose Recovery

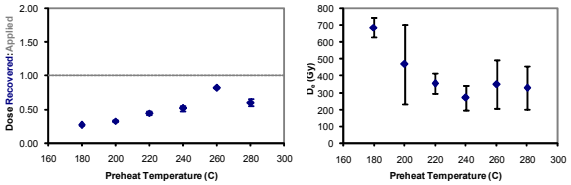

Fig. iii Inter-aliquot D_e distribution

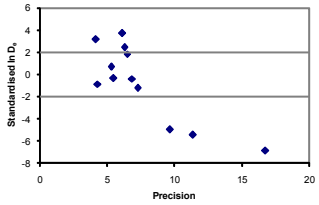

Fig. iv Low and High Repeat Regenerative-dose Ratio

Not available

Fig. v OSL to Post-IR OSL Ratio

Not available

Appendix 14
Sample: GL10014

Fig. vi Signal Analysis

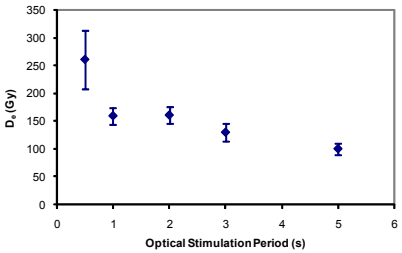

Fig. vii U Decay Activity

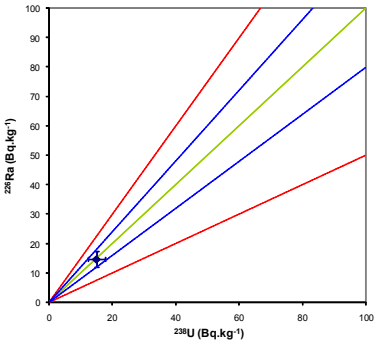

Fig. viii Age Range

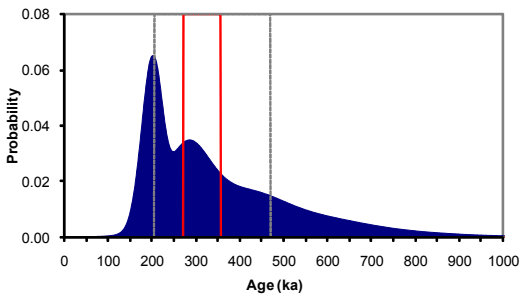

Fig. i Signal Calibration

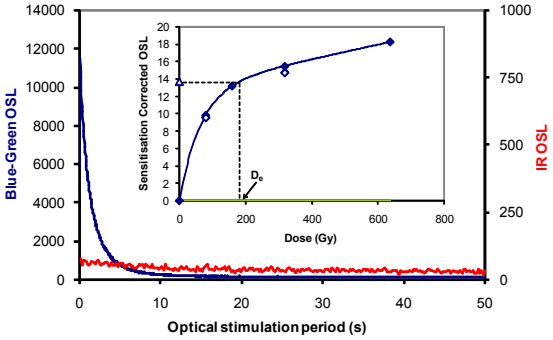

Fig. i Signal Calibration Natural blue and laboratory-induced infrared (IR) OSL signals. Detectable IR signal decays are diagnostic of feldspar contamination. Inset, the natural blue OSL signal (open triangle) of each aliquot is calibrated against known laboratory doses to yield equivalent dose (D_e) values. Repeats of low and high doses (open diamonds) illustrate the success of sensitivity correction.

Fig. ii Dose Recovery The acquisition of D_e values is necessarily predicated upon thermal treatment of aliquots succeeding environmental and laboratory irradiation. The Dose Recovery test quantifies the combined effects of thermal transfer and sensitisation on the natural signal using a precise lab dose to simulate natural dose. Based on this an appropriate thermal treatment is selected to generate the final D_e value.

Fig. iii Inter-aliquot D_e distribution Provides a measure of inter-aliquot statistical concordance in D_e values derived from **natural** irradiation. Discordant data (those points lying beyond **±2 standardised ln D_e**) reflects heterogeneous dose absorption and/or inaccuracies in calibration.

Fig. iv Low and High Repeat Regenerative-dose Ratio Measures the statistical concordance of signals from repeated **low** and **high** regenerative-doses. Discordant data (those points lying beyond **±2 standardised ln D_e**) indicate inaccurate sensitivity correction.

Fig. v OSL to Post-IR OSL Ratio Measures the statistical concordance of OSL and post-IR OSL responses to the same regenerative-dose. Discordant, underestimating data (those points lying below **-2 standardised ln D_e**) highlight the presence of significant feldspar contamination.

Fig.viSignal Analysis Statistically significant increase in **natural** D_e value with signal stimulation period is indicative of a partially-bleached signal, provided a significant increase in D_e results from **simulated partial bleaching** followed by insignificant adjustment in D_e for simulated **zero** and **full bleach** conditions. Ages from such samples are considered maximum estimates. In the absence of a significant rise in D_e with stimulation time, simulated partial bleaching and zero/full bleach tests are not assessed.

Fig. vii U Activity Statistical concordance (equilibrium) in the activities of the daughter radioisotope ^{226}Ra with its parent ^{238}U may signify the temporal stability of D_r emissions from these chains. Significant differences (disequilibrium; >50%) in activity indicate addition or removal of isotopes creating a time-dependent shift in D_r values and increased uncertainty in the accuracy of age estimates. A 20% disequilibrium marker is also shown.

Fig. viii Age Range The **mean age range** provides an estimate of sediment burial period based on mean D_e and D_r values with associated analytical uncertainties. The probability distribution indicates the inter-aliquot variability in age. The **maximum influence** of temporal variations in D_r forced by minima-maxima variation in moisture content and overburden thickness may prove instructive where there is uncertainty in these parameters, however the combined extremes represented should not be construed as preferred age estimates.

Fig.ii Dose Recovery

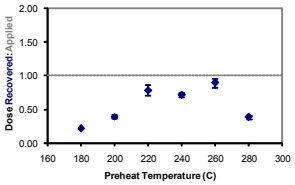

Fig. iii Inter-aliquot D_e distribution

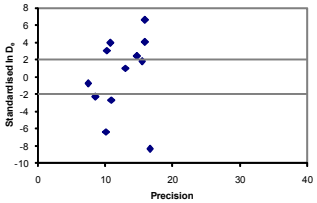

Fig. iv Low and High Repeat Regenerative-dose Ratio

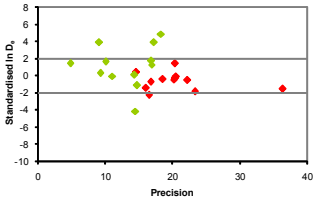

Fig. v OSL to Post-IR OSL Ratio

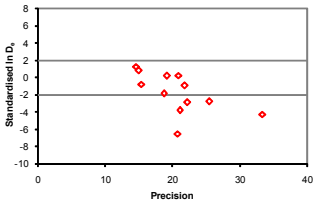

Appendix 15
Sample: GL10015

Fig. vi Signal Analysis

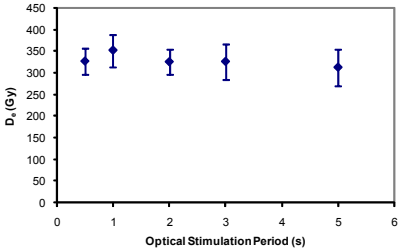

Fig. vii U Decay Activity

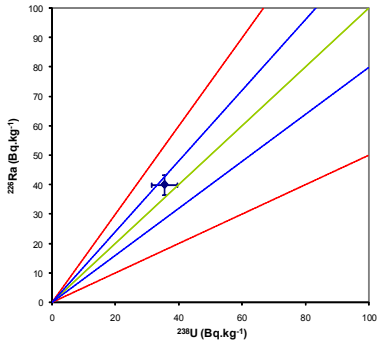

Fig. viii Age Range

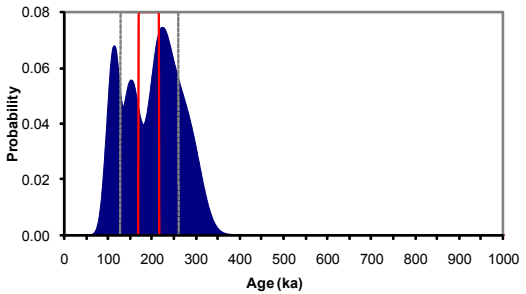

Fig. i Signal Calibration

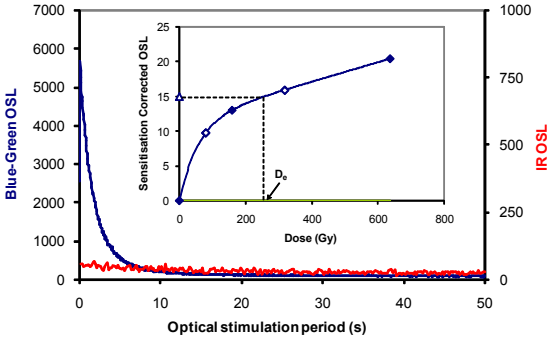

Fig. i Signal Calibration Natural blue and laboratory-induced infrared (IR) OSL signals. Detectable IR signal decays are diagnostic of feldspar contamination. Inset, the natural blue OSL signal (open triangle) of each aliquot is calibrated against known laboratory doses to yield equivalent dose (D_e) values. Repeats of low and high doses (open diamonds) illustrate the success of sensitivity correction.

Fig. ii Dose Recovery The acquisition of D_e values is necessarily predicated upon thermal treatment of aliquots succeeding environmental and laboratory irradiation. The Dose Recovery test quantifies the combined effects of thermal transfer and sensitisation on the natural signal using a precise lab dose to simulate natural dose. Based on this an appropriate thermal treatment is selected to generate the final D_e value.

Fig. iii Inter-aliquot D_e distribution Provides a measure of inter-aliquot statistical concordance in D_e values derived from **natural** irradiation. Discordant data (those points lying beyond **±2 standardised ln D_e**) reflects heterogeneous dose absorption and/or inaccuracies in calibration.

Fig. iv Low and High Repeat Regenerative-dose Ratio Measures the statistical concordance of signals from repeated **low** and **high** regenerative-doses. Discordant data (those points lying beyond **±2 standardised ln D_e**) indicate inaccurate sensitivity correction.

Fig. v OSL to Post-IR OSL Ratio Measures the statistical concordance of OSL and post-IR OSL responses to the same regenerative-dose. Discordant, underestimating data (those points lying below **-2 standardised ln D_e**) highlight the presence of significant feldspar contamination.

Fig.viSignal Analysis Statistically significant increase in **natural** D_e value with signal stimulation period is indicative of a partially-bleached signal, provided a significant increase in D_e results from **simulated partial bleaching** followed by insignificant adjustment in D_e for simulated **zero** and **full bleach** conditions. Ages from such samples are considered maximum estimates. In the absence of a significant rise in D_e with stimulation time, simulated partial bleaching and zero/full bleach tests are not assessed.

Fig. vii U Activity Statistical concordance (equilibrium) in the activities of the daughter radioisotope ^{226}Ra with its parent ^{238}U may signify the temporal stability of D_r emissions from these chains. Significant differences (disequilibrium; >50%) in activity indicate addition or removal of isotopes creating a time-dependent shift in D_r values and increased uncertainty in the accuracy of age estimates. A 20% disequilibrium marker is also shown.

Fig. viii Age Range The **mean age range** provides an estimate of sediment burial period based on mean D_e and D_r values with associated analytical uncertainties. The probability distribution indicates the inter-aliquot variability in age. The **maximum influence** of temporal variations in D_r forced by minima-maxima variation in moisture content and overburden thickness may prove instructive where there is uncertainty in these parameters, however the combined extremes represented should not be construed as preferred age estimates.

Fig.ii Dose Recovery

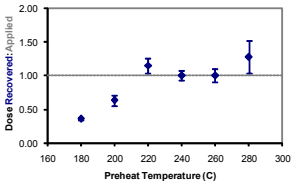

Fig. iii Inter-aliquot D_e distribution

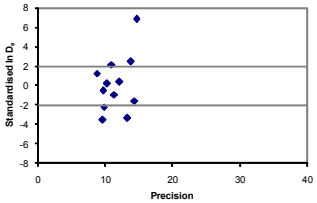

Fig. iv Low and High Repeat Regenerative-dose Ratio

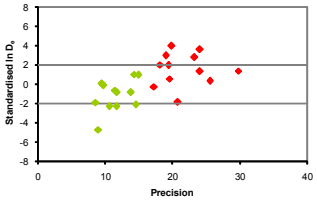

Fig. v OSL to Post-IR OSL Ratio

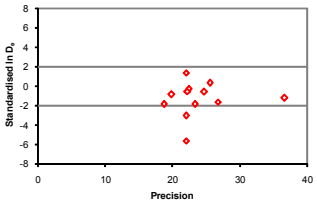

Appendix 16
Sample: GL10016

Fig. vi Signal Analysis

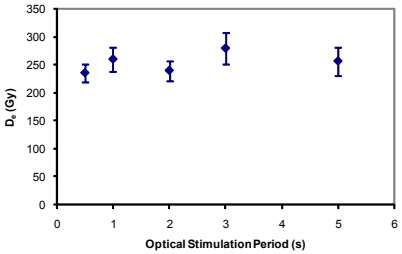

Fig. vii U Decay Activity

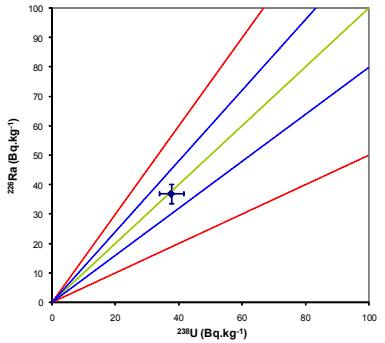

Fig. viii Age Range

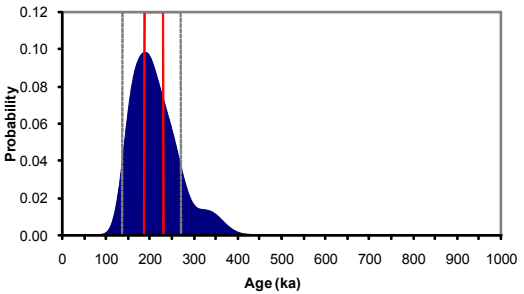

Fig. i Signal Calibration

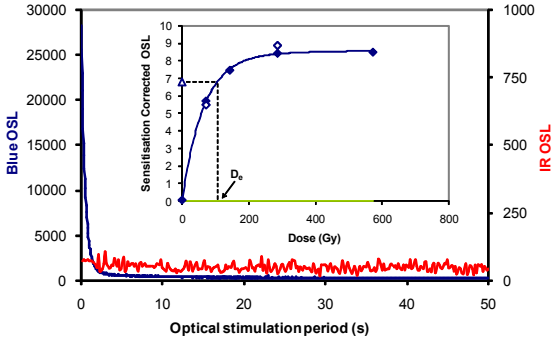

Fig. i Signal Calibration Natural blue and laboratory-induced infrared (IR) OSL signals. Detectable IR signal decays are diagnostic of feldspar contamination. Inset, the natural blue OSL signal (open triangle) of each aliquot is calibrated against known laboratory doses to yield equivalent dose (D_e) values. Repeats of low and high doses (open diamonds) illustrate the success of sensitivity correction.

Fig. ii Dose Recovery The acquisition of D_e values is necessarily predicated upon thermal treatment of aliquots succeeding environmental and laboratory irradiation. The Dose Recovery test quantifies the combined effects of thermal transfer and sensitisation on the natural signal using a precise lab dose to simulate natural dose. Based on this an appropriate thermal treatment is selected to generate the final D_e value.

Fig. iii Inter-aliquot D_e distribution Provides a measure of inter-aliquot statistical concordance in D_e values derived from **natural** irradiation. Discordant data (those points lying beyond **±2 standardised ln D_e**) reflects heterogeneous dose absorption and/or inaccuracies in calibration.

Fig. iv Low and High Repeat Regenerative-dose Ratio Measures the statistical concordance of signals from repeated **low** and **high** regenerative-doses. Discordant data (those points lying beyond **±2 standardised ln D_e**) indicate inaccurate sensitivity correction.

Fig. v OSL to Post-IR OSL Ratio Measures the statistical concordance of OSL and post-IR OSL responses to the same regenerative-dose. Discordant, underestimating data (those points lying below **-2 standardised ln D_e**) highlight the presence of significant feldspar contamination.

Fig.viSignal Analysis Statistically significant increase in **natural** D_e value with signal stimulation period is indicative of a partially-bleached signal, provided a significant increase in D_e results from **simulated partial bleaching** followed by insignificant adjustment in D_e for simulated **zero** and **full bleach** conditions. Ages from such samples are considered maximum estimates. In the absence of a significant rise in D_e with stimulation time, simulated partial bleaching and zero/full bleach tests are not assessed.

Fig. vii U Activity Statistical concordance (equilibrium) in the activities of the daughter radioisotope ^{226}Ra with its parent ^{238}U may signify the temporal stability of D_r emissions from these chains. Significant differences (disequilibrium; >50%) in activity indicate addition or removal of isotopes creating a time-dependent shift in D_r values and increased uncertainty in the accuracy of age estimates. A 20% disequilibrium marker is also shown.

Fig. viii Age Range The **mean age range** provides an estimate of sediment burial period based on mean D_e and D_r values with associated analytical uncertainties. The probability distribution indicates the inter-aliquot variability in age. The **maximum influence** of temporal variations in D_r forced by minima-maxima variation in moisture content and overburden thickness may prove instructive where there is uncertainty in these parameters, however the combined extremes represented should not be construed as preferred age estimates.

Fig.ii Dose Recovery

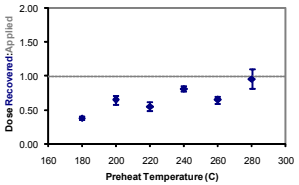

Fig. iii Inter-aliquot D_e distribution

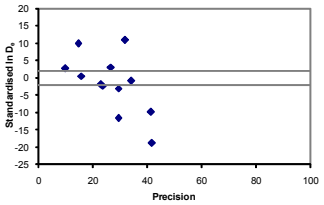

Fig. iv Low and High Repeat Regenerative-dose Ratio

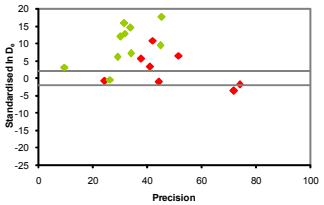

Fig. v OSL to Post-IR OSL Ratio

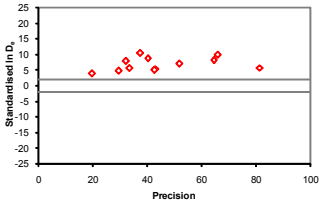

Appendix 17a
Sample: GL10001
Laboratory A

Fig. vi Signal Analysis

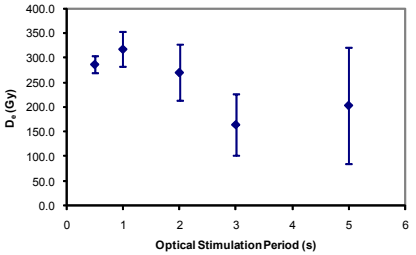

Fig. vii U Decay Activity

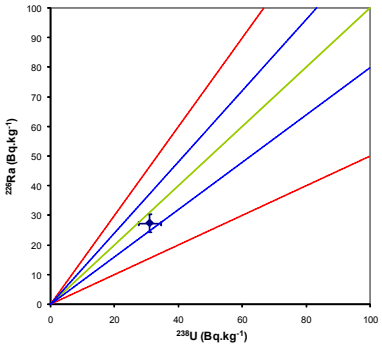

Fig. viii Age Range

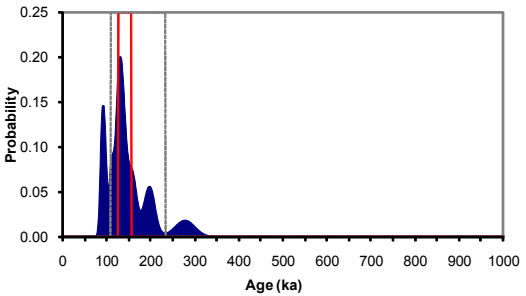

Fig. i Signal Calibration

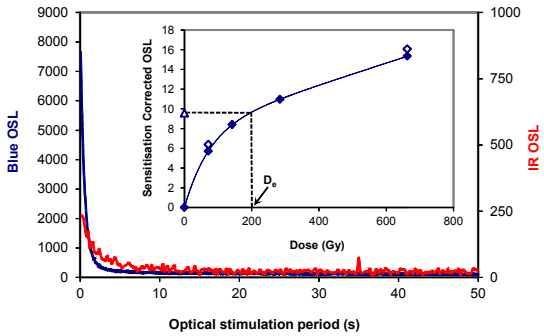

Fig. i Signal Calibration Natural blue and laboratory-induced infrared (IR) OSL signals. Detectable IR signal decays are diagnostic of feldspar contamination. Inset, the natural blue OSL signal (open triangle) of each aliquot is calibrated against known laboratory doses to yield equivalent dose (D_e) values. Repeats of low and high doses (open diamonds) illustrate the success of sensitivity correction.

Fig. ii Dose Recovery The acquisition of D_e values is necessarily predicated upon thermal treatment of aliquots succeeding environmental and laboratory irradiation. The Dose Recovery test quantifies the combined effects of thermal transfer and sensitisation on the natural signal using a precise lab dose to simulate natural dose. Based on this an appropriate thermal treatment is selected to generate the final D_e value.

Fig. iii Inter-aliquot D_e distribution Provides a measure of inter-aliquot statistical concordance in D_e values derived from **natural** irradiation. Discordant data (those points lying beyond **±2 standardised ln D_e**) reflects heterogeneous dose absorption and/or inaccuracies in calibration.

Fig. iv Low and High Repeat Regenerative-dose Ratio Measures the statistical concordance of signals from repeated **low** and **high** regenerative-doses. Discordant data (those points lying beyond **±2 standardised ln D_e**) indicate inaccurate sensitivity correction.

Fig. v OSL to Post-IR OSL Ratio Measures the statistical concordance of OSL and post-IR OSL responses to the same regenerative-dose. Discordant, underestimating data (those points lying below **-2 standardised ln D_e**) highlight the presence of significant feldspar contamination.

Fig.viSignal Analysis Statistically significant increase in **natural** D_e value with signal stimulation period is indicative of a partially-bleached signal, provided a significant increase in D_e results from **simulated partial bleaching** followed by insignificant adjustment in D_e for simulated **zero** and **full bleach** conditions. Ages from such samples are considered maximum estimates. In the absence of a significant rise in D_e with stimulation time, simulated partial bleaching and zero/full bleach tests are not assessed.

Fig. vii U Activity Statistical concordance (equilibrium) in the activities of the daughter radioisotope ^{226}Ra with its parent ^{238}U may signify the temporal stability of D_r emissions from these chains. Significant differences (disequilibrium; >50%) in activity indicate addition or removal of isotopes creating a time-dependent shift in D_r values and increased uncertainty in the accuracy of age estimates. A 20% disequilibrium marker is also shown.

Fig. viii Age Range The **mean age range** provides an estimate of sediment burial period based on mean D_e and D_r values with associated analytical uncertainties. The probability distribution indicates the inter-aliquot variability in age. The **maximum influence** of temporal variations in D_r forced by minima-maxima variation in moisture content and overburden thickness may prove instructive where there is uncertainty in these parameters, however the combined extremes represented should not be construed as preferred age estimates.

Fig.ii Dose Recovery

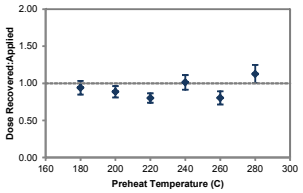

Fig. iii Inter-aliquot D_e distribution

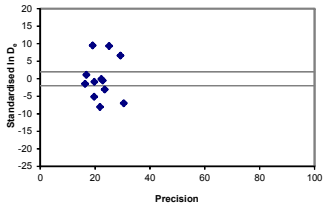

Fig. iv Low and High Repeat Regenerative-dose Ratio

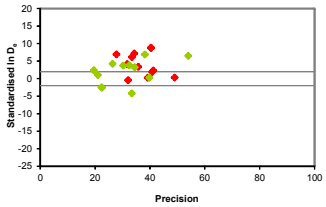

Fig. v OSL to Post-IR OSL Ratio

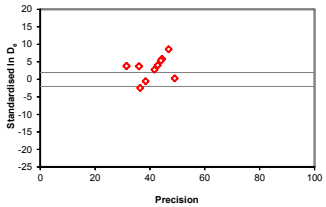

Appendix 17b
Sample: GL10001
Laboratory B

Fig. vi Signal Analysis

Not applicable to inter-laboratory comparison

Fig. vii U Decay Activity

Not applicable to inter-laboratory comparison

Fig. viii Age Range

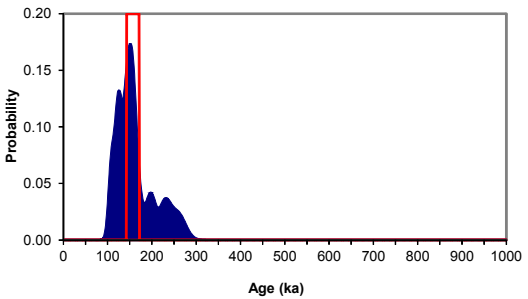

Fig. i Signal Calibration

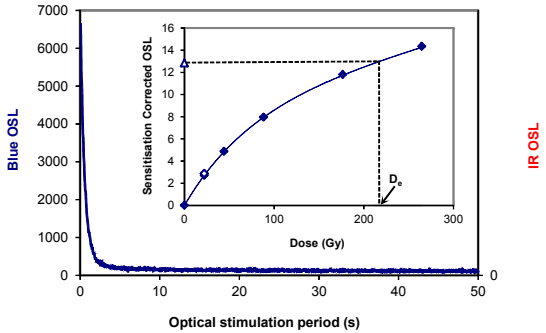

Fig. i Signal Calibration Natural blue and laboratory-induced infrared (IR) OSL signals. Detectable IR signal decays are diagnostic of feldspar contamination. Inset, the natural blue OSL signal (open triangle) of each aliquot is calibrated against known laboratory doses to yield equivalent dose (D_e) values. Repeats of low and high doses (open diamonds) illustrate the success of sensitivity correction.

Fig. ii Dose Recovery The acquisition of D_e values is necessarily predicated upon thermal treatment of aliquots succeeding environmental and laboratory irradiation. The Dose Recovery test quantifies the combined effects of thermal transfer and sensitisation on the natural signal using a precise lab dose to simulate natural dose. Based on this an appropriate thermal treatment is selected to generate the final D_e value.

Fig. iii Inter-aliquot D_e distribution Provides a measure of inter-aliquot statistical concordance in D_e values derived from **natural** irradiation. Discordant data (those points lying beyond **±2 standardised ln D_e**) reflects heterogeneous dose absorption and/or inaccuracies in calibration.

Fig. iv Low and High Repeat Regenerative-dose Ratio Measures the statistical concordance of signals from repeated **low** and **high** regenerative-doses. Discordant data (those points lying beyond **±2 standardised ln D_e**) indicate inaccurate sensitivity correction.

Fig. v OSL to Post-IR OSL Ratio Measures the statistical concordance of OSL and post-IR OSL responses to the same regenerative-dose. Discordant, underestimating data (those points lying below **-2 standardised ln D_e**) highlight the presence of significant feldspar contamination.

Fig.viSignal Analysis Statistically significant increase in **natural** D_e value with signal stimulation period is indicative of a partially-bleached signal, provided a significant increase in D_e results from **simulated partial bleaching** followed by insignificant adjustment in D_e for simulated **zero** and **full bleach** conditions. Ages from such samples are considered maximum estimates. In the absence of a significant rise in D_e with stimulation time, simulated partial bleaching and zero/full bleach tests are not assessed.

Fig. vii U Activity Statistical concordance (equilibrium) in the activities of the daughter radioisotope ^{226}Ra with its parent ^{238}U may signify the temporal stability of D_r emissions from these chains. Significant differences (disequilibrium; >50%) in activity indicate addition or removal of isotopes creating a time-dependent shift in D_r values and increased uncertainty in the accuracy of age estimates. A 20% disequilibrium marker is also shown.

Fig. viii Age Range The **mean age range** provides an estimate of sediment burial period based on mean D_e and D_r values with associated analytical uncertainties. The probability distribution indicates the inter-aliquot variability in age. The **maximum influence** of temporal variations in D_r forced by minima-maxima variation in moisture content and overburden thickness may prove instructive where there is uncertainty in these parameters, however the combined extremes represented should not be construed as preferred age estimates.

Fig.ii Dose Recovery

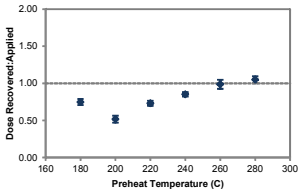

Fig. iii Inter-aliquot D_e distribution

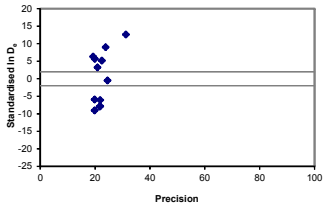

Fig. iv Low and High Repeat Regenerative-dose Ratio

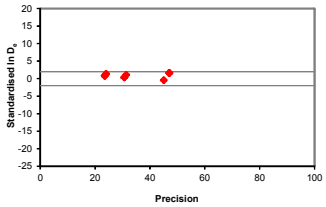

Fig. v OSL to Post-IR OSL Ratio

Not measured

Fig. vi Signal Analysis

Not applicable to inter-laboratory comparison

Fig. vii U Decay Activity

Not applicable to inter-laboratory comparison

Fig. viii Age Range

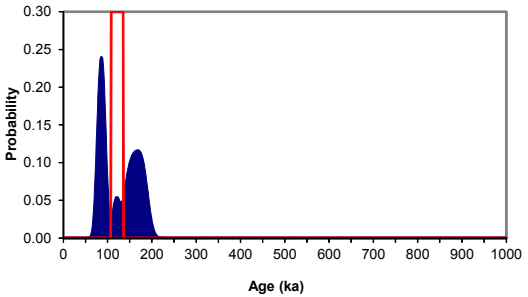

Appendix 17c
Sample: GL10001
Laboratory C

Fig. i Signal Calibration

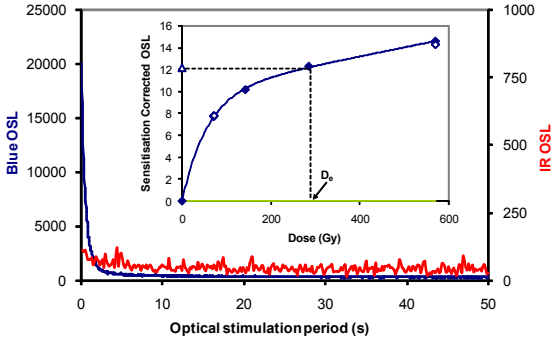

Fig. i Signal Calibration Natural blue and laboratory-induced infrared (IR) OSL signals. Detectable IR signal decays are diagnostic of feldspar contamination. Inset, the natural blue OSL signal (open triangle) of each aliquot is calibrated against known laboratory doses to yield equivalent dose (D_e) values. Repeats of low and high doses (open diamonds) illustrate the success of sensitivity correction.

Fig. ii Dose Recovery The acquisition of D_e values is necessarily predicated upon thermal treatment of aliquots succeeding environmental and laboratory irradiation. The Dose Recovery test quantifies the combined effects of thermal transfer and sensitisation on the natural signal using a precise lab dose to simulate natural dose. Based on this an appropriate thermal treatment is selected to generate the final D_e value.

Fig. iii Inter-aliquot D_e distribution Provides a measure of inter-aliquot statistical concordance in D_e values derived from **natural** irradiation. Discordant data (those points lying beyond **±2 standardised ln D_e**) reflects heterogeneous dose absorption and/or inaccuracies in calibration.

Fig. iv Low and High Repeat Regenerative-dose Ratio Measures the statistical concordance of signals from repeated **low** and **high** regenerative-doses. Discordant data (those points lying beyond **±2 standardised ln D_e**) indicate inaccurate sensitivity correction.

Fig. v OSL to Post-IR OSL Ratio Measures the statistical concordance of OSL and post-IR OSL responses to the same regenerative-dose. Discordant, underestimating data (those points lying below **-2 standardised ln D_e**) highlight the presence of significant feldspar contamination.

Fig.viSignal Analysis Statistically significant increase in **natural** D_e value with signal stimulation period is indicative of a partially-bleached signal, provided a significant increase in D_e results from **simulated partial bleaching** followed by insignificant adjustment in D_e for simulated **zero** and **full bleach** conditions. Ages from such samples are considered maximum estimates. In the absence of a significant rise in D_e with stimulation time, simulated partial bleaching and zero/full bleach tests are not assessed.

Fig. vii U Activity Statistical concordance (equilibrium) in the activities of the daughter radioisotope ^{226}Ra with its parent ^{238}U may signify the temporal stability of D_r emissions from these chains. Significant differences (disequilibrium; >50%) in activity indicate addition or removal of isotopes creating a time-dependent shift in D_r values and increased uncertainty in the accuracy of age estimates. A 20% disequilibrium marker is also shown.

Fig. viii Age Range The **mean age range** provides an estimate of sediment burial period based on mean D_e and D_r values with associated analytical uncertainties. The probability distribution indicates the inter-aliquot variability in age. The **maximum influence** of temporal variations in D_r forced by minima-maxima variation in moisture content and overburden thickness may prove instructive where there is uncertainty in these parameters, however the combined extremes represented should not be construed as preferred age estimates.

Fig.ii Dose Recovery

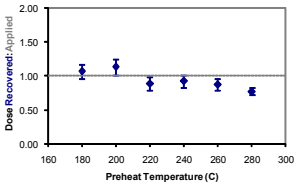

Fig. iii Inter-aliquot D_e distribution

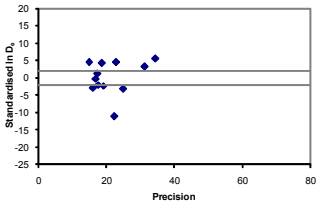

Fig. iv Low and High Repeat Regenerative-dose Ratio

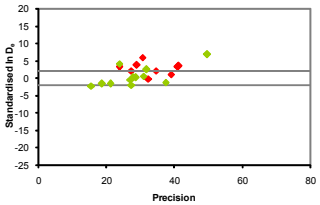

Fig. v OSL to Post-IR OSL Ratio

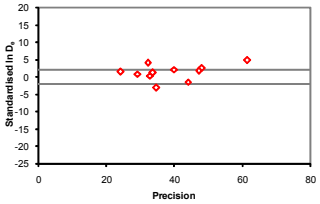

Appendix 18a
Sample: GL10002
Laboratory A

Fig. vi Signal Analysis

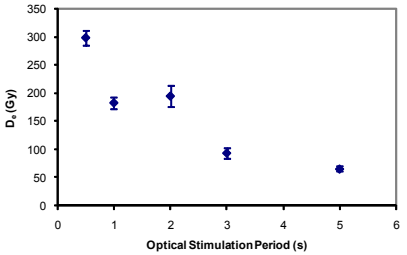

Fig. vii U Decay Activity

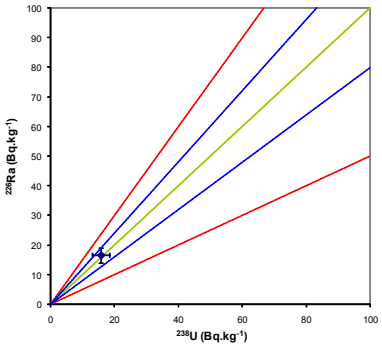

Fig. viii Age Range

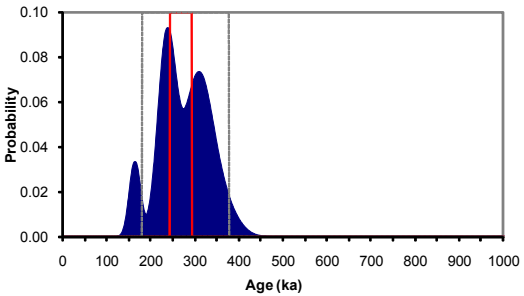

Fig. i Signal Calibration

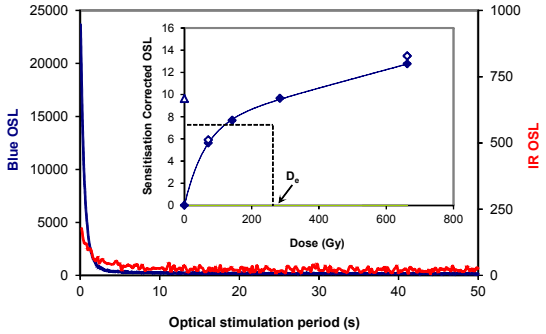

Fig. i Signal Calibration Natural blue and laboratory-induced infrared (IR) OSL signals. Detectable IR signal decays are diagnostic of feldspar contamination. Inset, the natural blue OSL signal (open triangle) of each aliquot is calibrated against known laboratory doses to yield equivalent dose (D_e) values. Repeats of low and high doses (open diamonds) illustrate the success of sensitivity correction.

Fig. ii Dose Recovery The acquisition of D_e values is necessarily predicated upon thermal treatment of aliquots succeeding environmental and laboratory irradiation. The Dose Recovery test quantifies the combined effects of thermal transfer and sensitisation on the natural signal using a precise lab dose to simulate natural dose. Based on this an appropriate thermal treatment is selected to generate the final D_e value.

Fig. iii Inter-aliquot D_e distribution Provides a measure of inter-aliquot statistical concordance in D_e values derived from **natural** irradiation. Discordant data (those points lying beyond **±2 standardised ln D_e**) reflects heterogeneous dose absorption and/or inaccuracies in calibration.

Fig. iv Low and High Repeat Regenerative-dose Ratio Measures the statistical concordance of signals from repeated **low** and **high** regenerative-doses. Discordant data (those points lying beyond **±2 standardised ln D_e**) indicate inaccurate sensitivity correction.

Fig. v OSL to Post-IR OSL Ratio Measures the statistical concordance of OSL and post-IR OSL responses to the same regenerative-dose. Discordant, underestimating data (those points lying below **-2 standardised ln D_e**) highlight the presence of significant feldspar contamination.

Fig.viSignal Analysis Statistically significant increase in **natural** D_e value with signal stimulation period is indicative of a partially-bleached signal, provided a significant increase in D_e results from **simulated partial bleaching** followed by insignificant adjustment in D_e for simulated **zero** and **full bleach** conditions. Ages from such samples are considered maximum estimates. In the absence of a significant rise in D_e with stimulation time, simulated partial bleaching and zero/full bleach tests are not assessed.

Fig. vii U Activity Statistical concordance (equilibrium) in the activities of the daughter radioisotope ^{226}Ra with its parent ^{238}U may signify the temporal stability of D_r emissions from these chains. Significant differences (disequilibrium; >50%) in activity indicate addition or removal of isotopes creating a time-dependent shift in D_r values and increased uncertainty in the accuracy of age estimates. A 20% disequilibrium marker is also shown.

Fig. viii Age Range The **mean age range** provides an estimate of sediment burial period based on mean D_e and D_r values with associated analytical uncertainties. The probability distribution indicates the inter-aliquot variability in age. The **maximum influence** of temporal variations in D_r forced by minima-maxima variation in moisture content and overburden thickness may prove instructive where there is uncertainty in these parameters, however the combined extremes represented should not be construed as preferred age estimates.

Fig.ii Dose Recovery

Extrapolated from GL10001 Laboratory B data

Fig. iii Inter-aliquot D_e distribution

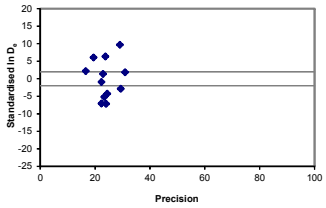

Fig. iv Low and High Repeat Regenerative-dose Ratio

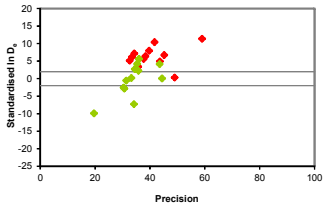

Fig. v OSL to Post-IR OSL Ratio

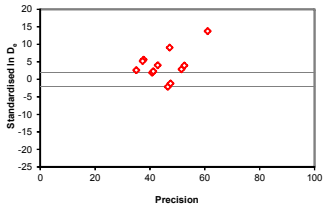

Appendix 18b
Sample: GL10002
Laboratory B

Fig. vi Signal Analysis

Not applicable to inter-laboratory comparison

Fig. vii U Decay Activity

Not applicable to inter-laboratory comparison

Fig. viii Age Range

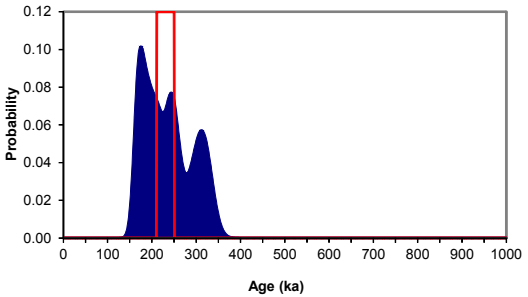

Fig. i Signal Calibration

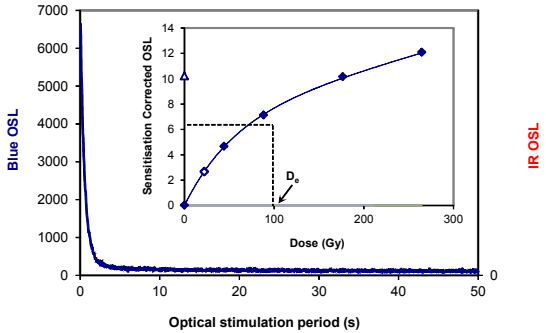

Fig. i Signal Calibration Natural blue and laboratory-induced infrared (IR) OSL signals. Detectable IR signal decays are diagnostic of feldspar contamination. Inset, the natural blue OSL signal (open triangle) of each aliquot is calibrated against known laboratory doses to yield equivalent dose (D_e) values. Repeats of low and high doses (open diamonds) illustrate the success of sensitivity correction.

Fig. ii Dose Recovery The acquisition of D_e values is necessarily predicated upon thermal treatment of aliquots succeeding environmental and laboratory irradiation. The Dose Recovery test quantifies the combined effects of thermal transfer and sensitisation on the natural signal using a precise lab dose to simulate natural dose. Based on this an appropriate thermal treatment is selected to generate the final D_e value.

Fig. iii Inter-aliquot D_e distribution Provides a measure of inter-aliquot statistical concordance in D_e values derived from **natural** irradiation. Discordant data (those points lying beyond **±2 standardised ln D_e**) reflects heterogeneous dose absorption and/or inaccuracies in calibration.

Fig. iv Low and High Repeat Regenerative-dose Ratio Measures the statistical concordance of signals from repeated **low** and **high** regenerative-doses. Discordant data (those points lying beyond **±2 standardised ln D_e**) indicate inaccurate sensitivity correction.

Fig. v OSL to Post-IR OSL Ratio Measures the statistical concordance of OSL and post-IR OSL responses to the same regenerative-dose. Discordant, underestimating data (those points lying below **-2 standardised ln D_e**) highlight the presence of significant feldspar contamination.

Fig.viSignal Analysis Statistically significant increase in **natural** D_e value with signal stimulation period is indicative of a partially-bleached signal, provided a significant increase in D_e results from **simulated partial bleaching** followed by insignificant adjustment in D_e for simulated **zero** and **full bleach** conditions. Ages from such samples are considered maximum estimates. In the absence of a significant rise in D_e with stimulation time, simulated partial bleaching and zero/full bleach tests are not assessed.

Fig. vii U Activity Statistical concordance (equilibrium) in the activities of the daughter radioisotope ^{226}Ra with its parent ^{238}U may signify the temporal stability of D_r emissions from these chains. Significant differences (disequilibrium; >50%) in activity indicate addition or removal of isotopes creating a time-dependent shift in D_r values and increased uncertainty in the accuracy of age estimates. A 20% disequilibrium marker is also shown.

Fig. viii Age Range The **mean age range** provides an estimate of sediment burial period based on mean D_e and D_r values with associated analytical uncertainties. The probability distribution indicates the inter-aliquot variability in age. The **maximum influence** of temporal variations in D_r forced by minima-maxima variation in moisture content and overburden thickness may prove instructive where there is uncertainty in these parameters, however the combined extremes represented should not be construed as preferred age estimates.

Fig.ii Dose Recovery

Extrapolated from GL10001 Laboratory C data

Fig. iii Inter-aliquot D_e distribution

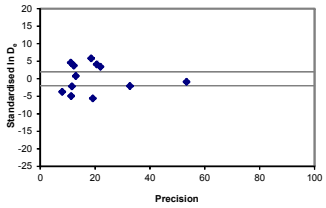

Fig. iv Low and High Repeat Regenerative-dose Ratio

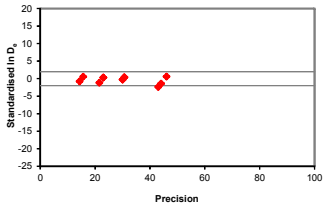

Fig. v OSL to Post-IR OSL Ratio

Not measured

Fig. vi Signal Analysis

Not applicable to inter-laboratory comparison

Fig. vii U Decay Activity

Not applicable to inter-laboratory comparison

Fig. viii Age Range

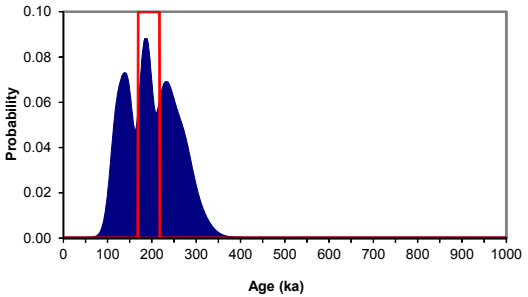

Appendix 18c
Sample: GL10002
Laboratory C

Fig. i Signal Calibration

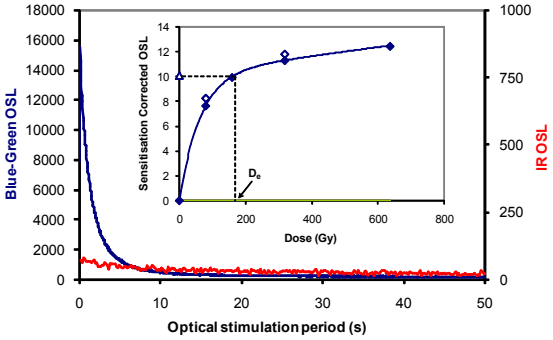

Fig. i Signal Calibration Natural blue and laboratory-induced infrared (IR) OSL signals. Detectable IR signal decays are diagnostic of feldspar contamination. Inset, the natural blue OSL signal (open triangle) of each aliquot is calibrated against known laboratory doses to yield equivalent dose (D_e) values. Repeats of low and high doses (open diamonds) illustrate the success of sensitivity correction.

Fig. ii Dose Recovery The acquisition of D_e values is necessarily predicated upon thermal treatment of aliquots succeeding environmental and laboratory irradiation. The Dose Recovery test quantifies the combined effects of thermal transfer and sensitisation on the natural signal using a precise lab dose to simulate natural dose. Based on this an appropriate thermal treatment is selected to generate the final D_L value.

Fig. iii Inter-aliquot D_e distribution Provides a measure of inter-aliquot statistical concordance in D_e values derived from **natural** irradiation. Discordant data (those points lying beyond **±2 standardised ln D_e**) reflects heterogeneous dose absorption and/or inaccuracies in calibration.

Fig. iv Low and High Repeat Regenerative-dose Ratio Measures the statistical concordance of signals from repeated **low** and **high** regenerative-doses. Discordant data (those points lying beyond **±2 standardised ln D_e**) indicate inaccurate sensitivity correction.

Fig. v OSL to Post-IR OSL Ratio Measures the statistical concordance of OSL and post-IR OSL responses to the same regenerative-dose. Discordant, underestimating data (those points lying below **-2 standardised ln D_e**) highlight the presence of significant feldspar contamination.

Fig.viSignal Analysis Statistically significant increase in **natural** D_e value with signal stimulation period is indicative of a partially-bleached signal, provided a significant increase in D_e results from **simulated partial bleaching** followed by insignificant adjustment in D_e for simulated **zero** and **full bleach** conditions. Ages from such samples are considered maximum estimates. In the absence of a significant rise in D_e with stimulation time, simulated partial bleaching and zero/full bleach tests are not assessed.

Fig. vii U Activity Statistical concordance (equilibrium) in the activities of the daughter radioisotope ^{226}Ra with its parent ^{238}U may signify the temporal stability of D_r emissions from these chains. Significant differences (disequilibrium; >50%) in activity indicate addition or removal of isotopes creating a time-dependent shift in D_r values and increased uncertainty in the accuracy of age estimates. A 20% disequilibrium marker is also shown.

Fig. viii Age Range The **mean age range** provides an estimate of sediment burial period based on mean D_e and D_r values with associated analytical uncertainties. The probability distribution indicates the inter-aliquot variability in age. The **maximum influence** of temporal variations in D_r forced by minima-maxima variation in moisture content and overburden thickness may prove instructive where there is uncertainty in these parameters, however the combined extremes represented should not be construed as preferred age estimates.

Fig.ii Dose Recovery

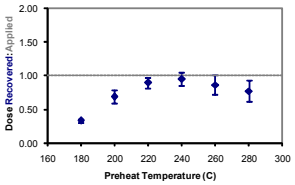

Fig. iii Inter-aliquot D_e distribution

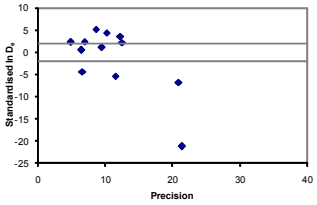

Fig. iv Low and High Repeat Regenerative-dose Ratio

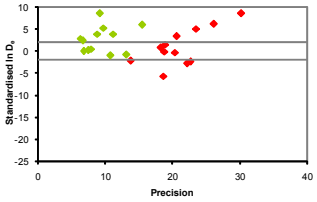

Fig. v OSL to Post-IR OSL Ratio

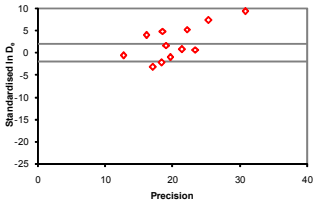

Appendix 19
Sample: GL10019

Fig. vi Signal Analysis

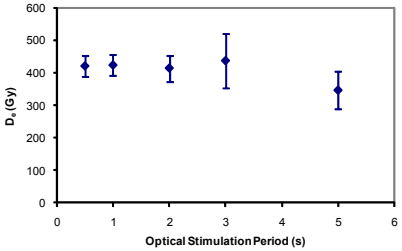

Fig. vii U Decay Activity

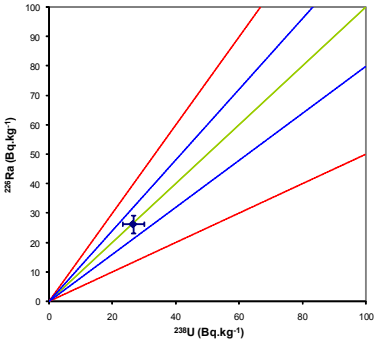

Fig. viii Age Range

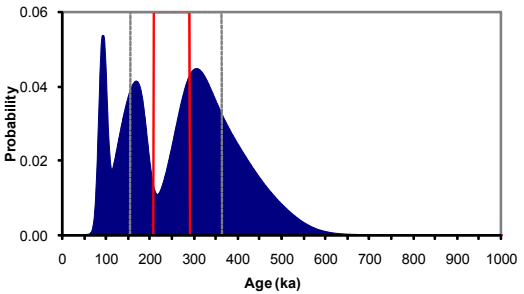

Fig. i Signal Calibration

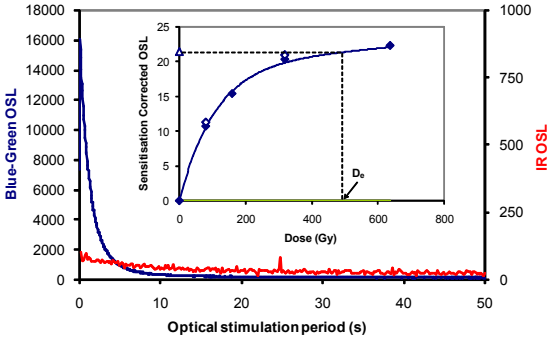

Fig. i Signal Calibration Natural blue and laboratory-induced infrared (IR) OSL signals. Detectable IR signal decays are diagnostic of feldspar contamination. Inset, the natural blue OSL signal (open triangle) of each aliquot is calibrated against known laboratory doses to yield equivalent dose (D_e) values. Repeats of low and high doses (open diamonds) illustrate the success of sensitivity correction.

Fig. ii Dose Recovery The acquisition of D_e values is necessarily predicated upon thermal treatment of aliquots succeeding environmental and laboratory irradiation. The Dose Recovery test quantifies the combined effects of thermal transfer and sensitisation on the natural signal using a precise lab dose to simulate natural dose. Based on this an appropriate thermal treatment is selected to generate the final D_e value.

Fig. iii Inter-aliquot D_e distribution Provides a measure of inter-aliquot statistical concordance in D_e values derived from **natural** irradiation. Discordant data (those points lying beyond **±2 standardised ln D_e**) reflects heterogeneous dose absorption and/or inaccuracies in calibration.

Fig. iv Low and High Repeat Regenerative-dose Ratio Measures the statistical concordance of signals from repeated **low** and **high** regenerative-doses. Discordant data (those points lying beyond **±2 standardised ln D_e**) indicate inaccurate sensitivity correction.

Fig. v OSL to Post-IR OSL Ratio Measures the statistical concordance of OSL and post-IR OSL responses to the same regenerative-dose. Discordant, underestimating data (those points lying below **-2 standardised ln D_e**) highlight the presence of significant feldspar contamination.

Fig.viSignal Analysis Statistically significant increase in **natural** D_e value with signal stimulation period is indicative of a partially-bleached signal, provided a significant increase in D_e results from **simulated partial bleaching** followed by insignificant adjustment in D_e for simulated **zero** and **full bleach** conditions. Ages from such samples are considered maximum estimates. In the absence of a significant rise in D_e with stimulation time, simulated partial bleaching and zero/full bleach tests are not assessed.

Fig. vii U Activity Statistical concordance (equilibrium) in the activities of the daughter radioisotope ^{226}Ra with its parent ^{238}U may signify the temporal stability of D_r emissions from these chains. Significant differences (disequilibrium; >50%) in activity indicate addition or removal of isotopes creating a time-dependent shift in D_r values and increased uncertainty in the accuracy of age estimates. A 20% disequilibrium marker is also shown.

Fig. viii Age Range The **mean age range** provides an estimate of sediment burial period based on mean D_e and D_r values with associated analytical uncertainties. The probability distribution indicates the inter-aliquot variability in age. The **maximum influence** of temporal variations in D_r forced by minima-maxima variation in moisture content and overburden thickness may prove instructive where there is uncertainty in these parameters, however the combined extremes represented should not be construed as preferred age estimates.

Fig.ii Dose Recovery

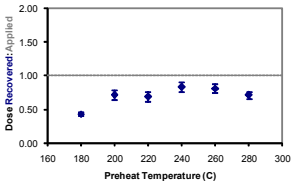

Fig. iii Inter-aliquot D_e distribution

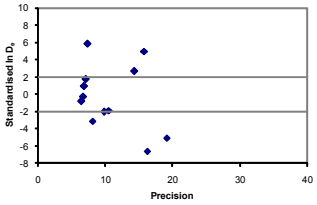

Fig. iv Low and High Repeat Regenerative-dose Ratio

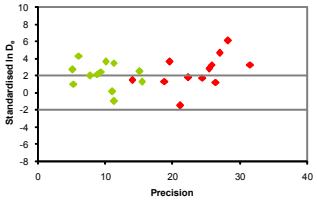

Fig. v OSL to Post-IR OSL Ratio

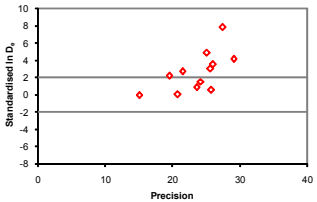

Appendix 20
Sample: GL10020

Fig. vi Signal Analysis

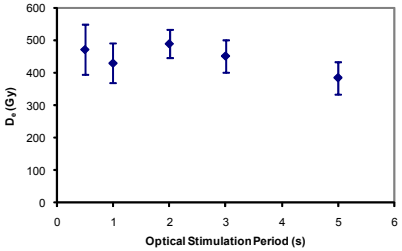

Fig. vii U Decay Activity

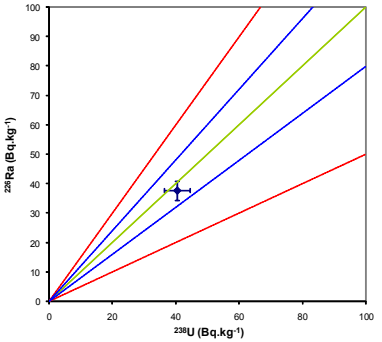

Fig. viii Age Range

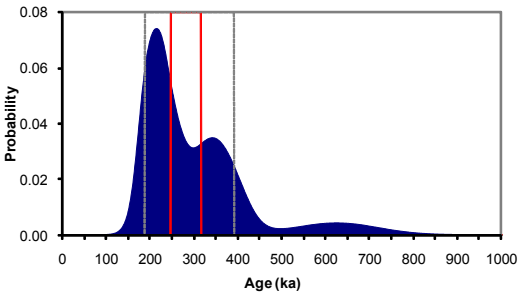

Fig. i Signal Calibration

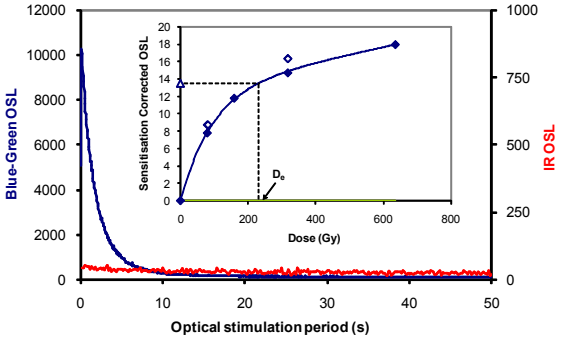

Fig. i Signal Calibration Natural blue and laboratory-induced infrared (IR) OSL signals. Detectable IR signal decays are diagnostic of feldspar contamination. Inset, the natural blue OSL signal (open triangle) of each aliquot is calibrated against known laboratory doses to yield equivalent dose (D_e) values. Repeats of low and high doses (open diamonds) illustrate the success of sensitivity correction.

Fig. ii Dose Recovery The acquisition of D_e values is necessarily predicated upon thermal treatment of aliquots succeeding environmental and laboratory irradiation. The Dose Recovery test quantifies the combined effects of thermal transfer and sensitisation on the natural signal using a precise lab dose to simulate natural dose. Based on this an appropriate thermal treatment is selected to generate the final D_e value.

Fig. iii Inter-aliquot D_e distribution Provides a measure of inter-aliquot statistical concordance in D_e values derived from **natural** irradiation. Discordant data (those points lying beyond **±2 standardised ln D_e**) reflects heterogeneous dose absorption and/or inaccuracies in calibration.

Fig. iv Low and High Repeat Regenerative-dose Ratio Measures the statistical concordance of signals from repeated **low** and **high** regenerative-doses. Discordant data (those points lying beyond **±2 standardised ln D_e**) indicate inaccurate sensitivity correction.

Fig. v OSL to Post-IR OSL Ratio Measures the statistical concordance of OSL and post-IR OSL responses to the same regenerative-dose. Discordant, underestimating data (those points lying below **-2 standardised ln D_e**) highlight the presence of significant feldspar contamination.

Fig.viSignal Analysis Statistically significant increase in **natural** D_e value with signal stimulation period is indicative of a partially-bleached signal, provided a significant increase in D_e results from **simulated partial bleaching** followed by insignificant adjustment in D_e for simulated **zero** and **full bleach** conditions. Ages from such samples are considered maximum estimates. In the absence of a significant rise in D_e with stimulation time, simulated partial bleaching and zero/full bleach tests are not assessed.

Fig. vii U Activity Statistical concordance (equilibrium) in the activities of the daughter radioisotope ^{226}Ra with its parent ^{238}U may signify the temporal stability of D_r emissions from these chains. Significant differences (disequilibrium; >50%) in activity indicate addition or removal of isotopes creating a time-dependent shift in D_r values and increased uncertainty in the accuracy of age estimates. A 20% disequilibrium marker is also shown.

Fig. viii Age Range The **mean age range** provides an estimate of sediment burial period based on mean D_e and D_r values with associated analytical uncertainties. The probability distribution indicates the inter-aliquot variability in age. The **maximum influence** of temporal variations in D_r forced by minima-maxima variation in moisture content and overburden thickness may prove instructive where there is uncertainty in these parameters, however the combined extremes represented should not be construed as preferred age estimates.

Fig.ii Dose Recovery

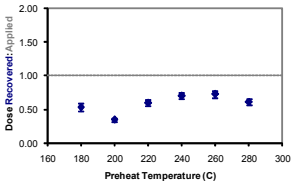

Fig. iii Inter-aliquot D_e distribution

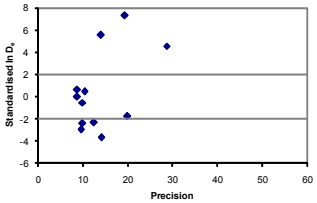

Fig. iv Low and High Repeat Regenerative-dose Ratio

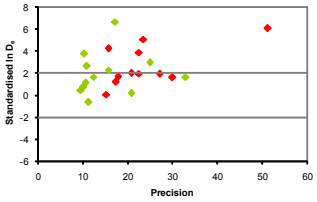

Fig. v OSL to Post-IR OSL Ratio

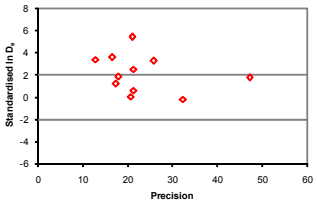

Appendix 21
Sample: GL10055

Fig. vi Signal Analysis

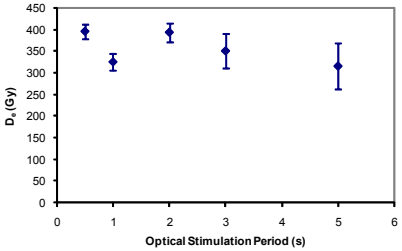

Fig. vii U Decay Activity

^{226}Ra peak beneath detection limits

Fig. viii Age Range

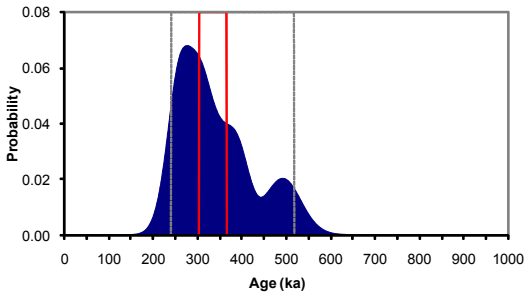

Fig. i Signal Calibration

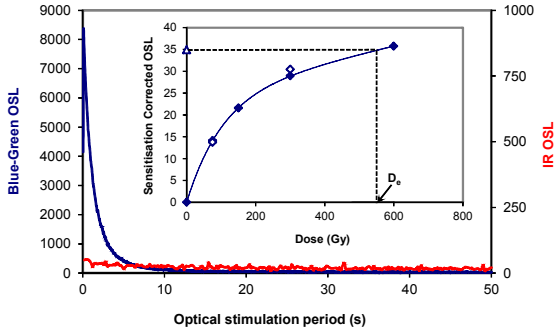

Fig. i Signal Calibration Natural blue and laboratory-induced infrared (IR) OSL signals. Detectable IR signal decays are diagnostic of feldspar contamination. Inset, the natural blue OSL signal (open triangle) of each aliquot is calibrated against known laboratory doses to yield equivalent dose (D_e) values. Repeats of low and high doses (open diamonds) illustrate the success of sensitivity correction.

Fig. ii Dose Recovery The acquisition of D_e values is necessarily predicated upon thermal treatment of aliquots succeeding environmental and laboratory irradiation. The Dose Recovery test quantifies the combined effects of thermal transfer and sensitisation on the natural signal using a precise lab dose to simulate natural dose. Based on this an appropriate thermal treatment is selected to generate the final D_e value.

Fig. iii Inter-aliquot D_e distribution Provides a measure of inter-aliquot statistical concordance in D_e values derived from **natural** irradiation. Discordant data (those points lying beyond ±2 standardised ln D_e) reflects heterogeneous dose absorption and/or inaccuracies in calibration.

Fig. iv Low and High Repeat Regenerative-dose Ratio Measures the statistical concordance of signals from repeated **low** and **high** regenerative-doses. Discordant data (those points lying beyond ±2 standardised ln D_e) indicate inaccurate sensitivity correction.

Fig. v OSL to Post-IR OSL Ratio Measures the statistical concordance of OSL and post-IR OSL responses to the same regenerative-dose. Discordant, underestimating data (those points lying below -2 standardised ln D_e) highlight the presence of significant feldspar contamination.

Fig.viSignal Analysis Statistically significant increase in **natural** D_e value with signal stimulation period is indicative of a partially-bleached signal, provided a significant increase in D_e results from **simulated partial bleaching** followed by insignificant adjustment in D_e for simulated **zero** and **full bleach** conditions. Ages from such samples are considered maximum estimates. In the absence of a significant rise in D_e with stimulation time, simulated partial bleaching and zero/full bleach tests are not assessed.

Fig. vii U Activity Statistical concordance (equilibrium) in the activities of the daughter radioisotope ^{226}Ra with its parent ^{238}U may signify the temporal stability of D_r emissions from these chains. Significant differences (disequilibrium; >50%) in activity indicate addition or removal of isotopes creating a time-dependent shift in D_r values and increased uncertainty in the accuracy of age estimates. A 20% disequilibrium marker is also shown.

Fig. viii Age Range The **mean age range** provides an estimate of sediment burial period based on mean D_e and D_r values with associated analytical uncertainties. The probability distribution indicates the inter-aliquot variability in age. The **maximum influence** of temporal variations in D_r forced by minima-maxima variation in moisture content and overburden thickness may prove instructive where there is uncertainty in these parameters, however the combined extremes represented should not be construed as preferred age estimates.

Fig.ii Dose Recovery

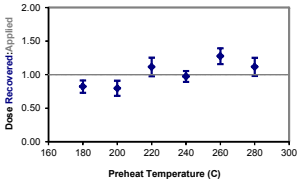

Fig. iii Inter-aliquot D_e distribution

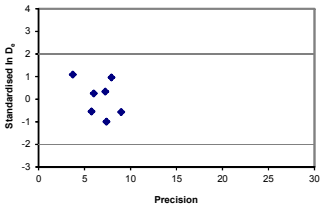

Fig. iv Low and High Repeat Regenerative-dose Ratio

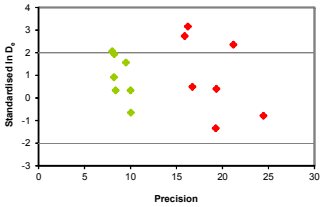

Fig. v OSL to Post-IR OSL Ratio

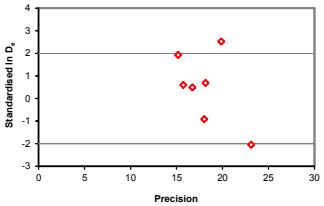

Appendix 22
Sample: GL10063

Fig. vi Signal Analysis

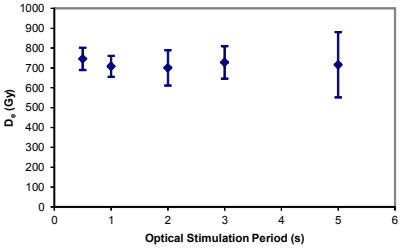

Fig. vii U Decay Activity

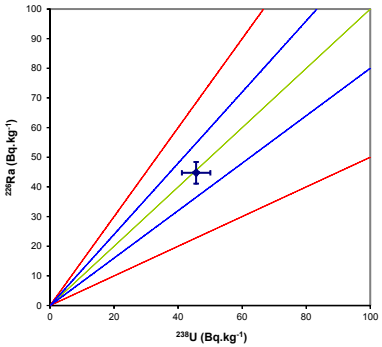

Fig. viii Age Range

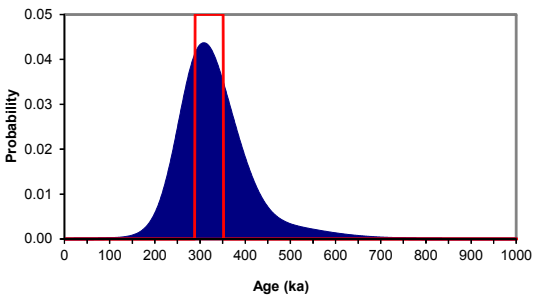

Fig. i Signal Calibration

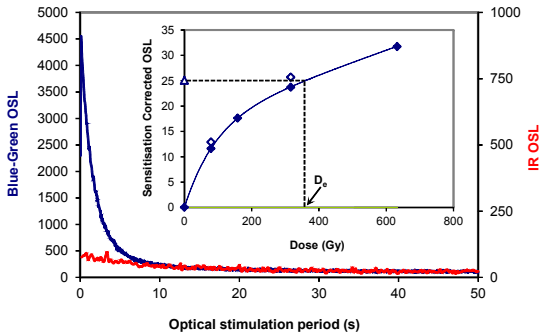

Fig. i Signal Calibration Natural blue and laboratory-induced infrared (IR) OSL signals. Detectable IR signal decays are diagnostic of feldspar contamination. Inset, the natural blue OSL signal (open triangle) of each aliquot is calibrated against known laboratory doses to yield equivalent dose (D_e) values. Repeats of low and high doses (open diamonds) illustrate the success of sensitivity correction.

Fig. ii Dose Recovery The acquisition of D_e values is necessarily predicated upon thermal treatment of aliquots succeeding environmental and laboratory irradiation. The Dose Recovery test quantifies the combined effects of thermal transfer and sensitisation on the natural signal using a precise lab dose to simulate natural dose. Based on this an appropriate thermal treatment is selected to generate the final D_e value.

Fig. iii Inter-aliquot D_e distribution Provides a measure of inter-aliquot statistical concordance in D_e values derived from **natural** irradiation. Discordant data (those points lying beyond **±2 standardised ln D_e**) reflects heterogeneous dose absorption and/or inaccuracies in calibration.

Fig. iv Low and High Repeat Regenerative-dose Ratio Measures the statistical concordance of signals from repeated **low** and **high** regenerative-doses. Discordant data (those points lying beyond **±2 standardised ln D_e**) indicate inaccurate sensitivity correction.

Fig. v OSL to Post-IR OSL Ratio Measures the statistical concordance of OSL and post-IR OSL responses to the same regenerative-dose. Discordant, underestimating data (those points lying below **-2 standardised ln D_e**) highlight the presence of significant feldspar contamination.

Fig.viSignal Analysis Statistically significant increase in **natural** D_e value with signal stimulation period is indicative of a partially-bleached signal, provided a significant increase in D_e results from **simulated partial bleaching** followed by insignificant adjustment in D_e for simulated **zero** and **full bleach** conditions. Ages from such samples are considered maximum estimates. In the absence of a significant rise in D_e with stimulation time, simulated partial bleaching and zero/full bleach tests are not assessed.

Fig. vii U Activity Statistical concordance (equilibrium) in the activities of the daughter radioisotope ^{226}Ra with its parent ^{238}U may signify the temporal stability of D_r emissions from these chains. Significant differences (disequilibrium; >50%) in activity indicate addition or removal of isotopes creating a time-dependent shift in D_r values and increased uncertainty in the accuracy of age estimates. A 20% disequilibrium marker is also shown.

Fig. viii Age Range The **mean age range** provides an estimate of sediment burial period based on mean D_e and D_r values with associated analytical uncertainties. The probability distribution indicates the inter-aliquot variability in age. The **maximum influence** of temporal variations in D_r forced by minima-maxima variation in moisture content and overburden thickness may prove instructive where there is uncertainty in these parameters, however the combined extremes represented should not be construed as preferred age estimates.

Fig.ii Dose Recovery

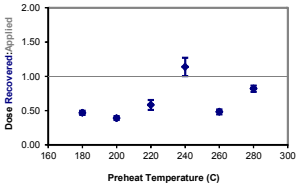

Fig. iii Inter-aliquot D_e distribution

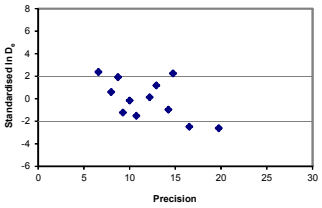

Fig. iv Low and High Repeat Regenerative-dose Ratio

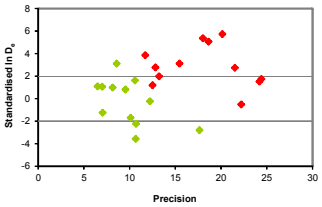

Fig. v OSL to Post-IR OSL Ratio

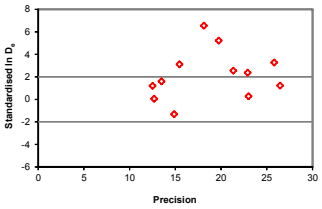

Appendix 23
Sample: GL10064

Fig. vi Signal Analysis

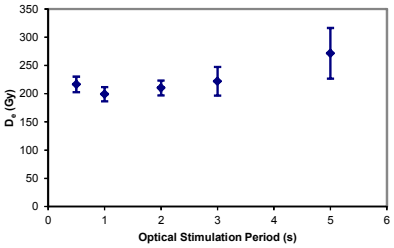

Fig. vii U Decay Activity

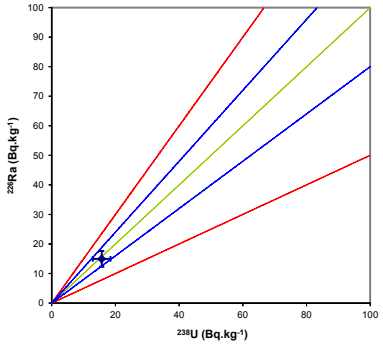

Fig. viii Age Range

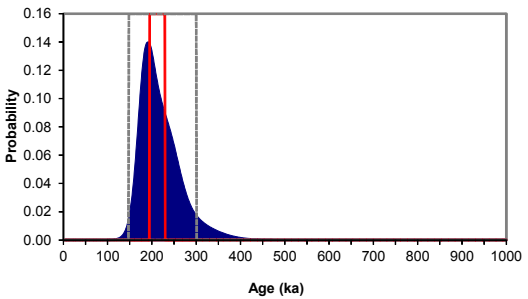

Fig. i Signal Calibration

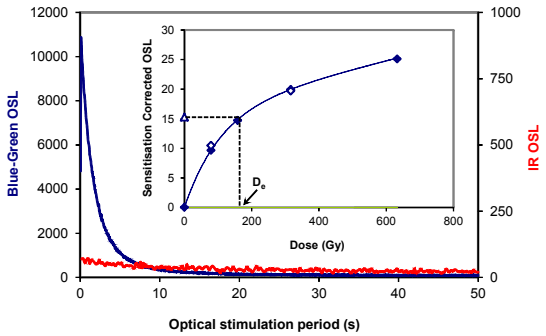

Fig. i Signal Calibration Natural blue and laboratory-induced infrared (IR) OSL signals. Detectable IR signal decays are diagnostic of feldspar contamination. Inset, the natural blue OSL signal (open triangle) of each aliquot is calibrated against known laboratory doses to yield equivalent dose (D_e) values. Repeats of low and high doses (open diamonds) illustrate the success of sensitivity correction.

Fig. ii Dose Recovery The acquisition of D_e values is necessarily predicated upon thermal treatment of aliquots succeeding environmental and laboratory irradiation. The Dose Recovery test quantifies the combined effects of thermal transfer and sensitisation on the natural signal using a precise lab dose to simulate natural dose. Based on this an appropriate thermal treatment is selected to generate the final D_e value.

Fig. iii Inter-aliquot D_e distribution Provides a measure of inter-aliquot statistical concordance in D_e values derived from **natural** irradiation. Discordant data (those points lying beyond **±2 standardised ln D_e**) reflects heterogeneous dose absorption and/or inaccuracies in calibration.

Fig. iv Low and High Repeat Regenerative-dose Ratio Measures the statistical concordance of signals from repeated **low** and **high** regenerative-doses. Discordant data (those points lying beyond **±2 standardised ln D_e**) indicate inaccurate sensitivity correction.

Fig. v OSL to Post-IR OSL Ratio Measures the statistical concordance of OSL and post-IR OSL responses to the same regenerative-dose. Discordant, underestimating data (those points lying below **-2 standardised ln D_e**) highlight the presence of significant feldspar contamination.

Fig.viSignal Analysis Statistically significant increase in **natural** D_e value with signal stimulation period is indicative of a partially-bleached signal, provided a significant increase in D_e results from **simulated partial bleaching** followed by insignificant adjustment in D_e for simulated **zero** and **full bleach** conditions. Ages from such samples are considered maximum estimates. In the absence of a significant rise in D_e with stimulation time, simulated partial bleaching and zero/full bleach tests are not assessed.

Fig. vii U Activity Statistical concordance (equilibrium) in the activities of the daughter radioisotope ^{226}Ra with its parent ^{238}U may signify the temporal stability of D_r emissions from these chains. Significant differences (disequilibrium; >50%) in activity indicate addition or removal of isotopes creating a time-dependent shift in D_r values and increased uncertainty in the accuracy of age estimates. A 20% disequilibrium marker is also shown.

Fig. viii Age Range The **mean age range** provides an estimate of sediment burial period based on mean D_e and D_r values with associated analytical uncertainties. The probability distribution indicates the inter-aliquot variability in age. The **maximum influence** of temporal variations in D_r forced by minima-maxima variation in moisture content and overburden thickness may prove instructive where there is uncertainty in these parameters, however the combined extremes represented should not be construed as preferred age estimates.

Fig.ii Dose Recovery

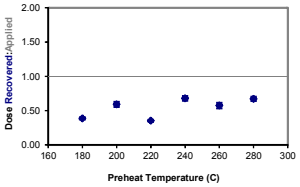

Fig. iii Inter-aliquot D_e distribution

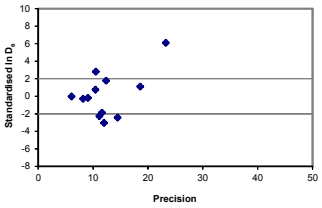

Fig. iv Low and High Repeat Regenerative-dose Ratio

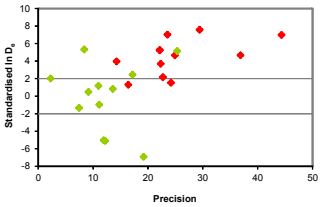

Fig. v OSL to Post-IR OSL Ratio

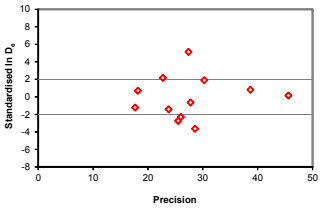

Appendix 24
Sample: GL10065

Fig. vi Signal Analysis

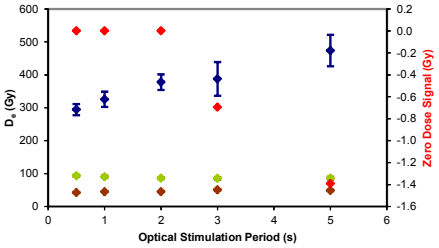

Fig. vii U Decay Activity

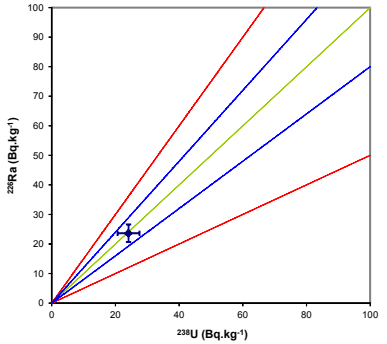

Fig. viii Age Range

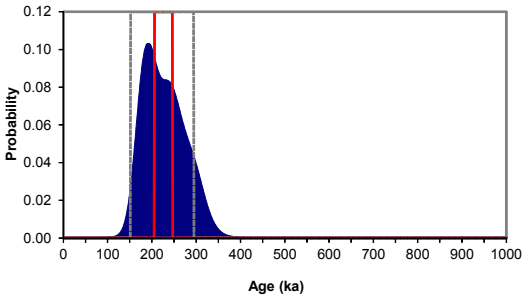

Fig. i Signal Calibration

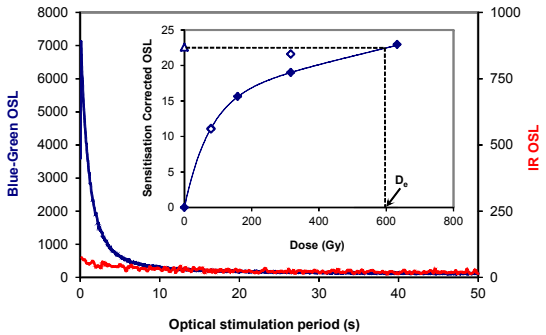

Fig. i Signal Calibration Natural blue and laboratory-induced infrared (IR) OSL signals. Detectable IR signal decays are diagnostic of feldspar contamination. Inset, the natural blue OSL signal (open triangle) of each aliquot is calibrated against known laboratory doses to yield equivalent dose (D_e) values. Repeats of low and high doses (open diamonds) illustrate the success of sensitivity correction.

Fig. ii Dose Recovery The acquisition of D_e values is necessarily predicated upon thermal treatment of aliquots succeeding environmental and laboratory irradiation. The Dose Recovery test quantifies the combined effects of thermal transfer and sensitisation on the natural signal using a precise lab dose to simulate natural dose. Based on this an appropriate thermal treatment is selected to generate the final D_e value.

Fig. iii Inter-aliquot D_e distribution Provides a measure of inter-aliquot statistical concordance in D_e values derived from **natural** irradiation. Discordant data (those points lying beyond **±2 standardised ln D_e**) reflects heterogeneous dose absorption and/or inaccuracies in calibration.

Fig. iv Low and High Repeat Regenerative-dose Ratio Measures the statistical concordance of signals from repeated **low** and **high** regenerative-doses. Discordant data (those points lying beyond **±2 standardised ln D_e**) indicate inaccurate sensitivity correction.

Fig. v OSL to Post-IR OSL Ratio Measures the statistical concordance of OSL and post-IR OSL responses to the same regenerative-dose. Discordant, underestimating data (those points lying below **-2 standardised ln D_e**) highlight the presence of significant feldspar contamination.

Fig.viSignal Analysis Statistically significant increase in **natural** D_e value with signal stimulation period is indicative of a partially-bleached signal, provided a significant increase in D_e results from **simulated partial bleaching** followed by insignificant adjustment in D_e for simulated **zero** and **full bleach** conditions. Ages from such samples are considered maximum estimates. In the absence of a significant rise in D_e with stimulation time, simulated partial bleaching and zero/full bleach tests are not assessed.

Fig. vii U Activity Statistical concordance (equilibrium) in the activities of the daughter radioisotope ^{226}Ra with its parent ^{238}U may signify the temporal stability of D_r emissions from these chains. Significant differences (disequilibrium; >50%) in activity indicate addition or removal of isotopes creating a time-dependent shift in D_r values and increased uncertainty in the accuracy of age estimates. A 20% disequilibrium marker is also shown.

Fig. viii Age Range The **mean age range** provides an estimate of sediment burial period based on mean D_e and D_r values with associated analytical uncertainties. The probability distribution indicates the inter-aliquot variability in age. The **maximum influence** of temporal variations in D_r forced by minima-maxima variation in moisture content and overburden thickness may prove instructive where there is uncertainty in these parameters, however the combined extremes represented should not be construed as preferred age estimates.

Fig.ii Dose Recovery

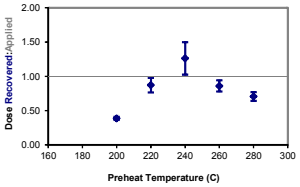

Fig. iii Inter-aliquot D_e distribution

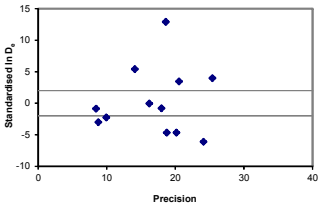

Fig. iv Low and High Repeat Regenerative-dose Ratio

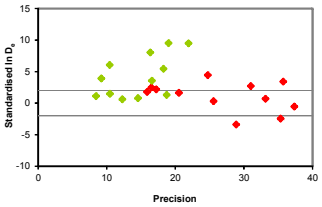

Fig. v OSL to Post-IR OSL Ratio

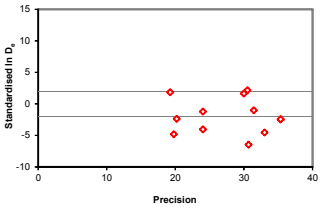

Appendix 25
Sample: GL10066

Fig. vi Signal Analysis

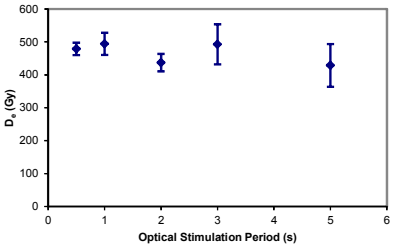

Fig. vii U Decay Activity

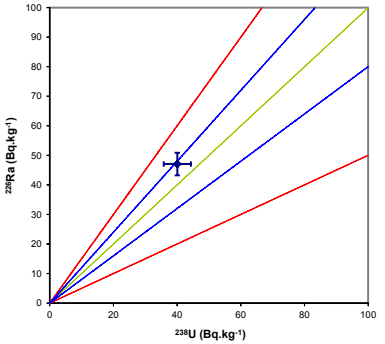

Fig. viii Age Range

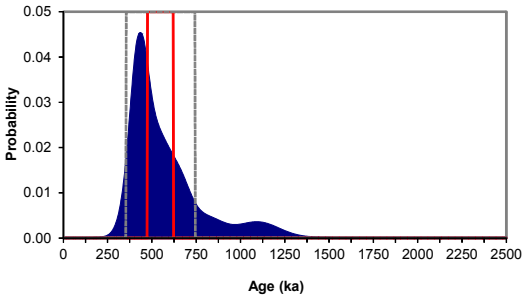

Fig. i Signal Calibration

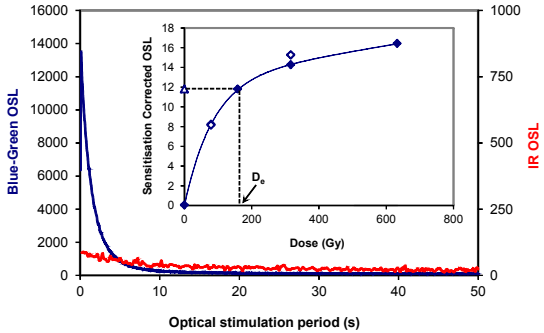

Fig. i Signal Calibration Natural blue and laboratory-induced infrared (IR) OSL signals. Detectable IR signal decays are diagnostic of feldspar contamination. Inset, the natural blue OSL signal (open triangle) of each aliquot is calibrated against known laboratory doses to yield equivalent dose (D_e) values. Repeats of low and high doses (open diamonds) illustrate the success of sensitivity correction.

Fig. ii Dose Recovery The acquisition of D_e values is necessarily predicated upon thermal treatment of aliquots succeeding environmental and laboratory irradiation. The Dose Recovery test quantifies the combined effects of thermal transfer and sensitisation on the natural signal using a precise lab dose to simulate natural dose. Based on this an appropriate thermal treatment is selected to generate the final D_e value.

Fig. iii Inter-aliquot D_e distribution Provides a measure of inter-aliquot statistical concordance in D_e values derived from **natural** irradiation. Discordant data (those points lying beyond **±2 standardised ln D_e**) reflects heterogeneous dose absorption and/or inaccuracies in calibration.

Fig. iv Low and High Repeat Regenerative-dose Ratio Measures the statistical concordance of signals from repeated **low** and **high** regenerative-doses. Discordant data (those points lying beyond **±2 standardised ln D_e**) indicate inaccurate sensitivity correction.

Fig. v OSL to Post-IR OSL Ratio Measures the statistical concordance of OSL and post-IR OSL responses to the same regenerative-dose. Discordant, underestimating data (those points lying below **-2 standardised ln D_e**) highlight the presence of significant feldspar contamination.

Fig.viSignal Analysis Statistically significant increase in **natural** D_e value with signal stimulation period is indicative of a partially-bleached signal, provided a significant increase in D_e results from **simulated partial bleaching** followed by insignificant adjustment in D_e for simulated **zero** and **full bleach** conditions. Ages from such samples are considered maximum estimates. In the absence of a significant rise in D_e with stimulation time, simulated partial bleaching and zero/full bleach tests are not assessed.

Fig. vii U Activity Statistical concordance (equilibrium) in the activities of the daughter radioisotope ^{226}Ra with its parent ^{238}U may signify the temporal stability of D_r emissions from these chains. Significant differences (disequilibrium; >50%) in activity indicate addition or removal of isotopes creating a time-dependent shift in D_r values and increased uncertainty in the accuracy of age estimates. A 20% disequilibrium marker is also shown.

Fig. viii Age Range The **mean age range** provides an estimate of sediment burial period based on mean D_e and D_r values with associated analytical uncertainties. The probability distribution indicates the inter-aliquot variability in age. The **maximum influence** of temporal variations in D_r forced by minima-maxima variation in moisture content and overburden thickness may prove instructive where there is uncertainty in these parameters, however the combined extremes represented should not be construed as preferred age estimates.

Fig.ii Dose Recovery

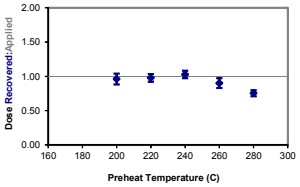

Fig. iii Inter-aliquot D_e distribution

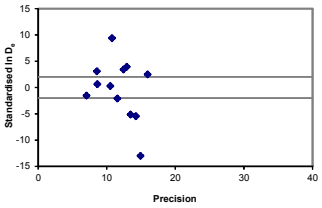

Fig. iv Low and High Repeat Regenerative-dose Ratio

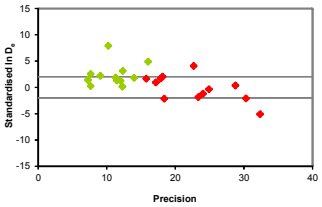

Fig. v OSL to Post-IR OSL Ratio

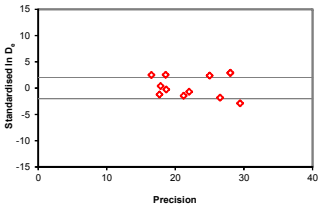

Appendix 26
Sample: GL10067

Fig. vi Signal Analysis

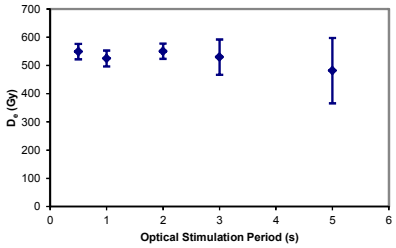

Fig. vii U Decay Activity

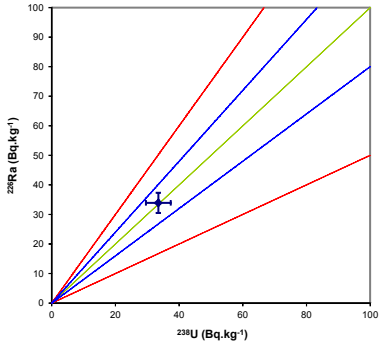

Fig. viii Age Range

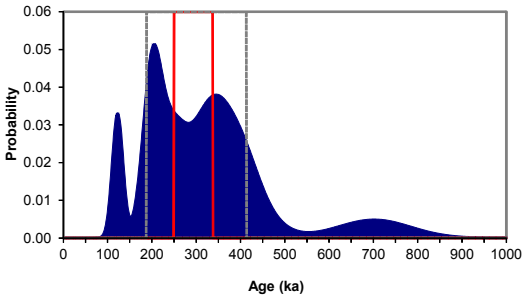

daughter radioisotope ^{234}U with its parent ^{238}U may signify the temporal stability of D_r emissions from these chains. Significant differences (disequilibrium; >50%) in activity indicate addition or removal of isotopes creating a time-dependent shift in D_r values and increased uncertainty in the accuracy of age estimates. A 20% disequilibrium marker is also shown.

Fig. viii Age Range The **mean age range** provides an estimate of sediment burial period based on mean D_e and D_r values with associated analytical uncertainties. The probability distribution indicates the inter-aliquot variability in age. The **maximum influence** of temporal variations in D_r forced by minima-maxima variation in moisture content and overburden thickness may prove instructive where there is uncertainty in these parameters, however the combined extremes represented should not be construed as preferred age estimates.

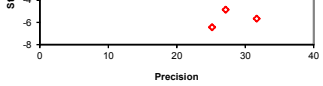

Appendix 27
Sample: GL10084

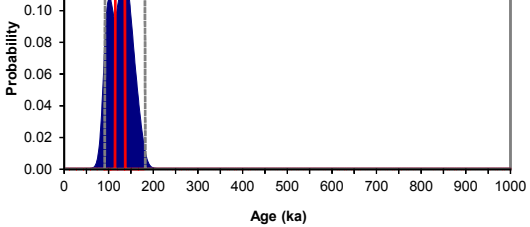

References

Adamiec, G. and Aitken, M.J. (1998) Dose-rate conversion factors: new data. *Ancient TL*, 16, 37-50.

Aitken, M. J. (1998) *An introduction to optical dating: the dating of Quaternary sediments by the use of photon-stimulated luminescence.* Oxford University Press.

Bailey, R.M. (2004) Paper I—simulation of dose absorption in quartz over geological timescales and its implications for the precision and accuracy of optical dating. *Radiation Measurements*, 38, 299-310.

Bailey, R.M., Singarayer, J.S. , Ward, S. and Stokes, S. (2003) Identification of partial resetting using D_e as a function of illumination time. *Radiation Measurements*, 37, 511-518.

Banerjee, D., Murray, A.S., Bøtter-Jensen, L. and Lang, A. (2001) Equivalent dose estimation using a single aliquot of polymineral fine grains. *Radiation Measurements*, 33, 73-94.

Bateman, M.D., Frederick, C.D., Jaiswal, M.K., Singhvi, A.K. (2003) Investigations into the potential effects of pedoturbation on luminescence dating. *Quaternary Science Reviews*, 22, 1169-1176.

Berger, G.W. (2003). Luminescence chronology of late Pleistocene loess-paleosol and tephra sequences near Fairbanks, Alaska. *Quaternary Research*, 60, 70-83.

Berger, G.W., Mulhern, P.J. and Huntley, D.J. (1980). Isolation of silt-sized quartz from sediments. *Ancient TL*, 11, 147-152.

Bøtter-Jensen, L., Mejdahl, V. and Murray, A.S. (1999) New light on OSL. *Quaternary Science Reviews*, 18, 303-310.

Bøtter-Jensen, L., McKeever, S.W.S. and Wintle, A.G. (2003) Optically Stimulated Luminescence Dosimetry. Elsevier, Amsterdam.

Brown, A.G. and Basell, L.S. (2008) New Lower Palaeolithic Finds from the Axe Valley, Dorset. PAST, 60, 1-4.

Duller, G.A.T. (2007) Luminescence Analyst. Aberystwyth University.

Galbraith, R.F. (1990) The radial plot: graphical assessment of spread in ages. *Nuclear Tracks and Radiation Measurements*, 17, 207-214.

Galbraith, R.F., Roberts, R.G., Laslett, G.M., Yoshida, H. and Olley, J.M. (1999) Optical dating of single and multiple grains of quartz from Jinmium rock shelter (northern Australia): Part I, Experimental design and statistical models. *Archaeometry*, 41, 339-364.

Hubble, J.H. (1982) Photon mass attenuation and energy-absorption coefficients from 1keV to 20MeV. *International Journal of Applied Radioisotopes*, 33, 1269-1290.

Huntley, D.J., Godfrey-Smith, D.I. and Thewalt, M.L.W. (1985) Optical dating of sediments. *Nature*, 313, 105-107.

Hütt, G., Jaek, I. and Tchonka, J. (1988) Optical dating: K-feldspars optical response stimulation spectra. *Quaternary Science Reviews*, 7, 381-386.

Jackson, M.L., Sayin, M. and Clayton, R.N. (1976). Hexafluorosilicic acid regent modification for quartz isolation. *Soil Science Society of America Journal*, **40**, 958-960.

Markey, B.G., Bøtter-Jensen, L., and Duller, G.A.T. (1997) A new flexible system for measuring thermally and optically stimulated luminescence. *Radiation Measurements*, 27, 83-89.

Mejdahl, V. (1979) Thermoluminescence dating: beta-dose attenuation in quartz grains. *Archaeometry*, 21, 61-72.

Murray, A.S. and Olley, J.M. (2002) Precision and accuracy in the Optically Stimulated Luminescence dating of sedimentary quartz: a status review. *Geochronometria*, 21, 1-16.

Murray, A.S. and Wintle, A.G. (2000) Luminescence dating of quartz using an improved single-aliquot regenerative-dose protocol. *Radiation Measurements*, 32, 57-73.

Murray, A.S. and Wintle, A.G. (2003) The single aliquot regenerative dose protocol: potential for improvements in reliability. *Radiation Measurements*, 37, 377-381.

Olley, J.M., Murray, A.S. and Roberts, R.G. (1996) The effects of disequilibria in the Uranium and Thorium decay chains on burial dose rates in fluvial sediments. *Quaternary Science Reviews*, 15, 751-760.

Olley, J.M., Caitcheon, G.G. and Murray, A.S. (1998) The distribution of apparent dose as determined by optically stimulated luminescence in small aliquots of fluvial quartz: implications for dating young sediments. *Quaternary Science Reviews*, 17, 1033-1040.

Olley, J.M., Caitcheon, G.G. and Roberts R.G. (1999) The origin of dose distributions in fluvial sediments, and the prospect of dating single grains from fluvial deposits using -optically stimulated luminescence. *Radiation Measurements,* 30**,** 207-217.

Olley, J.M., Pietsch, T. and Roberts, R.G. (2004) Optical dating of Holocene sediments from a variety of geomorphic settings using single grains of quartz. *Geomorphology*, 60, 337-358.

Pawley, S.M., Toms, P.S., Armitage, S.J., Rose, J. (submitted) Quartz luminescence dating of Anglian Stage fluvial sediments: Comparison of SAR age estimates to the terrace chronology of the Middle Thames valley, UK. *Quaternary Geochronology*.

Prescott, J.R. and Hutton, J.T. (1994) Cosmic ray contributions to dose rates for luminescence and ESR dating: large depths and long-term time variations. *Radiation Measurements*, 23, 497-500.

Singhvi, A.K., Bluszcz, A.., Bateman, M.D., Someshwar Rao, M. (2001). Luminescence dating of loess-palaeosol sequences and coversands: methodological aspects and palaeoclimatic implications. *Earth Science Reviews*, 54, 193-211.

Smith, B.W., Rhodes, E.J., Stokes, S. and Spooner, N.A. (1990) The optical dating of sediments using quartz. *Radiation Protection Dosimetry*, 34, 75-78.

Toms, P.S., Brown, A.G., Basell, L.S. and Hosfield, R.T. (2008) Palaeolithic Rivers of south-west Britain: Optically Stimulated Luminescence dating of residual deposits of the proto-Axe, Exe, Otter and Doniford. English Heritage Research Department Report Series, 2-2008.

Toms, P.S., Hosfield, R.T., Chambers, J.C., Green, C.P. and Marshall, P. (2005) Optical dating of the Broom Palaeolithic sites, Devon and Dorset. English Heritage Centre for Archaeology Report 16/2005.

Wallinga, J. (2002) Optically stimulated luminescence dating of fluvial deposits: a review. *Boreas*, 31, 303-322.

Wintle, A.G. (1973) Anomalous fading of thermoluminescence in mineral samples. *Nature*, 245, 143-144.

Zimmerman, D. W. (1971) Thermoluminescent dating using fine grains from pottery. *Archaeometry*, 13, 29-52.

Appendix E: Catalogue of OSL Sampling Locations

Please see separate file for Appendix E